PhD-FSTM-2021-59
The Faculty of Science, Technology and Medicine

DISSERTATION

Defence held on 22/09/2021 in Luxembourg (Luxembourg)

to obtain the degree of

DOCTEUR DE L'UNIVERSITÉ DU LUXEMBOURG

EN PHYSIQUE

by

Carl Johan Ingvar EKSTRÖM
born on 29/11/1990 in Lund (Sweden)

Quantum transport in topological condensed matter systems

Dissertation defense committee

Dr. Thomas Schmidt, Dissertation supervisor
Professor, Université du Luxembourg

Dr. Etienne Fodor, Chairman
Assistant professor, Université du Luxembourg

Dr. Susanne Siebentritt
Professor, Université du Luxembourg

Dr. Fabian Hassler
Professor, RWTH Aachen University

Dr. Alexander Holleitner
Professor, Technical University of Munich

Abstract

Topology in condensed matter physics is a field that has exploded in the last two decades. With the realization of its importance, some previously unexplained observations can now be explained. With the progress of time, many new topological phases of matter have been discovered, and topological materials have been shown to be fairly common in nature. Topological materials have further been shown to have properties that may be extremely useful for new technologies, such as spintronics and fault-tolerant quantum computation. The field is however, still evolving, and many properties of these materials are still unknown. In this thesis, we investigate how some of these types of materials react to applied external fields and the theories that can explain these observations.

First, we investigate systems of coupled Majorana bound states. More specifically, we focus on the transport properties of the Majorana box and the T-junction in the presence of charging effects, overlap between the Majorana bound states, and multiple terminals connected to the system. To obtain the transport properties, we apply a master equation and calculate the current through the systems as biases are applied to the different terminals. By tuning the gate voltage, the transport is investigated in both the regime where sequential tunneling is dominating as well as the Coulomb blockaded regime, where cotunneling is the leading transport process. When sequential tunneling is dominating, the transport is mediated by both single electrons tunneling as well as processes that involve the creation and annihilation of Cooper pairs. In the Coulomb blockaded regime, transport is driven by cotunneling processes by transitions via virtual states. The results here show that four-terminal measurements can be a useful tool to characterize the properties of Majorana bound states with finite overlap and charging energy.

Secondly, we study the optical activity of tilted nodal loop semimetals. The inherent Hall conductivity of topological materials makes the Kerr effect an excellent tool for investigating their properties. Here we first calculate the full conductivity tensor for a tilted nodal loop semimetal, where the tilt is in the $k_x - k_y$ plane. The conductivity tensor allows us to calculate the Kerr effect. We study this both for a thin film and a bulk material and we fin, in general, that the Kerr effect is large, similar to other topological materials.

Finally, we investigate electronic hydrodynamics in anomalous Hall insulators. First we derive the Navier-Stokes equations for topological materials and show that they are modified due to the Berry curvature. Secondly, we consider the flow in a narrow channel and the application of a small electric field. In this case, the Hall current can be neglected since it is much smaller than the longitudinal current. Flow in narrow channels conventionally leads to Poiseuille flow. However, as shown, the Berry curvature modifies the flow profile and shifts the maximum of the current profile towards one of the edges. Thirdly, we study the flow in an infinite geometry. In this case, it is shown that the Berry curvature induces whirlpools as well as causing an asymmetry in the profile of the electrical potential. Experimentally this can be observed by measuring the non-local resistance.

Acknowledgements

First of all I would like thank my advisor, Professor Thomas Schmidt, first of all for taking me aboard and allowing me both to widen my view on physics as well as on the world. Secondly for all the guidance and knowledge that he has shared. Thirdly I want to thank him for always keeping his door open for questions and scientific discussions as well as for his encouraging attitude.

Furthermore, I want especially to thank Dr. Eddwi Hesky Hasdeo for our scientific discussions, collaborations, and all the work he put in for the project on electronic hydrodynamics that I participated in. I further want to thank him for sharing his knowledge on light-matter interaction that was very valuable for the project on the Kerr effect in nodal loop semimetals. I am also thankful for the collaborations with Dr. Bélen Farias, Dr. Edvin Idrisov, and Professor Patrik Recher.

I want to thank Professor Susanne Siebentritt and Professor Fabian Hasseler for being part of my CET, for providing me with feedback during my Ph.D. and for taking part in the evaluation of my thesis, which I also thank Professor Etienne Fodor and Professor Alexander Holleitner for.

There are many people to thank outside the project I have been working on during my Ph.D. First of all, I want to thank Hugo Tschirhart with whom I shared much of the first year, both in the office as well as on the tennis court. Secondly, I want to thank Andreas Bock Michelsen for the friendship we have made ever since he arrived in Luxembourg, one year after me. I am most grateful for the impact he has had on my life the last three years and for all the new experiences our friendship has brought me.

I would also like to thank the friends that Andreas and I made from the economics department while sharing the same coffee room for a couple of months. Especially I want to acknowledge Nora Paulus and Nijat Hajikhanov. I am deeply grateful for our friendships, and I hope this will be something everlasting.

From the office, I would also like to thank my colleagues, and former ones, whom I have not already mentioned, Solofo Groenendijk, Sadeq Salehi, Kristof Moors, Alireza Habibi, Christophe De Beule, Kunmin Wu, and Andreas Haller, for making the last four years very enjoyable.

As for so many others, the last year and a half of my Ph.D. were impacted by the COVID-19 virus. This in many negative aspects. Nevertheless, the situation was bearable. Mainly because of the friendship I made with two of my then housemates Lisa Urban and Simone Rivabella. Among a few, they have become two of my closest friends, and I am deeply happy about this.

I also have to mention Lisa Gerla from whom I have received a lot of support the last couple of months.

Finally, I want to thank my parents. I'm mostly grateful for the support that I get from them. We did not get to see each other much during the last couple of years,

partially due to COVID-19, but I’m thankful for all the phone calls that were possible and the encouragement I got when I needed it.

Contents

Chapter 1

Introduction

1.1 Introduction

The development of condensed matter physics has been an exciting and blooming field of research for the last two centuries. One of the early observations came from the experiment by Edwin Herbert Hall, measuring a transverse voltage due to applied electric and magnetic fields [61]. The resulting transverse voltage is now known as the Hall voltage, and the effect itself as the Hall effect. Another important discovery was made in 1911 by Heike Kamerlingh Onnes, observing a vanishing resistance in mercury upon cooling the material to small temperatures ($< 10\,\mathrm{K}$) [45]. This effect is known as superconductivity. The experiment has since been followed by many others.

As the experimental observations progressed, it still took many years before the effects could be adequately explained, and a theoretical groundwork was laid out. The Hall effect could first be explained as the electron was discovered but then in terms of classical physics. Superconductivity, on the other hand, required the framework of quantum mechanics [16]. As quantum mechanics entered the picture, many other observations were also explained, and a powerful tool now existed to make new predictions.

With the technological improvements and the demand for better technologies, the importance of quantum mechanics has become even more evident. First, this is because many effects cannot be explained from a classical perspective. Second, many new technological improvements of devices require that they are made smaller. As we shrink devices, quantum mechanical effects become more evident. This becomes clear in, e.g., quantum dots, structures so small that they are essentially zero-dimensional and can be considered an artificial atom, [10].

A topic of condensed matter physics that has seen a considerable upswing in the last decades is topology. The importance of the discovery was to the extent that it awarded David J. Thouless, F. Duncan M. Haldane, and J. Michael Kosterlitz with the noble prize in 2016. Topology has led to many new exciting features. One important example is the quantized Hall conductivity first observed in the integer quantum Hall effect, [84].

Another interesting feature due to topology is edge and surface states that present themselves in some two and three-dimensional materials, respectively. An example of a topologically non-trivial two-dimensional material is the quantum spin Hall state, also more generally known as the topological insulator, [76, 23]. In three dimensions, there are different types of semimetals, such as the Weyl semimetal [166]. One of the essential features of the edge and surface states is that they are what is denoted as "topologically protected". This makes them stable even in the presence of different types of perturbations.

It is indeed the case that topology has also been carried over to superconducting materials. Just like the quasiparticles of topological insulators and those of Weyl semimetals are analogs to relativistic Dirac and Weyl fermions, respectively, so are those of topological superconductors. These are due to Ettore Majorana and are now known as Majorana fermions. The importance of Majorana fermions is that they may make topologically protected quantum computation realizable [139].

To develop new applications or just to please one's curiosity, these types of materials have to be understood. We can do this in many different ways, but as theorists we should develop a theory that can explain or lead to new experiments. Such experiments might be measurements of the electron transport through the material by applications of different currents and voltages. Another way is to study how the material interacts with light. For example, we can do this by measuring the properties of the reflection and transmission of an incident beam on the material surface. Some materials may change the properties of the light such that the reflected and transmitted beams are different from the incident one in more than their propagation direction. This is what is known as the Kerr and Faraday effects, respectively.

1.2 Outline

This thesis explores a variety of different topics. The structure is in the following manner: The thesis begins with a brief history and introduction to topology in condensed matter physics and how it is related to the concept of topology in mathematics. A discussion on some of the implications of topology as well as some common material classes are discussed. This chapter is then followed by three chapters on which this thesis is mainly based upon, where every chapter includes a small introduction, specific to the material of that chapter.

Chapter 3 is based on the results obtained in the paper titled *Transport in coupled Majorana bound states*. The chapter begins with giving an introduction to Majorana physics and explain how they can possibly be realized. We thereafter discuss two different setups of hosting Majorana bound states and the transport properties of these setups. Importantly the effects of finite overlap between the Majorana bound states and Coulomb interactions are taken into account.

In Chapter 4 we explore the Kerr and Faraday rotation of Nodal loop semimetals. This chapter is based on the paper titled *Kerr effect in tilted nodal loop semimetals*. Here the conductivity tensor for a tilted nodal loop semimetal is calculated using the Kubo formalism. With the knowledge of the conductivity tensor, the Kerr angle and ellipticity are calculated for both a thin film and a semi-infinite bulk material. The results give predictions on what different experimental measurable quantities correspond to with respect to the properties of the nodal loop. This includes the tilt velocity, tilt angle, and radius of the nodal loop. The theory we developed to obtain the results for the Kerr angle along with the theory for calculating the Faraday angle was further applied to obtain the Kerr and Faraday angles in the paper *Optical properties of topological flat and dispersive bands*.

Chapter 5 discuss the theory of electronic hydrodynamics. At first, an introduction is given, discussing the applicability of the theory, and furthermore it is presented how to obtain the hydrodynamic equations. To come to the final equations, we specifically consider a two-dimensional Hall material. This lead to the results obtained in the paper *Hydrodynamic equations of two dimensional anomalous Hall materials*.

Finally, a conclusion and future prospects are presented in Chapter 6.

Chapter 2

Topology in condensed matter physics

We begin this work by giving an introduction and an overview of the field of topology and how to apply it in condensed matter physics. We will further explain some different materials and how topology plays a role in some of the properties of these materials where topology plays an important role.

2.1 Topology

Topology originally stems from the field of mathematics and concerns itself with classifying different geometrical objects. However, the first real-world problem to which topology was applied was in a study made by Leonard Euler in the 18th century. The problem is the famous *Bridges of Königsberg* problem [148], that was posed by inhabitants of the city. The problem is as follows: The city was located on a river fork with an island in the center. The river hence separated the land into four areas which had been connected by a set of bridges, as seen in Fig. 2.1. Now, the question is, can a person stroll through the city and cross the bridges once and only once?

The problem is of a topological nature because the issue here is the connectivity rather than the specific geometry or the distance between the bridges and the islands. The paper that presented the solution was at the starting point of the foundational papers of modern mathematics. As we shall soon see, the field of topology has evolved into an essential tool in many areas, not just mathematics but, among others, the field of condensed matter physics. Before we delve into this, let us briefly discuss what its meaning is for classifying surfaces.

Two objects or, more precisely, two surfaces have the same topology if one can deform the surface of one and turn it into the other without tearing, gluing or poking holes in its surface. This means that a sphere and a torus do not have the same topology since to turn a sphere into a torus, one has to make a hole in the sphere. On the other hand, the topology of a torus and a cup is the same since we can smoothly shape the cup into a torus. The mathematical quantity describing the topology of a surface is the genus. The genus of a surface essentially states how many "holes" the

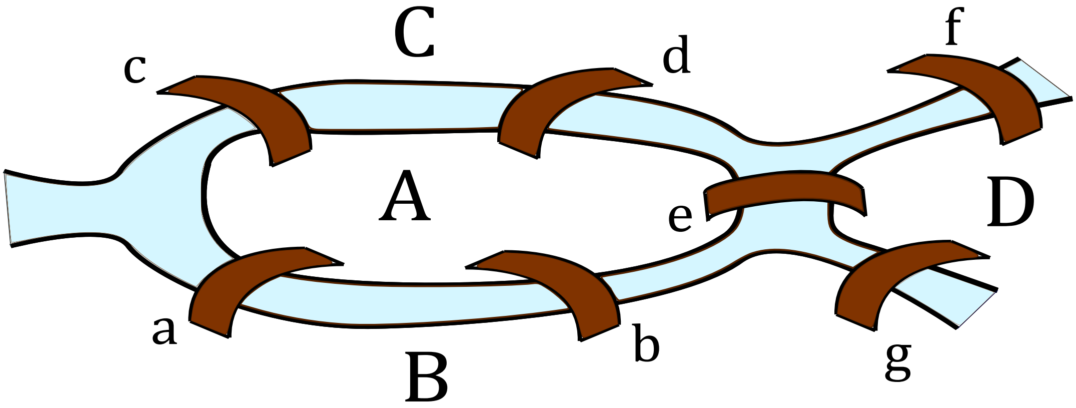

FIGURE 2.1: Cartoon of the city of Königsberg. The city is divided into four islands marked by capital letters. The lowercase letters mark the crossings. The question stated by the inhabitants reads: Can a person go on a stroll through the city and only cross the bridges once and only once?

object has. Hence the genus of a sphere is zero since it has no holes, while the genus of a torus has a genus of one. The genus is further said to be a topological invariant since it does not depend on the exact shape of the surface but only on the number of holes.

To mathematically be able to quantify the genus of a surface, one can introduce the concept of Gaussian curvature, which we denote by K. The Gaussian curvature tells how the surface changes locally. By orienting the surface such the point P lies in the tangent plane described by $z(x, y) = 0$, K can be defined as

$$K(P) = \begin{vmatrix} \partial_x^2 z\big|_P & \partial_x \partial_y z\big|_P \\ \partial_y \partial_x z\big|_P & \partial_y^2 z\big|_P \end{vmatrix}. \tag{2.1}$$

A beautiful theorem named after the mathematicians Gauss and Bonnet then states the the surface integral of K equals the Euler characteristic [114], i.e.

$$\chi = \frac{1}{2\pi} \int_S dA\, K, \tag{2.2}$$

where χ is the Euler characteristic. The Euler characteristic is directly related to the genus g of the surface by: $\chi = 2 - 2g$. For example, for a sphere $K = 1/R^2$, with R the radius of the sphere. Performing the integral, Eq. (2.2), one obtains $\chi = 2$, which further implies that $g = 0$, as expected for an object without a hole.

This concludes this section where we have presented the essential concepts of topology in mathematics. These will prove to have analogies in the field of condensed matter physics, which we delve into in the next section.

2.2 Topology in condensed matter physics

Just as topology can be used to classify different objects, it was discovered that topology could also be applied in the field of condensed matter physics. The discoveries led to the Nobel prize being awarded to the physicists David J. Thouless, F. Duncan M. Haldane, and J. Michael Kosterlitz. It has been shown to have a significant impact as it serves as a tool to characterize different phases of matter and explain many properties of different types of materials.

Similar to the geometrical concept of topology, topology in condensed matter physics has to do with smooth deformations. In this case, insulators are said to be topologically equivalent if their Hamiltonians can be smoothly deformed into each other without closing the energy gap.

Not only has the field of topology in condensed matter physics led to a way of characterizing materials, it has also led to technological advancements beyond just the characterization. It has turned out to have important implications for electron transport which in turn can be proven useful for different applications.

Another application of topology in condensed matter physics is towards the creation of topological quantum computation. This followed with the discovery of topological superconductors and Majorana bound states. This is still a complicated field, but if successful could lead to revolutionizing progress for the field of quantum computation. In this context, it must not only involve the band structure of the material but a general parameter space where we adjust some parameters, of the system under consideration, adiabatically.

The starting point of the story of topology and its importance in condensed matter physics can, of course, be discussed, but one recognized starting point is the quantum Hall (QH) effect . The story then continues with some concepts that play an essential role for topology in condensed matter physics. This is then followed by an overview of some more exotic materials such as quantum spin Hall insulators and topological insulators, and topological semimetals. Thus, let us dive back into the history of topological materials and as well introducing some of the important concepts.

2.2.1 Quantum Hall materials

The first step towards the rise of topology in condensed matter physics came from the discovery of the QH effect. In Hall experiments, a magnetic field is applied perpendicular to a sample. As a bias voltage is applied, which generates an electric field inside the material, it is possible to measure a longitudinal current and a transverse voltage difference. This is readily explained by using a semiclassical picture to describe the motion of the electrons. When the magnetic field is applied, the momentum of the electrons is not only proportional to the electric field but furthermore acquires a term produced by the Lorentz force that is perpendicular to the direction

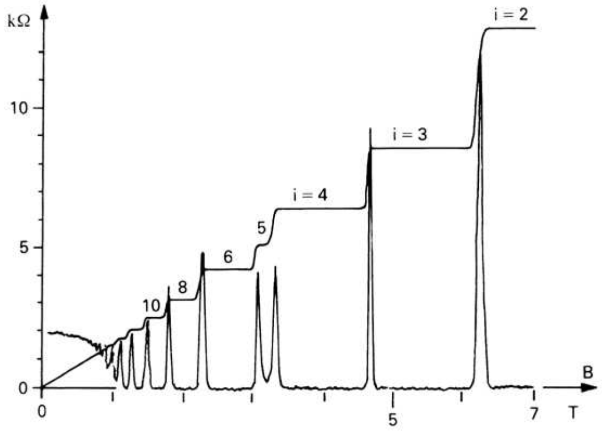

FIGURE 2.2: Measurement of the (integer) quantum Hall effect. The figure is adapted from [160]

of the electron trajectory. An interesting result is that the Hall resistivity (transverse resistivity) is proportional to the magnetic field [44]

$$\rho_{xy} = \frac{B}{ne}, \tag{2.3}$$

where e is the electron charge and n is the electron density. Furthermore, the Hall resisitvity is independent of sample dimensions making it a powerful quantity to measure for example the electron density of a material.

As technology advanced, the same setup was studied but with the application of strong magnetic fields. In this endeavor, von Klitzing discovered that the Hall resistivity, ρ_{ij}, strongly deviates from what one expects, giving the Hall measurements at small magnetic fields. The result from the measurements is depicted in Fig. 2.2. For small magnetic fields, the resistivity behaves as one would expect from the classical formulation and what had been previously observed. However, as the applied magnetic field is increased, one sees plateaus appearing in ρ_{xy}. These are shown to exactly correspond to

$$\rho_{xy} = \frac{h}{e^2}\frac{1}{\nu} \tag{2.4}$$

where ν is the filling factor. For the integer quantum Hall effect $\nu \in \mathbb{Z}$. However, in general, ν can take any number. Inverting the resistivity leads to the conductivity

$$\sigma_{xy} = \frac{e^2}{h}\nu. \tag{2.5}$$

The conductivity is hence quantized and takes, for the integer quantum Hall (IQH) effect, only integer values times one-half of the conductance quantum, $G_0 = 2e^2/h$. This is recognized as one of the first observations of topology in condensed matter physics. Another feature of the QH effect is the formation of edge states. Because of the magnetic field, the electrons are localized to cyclotron orbits. The cyclotron orbits are quantized and are the reason for the formation of the so-called Landau levels. In a classical picture, the electrons move in cyclotron circles. However, the electrons that are close to the edge of the sample cannot complete the orbit. This forces them to move along the edge by skipping orbits. These skipping orbits are what are now known as the edge states.

The quantized conductivity, Eq. (2.5), is a robust feature of a quantum Hall system. The phase transition between the system with quantized conductivity and the system with continuous conductivity cannot be explained by Landau theory. It can however be explained by a topological invariant. We delve into this concept in the following sections!

2.2.2 Berry connection, Berry curvature and Berry phase

One important ingredient in the study of topology in condensed matter systems is the Berry connection, curvature, and phase. In 1984 Micheal Berry discovered the Berry phase. It was at that time coined and is to some extent still known as the "Geometrical phase" [25]. The reason for its importance is not very complicated. The wave function is, in quantum mechanics, defined up to a phase, which in most cases is neglected as an irrelevant factor. However, as noticed by Berry, this cannot always be done. The phase can have observable consequences for a system that undergo an adiabatic change. Here "adiabatic change" is in the quantum mechanical sense. This means that a physical system remains in an instantaneous eigenstate if a perturbation is acting slowly and there is a gap between the corresponding eigenvalue and the rest of the spectrum of the Hamiltonian. To give a more precise mathematical statement, consider a Hamiltonian $H(\mathbf{R})$ that depends on the collective parameters $\mathbf{R}(t)$. The Hamiltonian satisfies the Schrödinger equation, and the eigenstates at $t = 0$ are given by

$$H(\mathbf{R}(\mathbf{0}))\,|n,\mathbf{R}(0)\rangle = E_n(\mathbf{R}(0))\,|n,\mathbf{R}(0)\rangle\,. \tag{2.6}$$

Now we are interested in the time evolution of the eigenstates. By the assumption of adiabaticity, we know that the system remains in the same eigenstate. As such the time-evolved state, $|\Psi(t)\rangle$ can only differ from $|n,\mathbf{R}(0)\rangle$ by a phase factor. Hence, one makes an anzats for the time evolved state and shows that it satisfies the time-dependent Schrödinger equation. The eigenstate that solves the problem is

$$|\Psi(t)\rangle = \exp\left[i\gamma_n(t) - i\int_0^t ds\,E_n(\mathbf{R}(s))\right]|n,\mathbf{R}(t)\rangle\,. \tag{2.7}$$

Here the second term in the exponential is the dynamical phase. It is the first term however that is of special interest. After some further mathematical manipulations one finds that it can be written as

$$\gamma_n(t) = i\int_{\mathbf{R}(0)}^{\mathbf{R}(t)} d\mathbf{R}\,\langle n,\mathbf{R}(t)|\,\nabla_{\mathbf{R}}\,|n,\mathbf{R}(t)\rangle\,. \tag{2.8}$$

This quantity, γ_n is what is the so-called *Berry phase*. Now the interesting fact about the Berry phase is that if we suppose that the system executes a closed loop in $\mathbf{R}$ space, such that $\mathbf{R}(0) = \mathbf{R}(T)$ then the integral in the expression for the Berry phase seems to vanish. However, since the integrand is not necessarily a total derivative, the integral will not always become zero.

The quantity under the integral sign of the Berry phase is the so called *Berry connection*. Opposite to the Berry phase this is a gauge dependent quantity and can hence not be observed in any experiments. We write the Berry connection as

$$\mathbf{A} = -i \langle n, \mathbf{R}(t) | \nabla_{\mathbf{R}} | n, \mathbf{R}(t) \rangle . \tag{2.9}$$

Assuming that we are considering a 3-dimensional space and that the system executes a closed loop, $\mathcal{C}$ in $\mathbf{R}$ space, then the Berry curvature can be re-written using, Stokes theorem, to obtain

$$\gamma_n = \int_{\mathcal{S}} d\mathbf{S} \cdot \mathbf{\Omega}, \tag{2.10}$$

where

$$\mathbf{\Omega} = \nabla \times \mathbf{A}, \tag{2.11}$$

is the *Berry curvature* and $\mathcal{S}$ is the surface with boundary given by $\mathcal{C}$. The Berry curvature has several important consequences. It for example plays an important role in the definition of the Chern number as well as it shows up as a modification of the semiclassical equations of motion. Comparing to Eq. (2.2) we note that the Berry curvature plays a similar role to the Gaussian curvature. Let us now explore some of the implications of the Berry curvature, the previously mentioned Chern number and how it modifies the semiclassical equations of motion.

2.2.3 Chern number – a topological invariant

We will now briefly discuss the Chern number and its relation to the IQH effect, the Berry phase and also how it is related the to genus of surfaces. For this we will consider a non-interacting particle on a two dimensional lattice and whose wave function in k space is described by the Bloch functions

$$\psi_{\mathbf{k}}(\mathbf{x}) = e^{i\mathbf{k}\cdot\mathbf{x}} u_{\mathbf{k}}(\mathbf{x}), \tag{2.12}$$

where we assume that $u_{\mathbf{k}}$ is periodic on a unit cell. The electron moving within each band can take momenta given by

$$-\frac{\pi}{a} < k_x < \frac{\pi}{a}, \quad -\frac{\pi}{b} < k_y < \frac{\pi}{b} \tag{2.13}$$

where a and b are the distances between the lattice sites in the x and y directions, respectively. This corresponds to a Brillouin zone (BZ) defined by a tours, $\boldsymbol{T}^2$. Furthermore, apart from assuming that the electrons are non-interacting, we have to assume that the spectrum of the particles forms bands that can each be parameterized by $\mathbf{k}$ that belongs to the set spanned by $\boldsymbol{T}^2$. We also assume that the Fermi-energy, E_F lies between the bands such that all bands below E_F are filled, and the ones above are empty.

Under the above assumptions one can assign, to every band, a topological invariant that is the so-called Chern number. This is a consequence of how the phase of the states winds as we move around $\boldsymbol{T}^2$. This can be formulated by a Berry connection over $\mathbf{T}^2$,

$$\mathcal{A}_i(\mathbf{k}) = -i \langle u_{\mathbf{k}} | \frac{\partial}{\partial k_i} | u_{\mathbf{k}} \rangle . \tag{2.14}$$

We can here draw a parallel to the Berry connection introduced in the previous section by identifying the space of parameters, $\mathbf{R}$ with the space spanned by $\mathbf{k}$. We now calculate the field strength that is associated with the Berry connection,

$$\mathcal{F}_{xy} = \frac{\partial \mathcal{A}_x}{\partial k_y} - \frac{\partial \mathcal{A}_y}{\partial k_x} = -i \left\langle \frac{\partial u}{\partial k_y} \middle| \frac{\partial u}{\partial k_x} \right\rangle + i \left\langle \frac{\partial u}{\partial k_x} \middle| \frac{\partial u}{\partial k_y} \right\rangle . \tag{2.15}$$

Integrating this quantity over the whole Brillouin zone can result in either that it is zero or an integer, hence

$$-\frac{1}{2\pi} \int_{BZ} dk_x dk_y \, F_{xy} = C, \tag{2.16}$$

where $C \in \mathbb{Z}$. This is the Chern number. We can furthermore for every band i associate a Chern number C. Now, we want to somehow relate this with the IQH effect. This was considered in the seminal work by Thouless, Kohomot, Nightingale, and den Nijs [159]. By applying the Kubo formula, they could essentially show that (a detailed calculation can be found in [24])

$$\sum_i C_i = \frac{h}{e^2} \sigma_{xy}. \tag{2.17}$$

Hence we see that the conductivity is directly proportional to the sum of the Chern numbers of the occupied bands. This explains the quantized Hall conductivity observed in Fig. 2.2.

We have already elucidated on its connection to the Berry phase. We further note that as perturbations to the system remain small, such that the adiabatic theorem holds, the system will remain in a specific state. Thus the Chern number should remain invariant as long as the system is not subject to any large perturbations.

Finally, we remark that the Chern number is related to the Euler characteristic by observing the close relationship between the Gauss-Bonnet theorem, Eq. (2.2), where essentially the Berry curvature takes the role of the Gaussian curvature.

2.2.4 Modified semiclassical equations of motion

One of the oldest problems in condensed matter physics is that of the dynamics of Bloch electrons under the applications of various fields. This has long been studied and the dynamics that were initially discovered can be written as [9]

$$\dot{\mathbf{r}} = \frac{1}{\hbar}\frac{\partial \mathcal{E}_n}{\partial \mathbf{k}}, \tag{2.18}$$

$$\hbar\dot{\mathbf{k}} = -e\left(\mathbf{E} + \dot{\mathbf{r}} \times \mathbf{B}\right), \tag{2.19}$$

where $\dot{\mathbf{r}}$ is the electron velocity in the one-band approximation and $\mathcal{E}$ is the energy spectrum of the nth band. The second equation describes the dynamics of the quasi-momentum $\mathbf{k}$, which is governed by the Lorentz force, where $\mathbf{E}$ and $\mathbf{B}$ are the external applied electric and magnetic field, respectively. These equations are known as the semiclassical equations of motion. However, not so long ago it was proven that these equation are not final [33]. They should in fact be modified to include a term that involves the Berry curvature.

To derive the semiclassical equations of motion. we consider a wave packet, write the Lagrangian for it and obtain the dynamics by writing the Euler-Lagrange equations [33]. First, we define the Hamiltonian that governs the dynamics of the wave packet. This is given by

$$H = \frac{1}{2m}\left[-i\hbar\frac{\partial}{\partial \mathbf{r}} + e\mathbf{A}_0(\mathbf{r}) + e\delta\mathbf{A}(\mathbf{r},t)\right]^2 + V(\mathbf{r}), \tag{2.20}$$

where $\mathbf{A}_0$ is the vector potential of a uniform magnetic field, $-\partial\delta\mathbf{A}/\partial t = \mathbf{E}$ and $\nabla \times \delta\mathbf{A} = \delta\mathbf{B}$ are external applied fields that can vary in space and time, and are small such that they can be considered as perturbations. Finally, $V(\mathbf{r})$ is the periodic potential. The wave packet is constructed from the Bloch functions $|\Psi_n(\mathbf{k})\rangle$ (for applied magnetic fields these are the magnetic Bloch functions), such that

$$|W_0\rangle = \int d\mathbf{k}\, w(\mathbf{k},t)\, |\Psi_n(\mathbf{k})\rangle\,, \tag{2.21}$$

where $w(\mathbf{k},t)$ is the envelope function. The envelope function has to fulfill that

$$\mathbf{k}_c = \int d\mathbf{k}\,\mathbf{k}|w(\mathbf{k},t)|^2 \tag{2.22}$$

This implies that $w(\mathbf{k},t)$ has a sharp distribution in the Brillouin zone such that it makes sense to speak about a wave packet. Furthermore, it has to be localized around its center of mass, $\mathbf{r}_c$, in real space, such that

$$\mathbf{r}_c = \langle W_0|\,\mathbf{r}\,|W_0\rangle\,. \tag{2.23}$$

The wave packet is depicted in Fig. 2.3. By a calculation we can obtain

$$\langle W_0|\,\mathbf{r}\,|W_0\rangle = \int d\mathbf{k}\left[w^*(\mathbf{k})i\frac{\partial}{\partial \mathbf{k}}w(\mathbf{k}) + |w(\mathbf{k})|^2\,\langle(\mathbf{k})|\,i\frac{\partial}{\partial \mathbf{k}}\,|u(\mathbf{k})\rangle_{cell}\right], \tag{2.24}$$

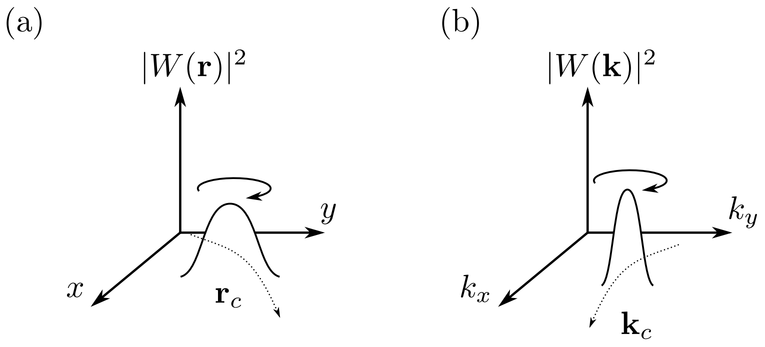

FIGURE 2.3: Illustration of the constructed wave packet in (a) real space and in (b) momentum space. The wave packet can possibly rotate due to an orbital magnetic moment.

where

$$\boldsymbol{\mathcal{A}}(\mathbf{k}) = i \langle(\mathbf{k})| \frac{\partial}{\partial \mathbf{k}} |u(\mathbf{k})\rangle_{cell} . \tag{2.25}$$

and $|u_n(\mathbf{k})\rangle = e^{-i\mathbf{k}\cdot\mathbf{r}} |\Psi_n(\mathbf{k})\rangle$ (see Eq. (2.12)). Here *cell* denotes that the integral should be over the unit cell (if magnetic fields are applied this should be the magnetic unit cell). This can clearly be seen to coincide with the Berry connection in k space (compare this with Eq. (2.9)). We now seek the Lagrangian for the wave packet. By a time dependent variational principle the Lagrangian can be written [89]

$$L(\mathbf{r}_c, \mathbf{k}_c, \dot{\mathbf{r}}_c, \dot{\mathbf{k}}_c) = \langle W| i\hbar \frac{\partial}{\partial t} |W\rangle - \langle W| H |W\rangle , \tag{2.26}$$

where $|W\rangle$ is a wave packet centered at $\mathbf{r}_c$ and $\mathbf{k}_c$ in the presence of external fields. A gauge can always be chosen such that the vector potential $\delta\mathbf{A}$ is locally gauged away for a specified point $\mathbf{r} = \mathbf{r}_c$ [33]. The wave packet $|W\rangle$ can then be approximated by

$$W(\mathbf{r}) = e^{-ie\hbar\delta\mathbf{A}(\mathbf{r}_c,t)\cdot\mathbf{r}} W_0(\mathbf{r}). \tag{2.27}$$

We now evaluate the terms of the Lagrangian. First we expand the Hamiltonian and neglect terms that are quadratic in $\delta\mathbf{A}$. For the first term we obtain

$$\langle W_0| i\hbar \frac{\partial}{\partial t} |W_0\rangle = -e\delta\mathbf{A}\cdot\mathbf{r}_c + \hbar\mathbf{k}_c\cdot\dot{\mathbf{r}}_c + \hbar\dot{\mathbf{k}}_c\cdot\boldsymbol{\mathcal{A}}(\mathbf{k}_c), \tag{2.28}$$

where we used that the amplitude can be written $w(\mathbf{k},t) \equiv |w(\mathbf{k},t)|e^{-i\gamma(\mathbf{k},t)}$ and that $|w(\mathbf{k},t)|^2 \approx \delta(\mathbf{k}-\mathbf{k}_c)$. The second part is given by

$$\langle W| H |W\rangle \simeq \mathcal{E}(\mathbf{k}_c) + \frac{e}{2m}\delta\mathbf{B}\cdot\langle W_0| \mathbf{L} |W_0\rangle , \tag{2.29}$$

where $\mathbf{L} = (\mathbf{r}-\mathbf{r}_c)\times\mathbf{P}$ and $\mathbf{P}$ is the mechanical momentum operator corresponding to $H_0 = \frac{1}{2m}\left[-i\hbar\frac{\partial}{\partial\mathbf{r}} + e\mathbf{A}_0(\mathbf{r})\right]^2 + V(\mathbf{r})$, and where we have explicitly used the symmetric gauge for which $\delta\mathbf{A}(\mathbf{r},t) = -\mathbf{E}t + \frac{1}{2}\delta\mathbf{B}\times\mathbf{r}$. The second term of Eq. (2.29) is a correction to the energy due to an orbital magnetic moment of the wave packet.

Assembling the two above equations the Lagrangian is written as

$$L(\mathbf{r}_c, \mathbf{k}_c, \dot{\mathbf{r}}_c, \dot{\mathbf{k}}_c) = -e\delta\mathbf{A}(\mathbf{r}, t) \cdot \dot{\mathbf{r}}_c + \hbar\mathbf{k}_c \cdot \dot{\mathbf{r}}_c + \hbar\dot{\mathbf{k}}_c \cdot \boldsymbol{\mathcal{A}}(\mathbf{k}_c) - \mathcal{E}(\mathbf{k}_c) + \frac{e}{2m}\delta\mathbf{B} \cdot \mathbf{L}(\mathbf{k}), \tag{2.30}$$

where $\mathbf{L}(\mathbf{k}) = \langle W_0 | \mathbf{L} | W_0 \rangle$. This equation can be shown to be gauge invariant because under a gauge transformation for $\mathbf{A}_0(\mathbf{r})$ will only change L by a total time derivative. This also holds when specifying a different gauge for $\delta\mathbf{B}$ and implies that the dynamics are invariant under a gauge transformation. The dynamics are now found by applying the Euler-Lagrange equation, $\frac{d}{dt}\left(\frac{\partial L}{\partial \dot{x}}\right) - \frac{\partial L}{\partial x} = 0$. We then obtain

$$\dot{\mathbf{r}} = \frac{1}{\hbar}\frac{\partial}{\partial \mathbf{k}}\left(\mathcal{E}_n(\mathbf{k}) + \frac{e}{2m}\delta\mathbf{B} \cdot \mathbf{L}(\mathbf{k})\right) - \dot{\mathbf{k}} \times \boldsymbol{\Omega}_n(\mathbf{k}), \tag{2.31}$$

$$\dot{\mathbf{k}} = -e\mathbf{E} - e\dot{\mathbf{r}} \times \delta\mathbf{B}, \tag{2.32}$$

where $\boldsymbol{\Omega}_n(\mathbf{k}) = \nabla \times \boldsymbol{\mathcal{A}}(\mathbf{k})$ is the Berry curvature. We have here also omitted the subscripts. From the first equation, we see the modification due to the Berry curvature that will induce a transverse component to the velocity, $\dot{\mathbf{r}}$. Hence, this term plays an essential role in understanding different transport phenomena. Let us, for example, consider the current in two dimensions,

$$\mathbf{J} = -e\sum_n \int \frac{d\mathbf{k}}{(2\pi)^2}\dot{\mathbf{r}} f(k), \tag{2.33}$$

where $f(k)$ is the Fermi distribution [147]. Let us assume that all bands below the Fermi levels are filled, and those above are empty. This results in the first term of Eq. (2.31) equals zero. The second term defines the Hall current,

$$J_\alpha = \sigma_H \varepsilon_{\alpha\beta} E_\beta, \tag{2.34}$$

where $\varepsilon_{\alpha\beta}$ is the Levi-Civita symbol and

$$\sigma_H = \frac{1}{2\pi}\frac{e^2}{\hbar}\sum_n \int_{BZ} d\mathbf{k}\,\Omega^n_{k_x,k_y}. \tag{2.35}$$

It furthermore follows that

$$\Omega^n_{k_x,k_y} = \Omega^n_{k_x+\pi,k_y} = \Omega^n_{k_x,k_y+\pi}. \tag{2.36}$$

Because of this the first Brillouin zone forms a torus. The above expression assumes that the valence band is fully occupied and that there is a gap to the conduction band that is empty. Integrating over a closed torus gives an integer and hence

$$\sigma_H = \nu\frac{e^2}{h}. \tag{2.37}$$

This again proves the quantization of the Hall conductivity. This is just one example of many. For an extensive review on Berry curvature effects on electronic properties, see for example [177]. Furthermore, in Chapter 5, we extend this to understand the effects of the Berry curvature in electronic hydrodynamics.

We have now, in the preceding sections, explained a few concepts that are important for understanding some of the physics that is observed in different materials from a perspective of topology. Importantly we saw that for a 2D system in a strong magnetic field, the Hall conductivity is directly related to the Chern number. However, a net magnetic field is not necessary. This was shown when Haldane considered a system where the lattice is threaded by different magnetic fluxes such that the net magnetic field is zero [60]. This system is known as a *Chern insultor*. The key for the non-zero Hall conductivity is the breaking of time-reversal (TR) symmetry.

2.3 Quantum spin Hall effect and $\mathbb{Z}_2$-invariant

In the previous section, we discussed Hall materials as the starting point of topology in condensed matter physics. We further introduced the concept of Berry curvature and showed how this leads to the topological invariant, the Chern number. We finally noted that the critical feature, as discovered by Haldane, [60], is the breaking of TR-symmetry. However, in 2005, Kane and Mele discovered a new state of matter that is symmetric under TR and for which furthermore a topological invariant can be defined. This state of matter is the quantum spin Hall (QSH) state, [76, 77].

The key idea of this state is the spin-orbit coupling, which acts as a magnetic field that is opposite for the different spin directions. As a result, electrons with opposite spin experience separate quantum Hall effects. Hence the QSH state can be viewed as two copies of the IQH state, where electrons with opposite spins propagate in opposite directions along the edges. Becuase of this the edge states are also known as being helical.

The fact that TR symmetry is preserved implies that the Chern number equals zero. However, this state is still not a normal insulator. Another topological invariant can be defined, the $\mathbb{Z}_2$ invariant, which may take the values $\nu = 0$ or $\nu = 1$. One consequence of this is that the edge states should be robust to perturbations. To understand the $\mathbb{Z}_2$ invariant, one has to understand the implications of TR symmetry.

Time-reversal means that $t \to -t$. This implies that $p \to -p$ and $\sigma \to -\sigma$. Formally this is written $\mathcal{T}^{-1} p \mathcal{T} = -p$ and $\mathcal{T}^{-1} \sigma \mathcal{T} = -\sigma$. Here $\mathcal{T}$ is the TR operator. One property of this operator is that it squares to minus one, $\mathcal{T}^2 = \pm 1$. When it squares to plus or minus one, it leads to what is known as Kramer's theorem, which states that all eigenstates of a TR invariant Hamiltonian are at least two-fold degenerate [138]. Because of Kramers theorem, eigenstates with momenta $-\mathbf{k}$ and $\mathbf{k}$, and given that the Hamiltonian has translational symmetry, must have the same energy. As a result, there are only certain points in the Brillouin zone where a pair of degenerate states exist, known as TR invariant momenta.

To understand the $\mathbb{Z}_2$ invariant, we argue from the perspective of the bulk-boundary correspondence [53]. Consider a band structure with a gap separating the valence and conduction bands. Inside the gap, bound states may exist, depending on the Hamiltonian. If they exist, then Kramers theorem requires that they are two-fold degenerate at the TR invariant momenta. Away from these points, the degeneracy is split by the SO coupling. If there are an odd number of states inside the gap, not all can be gapped out without violating TR-symmetry. On the other hand, if an even number of states reside in the gap, these can be gapped out without violating TR-symmetry.

The number of edge states in the gap depends on the topological class of the bulk band structure. Since each band crossing the Fermi level at momentum $\mathbf{k}$ has a Kramers partner at momentum $-\mathbf{k}$, the bulk-boundary correspondence relates the number of Kramers pairs of edge modes N_k that intersect the Fermi level to the change in the $\mathbb{Z}_2$ invariants such that

$$N_K = \Delta\nu \bmod 2. \tag{2.38}$$

Because of this, the QSH effect has topologically protected edge states. To conclude this section, let us mention a few materials that have been discovered belonging to the QSH phase. The first discovery of the QSH effect was based on graphene with strong SO coupling [76]. Soon after this, the QSH effect was proposed to exist in HgTe quantum wells [23]. This was later experimentally confirmed [88]. A suggestion for observing the QSH effect in the more conventional InAs/GaSb quantum wells was proposed [98]. However, experimentally it has been shown that the bulk remains conducting even at milli-Kelvin temperatures. Another discovery is the existence of the QSH effect in monolayer WTe_2 [133]. Another experimental work [175] shows that the QSH effect in WTe_2 survives for temperatures as large as 100 K!

The QSH state defines the topological insulator in two dimensions. These can be generalized to three dimensions, then characterized by four $\mathbb{Z}_2$ numbers [53]. We will not discuss these here but instead introduce another type of topological material, the topological semimetals.

2.4 Topological semimetals

A class of materials discovered not long after the topological insulators are the topological semimetals [8]. The most common are the Weyl semimetals, Dirac semimetals, and nodal line semimetals. These materials are three-dimensional phases of matter and exhibit gapless electronic excitations, that are induced by the bulk topology. Furthermore, topology and symmetries protect the gapless electronic excitations. The specific properties of the band structure further leads to protected surface states and unusual responses when electric and magnetic fields are applied. These responses include a variety of different phenomena such as an anomalous Hall effect [30] and large thermopower [102].

The gapless excitations of semimetals are equivalent to band crossings in the band structure. Two different types of band crossings exist, accidental band crossings and symmetry-enforced band crossings. Accidental band crossings are band crossings that are protected by symmorphic crystal symmetries but can be adiabatically gapped out by symmetry-preserving perturbations. On the other hand, symmetry-enforced band crossings are required to exist by certain symmetries and will protect the band crossing even against large perturbations. These exist due to nonsymmorphic symmetries or, in other words, screw and glide symmetries, which leave the crystal symmetric under fractional lattice translations. Let us now look at two examples of semimetals that exist due to accidental band crossings, Weyl semimetals and nodal loop semimetals.

2.4.1 Weyl semimetals

Weyl semimetals are such materials that realize band crossing at single points in k space. Hence, there exist points where the valence and conduction band touch. An example of this is presented in the left of Fig. 2.4. These points exist due to accidental band crossings and may arise due to presence and absence of certain symmetries. One example of this is if only TR symmetry is present. As we saw for the QSH state this typically leads to nondegenerate bands and only at the TR invariant momenta are Kramers degeneracies present. Another case that typically leads to nondegenerate bands is when only inversion symmetry is present. As mentioned above, they are, furthermore, stable against small perturbations. To understand this, we expand the full material Hamiltonian around such a point. This can be written as [8]

$$H(\mathbf{k}) = f_0(\mathbf{k})\mathrm{I}_{2\times 2} + f_1(\mathbf{k})\sigma_x + f_2(\mathbf{k})\sigma_y + f_3(\mathbf{k})\sigma_z, \tag{2.39}$$

where $f_{0,1,2,3}$ are real functions. Now, for the bands to coincide it is required that $f_1 = f_2 = f_3$ at the same time. First, this implies the requirement of three spatial dimensions. Second, the protection against small perturbations can be explained by considering the stability of the band crossings. Consider first the function f_1 and where it vanishes. This is typically spanned by a two-dimensional surface. To simultaneously have $f_1 = f_2 = f_3$ we do the same for f_2 and f_3, we hence look for the intersection of three 2D surfaces. Typically this happens at a single point. We now consider a small perturbation that changes f_i by a small amount. As a consequence the intersection point between the planes will change slightly. However, the intersection persist, hence the band crossings remains but at a different crystal momentum. By such the band crossings are stable against small perturbations.

Based on the above discussion, it may appear that a Weyl semimetal can be realized simply by breaking appropriate symmetries in 3D crystals exhibiting nondegenerate bands. Typically one also requires that they are close to the Fermi level, i.e.,

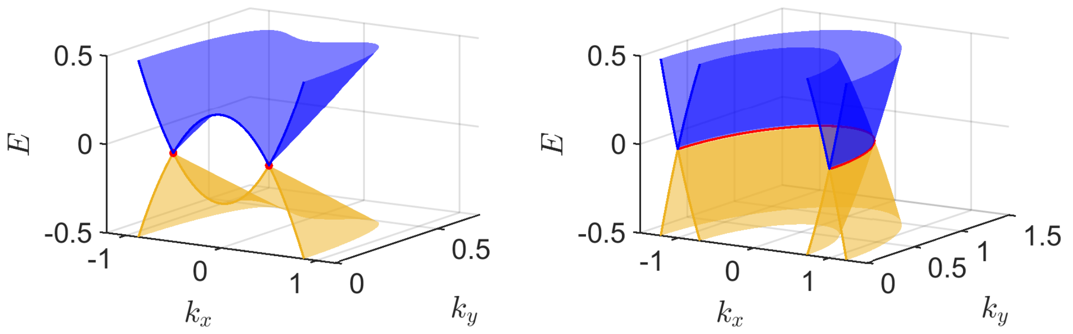

FIGURE 2.4: (Left) Spectrum of a Weyl semimetal at $k_z = 0$ with two Weyl nodes (red markers). (Right) Spectrum of a Nodal loop semimetal for $k_z = 0$. A nodal loop forms in the $x - y$ plane as indicated by the red line (the other half of the loop is cut by the plot range).

that $f_0(\mathbf{k})$ is small. Near the band touching point the Hamiltonian can further be approximated by a linear model such that

$$H_{Weyl} = \pm v\hbar\mathbf{k} \cdot \boldsymbol{\sigma}, \tag{2.40}$$

where ± denotes the chirality of the band crossing and $\boldsymbol{\sigma}$ is a vector of the Pauli matrices. This Hamiltonian is similar to the massless Dirac equation or the Weyl equation and is one example of where condensed matter physics finds analogies to particle physics. Band crossings that are described by this Hamiltonian are denoted Weyl nodes.

It is known that Weyl nodes must come in pairs of opposite chirality. This is, however, not obvious from the preceding discussion. For this, one has to topologically characterize the Weyl nodes. This is established by the Chern number of a Weyl node. One can find that this equals ± 1 given an integration surface enclosing a single Weyl node with a defined chirality. If the surface is expanded to enclose the whole Brillouin zone, it becomes, by periodicity, equivalent to a point and must hence have a Chern number equal to zero. Thus, the sum of the Chern numbers of the Weyl nodes must vanish.

Some interesting properties of Weyls semimetals are Fermi arc surface states and the chiral anomaly. Fermi arc surface states exist as a projection of the arc between the Weyl nodes onto the surface parallel to the arc. The chiral anomaly arises from the fact that at a quantum level the chiral symmetry is broken and hence, the chiral charge, $e(n_+ - n_-)$ (where $n_\pm$ is the number of electrons at the respective Weyl nodes), is not conserved. Because of this the, in the presence of electric, $\mathbf{E}$, and magnetic fields, $\mathbf{B}$, the number of electrons at a given Weyl node change as

$$\frac{dn_\pm}{dt} = \pm\frac{e^2}{\hbar^2}\mathbf{E} \cdot \mathbf{B}. \tag{2.41}$$

As a consequence of this, the electric and magnetic fields can pump charge between the Weyl nodes. This has some important consequences. It leads to the anomalous Hall effect in Weyl semimetals and negative magnetoresistance [30].

Finally, let us mention some materials that are or are expected to be Weyl semimetals. For example, the materials TaAs, TaP, NbAs an NbP has been theoretically [169, 68] shown to be Weyl semimetals. Experiments has further confirmed that this is the case for TaAs [180, 181]. Two other compounds that have been proposed to host Weyl nodes are $\mathrm{WTe_2}$ [149] and $\mathrm{MoTe_2}$ [154]. These are of the second class of Weyl semimetals, the type-II Weyl semimetals, for which the Weyl cones exhibit strong titling. In contrast to the type-I Weyl semimetal, to which the above discussion apply to, the type-II Weyls semimetals display an anisotropic chiral anomaly that depends on the direction of the current [149]. Experimentally, there is strong evidence for that $\mathrm{WTe_2}$ is a type-II Weyl semiemtal [97]. Let us next consider the nodal loop semimetals

2.4.2 Nodal loop semimetal

Nodal loop semimetals are similar to the Weyl semimetals, but contrary to the Weyl semimetal, they do not only realize isolated points in k space where the bands cross but rather a loop as depicted in the right of Fig. 2.4. These band crossing exhibit TR symmetry and reflection symmetry. The stabilization of the nodal loop is due to the reflection symmetry, which protects the band crossing from gap opening perturbations. Materials where the nodal rings has been observed are, for example, in ZrSiS [141, 161, 34], $\mathrm{PbTaSe_2}$ [26], $\mathrm{NbAs_2}$, [146]. There are further theoretical evidence that nodal rings would exist in $\mathrm{Ca_3P_2}$ [32] and CaAgP [167, 179].

Just like the Weyl semimetal, the stability of the nodal loop is guaranteed by a topological invariant. In this case by the Berry phase. Consider a loop in momentum space. One can show that the Berry phase, Eq. (2.8), equals 0 if the loop does not link with nodal loop. On the other hand, if the loop link with the nodal loop, the phase equals π. Hence, the Berry phase either takes the values 0 or π. It can furthermore be shown that reflection and time-inversion symmetry is the reason for this.

Due to the non-trivial topology of the nodal loop is also exhibit surface states. These are so called drum head surface states. In the configuration seen in Fig. 2.4 (b), these will live on the (001) surface and encapsulated by the area spanned by the projected nodal loop. These have shown to display some interesting transport properties but suffers from that they might require the fabrication of devices that filters electrons of different momentum [136].

Another observation was made by Martin-Ruiz and Cortijo [106] that by breaking time-reversal symmetry by a tilt term in the Hamiltonian, the material becomes optically active. This, furthermore, motivates the investigation of the optical activity, in terms of the Kerr effect, in these materials. This is discussed in detail in chapter 4.

2.5 Topological classification

Contrary to what we have seen above, topological states and phenomena were long thought to be rare in nature. However, with the discovery of the QSH effect, this was no longer the case. This discovery also led to a deepened interest in the relation between symmetries and topology, which is also clear from the previous discussions. Symmetries are already known to play an important role in Landau-Ginzburg theory of spontaneous symmetry breaking, which can be used to classify different states of matter. In combination with topology, this can again be the case – however, this time in a different way from the Landau-Ginzburg theory. Symmetries can not simply be used to differentiate topological insulators from topologically trivial insulators. Neither can their topological nontriviallity be detected by a local order parameter. [36].

For classifying topological phases, symmetries rather determine whether one can continuously interpolate between two Hamiltonians (assuming that there exists a full bulk gap) such that their symmetries are preserved and without closing the bulk gap. Hence, if this is the case, two Hamiltonians belong to the same equivalence class. Different equivalence classes with the same symmetries are set apart by the topological invariants that characterize the global phase of the bulk wave functions.

The first classification was made in terms of non-spatial symmetries and resulted in the so-called ten-fold way or the Altland-Zirnbauer classification. Non-spatial symmetries are three; time-reversal (TR) symmetry, particle-hole (PH) symmetry, and chiral symmetry. The three symmetries can be expressed as operators. These are denoted $\mathcal{T}$, $\mathcal{C}$ and $\mathcal{S} = \mathcal{T}\mathcal{C}$, respectively. Note that chiral symmetry is the combination of TR and PH symmetry. One can prove that the TR and PH symmetry operators square to ± 1 whereas the operator for chiral symmetry squares to one [36]. Furthermore, the effect the symmetry operators have on a Hamiltonian are as follows: a Hamiltonian preserves TR symmetry if $\mathcal{T}H\mathcal{T}^{-1} = H$, if it preserve PH symmetry, then $\mathcal{C}H\mathcal{C}^{-1} = -H$ and if chiral symmetry is preserved, then $\mathcal{S}H\mathcal{S} = -H$. By combining the presence or absence of these symmetries and whether the operators square to plus or minus one results in ten different possibilities. This is the foundation of the Altland-Zinbauer classification [144]. The classification furthermore depends on the dimensionality of the Hamiltonian. For every dimension, one finds, possibly, a different topological invariant corresponding to a given combination of symmetries. The equivalence classes are presented in Table 2.1.

The different types of materials discussed in the previous sections can be put in one of the classes presented in the table. For example, the AII class, in two dimensions, describes systems with neither PH symmetry nor chiral symmetry but with TR symmetry, for which $\mathcal{T}^2 = -1$. The QSH state falls into this class, and we see that it is indeed protected by a $\mathbb{Z}_2$ topological invariant.

The classification scheme can be extended to take into account for spatial symmetries. These are not considered here, but the interested reader can find the full

TABLE 2.1: Altland-Zirnbauer classification for topological insulators and topological superconductors. Here d represents the dimension of the system. The leftmost column denotes the different symmetry classes characterized by the presence (± , 1) or absence (0) of time-reversal, particle-hole, and chiral symmetry. The entries $\mathbb{Z}$, $\mathbb{Z}_2$, $2\mathbb{Z}$ and 0 marks the presence or absence of a non-trivial phase.

Class	$\mathcal{T}$	$\mathcal{C}$	$\mathcal{S}$	$d=1$	$d=2$	$d=3$
A	0	0	0	0	$\mathbb{Z}$	0
AIII	0	0	1	$\mathbb{Z}$	0	$\mathbb{Z}$
AI	+	0	0	0	0	0
BDI	+	+	1	$\mathbb{Z}$	0	0
D	0	+	0	$\mathbb{Z}_2$	$\mathbb{Z}$	0
DIII	-	+	1	$\mathbb{Z}_2$	$\mathbb{Z}_2$	$\mathbb{Z}$
AII	-	0	0	0	$\mathbb{Z}_2$	$\mathbb{Z}_2$
CII	-	-	1	$2\mathbb{Z}$	0	$\mathbb{Z}_2$
C	0	-	0	0	$2\mathbb{Z}$	0
CI	+	-	1	0	0	$2\mathbb{Z}$

extension in [36]. We have now presented a brief introduction to topology in condensed matter physics. In the following three chapters, we will discuss three different topics that are related to what has been discussed in this chapter. We will now dive into transport in one-dimensional topological superconductors.

Chapter 3

Transport in coupled Majorana bound states

This chapter concerns itself with the work that has been done for the paper titled *Transport properties of coupled Majorana bound states in the Coulomb blockade regime*. In this work, we investigated two different structures hosting Majorana bound states (MBS). MBSs appear as quasiparticles in topological superconductors, and in such 1D systems, they localize at the endpoints where they form bound states. However, these bound states are not independent of each other but rather a pair of MBSs form a Dirac fermion. Thinking of the 1D system as a single wire, the MBSs sits on opposite sides, and hence the Dirac state they constitute is highly non-local.

Majorana bound states are not localized to endpoints of 1D wires but rather decay into the wire. When the wire becomes smaller, the overlap between the wave functions of the MBSs will increase. In a single wire, there is, evidently, only a single way they can overlap. However, by combining multiple of these, different structures can be created. In reality, these structures are physical objects, but in a theoretical picture, we model the system by different MBSs wave functions overlapping with each other.

The above-imagined wires are, of course, electronic systems. Hence, as they are made smaller, a necessary feature to consider is interactions. There are different ways to describe interactions. One model for describing these is the constant interaction model. In this effective model, interactions are taken into account by considering the total electrostatic potential given by the total charge in the system. To add another electron to the system, it has to have energy exceeding the electrostatic potential.

MBSs have been widely researched the last decade [94, 3, 103, 152]. This has its foundation in that MBSs have been proposed as building blocks for fault-tolerant quantum computation [82, 117, 140]. Two essential proposed structures that make up a single qubit are the T-junction and the Majorana box, both of which host four MBSs. The two different structures have been proposed for different types of quantum computation schemes. The T-junction schemes where the Majoranas are physically moved around have been suggested for physically braiding Majoranas, whereas the Majorana box relies on measurement only and has been suggested to implement the Toric code. As one wants to perform specific quantum computation protocols, an important part is understanding how electrons move through these structures.

The dynamics of single wires, i.e., structures with only two MBSs that are possibly overlapping have been studied in great detail, both when connected to leads [27, 54, 70, 174, 64, 35, 104] as well as set-ups that include quantum dots [99, 184, 100, 79]. These studies include both non-interacting and interacting systems. In the transport dynamics this has showed to lead to an interesting effects such as quantum teleportation [54].

The inclusion of a second wire opens up for other interesting transport features. In the T-junction geometry, for example, a process dubbed "double-crossed Andreev reflection" appears [168]. This is a process that involves concurrent Andreev reflection processes as well as a resonant process. However, this structure has not received much attention, most likely due to the complexity of realizing it experimentally. The Majorana box has on the other hand been more widely investigated [22, 21, 6, 5, 56]. In this context the Majorana box has been shown to host a topological Kondo effect [22, 21, 5, 4, 92, 107, 20]. The transport properties of coupled boxes have also been studied in detail in [56].

There is still more to learn about these two structures. The details of the interplay between interactions and overlap between the MBSs and their implications for the transport properties have been looked at in less detail. To this end, we investigate these for the two structures as mentioned above, as they are connected to metallic leads.

We begin this chapter by introducing the field of MBSs and how they appear in the context of condensed matter physics. A toy model, the Kitaev chain, is introduced, which demonstrates the formation of MBSs in 1D wires. After that, a more experimental realizable system is presented. Afterward, the state of the current experimental progress is briefly discussed. We highlight some of the pioneering experiments and some of the difficulties that the community is facing at the moment.

As we have introduced the field of MBSs, we delve into the problem that we have studied. The different set-ups are introduced, and the constant interaction model is discussed in more detail. After that, we introduce the theory of master equations, which has been used to calculate the transport properties of the specific set-ups. Finally, the results from the investigation are presented with an explanation for the different physical processes occurring in these types of systems[1].

Majorana Physics

The concept of Majorana fermions stems from the area of particle physics by which it was discovered by Ettore Majorana that there possibly exist particles that are their own antiparticles. This concept has lately been adopted by the condensed matter

---

[1] In this chapter we set $\hbar = e = k_B = 1$

physics community. We are now seeing many proposals for which they can, for example, serve as a platform for fault-tolerant quantum computation. Many excellent reviews already exist on the topic (see for example [3, 17, 152, 85]), and we will here only give a brief introduction to the important concepts.

3.1 Majorana fermions

In 1937 Ettore Majorana discovered that for particular choice of equation variables the Dirac equation exhibits solutions for which $\Psi(\mathbf{x}) = \Psi(\mathbf{x})^*$. The meaning of this is that the particle must be equal to its antiparticle.

The Dirac equation is given by

$$\left[i\gamma^\mu\partial_\mu - m\right]\Psi(\mathbf{x}) = 0. \tag{3.1}$$

The equation describes the dynamics of a particle with mass m. $\mathbf{x}$ is here a four vector and γ^μ are 4 by 4 matrices. Under the conditions

$$\{\gamma^\mu, \gamma^\nu\} = 2g^{\mu\nu} I_{4\times 4}, \quad \gamma^0\gamma^\mu\gamma^0 = \left(\gamma^\mu\right)^\dagger, \tag{3.2}$$

the Dirac equation describes the dynamics of a spin $\frac{1}{2}$ particle. In the above equation $g^{\mu\nu} = diag(1,-1,-1,-1)$ and $I_{4\times 4}$ is the identity matrix of size 4. Commonly the Dirac equation is solved by using the γ - matrices as determined by Dirac, however, Majorana discovered another set of matrices [170],

$$\gamma^0 = \begin{pmatrix} 0 & \sigma_y \\ \sigma_y & 0 \end{pmatrix}, \quad \gamma^1 = \begin{pmatrix} i\sigma_x & 0 \\ 0 & i\sigma_x \end{pmatrix}, \quad \gamma^2 = \begin{pmatrix} 0 & \sigma_y \\ -\sigma_y & 0 \end{pmatrix}, \quad \gamma^3 = \begin{pmatrix} i\sigma_z & 0 \\ 0 & i\sigma_z \end{pmatrix}, \tag{3.3}$$

where σ_i denote the Pauli matrices. We note that all the given matrices are now imaginary. It can further be shown that the above-given matrices indeed satisfy the relations given by Eq. (3.2) and hence the particles described by the Dirac equation using the above matrices should still describe the dynamics of a spin $\frac{1}{2}$ particle. The fact that the new γ-matrices are purely imaginary implies that all coefficients of Eq. (3.1) are real. Hence, the solution to the Dirac equation, given the matrices defined by Majorana, must be real, i.e. $\Psi(\mathbf{k}) = \Psi^*(\mathbf{k})$. As stated above, the solutions correspond to a particle that is its own anti-particle. Particles that obey the Dirac equation, given the γ_is introduced in Eq. (3.3), are now commonly known as Majorana fermions. As a proposal, neutrinos have been suggested to be a Majorana fermion; however, experiments have yet to confirm that this is the case [12].

3.2 Majoranas in condensed matter physics

Instead of searching for fundamental particles with this property, one can turn to condensed matter physics and instead analogously look for excitations with the same property, i.e., if we denote such an excitation by γ then $\gamma = \gamma^\dagger$. If such an excitation exists, this further implies that it must be its own "hole". One then has to ask the question, in what kind of system can one find excitations which obey $\gamma = \gamma^\dagger$? Although it is not trivial, the answer lies in superconductors.

Excitations in a normal superconductor are Bogoliubov quasiparticles and are given by the following relation

$$\gamma = uc_\uparrow^\dagger + vc_\downarrow, \tag{3.4}$$

where $c, c^\dagger$ are fermionic annihilation and creations operators and u and v are complex numbers. One notice that even in the case of $u = v$ the excitation does not equal its conjugate. This is because, as one see from the indices, Bogoliubov quasiparticles arise from pairing between electrons with opposite spin.

The above-described excitation corresponds to the excitation in the most common superconductor found in nature, the s-wave superconductor, which exhibits spin-singlet pairings. On the contrary to s-wave superconductors, p-wave superconductors exhibit spin-triplet pairing. This means that the Bogoliubov quasi-particles of a p-wave superconductor are formed by pairing electrons with the same spin direction. Furthermore, the requirement that the excitation should be its own hole implies that $u = v$. Hence, the excitation we are looking for is given by

$$\gamma = uc_\sigma^\dagger + u^* c_\sigma, \tag{3.5}$$

where $\sigma =\uparrow, \downarrow$.

Unfortunately, p-wave superconductors seem to be very uncommon in nature. There are existing suggestions that the pairing in some iron-based compounds exhibit p-wave pairing [156]. The compound Sr_2RuO_4 has been studied and for a long time been thought of as having a p-wave pairing. There is yet no conclusion about this [63]. The first step towards the solution of this problem was based on an idea of engineering the model introduced by A. Kitaev in 2001. The idea was to combine a nanowire with spin-orbit coupling, apply a magnetic field, and put the nanowire in proximity to an s-wave superconductor. Before we dive into this, let us briefly look at the Kitaev model and how MBSs form in this model.

3.2.1 Kitaev chain

In 2001 Alexey Kitaev suggested a simple model which exhibits excitations $\gamma = \gamma^\dagger$, [81]. The model is based on a one-dimensional (1D) fermionic lattice with nearest-neighbor hopping and p-wave superconducting pairing, and by such, the model is "spinless". The Hamiltonian describing this model is given by

$$H_{Kitaev} = -\mu \sum_i^N n_i - \sum_i^{N-1} \left[tc_i^\dagger c_{i+1} + \Delta c_i c_{i+1} + h.c. \right] \tag{3.6}$$

where N is the number of sites of the lattice, μ is the chemical potential, $n_i = c_i^\dagger c_i$ is the number operator, t is the hopping parameter between different lattice sites and Δ is the superconducting gap. The model is presented in Fig. 3.1(a). Now we want to represent the Hamiltonian in terms of Majoranas operators. A Majorana operator is constructed by splitting a Dirac fermion into a real and imaginary part. Hence we can write

$$\hat{c}_i = \frac{1}{2}\left(\gamma_{i,A} + i\gamma_{i,B}\right), \quad \hat{c}_i^\dagger = \frac{1}{2}\left(\gamma_{i,A} - i\gamma_{B,2}\right), \tag{3.7}$$

where $\gamma_{i,j}$ are the Majorana operators corresponding to the Dirac fermion occupying site i with sublattice sites A and B. Inverting these relations we obtain

$$\gamma_{i,A} = c_i^\dagger + c_i, \quad \gamma_{i,B} = i\left(c_i^\dagger - c_i\right). \tag{3.8}$$

From the fermionic commutation relations

$$\left\{c_i^\dagger, c_j\right\} = \delta_{ij}, \quad \left\{c_i, c_j\right\} = \left\{c_i^\dagger, c_j^\dagger\right\} = 0, \tag{3.9}$$

it follows that

$$\left\{\gamma_i, \gamma_j\right\} = 2\delta_{ij}. \tag{3.10}$$

Kitaev noticed that by tuning the different parameters of the model, different regimes can be reached. Both a topological and a trivial regime exist. The less interesting trivial regime is easiest obtained by tuning $|\mu| \neq 0$ and $\Delta = t = 0$. In this case the Hamiltonian is reduced to

$$H_{\text{triv}} = -\mu \sum_i \frac{1 - \gamma_{i,A}\gamma_{i,B}}{2}. \tag{3.11}$$

This Hamiltonian has a well-defined ground state which corresponds to either all sites being empty or occupied for μ being negative and positive, respectively. One furthermore notes that all Majoranas on the same lattice sites couple to each other, and hence there are no de-localized Majoranas, as is also depicted in Fig. 3.1(b).

The more interesting regime is easily obtained by setting $\mu = 0$ and $t = \Delta$. For the given parameters the Hamiltonian can be written

$$H_{top} = -it \sum_i^{N-1} \gamma_{i,B}\gamma_{i+1,A}. \tag{3.12}$$

By careful inspection it's seen that the Majoranas $\gamma_{1,A}$ and $\gamma_{N,B}$ are not present in the Hamiltonian. The situation is depicted in Fig. 3.1(c). The first consequence of this is that these operators commute with the Hamiltonian, $\left[H_{top}, \gamma_{1,A}\right] = \left[H_{top}, \gamma_{N,B}\right] = 0$. Secondly, these two operators form a de-localized fermionic state at zero energy, which is written

$$\tilde{c} = \frac{1}{2}\left(\gamma_{1,i} - i\gamma_{N,2}\right). \tag{3.13}$$

From this we make two observations

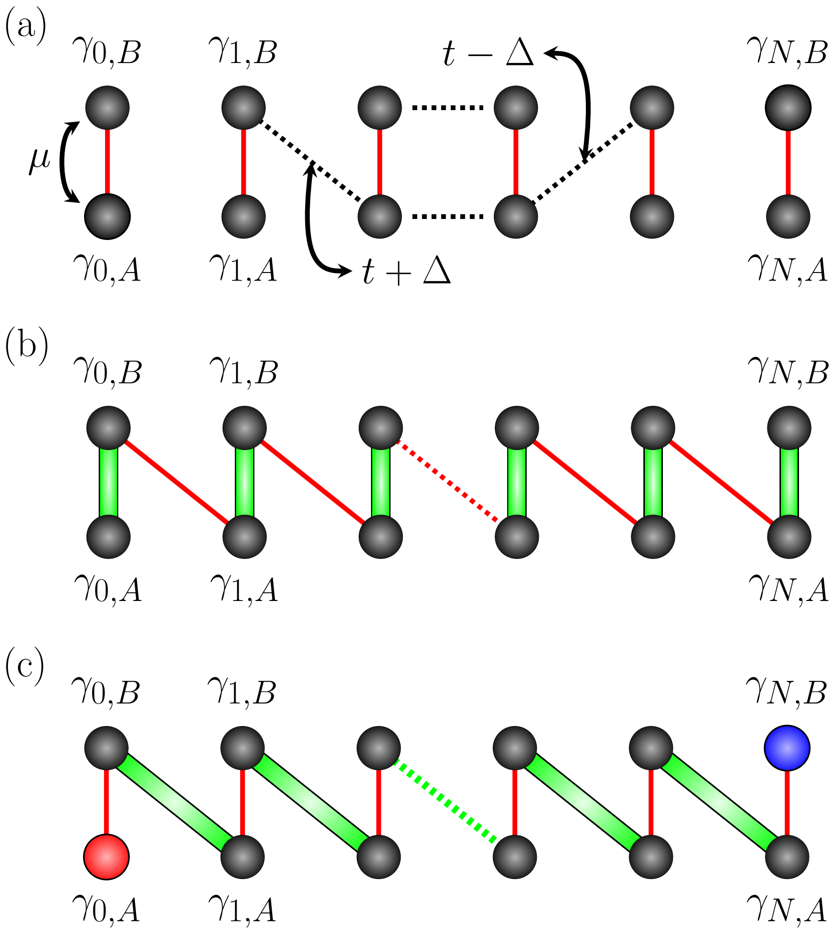

FIGURE 3.1: Illustration of the Kitaev toy model, Eq. (3.6). The green bars marks the coupling between different Majoranas living on the sublattices A and B and lattice site N. (a) General figure of the Kitaev chain where the chemical potential, hopping and superconducting order parameter are marked in correspondance with the model. (b) Trivial regime of the Kitaev chain, $|\mu| \neq 0$ and $\Delta = t = 0$. The coupling is between the Majoranas on each lattice and no edge modes form. (c) Topological regime, $\mu = 0$, $\Delta = t \neq 0$. The coupling is between Majoranas on different lattice sites. This leaves two Majoranas decoupled (sublattice sites marked in red and blue) from the rest, that forms a non-local states.

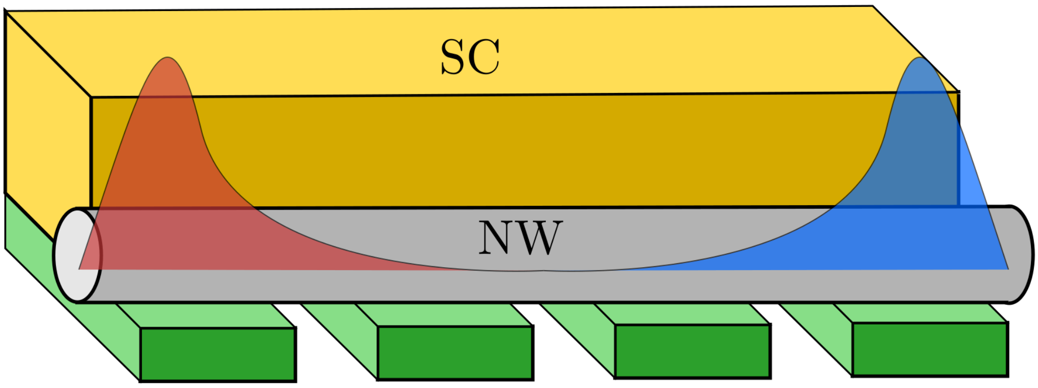

FIGURE 3.2: The figure displays a cartoon of a set-up that hosts Majorana bound states. A nanowire (NW) (grey) with strong spin-orbit coupling is placed on top of a set of gate-voltages (green) and in proximity to a superconductor (SC) (yellow). Applying a magnetic field perpendicular to the nanowire, two Majorana bound states (red and blue) emerge at the nanowire ends.

- The ground state is two-fold degenerate corresponding to either $\tilde{c}^{\dagger}\tilde{c} = 0, 1$.
- The fact that the constituents of this fermionic mode are separated by a far distance makes this state highly non-local. One property of this is that a local perturbation on one side of the chain will not have an effect on the total state and hence it should be robust against perturbations.

This model still relies on the p-wave superconductor. Let us now see how this system can be engineered using the common s-wave superconductor.

3.2.2 Semiconductor-superconductor hybrid structures

The Kitaev chain is only a toy model. Hence it is necessary to find a model that mimics it but at the same time is experimentally realizable. From an experimental perspective, the Kitaev chain has two drawbacks. As mentioned previously, it relies on a p-wave superconductor, and it is still unclear whether this exist or not. Furthermore, it incorporates spinless electrons, which can only be discussed theoretically.

Apart from these two drawbacks, the model seems relatively uncomplicated, yet it took almost ten years before an experimentally realizable model was proposed in 2010 [122, 105]. The model consists of a semiconductor nanowire with a strong spin-orbit coupling in proximity to an s-wave superconductor. The final ingredient is an applied magnetic field applied perpendicularly to the spin-orbit coupling of the nanowire. A cartoon of the system is shown in Fig. 3.2.

The Hamiltonian for a nanowire that lies along the x - direction with spin-orbit interaction λ_{SO} in the y-direction and a magnetic field $B\hat{z}$ applied in the z-direction is given by, [3]

$$H_{\text{Wire}} = \int dy\, \psi_{\sigma}^{\dagger}(x) \left[-\frac{\partial_x^2}{2m^*} - \mu - i\lambda_{SO}\sigma_y + B\sigma_z \right]_{\sigma,\sigma'} \psi_{\sigma'}(x). \tag{3.14}$$

Here $\psi_{\sigma}^{(\dagger)}(x)$ annihilates (creates) an electron with spin direction $\sigma = \uparrow, \downarrow$, chemical potential μ and effective mass m^* at position x. The spin-orbit coupling strength, λ_{SO} is taken to be positive and favors aligning spins along the y-axis. We furthermore assume that only the lowest transverse subband is relevant. The full spectrum is given by

$$E_{\pm} = \frac{k_x^2}{2m^*} - \mu \pm \sqrt{(\lambda_{SO}k_x)^2 + B^2}. \tag{3.15}$$

When the spin-orbit coupling and magnetic field are turned off, the Hamiltonian simply models a 1D electron gas (1DEG) and admits the normal parabolic spectrum, see Fig. 3.3 (a). Introducing the spin-orbit coupling shifts the bands such that the energy of the different spins becomes momentum dependent as seen in Fig. 3.3 (b). Hence the spectrum admits two spin-polarized bands. By instead turning on the magnetic field, the parabolic bands of the 1DEG are split into two. The Zeeman splitting, the splitting between the two bands, is equal to $2B$. This is demonstrated in Fig. 3.3 (c). When the system has both spin-orbit coupling and an applied magnetic field, the two bands observed in Fig. 3.3 (b) hybridize, and a gap opens up. This is due to the combination of the spin-orbit coupling and the applied magnetic field.

We now introduce the coupling to the superconductor. This is described by

$$H_{\text{SC}} = \int dx\, \Delta \psi_{\uparrow}^{\dagger}(x)\psi_{\downarrow}^{\dagger}(x) + h.c., \tag{3.16}$$

where Δ is the superconducting pairing strength that is induced in the wire. If we denote by $\psi_{\pm}(k)$ the operators that add a particle to the bands $E_{\pm}(k)$ respectively, then Eq. (3.16) can be written

$$H_{\Delta} = \int \frac{dk_x}{2\pi} \left[\sum_{\alpha=\pm} \frac{\Delta_p(k)}{2} \psi_{\alpha}(-k)\psi_{\alpha}(k) + \Delta_S(k)\psi_{-}(-k)\psi_{+}(k) \right] + h.c., \tag{3.17}$$

where

$$\Delta_p(k) = \frac{\lambda_{SO}k\Delta}{\sqrt{(\lambda_{SO}k)^2 + B^2}}, \tag{3.18}$$

$$\Delta_S(k) = \frac{B\Delta}{\sqrt{(\lambda_{SO}k)^2 + B^2}}. \tag{3.19}$$

In this picture we directly note the effective p-wave pairing this system admits. The p-wave pairing stems from the fact that the spins at momenta $\pm k$ are misaligned. The spectrum of the Hamiltonian $H_{\text{W+SC}} = H_{\text{Wire}} + H_{\text{SC}}$ is given by

$$E'_{\pm}(k) = \sqrt{\Delta^2 + \frac{E_+^2 + E_-^2}{2} \pm (E_+ - E_-)\sqrt{\Delta_S^2 + \mu^2}}. \tag{3.20}$$

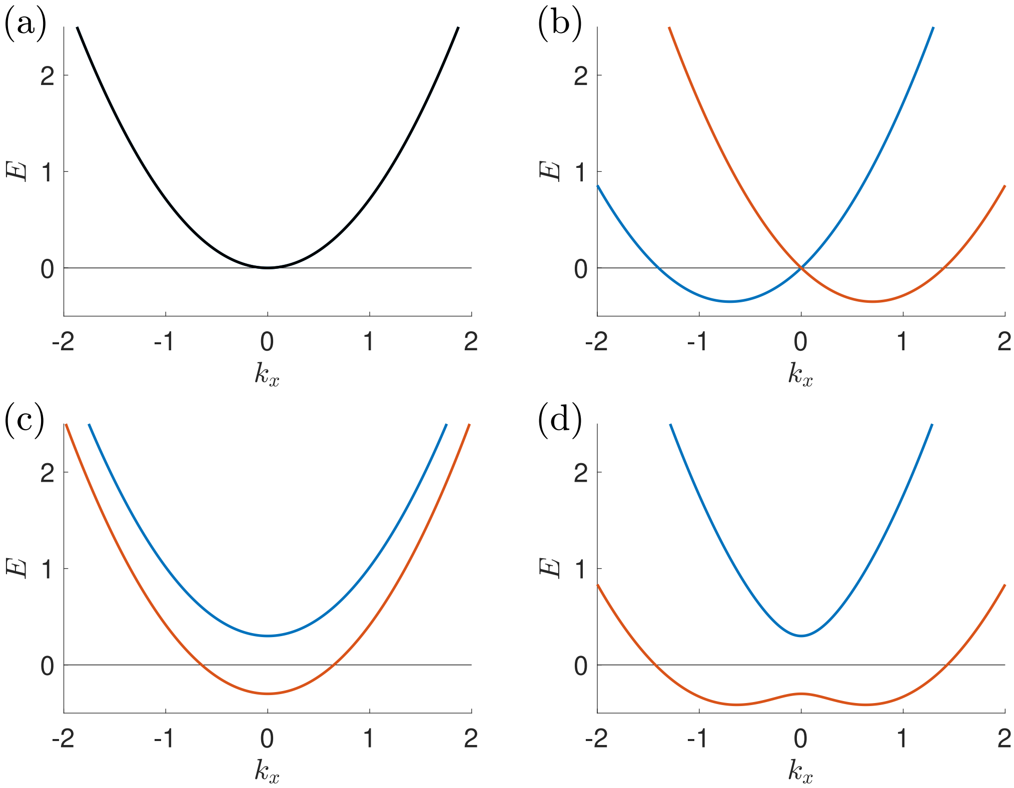

FIGURE 3.3: Spectrum of the Majorana nanowire, given by Eq. (3.15). (a) Spectrum without magnetic field and spin-orbit coupling. (b) With the spin-orbit coupling turned on the spectrum splits into two spin polarized bands. (c) Without the spin-orbit coupling but having the magnetic field turned on the bands are Zeemann split without a preferred spin polarization of the bands. (d) As both the magnetic field and spin-orbit coupling present the spin polarized bands in (b) hybridize and a gap is opened up. As the chemical potential lies within this gap the system is effectively spinless.

For $k = 0$ the energy gap closes, i.e., $E_\pm(0) = 0$, given that $B_c^2 = \Delta^2 + \mu^2$. If the magnetic field is smaller than this critical value, B_c, then the system is no longer spinless and the system is in the trivial state. On the other hand, when

$$B > \sqrt{\Delta^2 + \mu^2}, \tag{3.21}$$

the system appears spinless and enters the topological regime. Eq. (3.21) defines the *topological criterion*, for which the system is in the topological phase.

We have here presented an experimental realizable set-up for realizing MBSs by engineering a system that acts like a p-wave superconductor. There are, however, other systems where MBSs should also be possible to be observed. One system considered even before the "Majorana wire" is a system where an s-wave superconductor is in proximity to a strong topological insulator, [55]. This system is shown to host MBSs at vortices. Another system that might host MBSs is an antiferromagnetically ordered chain of magnetic adatoms. By placing the atom chain on top of a superconductor, the system realizes Yu-Shiba-Rusinov (YSR) states, [112]. As the adatoms come close to each other, the YSR states hybridize. Because of this particle-hole symmetric bands can form. When the negative and positive-energy bands finally overlap, p-wave correlations can reopen the gap, which turns the atomic chain into an effective topological superconductor that hosts MBSs.

This concludes the theoretical proposals. Let us now discuss the experimental progress.

3.2.3 Experimental signatures of Majorana bound states

The theoretical proposals of the existence of MBSs in the nanowire set-up [105, 122] sparked an immense amount of work for experimentally verifying their existence [110, 41, 46, 37, 48, 113, 135, 47, 2, 119, 183]. These experiments further also include the magnetic chains that were briefly discussed at the end of the previous section.

Two features have been proposed to signify the MBSs by either using a grounded or a floating superconductor. For the set-up with a grounded superconductor, tunnel spectroscopy should lead to a zero-bias conductance peak (ZBCP), indicating the presence of zero energy states. Moreover, the topological origin of these states should result in a ZBCP that is quantized at $2e^2/h$.

The second set-up, using a floating superconductor in the Coulomb blockade regime (detailed in Sec. 3.4.2) uses two-terminal measurements to determine the ground state periodicity. In the trivial state, the ground state periodicity should be of $2e$, reflecting that a Cooper pair consists of two electrons. On the other hand, when the system is tuned to the topological phases, the periodicity should be approximately $1e$ [54]. This is because, in the topological phase, non-local MBSs are formed, providing a state which does not cost any energy to be occupied. Of course, the transition from a $2e$ to $1e$ periodicity can be due to that the applied magnetic field that drives the system into the topological phase destroys the superconductor, and the system is in the normal state. The signature of the MBSs lies in the "approximately" $1e$-periodicity. Due to finite-length wires, the MBSs will have a finite overlap causing a small splitting that scales as $e^{-L/\xi}$, where L is the length of the wire and ξ is the coherence length of the superconductor [42]. This splitting will cause an even-odd effect, meaning that even valleys are slightly narrower than the odd ones [2].

It is essential to point out that so far, none of these experiments have been able to conclusively state that what is observed is due to the existence of MBSs.

Much work is being poured into understanding what is actually observed in these experiments and what is needed to improve on them [173, 123, 124, 125, 43]. To explain the differences between the observed conductance peaks Pan and das Sarma introduced the good, the bad, and the ugly conductance peaks [123]. These generally classify whether the conductance peaks stem from topologically non-trivial MBSs, which is the good conductance peak and should be what the experimentalist should find. However, a "bad" conductance peak is also found. This conductance peak is due to topologically trivial states; subgap Andreev bound states that merge to form a zero-bias conductance peak. The zero-bias conductance peak due to these states is predicted to as well be possible to observe below the point of the transition of the trivial and topological regime. Finally, they also discuss the "ugly" conductance peak, which is a disorder-induced conductance peak. Like the "bad" conductance peak, this is topologically trivial. It is further shown that the disorder can induce a zero-bias conductance peak that is well-correlated. This is, however, case-dependent and may or may not happen depending on the disorder configuration.

A more decisive proof of whether these systems host MBSs or not would be to perform braiding experiments. Such experiments would elucidate on the non-Abelian statistics that are a feature of the MBSs but not of ABSs.

3.3 Towards quantum computation based on Majorana bound states

In this section, we briefly discuss quantum computation based on MBSs. There are two main proposals for realizing quantum computation using MBSs. Either we aim to move the MBSs around each other or, which at the moment seems more feasible, to keep the MBSs static and rely on measurement-only based computation [103]. The second approach is what is has been proposed to be utilized in the implementation of the Toric code [142, 158, 130].

The first important fact that MBSs might be useful for realizing topologically protected quantum computation lies in the fact that they are, in two dimensions, so-called non-Abelian anyons [153]. Anyons are a third class of particles that, in contrast to bosons and fermions that, upon particle exchange, undergo a multiplication of $+1$ and -1 respectively, instead are either subjected to an arbitrary phase shift (if Abelian) or to a unitary transformation (non-Abelian). By such, exchanging two Majoranas results in them being subject to a unitary transformation.

Let us now discuss braiding of MBSs. This is a procedure where we exchange two MBSs, either by physically moving them around, or by performing a set of measurements. From the definition of a Majorana operator and Eq. (3.10) we have that

$$\gamma_i = \gamma_i^\dagger, \quad \{\gamma_i, \gamma_j\} = 2\delta_{ij}. \tag{3.22}$$

We furthermore saw that we can create a fermionic state out of Majoranas,

$$c = \frac{1}{2}\left(\gamma_1 - i\gamma_2\right). \tag{3.23}$$

The fermion number operator can furthermore be defined in terms of Majorana operators and is given by

$$\hat{n} = c^\dagger c = \frac{1}{2}\left(1 + i\gamma_1\gamma_2\right). \tag{3.24}$$

Let us now construct the unitary transformation resulting from the exchange of two Majoranas. Let us denote it B_{12} (commonly known as a braid operator). The resulting unitary transformation, $B_{12}\gamma_i B_{12}^{-1}$ must be a Majorana. Furthermore, parity must be conserved, i.e., $[\hat{n}, B_{12}] = 0$. We are left with the following possibilities, [95]

$$B_{12}\gamma_1 B_{12}^{-1} = \mp\gamma_2, \tag{3.25}$$

$$B_{12}\gamma_2 B_{12}^{-1} = \pm\gamma_1, \tag{3.26}$$

$$\tag{3.27}$$

where the signs depends whether the exchange is done in a clockwise or anticlockwise manner. It then follows that

$$B_{12} = \frac{1}{\sqrt{2}}\left(1 + \gamma_1\gamma_2\right), \tag{3.28}$$

up to some phase factor. The uniqueness of this operator is satisfied by requiring that in a system with more than two Majoranas, all other Majoranas are unaffected by the exchange of γ_1 and γ_2. If we let this operator act on the subspace spanned by the eigenstates of the number operator, $\hat{n}\,|n\rangle = n\,|n\rangle$ we obtain

$$B_{12}\,|0\rangle = \frac{1}{\sqrt{2}}\left(1 + i\right)|0\rangle, \tag{3.29}$$

$$B_{12}\,|1\rangle = \frac{1}{\sqrt{2}}\left(1 - i\right)|1\rangle. \tag{3.30}$$

This effectively demonstrates that by exchanging two Majoranas we can change the quantum state. The effect of this is however rather mundane since it only multiplies the state by a phase factor. To find non-trivial effects one has to consider a system with at least four Majoranas.

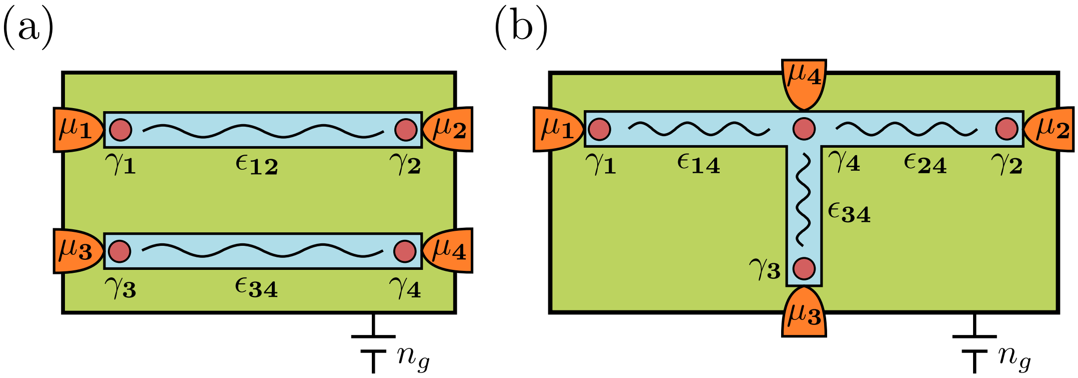

FIGURE 3.4: Smallest set-ups for a single Majorana qubit. (a) Majorana box, (b) T-junction. γ_i marks Majorana i, ϵ_{ij} denotes the overlap between Majorana i and j and μ_i is the chemical potential of lead i. The gate voltage is represented by the dimensionless parameter n_g.

3.4 Coupled Majorana systems

In the previous section, we have introduced a platform for which MBSs can be experimentally realizable and that they can be useful for performing quantum computation. We have seen that for performing useful operations on a qubit based on MBSs, at least four Majoranas have to be present. The simplest structures that host four MBSs are the T-junction and the Majorana box.

The main purpose of the rest of this chapter is to investigate how these two structures behave when varying biases are applied to the systems. This is based on what we report in *Transport properties of coupled Majorana bound states in the Coulomb blockade regime* [50]. In this work, the T-junction and Majorana box are investigated, not only in the presence of the finite overlap between the MBS:s but also in the inclusion of charging energy, a way to take interactions in the structures into account and the presence of more than two terminals.

Let us now, first, present the details of the T-junction and the Majorana box. Thereafter we introduce the constant interaction model and the master equation formalism to describe transport in these structures.

3.4.1 Set-ups

The specific set-ups for the Majorana box and the T-junction are shown in Fig. 3.4 (a) and (b) respectively. The Majorana box constitutes two wires placed on top of a superconducting island. The T-junction, on the other hand, constitutes two wires that have been crossed such that they form a T shape. This is a more difficult feat experimentally but is also being pursued by experimentalists [129].

The MBSs that appear in the two systems, given that the systems are in a topological regime, are represented by γ_1 - γ_4 and as described in 3.2.1 localize at the edges of the wires. As can be seen for the T-junction, one of the MBSs localizes at the crossing point of the two wires that make up the T-junction. A general Hamiltonian describing a system with $2M$ MBSs can be formulated as

$$H_{\text{MBS}} = -i \sum_{k=1}^{2M} \sum_{l=k+1}^{2M} \epsilon_{kl} \gamma_k \gamma_l, \tag{3.31}$$

where ϵ_{kl} is the coupling energy between the MBSs due to their overlapping wave functions. As presented in Eq. (3.10) the MBSs satisfy the anticommutaion relations $\{\gamma_k, \gamma_l\} = 2\delta_{kl}$. To simplify the understanding of the system, the MBSs are re-written in terms of Dirac operators. This can be done in the same fashion as done is in Eq. (3.8) by the following relations

$$\gamma_{2j-1} = c_j + c_j^\dagger, \quad \gamma_{2j} = i(c_j^\dagger - c_j). \tag{3.32}$$

For a system of four MBSs these equations reduce to

$$\begin{aligned} \gamma_1 &= c_1 + c_1^\dagger, \quad \gamma_2 = i(c_1^\dagger - c_1), \\ \gamma_3 &= c_2 + c_2^\dagger, \quad \gamma_4 = i(c_2^\dagger - c_2). \end{aligned} \tag{3.33}$$

The Hamiltonian describing the MBSs of the system can then be re-written in terms of Dirac operators by inserting these into Eq. (3.31). Depending on the overlaps or how the different MBSs couple to each other, the resulting Hamiltonian may or may not be diagonal. In the case that is is not diagonal, the Hamiltonian can be diagonalized by a Bogoliubov transform. For a brief but general treatment of this, see Appendix C. The diagonal Hamiltonian can be written as

$$H_{\text{MBS}} = \sum_{j=1}^{M} \xi_j d_j^\dagger d_j. \tag{3.34}$$

Here $d_j^{(\dagger)}$ are the resulting Dirac operators obtained from the Bogoliubov transformation. The ξ_js are the corresponding eigenenergies and are related to the overlap between the MBSs. Advertently, the MBSs can reversely be written in the Dirac operator representation as

$$\gamma_l = \sum_{j=1}^{M} \left(\alpha_{lj} d_j + \alpha_{lj}^* d_j^\dagger \right). \tag{3.35}$$

The coefficients, α_{lj}, are the elements of a $2M \times M$ matrix that is obtained from the Bogoliubov transformation. Let us now introduce the Hamiltonians for the two different set-ups.

Majorana box

The Majorana box is the simpler of the two set-ups. As seen from Fig. 3.4 (a) only the MBSs on the same wire overlap with each other. We write the Hamiltonian for

TABLE 3.1: Coupling, α_{ij} constants for the Majorana box.

α_{lj}	$j=1$	$j=2$
$l=1$	1	0
$l=2$	i	0
$l=3$	0	1
$l=4$	0	i

the Majorana box in the representation of the MBSs as

$$H_{\text{Box}} = -i\epsilon_{12}\gamma_1\gamma_2 - i\epsilon_{34}\gamma_3\gamma_4. \tag{3.36}$$

By inserting Eq. (3.33) into (3.36), the Hamiltonian represented by Dirac operators is directly obtained on diagonal form,

$$H_{\text{Box}} = \xi_1 d_1^\dagger d_1 + \xi_2 d_2^\dagger d_2, \tag{3.37}$$

where $\xi_1 = \epsilon_{12}$ and $\xi_2 = \epsilon_{34}$. The different coupling coefficients, α_{lj} are collected in Table 3.1

This describes the Majorana box. So far, it is not evident how the MBSs on the different wires couple to each other. As will be seen in subsequent sections, the superconducting island, on which the wires are placed, allows electrons to move via the superconducting condensate. Hence, the MBSs on the two different wires can interact with each other.

T-junction

The T-junction (see Fig. 3.4 (b)) is slightly more complicated than the Majorana box. Since the wave functions of the MBSs decay exponentially [42], we can assume that only nearest neighbor MBSs couple to each other. We consider a set-up such that the coupling between the different MBSs are equal, i.e., $\epsilon_{14} = \epsilon_{24} = \epsilon_{34} = \epsilon$. Hence the Hamiltonian for the MBSs of the T-junction can be written

$$H_{\text{T-junction}} = -i\epsilon\left(\gamma_1 + \gamma_2 + \gamma_3\right)\gamma_4. \tag{3.38}$$

Here we have furthermore assumed that the overlap between the outer MBSs (γ_1 - γ_3) and the central MBSs (γ_4) are equal. The Hamiltonian can be diagonalized in the basis of the Majorana operators. In this case one obtains two linear combinations of the MBSs at a finite energy $\xi_T = 2\sqrt{3}\epsilon$ and two linear combinations at zero energy.

Compared to the Majorana box the T-junction does not take a diagonal form when Eq. (3.33) is inserted in Eq. (3.38). It can instead be written as $\frac{1}{2}\mathbf{C}^\dagger\mathcal{H}\mathbf{C}$, where

$\mathcal{H}$ is given by

$$\mathcal{H} = \epsilon \begin{pmatrix} 0 & -(1+i) & 0 & (1+i) \\ -(1-i) & -2 & -(1+i) & 0 \\ 0 & -(1-i) & 0 & (1-i) \\ (1-i) & 0 & (1+i) & 2 \end{pmatrix}. \tag{3.39}$$

and the vector $\mathbf{C}^\dagger = (c_1^\dagger, c_2^\dagger, c_1, c_2)$. Now following Appendix C, we perform a Bogoliubov transform by finding a matrix T_n that diagonalizes the Hamiltonian and such that

$$\mathbf{C} = T_n \mathbf{D}, \tag{3.40}$$

where $\mathbf{D}^\dagger = \left(d_1^\dagger, d_2^\dagger, d_1, d_2\right)$. The matrix $T_n^\dagger$ is then found to be

$$T_n^\dagger = \begin{pmatrix} \frac{1}{2\sqrt{3}}(1-i) & \frac{1}{2\sqrt{3}}(1-\sqrt{3}) & -\frac{1}{2\sqrt{3}}(1-i) & \frac{1}{2\sqrt{3}}(1+\sqrt{3}) \\ \frac{1}{2\sqrt{3}}(1+\sqrt{3})) & -\frac{1}{2\sqrt{3}}(1+i) & \frac{i}{2\sqrt{3}}(1-\sqrt{3}) & -\frac{1}{2\sqrt{3}}(1+i) \\ \frac{1}{2\sqrt{3}}(1-i) & \frac{1}{2\sqrt{3}}(1+\sqrt{3}) & \frac{1}{2\sqrt{3}}(1+i) & \frac{1}{2\sqrt{3}}(1-\sqrt{3}) \\ -\frac{i}{2\sqrt{3}}(1-\sqrt{3}) & -\frac{1}{2\sqrt{3}}(1-i) & \frac{1}{2\sqrt{3}}(1+\sqrt{3}) & -\frac{1}{2\sqrt{3}}(1-i) \end{pmatrix}. \tag{3.41}$$

From this, we obtain the diagonalized Hamiltonian

$$H_{\text{T-junction}} = 0 d_1^\dagger d_1 + \xi_T d_2^\dagger d_2. \tag{3.42}$$

From Eq. (3.33) it follows that

$$\mathbf{C} = \frac{1}{2} \underbrace{\begin{pmatrix} 1 & i & 0 & 0 \\ 0 & 0 & 1 & i \\ 1 & -i & 0 & 0 \\ 0 & 0 & 1 & i \end{pmatrix}}_{\mathrm{M}} \begin{pmatrix} \gamma_1 \\ \gamma_2 \\ \gamma_3 \\ \gamma_4 \end{pmatrix}. \tag{3.43}$$

Combined with Eq. (3.40) we find a relation between the Majorana operators and the Dirac operators in the diagonal basis,

$$\begin{pmatrix} \gamma_1 \\ \gamma_2 \\ \gamma_3 \\ \gamma_4 \end{pmatrix} = \mathrm{M}^{-1} T_n \mathbf{D}, \tag{3.44}$$

where we have used the fact that T_n is a unitary matrix. From this, we can, as for the Majorana box, construct Table 3.2.

We note from the table that the Dirac fermion described by the d_1 operator does not involve the γ_4 operator, indicating that this operator is highly non-local since it only involves the Majoranas on the outermost parts of the T-junction. On the other hand, the d_2 state involves all Majorana operators. The choice of symmetric overlaps

TABLE 3.2: Coupling, α_{ij} constants for the T-junction.

α_{lj}	$j=1$	$j=2$
$l=1$	$\sqrt{\frac{2}{3}}e^{i\pi/12}$	$\frac{1}{\sqrt{3}}$
$l=2$	$\sqrt{\frac{2}{3}}e^{-7i\pi/12}$	$\frac{1}{\sqrt{3}}$
$l=3$	$\sqrt{\frac{2}{3}}e^{3i\pi/4}$	$\frac{1}{\sqrt{3}}$
$l=4$	0	i

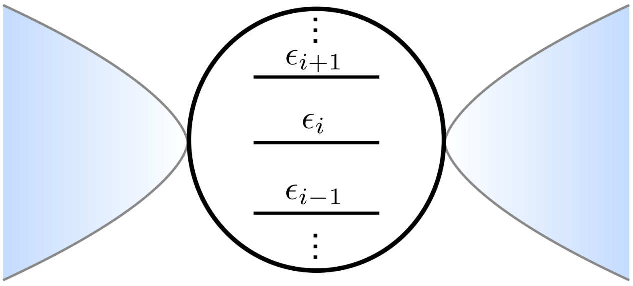

FIGURE 3.5: Mesoscopic island, with discrete energy levels ϵ_i, connected to two electron reservoirs.

is clearly shown in the weight given to γ_1 - γ_3 (compare Table 3.2 with Eq. (3.35)).

We have now presented the formation of the MBSs in the two systems under consideration. Another important ingredient in this study is that we want to account for interactions. As mentioned in the introduction, we apply the constant interaction model, which is described in the next section.

3.4.2 Constant interaction model

The constant interaction model is a model used to describe interactions in a simple but effective manner on a mesoscopic "island", a quantum dot, for instance, or as here considered, a system of nanowires[2].

A simplified model of the system we have in mind is depicted in Fig. 3.5. For simplicity, we model the mesoscopic island as a quantum dot with a discrete set of energy levels and that is connected to a set of leads. We furthermore let the system be capacitively coupled to a gate electrode, with which the charge on the island can be tuned.

The constant interaction model now tells us that the energy of the N- electron state of the island is given by

$$E(N) = \sum_i \epsilon_i + U(N). \tag{3.45}$$

---

[2] In this section we have re-introduce e for pedagogical purposes.

Here ϵ_i is the energy of the single-particle states, and $U(N)$ is the electrostatic energy of the system with N particles. To obtain an expression for $U(N)$, we have to consider the details of the set-up. By neglecting the capacitances between the contacts of the system, we can write the electrostatic potential of the island as

$$\phi_{island} = \frac{1}{C_\Sigma}\left(Q + \sum_i V_i C_i\right). \tag{3.46}$$

In the above equation C_Σ denotes the total capacitance of the system, i.e. $C_\Sigma = \sum_i C_i$ where C_i is the capacitance between the island and the i:th junction, V_i is the applied voltage at the same junction and Q is the total charge on the island. The second term is to be understood as the contribution from external charges. From here we can determine the electrostatic energy, $U(N)$. We obtain it as follows

$$U(N) = \int_0^{-eN} dQ\,\phi_{island} = \frac{e^2N^2}{2C_\Sigma} - eN\sum_i \frac{C_i}{C_\Sigma}V_i. \tag{3.47}$$

However, the above expression can be put on a form that is more widely seen in the literature. As noted, the second term of Eq. (3.46) plays the role of a displacement charge and can be varied by an external gate voltage, n_g. We can then write

$$U(N) = \frac{(eN - n_g)^2}{2C_\Sigma} + constant. \tag{3.48}$$

This is written in operator form by introducing an operator that counts the charge on the island, $\hat{N}$. The electrostatic energy of the island can then be represented by the following Hamiltonian

$$H_C = E_C\left(\hat{N} + n_g\right)^2, \tag{3.49}$$

where $E_C = e^2/2C_\Sigma$ is the charging energy. The electron number operator is for a normal system given by the number of occupied electron states. For a superconducting system one also have to account for the number of Cooper pairs on the island. Hence the total charge of a superconducting island is counted by the operator $\hat{N} = \hat{N}_C + \hat{n}$, where $\hat{N}_C$ is the Cooper pair number operator and $\hat{n}$ is the number operator for the electrons that occupy the MBSs. In terms of the Dirac operators constructed in the previous section it can be written as $\hat{n} = \sum_i d_i^\dagger d_i$. Hence, the charging energy is written as

$$H_C = E_C\left(\hat{N}_C + \hat{n} + n_g\right)^2 \tag{3.50}$$

It is important to note that the energy of the island can be tuned via the gate voltage. Hence it is possible to tune the system such that two states with a different number of particles can have the same energy. This is depicted in Fig. 3.7 (a). The opposite situation is also possible to obtain, where a single state on the island with a given energy is separated from the other states by the charging energy, which is typically large, see Fig. 3.7 (b). This effect is what is commonly known as Coulomb blockade. Consider a system as described above. As the gate voltage is tuned such

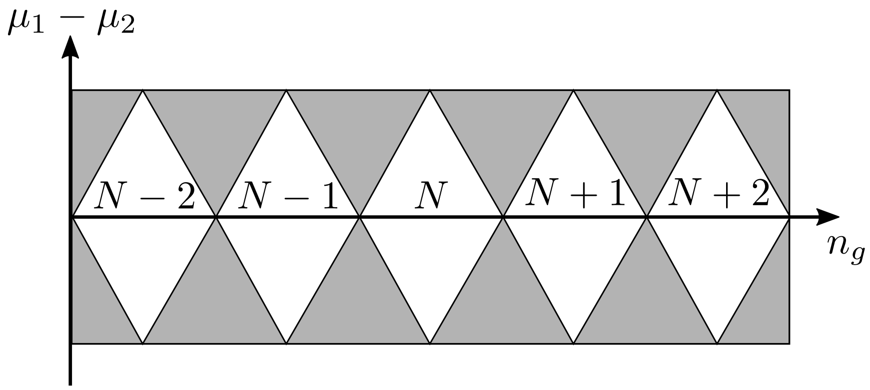

FIGURE 3.6: Stability diagrams representing the conductance through a quantum dot structure as a function of the dimensionless gate-voltage n_g and the difference between the chemical potential of the leads, $\mu_1 - \mu_2$. N marks the number of electrons on the dot. Within the white areas, known as Coulomb diamonds, the system is non-conducting due to that the electrons have insufficient energy to tunnel through the dot. By increasing the bias, the system becomes conducting (grey areas).

that two charge states on the island have the same energy, electrons can flow freely through the island. This is because adding an extra electron to the island does not cost any energy. We refer to this regime as the the sequential tunneling regime because sequential tunneling is the dominant transport mechanism.

On the contrary, when the system is tuned such that a single charge state is separated from the rest by a large energy gap (commonly denoted as a Coulomb valley), a crude assumption is that there is no flow of electrons unless a large bias is applied. The system is "Coulomb blockaded". This normally results in stability diagrams, depicted in Fig. 3.6. A diamond structure pattern is clearly observed, which indicates whether electrons tunnel through the system or not. Inside the white regions, the system is non-conducting due to that the electrons have insufficient energy to tunnel through it. By increasing the applied bias, the system naturally becomes conducting, represented by the gray areas. The assumption that there can be no flow of electrons through the system when it is Coulomb blockaded is however not entirely true. There is a possibility that electrons tunnel via virtual states, which leads to so-called cotunneling processes. We thus refer to this transport regime as the cotunneling regime. This leads to a weak but still existing signal when measuring the conductance inside the white regions depicted in Fig. 3.6.

3.5 Transport in coupled Majorana bound states

In the previous section, we have set up the models for describing the two systems we are interested in, the Majorana box and the T-junction and described how interactions can be taken into account. To account for electron transport through these systems, we have to consider the leads connected to the systems and the tunneling of electrons between the leads and the island. The metallic leads can be described

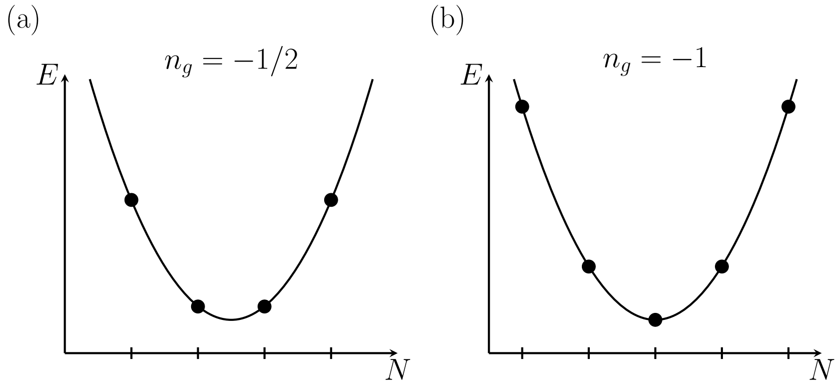

FIGURE 3.7: Energy of the superconducting island, given by Eq. (3.50). Two distinct regimes are obtained by tuning the gate voltage, n_g. (a) As $n_g = -1/2 + k$ with $k \in \mathbb{Z}$, two charge states are on the bottom of the parabola. The dominant transport mechanism is sequential tunneling. (b) On the other hand, by tuning $n_g = -1 + k$ the system is Coulomb blockaded. For small biases transitions has to occur via virtual states since only a single charge state is at the bottom of the parabola. The leading transport process is cotunneling.

by non-interacting fermions. The Hamiltonian for the leads is given by,

$$H_{\text{leads}} = -iv_F \sum_{l=1}^{4} \int dx \psi_l^\dagger(x) \partial_x \psi_l(x), \tag{3.51}$$

where $\psi_l^{(\dagger)}(x)$ annihilates (creates) an electron in lead l and v_F is the Fermi velocity. As we in this study are interested in the low energy properties of these systems, the leads can be approximated as one-dimensional systems which have a constant density of states. The electrons of the leads can furthermore be considered spinless as only one spin orientation of the electrons couple to the MBSs [27]. For further considerations, the lead will be considered Fermi seas that are held at a chemical potential μ_l.

The tunneling of electrons from the leads to the island is described by the tunneling Hamiltonian. We begin by considering the tunneling of electrons from the leads into the MBSs of a grounded island and vice versa. The Hamiltonian describing these processes are given by [27]

$$H_{\text{tun}} = \sum_{l=1}^{4} t_l \psi_l^\dagger(x=0) \gamma_l + \text{h.c.}, \tag{3.52}$$

where t_l is the tunneling amplitude between lead l and the MBS γ_l to which it is connected. We are now left with two important steps. First, we transform the tunneling Hamiltonian into the pure Dirac basis, using Eq. (3.35). This gives us the tunneling Hamiltonian

$$H_{\text{tun}} = \sum_{l=1}^{2M} \sum_{j=1}^{2} t_l \psi_l^\dagger(x=0) \left(\alpha_{lj} d_j + \alpha_{lj}^* d_j^\dagger \right) + \text{h.c.}, \tag{3.53}$$

where α_{lj} are the coefficients that are given in Table 3.1 for the Majorana box and in Table 3.2 for the T-junction.

As a starting point for the above given Hamiltonian, we chose a grounded superconductor. However, this is not what we want to consider. We want to consider a system with a floating superconductor. Hence, due to the electrostatic energy, we cannot allow terms that create electrons at some point in space without taking them from somewhere else. The fact that this occurs in the above Hamiltonian can be seen, for example, from the term $\psi_l^\dagger d_j^\dagger$ which creates one electron in lead l and one electron on the island. However, there is no term present that removes them from somewhere else, and hence at the moment, the system contains terms that do not conserve charge. Thus, the Hamiltonian has to be made charge conserving.

Whenever two electrons are created, they arise from the breaking of a Cooper pair in the superconductor. The operator that creates respectively annihilates a Cooper pair is given by $e^{\pm i\phi}$, where ϕ is the superconducting phase. The fact that this is the case follows from that the superconducting phase and the number of Cooper pairs are conjugate variables, $\left[\hat{N}_C, \phi\right] = i$ [54] and is proven in Appendix B.

We can now make the tunneling Hamiltonian charge conserving by introducing the Cooper pair creation and annihilation operators to the terms that either creates or annihilates two electrons. The tunneling Hamiltonian that now conserves charge is written [182]

$$H'_{\text{tun}} = \sum_{l=1}^{4} \sum_{j=1}^{M} t_l \psi_l^\dagger(x=0) \left(\alpha_{lj} d_j + \alpha_{lj}^* d_j^\dagger e^{-i\phi} \right) + \text{h.c.} \tag{3.54}$$

We have now introduced all the parts of the system and the full Hamiltonian of the island interacting with the leads can be written as (combining Eqs. (3.34), (3.50), (3.51) and (3.54))

$$H = H_{\text{leads}} + H_{\text{MBS}} + H_{\text{charging}} + H'_{\text{tun}}, \tag{3.55}$$

where H_{MBS} takes the form of the Majorana box Hamiltonian, Eq. (3.37) or of the T-junction Hamiltonian, Eq. (3.42). We further note that the Hilbert space of the island Hamiltonian $H_{MBS} + H_{charging}$ is spanned by the states $|\mathbf{n}, N_C\rangle$. Here $\mathbf{n}$ represent the occupation of the Dirac states, $\mathbf{n} = (n_1, n_2)$ and $n_j \in \{0, 1\}$ denotes whether the Dirac states d_j are empty ot occupied and N_C denotes the number of Cooper pairs.

As a next step, we want to consider electron transport through the Majorana box and the T-junction. We will begin with considering the sequential tunneling regime and, after that, consider the cotunneling regime. A theory especially useful for describing transport when interactions are taken into account is the master equation formalism. Before we outline the specific calculations for the sequential tunneling regime, we briefly discuss the general theory for master equations.

3.6 Transport

This section will present the calculations and the corresponding results for transport through the structures outlined in the previous section. Through the following calculations, we will obtain the current and differential conductance of the two structures when various biases are applied at the different leads. We will furthermore consider the weak coupling regime such that we can use the master equation approach. This means that the tunneling amplitudes t_l from lead l to the island are considered to be small compared to either temperature or the chemical potentials. We will furthermore assume that the temperature is much smaller than the charging energy, i.e., $T \ll E_C$, which should allow for the Coulomb blockade regime to be observed [118]. Let us now briefly introduce the theory of a master equation.

3.6.1 Master equation

There are many different ways of describing particle transport in mesoscopic physics[3]. One way to describe the state of a quantum mechanical system is by writing a master equation for the density matrix, i.e., an equation that describes the time evolution of the system. We consider a Hamiltonian describing a small system coupled to an environment by some kind of interaction. For the subsequent chapter, this will be a "coupling" that lets electrons tunnel from the environment to the system and vice versa. The Hamiltonian describing the full system can then be written as

$$H = H_S + H_B + H_I, \tag{3.56}$$

where S denotes the system, B denotes the bath (surrounding environment), and I denotes the interaction. We will now proceed by working in the interaction picture.

The time evolution of the density matrix is given by the von Neumann equation which states that

$$\frac{d}{dt}\rho(t) = \frac{i}{\hbar}\left[H_I(t), \rho(t)\right], \tag{3.57}$$

The equation can formally be solved by integrating the expression. One obtains

$$\rho(t) = \rho(0) - \frac{i}{\hbar}\int_{t_0}^{t} ds\, \left[H_I(s), \rho(s)\right] \tag{3.58}$$

Solving this integral equation is still a complicated feat, and hence one often turns to perturbative methods. To this end, we will first derive, starting from Eq. (3.58), the Redfield equation. The Redfield equation is an equation for the time evolution of the density matrix to second order in the interaction Hamiltonian.

As a first step we re-insert Eq. (3.58) into (3.57). We obtain

$$\frac{d}{dt}\rho(t) = \frac{i}{\hbar}\left[H_I, \rho(0)\right] - \frac{1}{\hbar^2}\int_{t_0}^{t} ds\, \left[H_I(t), \left[H_I(s), \rho(s)\right]\right]. \tag{3.59}$$

---

[3] In this section we have re-introduce $\hbar$ for pedagogical purposes.

We furthermore integrate out the bath degree of freedoms by taking the trace over the bath, and assume that $\mathrm{tr}_B\left[H_I, \rho(0)\right] = 0$. This gives us

$$\frac{d}{dt}\rho(t) = -\frac{1}{\hbar^2}\int_{t_0}^{t} ds\, \mathrm{tr}_B\left[H_I(t), \left[H_I(s), \rho(s)\right]\right] \tag{3.60}$$

We have, at this point, obtained an equation that is second order in the interaction Hamiltonian. Let us assume that the interaction Hamiltonian can be written $H_I = \lambda H_I'$. We then observe that the coefficient in front of the integral is of second order in λ. Continuing the process of inserting the obtained integral equation into Eq. (3.57), we will obtain an expression where every next term produced is of order λ^{n+1}, where n is the number of iterations. Keep iterating in this manner does not make the equation easier to solve. One way to proceed here is to perform two approximations, the Born and Markov approximations.

The Born approximation, also known as the weak coupling limit, assumes that the coupling between the subsystem and the bath is weak, i.e., $\lambda \ll 1$, and due to this, it is a good approximation to only keep terms that are of second order in λ, or to be more precise, the term of lowest order in λ. By assuming that the environment is essentially not affected by the subsystem, the density matrix can be written as a tensor product between the environment and the subsystem. The density matrix of the environment thus also becomes independent of time. Hence

$$\rho(t) = \rho_S(t) \otimes \rho_B. \tag{3.61}$$

One should however note that this does not mean that there are no excitations occurring in the bath. We however assume that environmental excitations decay over time scales that are not resolved. This can be seen as a first step of the Markov approximation. We now insert this expression into Eq. (3.60) and obtain

$$\frac{d}{dt}\rho_S(t) = -\frac{\lambda^2}{\hbar^2}\int_{t_0}^{t} ds\, \mathrm{tr}_B\left[H_I(t), \left[H_I(s), \rho_S(s) \otimes \rho_B\right]\right]. \tag{3.62}$$

As a next step we perform the second step of the Markov approximation. First $\rho_S(s)$ is replaced by $\rho_S(t)$ resulting in

$$\frac{d}{dt}\rho_S(t) = -\frac{\lambda^2}{\hbar^2}\int_{t_0}^{t} ds\, \mathrm{tr}_B\left[H_I(t), \left[H_I(s), \rho_S(t) \otimes \rho_B\right]\right]. \tag{3.63}$$

The above equation now gives the time evolution for the density matrix of the subsystem and depends only on its value at the present state $\rho_S(t)$. The above equation is the Redfield equation. The final problem with this equation is that it is not a Markovian master equation, or in other words, it still depends on the initial preparation at time t_0 (which we can without loss of generality set equal to zero, i.e., $t_0 = 0$). We next substitute s by $t - s$ in the integral. The upper limit of the integral is furthermore pushed to infinity. This is allowed if the integrand disappears sufficiently fast compared to the time scale over which the bath correlation functions decay. Hence, the Markov approximation is valid if the time scale over which the subsystem varies is much larger than that over which the bath correlation functions decay. The Born-Markov master equation is finally obtained

$$\frac{d}{dt}\rho_S(t) = -\frac{\lambda^2}{\hbar^2}\int_0^\infty ds\,\left[H_I(t), \left[H_I(t-s), \rho_S(t)\otimes\rho_B\right]\right]. \tag{3.64}$$

We will now apply the introduced formalism to the systems we introduced in the previous section.

3.6.2 Sequential tunneling regime

The previous section introduced the theory for investigating transport through the considered structures. However, as noted from the theory of the master equation, we integrate out the bath degrees of freedom. We are left without a possibility to keep track of the change of electron numbers in the respective leads. To this end, we introduce an operator that counts the number of electrons in the leads. We therefore define the lead number operator $\hat{N}_l$. This operator is considered part of the reduced system and remains as the bath degrees of freedom are integrated out. Hence, this operator allows for a way to count the number of electrons that have tunneled from/to the respective leads.

The lead number operator is canonically conjugate to a unitary lowering Y_l and raising $Y_l^\dagger$ operator and it follows that [38, 143],

$$\left[\hat{N}_l, Y_l\right] = -Y_l, \tag{3.65}$$

$$\left[\hat{N}_l, Y_l^\dagger\right] = Y_l^\dagger. \tag{3.66}$$

We include the lead raising and lowering operators by straightforwardly attaching them to any operator that acts on the leads that increases respectively decrease the number of electrons. The final tunneling Hamiltonian is therefore written

$$H''_{\text{tun}} = \sum_{l=1}^{2M}\sum_{j=1}^{M} t_l \psi_l^\dagger(x=0) Y_l^\dagger \left(\alpha_{lj} d_j + \alpha_{lj}^* d_j^\dagger e^{-i\phi}\right) + \text{h.c.} \tag{3.67}$$

We now write the master equation for the reduced system which constitutes the Majorana island but for which the leads have been integrated out. The tunneling Hamiltonian acts as the interaction between the bath and island. Hence, given the theory introduced in Section 3.6.1, $H_I = H'_{tun}$. The master equation is written

$$\begin{aligned}\frac{d}{dt}\rho_S(t) &= \int_0^\infty ds\,\mathrm{tr}_B\{\left[H'_{\text{tun}}(t), \left[\rho_S(t)\otimes\rho_B, H'_{\text{tun}}(t-s)\right]\right]\}\\ &= \sum_{n=1}^{4}|t_n|^2\int_0^\infty ds\,\left(\left\langle\psi_n^\dagger(-s)\psi_n(0)\right\rangle_B \left[X_n^\dagger(t)Y_n(t), \rho_S(t)X_n(t-s)Y_n^\dagger(t-s)\right]\right.\end{aligned}$$

$$- \left\langle \psi_n(0)\psi_n^\dagger(-s)\right\rangle_B \left[X_n^\dagger(t)Y_n(t), X_n(t-s)Y_n^\dagger(t-s)\rho_S(t)\right]$$
$$+ h.c.\Big), \tag{3.68}$$

where $X_n = \sum_{j=1}^4 \left(\alpha_{nj}d_j + \alpha_{nj}^* d_j^\dagger\right)$. The time evolution of the operators are evaluated using the Heisenberg equation of motion. For the bath correlation functions we have that

$$\langle \psi_k^\dagger(-s)\psi_k(0)\rangle = \frac{1}{L}\sum_q n_F(v_F q)e^{-i(v_F q+\mu_k)s}, \tag{3.69}$$

where L is the length of the one dimensional leads, μ_k is the chemical potential of lead k and $n_F(x) = (1-e^{\beta x})^{-1}$ is the Fermi distribution with $\beta = 1/T$. The sum can be evaluated in the continuum limit and by applying the following identity:

$$\int_{-\infty}^{\infty} dq f(q)\int_0^\infty ds e^{\pm i(q-a)s} = \pi f(a) \pm i\mathcal{P}\int_{-\infty}^{\infty} dq \frac{f(q)}{q-a}, \tag{3.70}$$

where $\mathcal{P}$ denotes the Cauchy principal value. To make progress and to be able to calculate the current of the systems, we need information about the elements of the density matrix. These are obtained by calculating $\langle \mathbf{n}; N_C|\frac{d}{dt}\rho_S(t)|\mathbf{n}'; N_C'\rangle$, where $\frac{d}{dt}\rho_S(t)$ is given in (3.68). This results in a set of equations for which many involve fast oscillating terms. In this study, we are interested in the current in the steady state. In this limit, fast oscillating terms average out, and by making a secular approximation, these are neglected. This leads to a set of equations for the occupation probabilities of the different states $P(\mathbf{n}; N_C) = \langle \mathbf{n}; N_C|\,\mathrm{Tr}_{\hat{N}_l}\rho_S\,|\mathbf{n}; N_C\rangle$ which decouple from the off-diagonal elements. We now seek stationary solutions to the differential equations i.e., $\frac{d}{dt}P(\mathbf{n}; N_C) = 0$. We furthermore have to demand that $\sum_{\mathbf{n},N_C} P(\mathbf{n}, N_C) = 1$. The equations are solved numerically. Once the occupation probabilities are obtained the current can be calculated from

$$\langle I_l\rangle = \mathrm{Tr}\left\{\hat{N}_l\frac{d}{dt}\rho_S\right\} = \sum_{\mathbf{n},N_C}\left(\Gamma_l^{1,+} - \Gamma_l^{1,-}\right)P(\mathbf{n}, N_C). \tag{3.71}$$

Here $\Gamma_l^{1,+(-)}$ denotes the transition probabilities and arise due to single transitions to and from the lead. The transition rates are explicitly given by

$$\Gamma_l^{1,+} = \Gamma_l|\alpha_{li}|^2\Big\{2 - n_F\Big[-\xi(\mathbf{n}) - E_C\Big(1-2n_g-4N_C\Big) - \mu_l\Big]$$
$$- n_F\Big[\xi(\mathbf{n}) + E_C\Big(1-2n_g-4N_C\Big) - \mu_l\Big]\Big\}, \tag{3.72}$$
$$\Gamma_l^{1,-} = \Gamma_l|\alpha_{li}|^2\Big\{n_F\Big[-\xi(\mathbf{n}) - E_C\Big(1-2n_g-4(N_C+1)\Big) - \mu_l\Big]$$
$$+ n_F\Big[\xi(\mathbf{n}) + E_C\Big(1-2n_g-4N_C\Big) - \mu_l\Big]\Big\}, \tag{3.73}$$

where $\Gamma_l = |t_l|^2/v_F$ and

$$\xi(\mathbf{n}) = \sum_j \xi_j n_j \tag{3.74}$$

is the energy of the state $|\mathbf{n}\rangle$. We calculate the local and non-local differential conductance by taking the derivative of the current in lead l with respect to the applied chemical potential at lead k, i.e. $d\langle I_l\rangle/d\mu_k$.

Including the charging energy restrict the number of available states unless the applied bias is large, as explained in section 3.4.2. Furthermore, tunneling in the sequential tunneling regime depends widely on the energy of the island,

$$E(\mathbf{n},N_C)=\xi(\mathbf{n})+E_C\left(\sum_j n_j+n_g+2N_C\right)^2. \tag{3.75}$$

As was explained in Section 3.4.2, the system is periodic in the gate voltage, and we can hence, without any loss of generality, consider $N_C=0$ and $-1<n_g<0$. We will furthermore consider, for most cases $\xi_j>0$, illustrating the finite overlap between the MBSs, as is of interest here.

Let us first consider the Majorana box. We vary the chemical potential on the different leads and calculate the differential conductance. The chemical potentials are chosen such that the chemical potential $\mu_1=\mu$ and the chemical potentials of the other leads are all held at the same value, $\mu_2=\mu_3=\mu_4=\mu$. The overlap between the MBSs are set finite but unequal, $\xi_1=0.1$ and $\xi_2=0.3$. The stability diagrams for the Majorana box are presented in Fig. 3.8. Figure 3.8 (a) and (b) represents the stability diagrams of the first wire (top wire of Fig. 3.2 (a)) with the smallest overlap between the MBSs and Fig. 3.8 (c) and (d) the stability diagrams of the second wire (bottom wire of Fig. 3.2 (a)) for which the MBSs have a larger overlap than the MBSs on the first wire. For an infinitesimal bias we observe two differential conductance peaks in the stability diagrams. Let us focus on the right one. This conductance peak occur at $n_g^0=-(\xi_1+E_C)/2E_C=-0.55$. This corresponds to the charge states $|00;N_C\rangle$ and $|10;N_C\rangle$ being degenerate.

As the bias is increased, transport can also be seen to occur in leads 3 and 4. As they are held at the same bias, we observe, as one should expect, equality between the two diagrams. One interesting feature here is that the conductance peak for the smallest possible applied bias is not observed at n_g^0 but rather slightly to the right of it. Furthermore, the peak does not have a symmetric partner to the left of n_g^0. This is shown by the boxes of Fig. 3.8 (d). The peak appears at $n_g=-0.45$ which corresponds to $-(\xi_1-\xi_2+2E_c)/E_C$. The presence and absence of the peaks boil down to the available states at the given gate voltage. Where we were expecting a peak, $n_g=-0.65$, only the states $|00;N_C\rangle$ and $|10;N_C\rangle$ have a finite occupation probability and hence only transport involving the d_1 state is possible. Hence, no transport can occur on the second wire since there is no involvement of the d_2 state neither is there a change in the number of Cooper pairs. On the other, hand given $n_g=-0.45$ the states $|11;N_C-1\rangle$, $|00;N_C\rangle$, $|10;N_C\rangle$ and $|01;N_C\rangle$ can all be occupied since they all have a finite occupation probability.

The transport process at $n_g=n_g^0$ is easy to understand, an electron tunnels from lead 1 to lead 2 without any involvement of the Cooper pairs since only $|00;N_C\rangle$ and

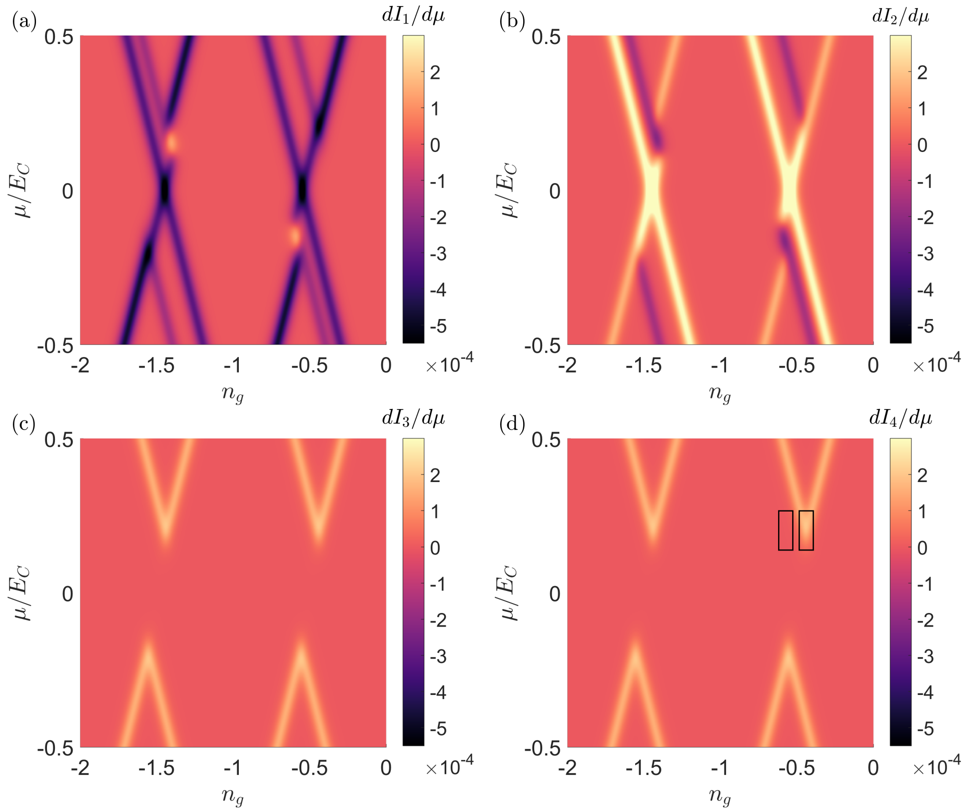

FIGURE 3.8: Differential conductances at the different leads for varying chemical potential and gate voltage, for the Majorana box. The chemical potential at lead 1, $\mu_1 = \mu$. At lead 2-4, $\mu_2 = \mu_3 = \mu_4 = -\mu$. (a) $dI_1/d\mu$, (b) $dI_2/d\mu$, (c) $dI_3/d\mu$ and (d) $dI_4/d\mu$. The left box in (d) marks the value of n_g for which no peak in the differential conductance is observed. The right box marks the value for which a peak is observed. The parameters are $\xi_1 = 0.1$, $\xi_2 = 0.3$, $\Gamma_i = 10^{-4}$, $E_C = 1$ and $\beta = 25$.

$|10; N_C\rangle$ have finite occupation probabilities for small biases. Contrary to this the transport process for $n_g = -0.45$ is more complicated. The transport between leads 1 and 2 is still mitigated by the same process as for $n_g = n_g^0$. However, the process that allows for transport between lead 1 and leads 3 and 4 is mitigated by the Cooper pairs. The specific transport process is visualized in Fig. 3.9. We explain the process as follows: an electron initially sits on lead 1. As a large bias is applied, the electron on lead 1 easily tunnels onto the first wire, moving the system into $|10; N_C\rangle$ state. Either the electron now tunnels into lead 2, as previously explained, or it is also possible that a Cooper pair from the condensate splits for which one of the electrons goes to occupy the d_2 state, and the other electron moves either to lead 3 or 4. The system is then in the $|11; N_C - 1\rangle$ state. Now the electron that occupies the d_1 state can form a Cooper pair with an electron from either lead 1 or 2. This moves the system to the $|01; N_C\rangle$ state. The electron that is occupying the d_2 state then tunnels to either lead 3 or 4, opposite to where the first one went. Summing up, we note that one electron has effectively been transported from the first wire to the second. This signifies a non-local transport between the first and the second wire that is driven

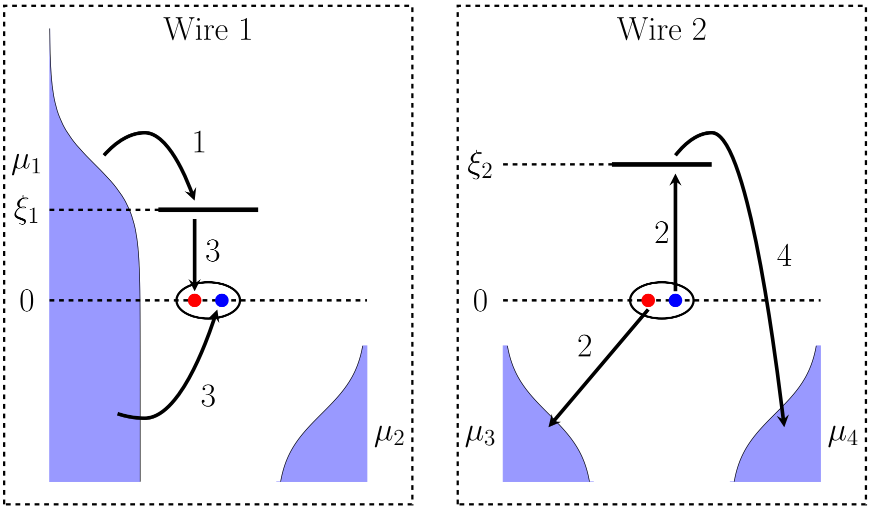

FIGURE 3.9: Illustration of transport between the two wires of the Majorana box, specifically from the first wire to the second wire. Step 1: The bias configuration is such that first an electron will tunnel from lead 1 into the MBSs of the first wire, $|00; N_C\rangle \to |10; N_C\rangle$. Step 2: A Cooper pair is split and one of the electrons goes to either lead 3 or 4 whereas the other occupies the MBSs on the second wire, $|10; N_C\rangle \to |11; N_C - 1\rangle$. Step 3: An electron from either lead 1 or 2 forms a Cooper pair with the electron in the MBSs on the first wire, $|11, N_C - 1\rangle \to |01, N_C\rangle$ Step 4: The electron occupying the MBSs on the second wire finally tunnels to lead, opposite from where the first electron went, $|01, N_C\rangle \to |00, N_C\rangle$.

by the Cooper pairs.

Figure 3.8 (a) shows further interesting transport phenomena. For certain choices of bias configuration, there are regions where the differential conductance takes positive values contrary to the rest of the stability diagram. This means that for certain bias configurations, the amplitude of the current in lead 1 decreases even though the bias is increased. To highlight this effect we consider a slightly larger overlap configuration, $\xi_1 = 0.3$ and $\xi_2 = 0.5$. We plot the current and differential conductance in Fig. 3.10 for which the gate voltage has been tuned to the resonance condition of the first wire, $n_g = n_g^0$. As seen in the figure, the current is both monotonic and, for certain biases vanishing. This phenomenon can be thought of as a non-local Coulomb blockade. The explanation for it is that as the bias on leads 3 and 4 become larger than the difference $\xi_2 - \xi_1$ the $|01; N_C\rangle$ state will be occupied. As both μ_3 and μ_4 are at biases (in this case, the same) that are larger than the energy of the d_2 state, the electron is trapped on the island. Since an extra electron has been added to the system, adding another now requires it to overcome the charging energy. Thus, since the system is now in the state $|01; N_C\rangle$, transport through the first wire requires that the system makes transitions via the $|11; N_C\rangle$ state. Hence, for transport to occur, a much larger bias has to be applied between the first and the second lead.

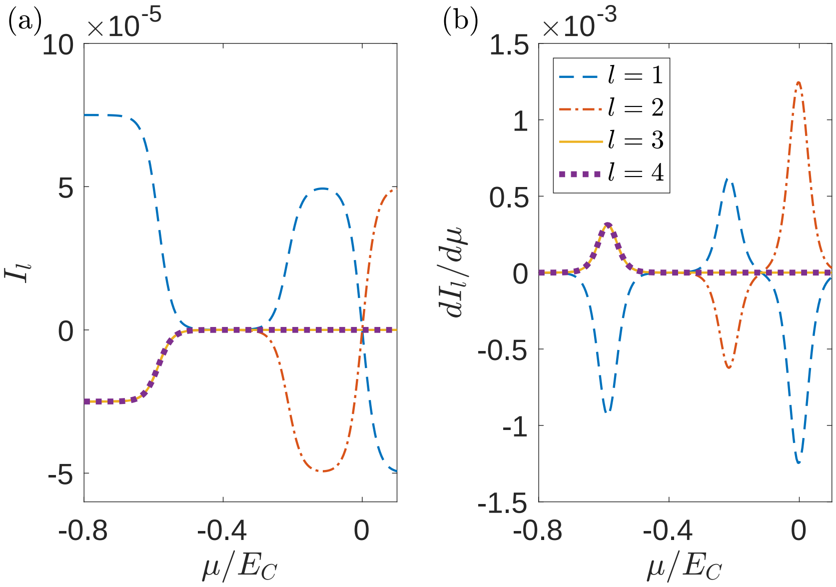

FIGURE 3.10: (a) Currents and (b) differential conductances for the Majorana box as the chemical potential is varied. The chemical potential on lead 1 is $\mu_1 = \mu$. On leads $2-4$ we apply $\mu_2 = \mu_3 = \mu_4 = -\mu$. The parameters are $\xi_1 = 0.3$, $\xi_2 = 0.5$, $\Gamma_i = 10^{-4}$, $E_C = 1$ and $\beta = 50$. The currents vanish in the bias region $-0.6 < \mu/E_C < -0.2$ due to nonlocal Coulomb blockade.

Let us now consider the transport properties of the T-junction in the sequential tunneling regime. First we consider the non-interacting regime where the transport properties are already known [168]. In the non-interacting limit we set $E_C = 0$. Under the assumption that $|\mu_l|, T \ll \xi_T$ we find that the current in lead l is given by

$$\langle I_l \rangle = \Gamma_l |\alpha_{l1}|^2 \left[1 - n_F(-\mu_l)\right]. \tag{3.76}$$

Comparing to [168], where exact results are obtained, we note that we can reproduce the results that are of linear order in Γ_l. Our results also confirm that up to linear order in Γ_l no current is observed in the fourth lead as α_{41} equals zero for the T-junction (see table 3.2). The leading process on the fourth lead is double crossed Andreev reflection, which is of higher order in Γ_l, explained in [168].

Returning to the interacting system, we plot the stability diagrams for the T-junction in Fig. 3.11. The bias configuration is chosen in the same manner as for the Majorana box, i.e., $\mu_1 = \mu$ and $\mu_2 = \mu_3 = \mu_4 = -\mu$. We observe zero-bias conductance peaks on the outer leads as the system is tuned on the degeneracy points, $n_g = -1/2 \pm k$, where k is an integer. Transport on the central lead is, on the other hand, blocked. The transport on the outer leads is here mediated by the island changing between being in the $|00; N_C\rangle$ and the $|10; N_C\rangle$ states. This is depicted in Fig. 3.12. The fact that transport occurs only on the outer leads indicates a strong non-locality in the transport features of the T-junction. The transport is, however, still mediated by the central MBS, which in this case serve as a bridge for connecting

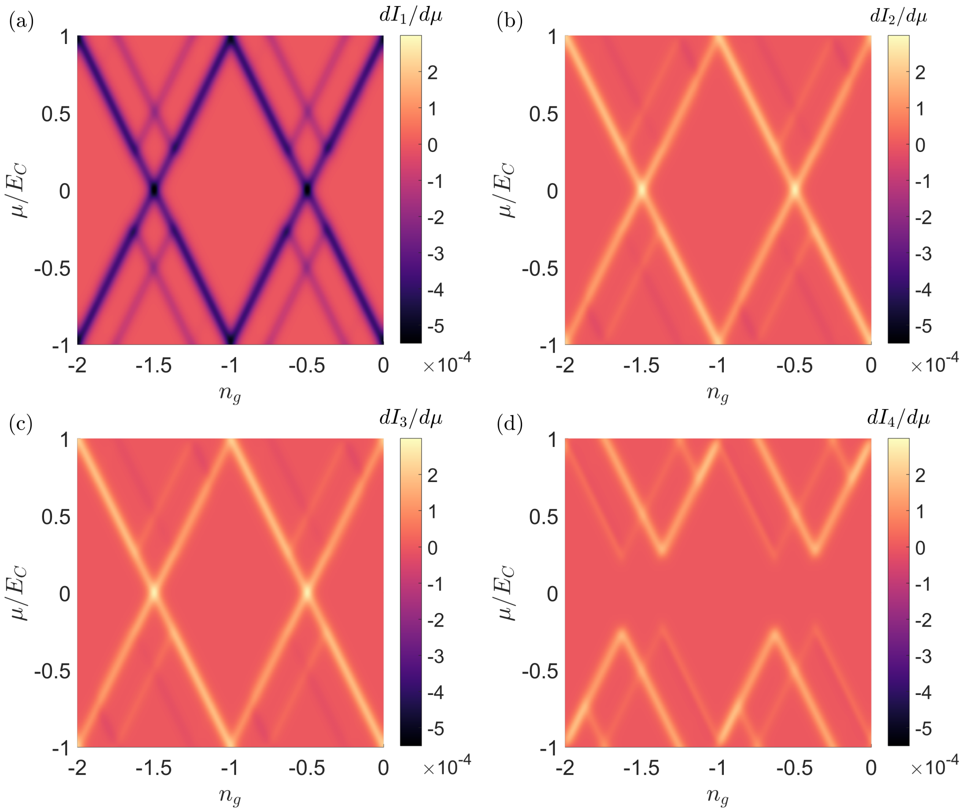

FIGURE 3.11: Differential conductances at the different leads for varying chemical potential and gate voltage, for the T-junction. The chemical potential at lead 1, $\mu_1 = \mu$. At lead 2-4, $\mu_2 = \mu_3 = \mu_4 = -\mu$. The plots show (a) $dI_1/d\mu$, (b) $dI_2/d\mu$, (c) $dI_3/d\mu$ and (d) $dI_4/d\mu$. The parameters are $\xi_1 = 0.1$, $\xi_2 = 0.3$, $\Gamma_i = 10^{-4}$, $E_C = 1$ and $\beta = 25$.

the outer MBSs to each other.

We now study the stability diagram as the bias is increased. We observe a conductance peak on the central lead as $|\mu| > \xi_T$. The bias increase further provides additional transport processes in the outer leads. These presents themselves as the sidebands observed in Fig. 3.11(a) - (c). The transport is now mediated both by single electrons as well as by processes that involves creation and annihilation of Cooper pairs, much in the same way as depicted in Fig. 3.9. The system now changes between $|00; N_C\rangle \rightleftharpoons |10; N_C\rangle$, $|10; N_C\rangle \rightleftharpoons |11; N_C - 1\rangle$, $|01; N_C\rangle \leftrightharpoons |11; N_C - 1\rangle$ and $|00; N_C\rangle \leftrightharpoons |01; N_C\rangle$. This is also depicted in Fig. 3.12.

As a final study in the sequential tunneling regime, we consider in more detail the non-local transport that we have now observed in both the Majorana box and the T-junction. This non-local transport can be understood as the "teleportation" process that was first suggested by Liang Fu [54]. The teleportation process is defined as a non-local current that does not depend on the length of the wires and hence neither on the overlap between the MBSs. We isolate this process by considering infinite wires; hence there is no overlap between the MBSs. This corresponds to setting $\xi_1 = \xi_2 = \xi_T = 0$. This then implies that we can not distinguish between the two structures.

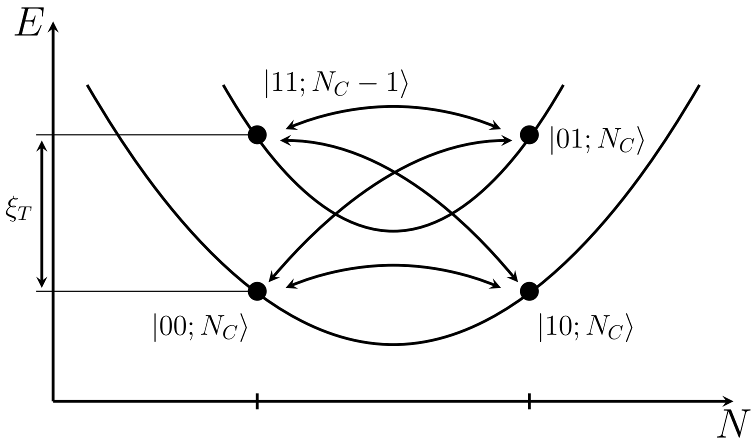

FIGURE 3.12: The charge states that contribute to sequential tunneling in the T-junction as $n_g = -1/2$. When the applied bias is small, transitions between $|00;0\rangle \rightleftharpoons |10;0\rangle$ are the only allowed ones. When the bias window is increased, the system can cycle between $|00;N_C\rangle \rightleftharpoons |10;N_C\rangle$, $|10;N_C\rangle \rightleftharpoons |11;N_C-1\rangle$, $|01;N_C\rangle \leftrightharpoons |11;N_C-1\rangle$ and $|00;N_C\rangle \leftrightharpoons |01;N_C\rangle$, under the condition that the applied bias is larger than ξ_T.

By applying a bias μ_1 on lead μ_1 while keeping the other leads grounded, we calculate the non-local differential conductance $d\langle I_l\rangle/d\mu_1$. A zero-bias conductance peak is observed at all the leads, as presented in Fig. 3.13. The conductance peak is a signature that non-local currents are present. However, the sequential tunneling approximation does not allow for studying phase coherence which is a further property of the teleportation process [54]. On the other hand, the analogy between the Hamiltonian in Eq.(3.54) and the one studied in [182] allows us to interpret the observed transport as teleportation.

We summarize the transport calculations so far by noting that we have here found all transport processes that are of leading order in Γ_l and explained the physical reasons behind the observed signatures. We have furthermore explained the non-local signatures of the two structures. An important detail to highlight from the discussion on non-local transport is the fact that the overlap plays a significant role. As the overlap between the MBSs become zero, the system loses all structure and can "simply" be regarded as a multiterminal junction where each lead connects to a single MBS. On the other hand, when the overlap is taken into account, the differences in the transport properties between the two structures prove that they are distinct from each other.

To increase our understanding of the two structures, we will, in the next section, consider transport processes that are of second order in Γ_l, i.e., transport that is dominating in the cotunneling regime.

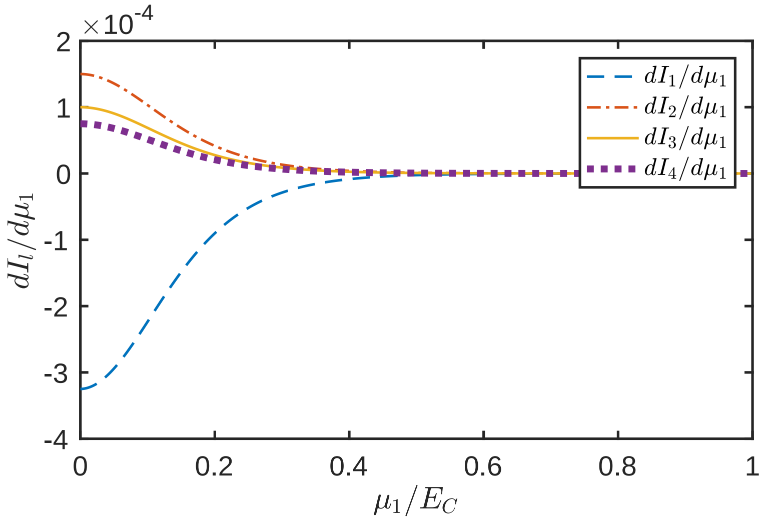

FIGURE 3.13: Non-local conductance $dI_l/d\mu_1$ for a system hosting four MBSs. The bias on lead 1 is μ_1. The other leads are grounded. In this case we consider that there is no overlap between the MBSs. The other parameters are $\Gamma_1 = 10^{-4}$, $\Gamma_2 = \Gamma_1/2$, $\Gamma_3 = \Gamma_1/3$, $\Gamma_4 = \Gamma_1/4$, $E_C = 1$ and $\beta = 25$.

3.6.3 Cotunneling regime

As explained in Section 3.4.2, in the cotunneling regime the system is tuned such that there are no degenerate charge states within a small bias window. Hence, for transport to occur either a large bias has to be applied, which then gives the results as seen for large bias in the sequential tunneling regime, or transport can occur via virtual states. We will consider the second possibility in this section. As in the sequential tunneling regime we look for a set of equations that allows us to calculate the occupation probabilities. We will here write a rate equation. The rate equation for the occupation probabilities can be written

$$\dot{P}_\alpha = -\sum_\alpha W^\alpha_\beta P_\alpha + \sum_\beta W^\beta_\alpha P_\beta, \tag{3.77}$$

where α denotes the state $|\alpha\rangle = |\mathbf{n}, N_C\rangle$ and P_α is the occupation probability of this state. The equation describes how the occupation probabilities changes due to different transitions occurring in the system. These transitions are given by the transition rates W^α_β. Here the notation is such that W^α_β describes a transition from the initial state $|\alpha\rangle$ to a final state $|\beta\rangle$.

Since we want to remain in the cotunneling regime we restrict ourselves to small biases, i.e., $|\mu_l| \ll E_C$. We tune the system to $n_g = -1$, which is the condition for the system to be in a Coulomb valley, around which cotunneling processes are dominant. This furthermore allows us to restrict ourselves to only consider the charge states with the smallest energy. These correspond to $|11; N_C - 1\rangle$, $|00; N_C\rangle$, $|10; N_C\rangle$, $|01; N_C\rangle$, $|00; N_C + 1\rangle$ and $|11; N_C\rangle$. There are in total six since we for each charge

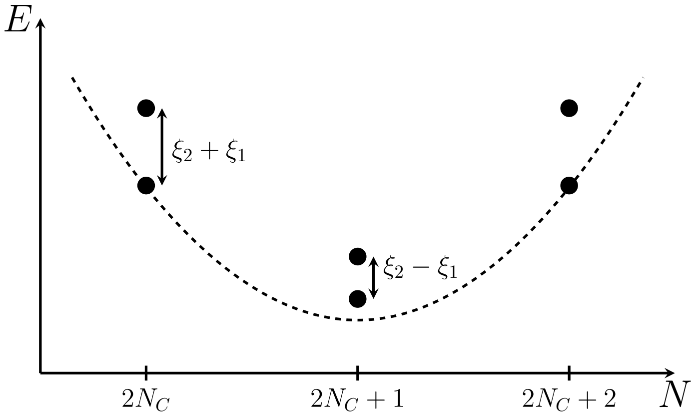

FIGURE 3.14: Distribution of the charge states in the Coulomb blockade. The figure shows the six charge states with the lowest energies when $n_g = -1$. Here it is assumed that $\xi_2 > \xi_1$.

state have to possibility to either occupy the d_1 or the d_2 state. The situation is depicted in Fig. 3.14. From the figure it is obvious that the low energy states are $|10; N_C\rangle$ and $|01; N_C\rangle$ and the rest makes up the virtual states. We denote by $P_{11;-1}$, $P_{00;0}$, $P_{10;0}$, $P_{01;0}$, $P_{00;1}$ and $P_{11;0}$ the occupation probabilities for the different states. We furthermore have to require that the occupation probabilities are normalized, i.e., $\sum_\alpha P_\alpha = 1$.

To obtain the transition rates, we apply Fermi's golden rule. Higher-order transitions are taken into account in Fermi's golden rule by writing it in the T-matrix representation [29]. Hence the transition rates are given by

$$W^\alpha_\beta = 2\pi \sum_{i,f} \left| \langle \psi_f, \beta | \hat{T} | \psi_i, \alpha \rangle \right|^2 \delta(E_{f,\beta} - E_{i,\alpha}). \tag{3.78}$$

Here the initial state of the total system, subsystem and leads are given by $|\psi_i, \alpha\rangle$, $|\psi_f, \beta\rangle$ correspond to the final states and $E_{i,\alpha}$ and $E_{f,\beta}$ denotes the respective energies of these. The T matrix is written as

$$\hat{T} = H'_{\text{tun}} + H'_{\text{tun}} \frac{1}{H_0 - E_{i,\alpha}} \hat{T}, \tag{3.79}$$

where H_0 is the unperturbed Hamiltonian and reads

$$H_0 = H_{\text{leads}} + H_{\text{MBS}} + H_{\text{charging}}. \tag{3.80}$$

The tunneling Hamiltonian is the same as in the sequential tunneling regime and is given in Eq. (3.54). The second order transitions rates can now be obtained if we expand the T matrix to second order. In total we obtain 14 different transition rates,

$$W^{11;-1}_{11;0}(l_1, l_2) = \frac{W_{l_1} W_{l_2}}{2\pi} \int dE n_F(E - \mu_{l_1}) n_F(-E + E_C(4 + 4n_g) - \mu_{l_2})$$

$$\begin{aligned} &\times \Bigg| \frac{\alpha^*_{l_1 1}\alpha_{l_2 1}}{\xi_1 + E_C(3+2n_g) - E} - \frac{\alpha^*_{l_2 1}\alpha_{l_1 1}}{\xi_1 - E_C(1+2n_g) + E} \\ &+ \frac{\alpha^*_{l_1 2}\alpha_{l_2 2}}{\xi_2 + E_C(3+2n_g) - E} - \frac{\alpha^*_{l_2 2}\alpha_{l_1 2}}{\xi_2 - E_C(1+2n_g) + E} \Bigg|^2 \end{aligned} \tag{3.81}$$

$$\begin{aligned} W^{11;0}_{11;-1}(l_1,l_2) = \frac{W_{l_1}W_{l_2}}{2\pi} \int dE\, &[1 - n_F(E - \mu_{l_1})] \left[1 - n_F(-E + E_C(4+4n_g) - \mu_{l_2})\right] \\ &\times \Bigg| \frac{\alpha^*_{l_1 1}\alpha_{l_2 1}}{\xi_1 - E_C(1+2n_g) + E} - \frac{\alpha^*_{l_2 1}\alpha_{l_1 1}}{\xi_1 + E_C(3+2n_g) - E} \\ &+ \frac{\alpha^*_{l_1 2}\alpha_{l_2 2}}{\xi_2 - E_C(1+2n_g) + E} - \frac{\alpha^*_{l_2 2}\alpha_{l_1 2}}{\xi_2 + E_C(3+2n_g) - E} \Bigg|^2 \end{aligned} \tag{3.82}$$

$$\begin{aligned} W^{00;0}_{00;1}(l_1,l_2) = \frac{W_{l_1}W_{l_2}}{2\pi} \int dE n_F&(E - \mu_{l_1}) n_F(-E + E_C(4+4n_g) - \mu_{l_2}) \\ &\times \Bigg| \frac{\alpha_{l_1 1}\alpha^*_{l_2 1}}{-\xi_1 + E_C(3+2n_g) - E} - \frac{\alpha_{l_2 1}\alpha^*_{l_1 1}}{-\xi_1 - E_C(1+2n_g) + E} \\ &+ \frac{\alpha_{l_1 2}\alpha^*_{l_2 2}}{-\xi_2 + E_C(3+2n_g) - E} - \frac{\alpha_{l_2 2}\alpha^*_{l_1 2}}{-\xi_2 - E_C(1+2n_g) + E} \Bigg|^2 \end{aligned} \tag{3.83}$$

$$\begin{aligned} W^{00;1}_{00;0}(l_1,l_2) = \frac{W_{l_1}W_{l_2}}{2\pi} \int dE\, &[1 - n_F(E - \mu_{l_1})] \left[1 - n_F(-E + E_C(4+4n_g) - \mu_{l_2})\right] \\ &\times \Bigg| \frac{\alpha_{l_1 1}\alpha^*_{l_2 1}}{-\xi_1 - E_C(1+2n_g) + E} - \frac{\alpha_{l_2 1}\alpha^*_{l_1 1}}{-\xi_1 + E_C(3+2n_g) - E} \\ &+ \frac{\alpha_{l_1 2}\alpha^*_{l_2 2}}{-\xi_2 - E_C(1+2n_g) + E} - \frac{\alpha_{l_2 2}\alpha^*_{l_1 2}}{-\xi_2 + E_C(3+2n_g) - E} \Bigg|^2 \end{aligned} \tag{3.84}$$

$$\begin{aligned} W^{01;0}_{10;0}(l_1,l_2) = \frac{W_{l_1}W_{l_2}}{2\pi} \int dE n_F&(E - \mu_{l_1}) \left[1 - n_F(E + \xi_2 - \xi_1 - \mu_{l_2})\right] \\ &\times \Bigg| \frac{\alpha_{l_2 2}\alpha^*_{l_1 1}}{-\xi_1 - E_C(3+2n_g) + E} - \frac{\alpha_{l_1 2}\alpha^*_{l_2 1}}{-\xi_2 + E_C(1+2n_g) - E} \\ &+ \frac{\alpha^*_{l_1 1}\alpha_{l_2 2}}{2\xi_2 - \xi_1 - E_C(3+2n_g) + E} - \frac{\alpha^*_{l_2 1}\alpha_{l_1 2}}{\xi_2 + E_C(1+2n_g) - E} \Bigg|^2 \end{aligned} \tag{3.85}$$

$$\begin{aligned} W^{10;0}_{01;0}(l_1,l_2) = \frac{W_{l_1}W_{l_2}}{2\pi} \int dE n_F&(E - \mu_{l_1}) \left[1 - n_F(E + \xi_1 - \xi_2 - \mu_{l_2})\right] \\ &\times \Bigg| \frac{\alpha_{l_2 1}\alpha^*_{l_1 2}}{-\xi_2 - E_C(3+2n_g) + E} - \frac{\alpha_{l_1 1}\alpha^*_{l_2 2}}{-\xi_1 + E_C(1+2n_g) - E} \\ &+ \frac{\alpha^*_{l_1 2}\alpha_{l_2 1}}{2\xi_1 - \xi_2 - E_C(3+2n_g) + E} - \frac{\alpha^*_{l_2 2}\alpha_{l_1 1}}{\xi_1 + E_C(1+2n_g) - E} \Bigg|^2 \end{aligned} \tag{3.86}$$

$$\begin{aligned} W^{11;0}_{00;1}(l_1,l_2) = \frac{W_{l_1}W_{l_2}}{2\pi} \int dE n_F(E-\mu_{l_1}) \left[1-n_F(E+\xi_1+\xi_2-\mu_{l_2})\right] \\ \times \left| \frac{\alpha_{l_2 1}\alpha_{l_1 2}}{\xi_2 - E_C(5+2n_g)+E} - \frac{\alpha_{l_1 1}\alpha_{l_2 2}}{-\xi_1 + E_C(3+2n_g)-E} \right. \\ \left. + \frac{\alpha_{l_2 2}\alpha_{l_1 1}}{\xi_1 - E_C(5+2n_g)+E} - \frac{\alpha_{l_1 2}\alpha_{l_2 1}}{-\xi_2 + E_C(3+2n_g)-E} \right|^2 \end{aligned} \tag{3.87}$$

$$\begin{aligned} W^{00;1}_{11;0}(l_1,l_2) = \frac{W_{l_1}W_{l_2}}{2\pi} \int dE n_F(E-\mu_{l_1}) \left[1-n_F(E-\xi_1-\xi_2-\mu_{l_2})\right] \\ \times \left| \frac{\alpha^*_{l_1 1}\alpha^*_{l_2 2}}{\xi_1 + E_C(3+2n_g)-E} - \frac{\alpha^*_{l_2 1}\alpha^*_{l_1 2}}{-\xi_2 - E_C(5+2n_g)+E} \right. \\ \left. + \frac{\alpha^*_{l_1 2}\alpha^*_{l_2 1}}{\xi_2 + E_C(3+2n_g)-E} - \frac{\alpha^*_{l_2 2}\alpha^*_{l_1 1}}{-\xi_1 - E_C(5+2n_g)+E} \right|^2 \end{aligned} \tag{3.88}$$

$$\begin{aligned} W^{11;-1}_{00;0}(l_1,l_2) = \frac{W_{l_1}W_{l_2}}{2\pi} \int dE n_F(E-\mu_{l_1}) \left[1-n_F(E+\xi_1+\xi_2-\mu_{l_2})\right] \\ \times \left| \frac{\alpha_{l_2 1}\alpha_{l_1 2}}{\xi_2 - E_C(1+2n_g)+E} - \frac{\alpha_{l_1 1}\alpha_{l_2 2}}{-\xi_1 - E_C(1-2n_g)-E} \right. \\ \left. + \frac{\alpha_{l_2 2}\alpha_{l_1 1}}{\xi_1 - E_C(1+2n_g)+E} - \frac{\alpha_{l_1 2}\alpha_{l_2 1}}{-\xi_2 - E_C(1-2n_g)-E} \right|^2 \end{aligned} \tag{3.89}$$

$$\begin{aligned} W^{00;0}_{11;-1}(l_1,l_2) = \frac{W_{l_1}W_{l_2}}{2\pi} \int dE n_F(E-\mu_{l_1}) \left[1-n_F(E-\xi_1-\xi_2-\mu_{l_2})\right] \\ \times \left| \frac{\alpha^*_{l_1 1}\alpha^*_{l_2 2}}{\xi_1 - E_C(1-2n_g)-E} - \frac{\alpha^*_{l_2 1}\alpha^*_{l_1 2}}{-\xi_2 - E_C(1+2n_g)+E} \right. \\ \left. + \frac{\alpha^*_{l_1 2}\alpha^*_{l_2 1}}{\xi_2 - E_C(1-2n_g)-E} - \frac{\alpha^*_{l_2 2}\alpha^*_{l_1 1}}{-\xi_1 - E_C(1+2n_g)+E} \right|^2 \end{aligned} \tag{3.90}$$

$$\begin{aligned} W^{11;-1}_{00;1}(l_1,l_2) = \frac{W_{l_1}W_{l_2}}{2\pi} \int dE n_F(E-\mu_{l_1}) n_F(-E-\xi_1-\xi_2+E_C(4+4n_g)-\mu_{l_2}) \\ \times \left| \frac{\alpha_{l_2 1}\alpha_{l_1 2}}{\xi_2 - E_C(1+2n_g)+E} - \frac{\alpha_{l_1 1}\alpha_{l_2 2}}{-\xi_1 + E_C(3+2n_g)-E} \right. \\ \left. + \frac{\alpha_{l_2 2}\alpha_{l_1 1}}{\xi_1 - E_C(1+2n_g)+E} - \frac{\alpha_{l_1 2}\alpha_{l_2 1}}{-\xi_2 + E_C(3+2n_g)-E} \right|^2 \end{aligned} \tag{3.91}$$

$$\begin{aligned} W^{00;1}_{11;-1}(l_1,l_2) = \frac{W_{l_1}W_{l_2}}{2\pi} \int dE \left[1-n_F(E-\mu_{l_1})\right] \left[1-n_F(-E-\xi_1-\xi_2+E_C(4+4n_g)-\mu_{l_2})\right] \\ \times \left| \frac{\alpha^*_{l_2 1}\alpha^*_{l_1 2}}{-\xi_2 + E_C(3+2n_g)-E} - \frac{\alpha^*_{l_1 1}\alpha^*_{l_2 2}}{\xi_1 - E_C(1+2n_g)+E} \right. \end{aligned}$$

$$
+\frac{\alpha^*_{l_2 2}\alpha^*_{l_1 1}}{-\xi_1 + E_C(3+2n_g) - E} - \frac{\alpha^*_{l_1 2}\alpha^*_{l_2 1}}{\xi_2 - E_C(1+2n_g) + E}\Bigg|^2 \tag{3.92}
$$

$$
\begin{aligned}
W^{00;0}_{11;0}(l_1,l_2) = \frac{W_{l_1}W_{l_2}}{2\pi}\int dE n_F(E-\mu_{l_1}) n_F(-E+\xi_1+\xi_2+E_C(4+4n_g)-\mu_{l_2}) \\
\times\Bigg|\frac{\alpha^*_{l_2 1}\alpha^*_{l_1 2}}{-\xi_2 - E_C(1+2n_g) + E} - \frac{\alpha^*_{l_1 1}\alpha^*_{l_2 2}}{\xi_1 + E_C(3+2n_g) - E} \\
+\frac{\alpha^*_{l_2 2}\alpha^*_{l_1 1}}{-\xi_1 - E_C(1+2n_g) + E} - \frac{\alpha^*_{l_1 2}\alpha^*_{l_2 1}}{\xi_2 + E_C(3+2n_g) - E}\Bigg|^2
\end{aligned} \tag{3.93}
$$

$$
\begin{aligned}
W^{11;0}_{00;0}(l_1,l_2) = \frac{W_{l_1}W_{l_2}}{2\pi}\int dE\,[1-n_F(E-\mu_{l_1})]\,[1-n_F(-E+\xi_1+\xi_2+E_C(4+4n_g)-\mu_{l_2})] \\
\times\Bigg|\frac{\alpha_{l_2 1}\alpha_{l_1 2}}{\xi_2 + E_C(3+2n_g) - E} - \frac{\alpha_{l_1 1}\alpha_{l_2 2}}{-\xi_1 - E_C(1+2n_g) + E} \\
+\frac{\alpha_{l_2 2}\alpha_{l_1 1}}{\xi_1 + E_C(3+2n_g) - E} - \frac{\alpha_{l_1 2}\alpha_{l_2 1}}{-\xi_2 - E_C(1+2n_g) + E}\Bigg|^2,
\end{aligned} \tag{3.94}
$$

where $W_l = 2\pi|t_l|^2 D_l$ and $D_l = 1/(2\pi v_F)$ as we are assuming a constant density of states in the leads.

For finite temperatures, the tunneling rates diverge and must be regularized to remain physical. To this end, one introduces a finite broadening [87, 86], $\gamma \sim W_i$ which shifts the poles away from the real line. Once the broadening has been introduced, the absolute values seen in the transitions rates are expanded in the broadening parameter γ. The procedure is finished by subtracting the $1/\gamma$ term. The procedure leads to integrals of two types,

$$
\begin{aligned}
I(E_1,E_2,\epsilon_1,\epsilon_2) =& \lim_{\gamma\to 0}\mathrm{Re}\int dE\, n_F(E-E_1)\,[1-n_F(E-E_2)]\,\frac{1}{E-\epsilon_1-i\gamma}\frac{1}{E-\epsilon_2+i\gamma} \\
=& \frac{n_B(E_2-E_1)}{\epsilon_1-\epsilon_2}\mathrm{Re}\{\psi(1/2+i\beta\,[E_2-\epsilon_1]\,/2\pi) \\
&-\psi(1/2-i\beta\,[E_2-\epsilon_2]\,/2\pi) \\
&-\psi(1/2+i\beta\,[E_1-\epsilon_1]\,/2\pi) \\
&+\psi(1/2-i\beta\,[E_1-\epsilon_2]\,/2\pi)\},
\end{aligned} \tag{3.95}
$$

$$
\begin{aligned}
J(E_1,E_2,\epsilon) =& \lim_{\gamma\to 0}\left[\int dE\, n_F(E-E_1)\,[1-n_F(E-E_2)]\,\frac{1}{(E-\epsilon)^2+\gamma^2} - \mathcal{O}(1/\gamma)\right] \\
=& \frac{\beta}{2\pi}n_B(E_2-E_1)\mathrm{Im}\{\psi'(1/2+i\beta\,[E_2-\epsilon]\,/2\pi) \\
&-\psi'(1/2+i\beta\,[E_1-\epsilon]\,/2\pi)\},
\end{aligned} \tag{3.96}
$$

where $n_B(x) = \frac{1}{e^{\beta x}-1}$ and $\psi^{(n)}$ denotes the polygamma function.

Given the calculated transition rates we can now find the occupation probabilities. Like in the case of transport in the sequential tunneling regime we are interested in the steady state limit, hence $\dot{P}_\alpha = 0$. This allows us to write Eq. (3.77) as

$$\underline{W}\mathbf{P} = \mathbf{0}. \tag{3.97}$$

The last row is replaced by the normalization condition, $\sum_\alpha P_\alpha = 1$ and the system of equations is then solved numerically. For the gate voltage tuned to $n_g \approx -1$ and $\mu_l < E_C$ we obtain finite occupation probabilities for the two states lowest in energy, $|10; N_C\rangle$ and $|01; N_C\rangle$. The other occupation probabilities are $P_{11;-1} \approx P_{00;0} \approx P_{00;1} \approx P_{11;0} \propto e^{-E_C/T} \approx 0$. The values of the $P_{10;0}$ and $P_{01;0}$ depends on how the bias is applied. The fact that $P_{10;0}$ and $P_{01;0}$ are the only occupation probabilities that remain finite should be expected since we only apply a small bias. Hence, we do not supply the electrons with enough energy to be able to occupy states with higher energy. This does not however mean that transport is completely cut off. Indeed transitions can occur via higher states by means of virtual transitions.

Similar to Eq. (3.71) the expression for the current taking second order tunneling processes into account is given by

$$\langle I_l \rangle = \sum_{\mathbf{n},N_C} \left(W_l^{1,+} - W_l^{1,-} \right) P(\mathbf{n}, N_C) + 2 \sum_{\mathbf{n},N_C} \left(W_l^{2,+} - W_l^{2,-} \right) P(\mathbf{n}, N_C). \tag{3.98}$$

In this expression $W_l^{1,+(-)}$ correspond to the transition rates found in Eq. (3.78). As previously explained, these are processes that either increase or decrease the particle number by one, in contrast to $W_l^{2,+(-)}$, which corresponds to a change of number of particles by two. We further learn from that $P_{10;0}$ and $P_{10;0}$ are the only finite occupation probabilities, that the current is purely driven by elastic (ECT) and inelastic (ICT) cotunneling processes. An ECT process is such that the initial and final state of the system remains the same. Hence, these are described by tunneling rates $W_{10;0}^{10;0}$ and $W_{01;0}^{01;0}$. The ICT, on the other hand, describes the process where the initial and final states are different but with the number of particles still being conserved. The transition rates that describe this effect are $W_{10;0}^{01;0}$ and $W_{01;0}^{10;0}$. This implies that the current, Eq. (3.98) can be written as

$$\langle I_l \rangle = I_l^{\mathrm{ECT}} + I_l^{\mathrm{ICT}}, \tag{3.99}$$

where

$$I_l^{\mathrm{ECT}} = \sum_k \left\{ \left[W_{10;0}^{10;0}(l,k) - W_{10;0}^{10;0}(k,l) \right] P_{10;0} + \left[W_{01;0}^{01;0}(l,k) - W_{01;0}^{01;0}(k,l) \right] P_{01;0} \right\}, \tag{3.100}$$

and

$$I_l^{\mathrm{ICT}} = \sum_k \left\{ \left[W_{10;0}^{01;0}(l,k) - W_{10;0}^{01;0}(k,l) \right] P_{01;0} + \left[W_{01;0}^{10;0}(l,k) - W_{01;0}^{10;0}(k,l) \right] P_{10;0} \right\}. \tag{3.101}$$

Analytical results for the transition rates can be found in the limit $\xi_j, |\mu| \ll E_C$ and $T = 0$. For the Majorana box, these are given by

$$W^{10;0}_{10;0}(l,k) = \frac{2W_l W_k}{\pi E_C^2}(\mu_l - \mu_k)\Theta(\mu_l - \mu_k), \tag{3.102}$$

$$W^{10;0}_{01;0}(l,k) = \frac{2W_l W_k}{\pi E_C^2}(\mu_l - \mu_k + \xi_1 - \xi_2) \times \Theta(\mu_l - \mu_k + \xi_1 - \xi_2), \tag{3.103}$$

where $k, l \in \{1, 2\}$ in the first line, and $k, l \in \{3, 4\}$ in the second line and for the T-junction by

$$W^{10;0}_{10;0}(l,k) = \frac{2W_l W_k}{\pi E_C^2}(\mu_l - \mu_k)\Theta(\mu_l - \mu_k), \tag{3.104}$$

$$W^{10;0}_{01;0}(l,k) = \frac{2W_l W_k}{\pi E_C^2}(\mu_l - \mu_k - \xi_T)\Theta(\mu_l - \mu_k - \xi_T), \tag{3.105}$$

with $k, l \in \{1, \ldots, 4\}$. As a consistency check consider zero overlap between the MBSs, i.e., $\xi_1 = \xi_2 = \xi_T = 0$. This results in $W^{10;0}_{10;0}(l,k) = W^{01;0}_{01;0}(l,k) = W^{10;0}_{01;0}(l,k) = W^{01;0}_{10;0}(l,k)$ for all $k, l \in \{1, 2, 3, 4\}$. We note that the results are in agreement with what is discussed in the end of the sequential tunneling regime. As the overlap goes to zero the structures become indistinguishable and hence the transport looks the same in the two structures.

We now consider the Majorana box in the cotunneling regime. The bias configuration is such that $\mu_1 = \mu$ and $\mu_2 = \mu_3 = \mu_4 = -\mu$. We plot the results in Fig. 3.15. A current between leads 1 and 2 is observed for an infinitesimal bias, which is due to ECT. We note that the numerical results are in good agreement with the analytical calculations. Consider the derivative of the ECT cotunneling rate, Eq. (3.102), with respect to the chemical potential, and one finds that it is constant as observed in Fig. 3.15. The fact that no current is observed in leads 3 and 4 is due to that these do not couple to the d_1 state. Hence no current between lead 1 and leads 3 and 4 can stem from ECT.

As the bias is increased and becomes larger than the difference $|\xi_2 - \xi_1|$, a current is observed in leads 3 and 4. As explained no current between lead 1 and leads 3 and 4 can be due to ECT and hence this current is solely driven by ICT processes. This is furthermore explained by the analytical results, Eq. (3.103), from which it is clear that as long as $\mu < |\xi_2 - \xi_1|$, $W^{10;0}_{01;0} = W^{01;0}_{10;0} = 0$.

To help to understand the physical details of the processes that give rise to the specific currents, we look to Fig. 3.16. The island is initially in the $|10; N_C\rangle$ state. Now, the electron residing on the island tunnels into lead 2 (see Fig. 3.16 (a)). The system is now in the $|00; N_C\rangle$ state. An electron from lead 1 can now tunnel onto the island, bringing the system back to its initial state, $|10; N_C\rangle$.

The tunneling from lead 1 to leads 3 and 4 is like in the sequential tunneling regime driven by Cooper pairs. The transport is depicted in Fig. 3.16 (b). As in the first case, we consider an electron residing in the d_1 state. As the bias on leads 3

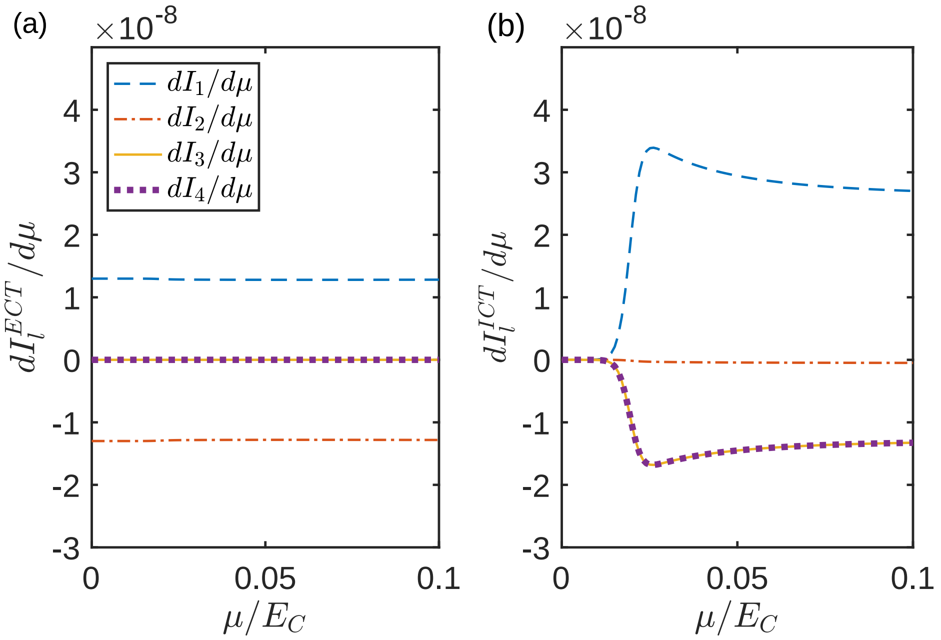

FIGURE 3.15: Differential conductance in the Coulomb blockade regime for the Majorana box. The bias on lead 1 is $\mu_1 = \mu$. The biases applied to leads $2-4$ are $\mu_2 = \mu_3 = \mu_4 = -\mu$. The differential conductance is due to (a) elastic cotunneling and (b) inelastic cotunneling. Note that in both plots $dI_3/d\mu = I_4/d\mu$. The parameters are $E_C = 1$, $W_i = 1 \cdot 10^{-4}$, $\xi_1 = 0.01$, $\xi_2 = 0.03$, $\beta = 900$ and $n_g = -1$.

and 4 become smaller than $-(\xi_2 - \xi_1)$, a possibility for a Cooper pair to split becomes possible. Upon being split, the two electrons that are being produced are transferred either to lead 3 or 4 and to the d_2 state. The system is now in the virtual state $|11; N_C - 1\rangle$. The electron in the d_1 state now favorably forms a Cooper pair with an electron from lead 1, which brings the system to the $|01; N_C\rangle$ state. Hence an electron has been removed from lead 1, and an electron has been created in either lead 3 or 4.

We now consider the T-junction. The differential conductance is plotted in Fig. 3.17. Comparing this to the results of the Majorana box, we note that they are in most regards almost identical. The difference lies in that for the T-junction, a current due to both ECT and ICT is observed in all leads in contrast to the Majorana box, for which ECT only occurs between leads 1 and 2 and ICT between lead 1 and leads 3 and 4. A current due to ECT is observed for an infinitesimal applied bias. as $|\mu|$ becomes larger than ξ_T a current due to ICT is observed as well.

Contrary to the sequential tunneling regime, in the cotunneling regime a current is observed in the central lead even for $|\mu| < \xi_T$. This results from the fact that cotunneling processes are now possible, and electrons can tunnel via virtual states. Let us consider the system being in the $|10; N_C\rangle$ state. As all leads couple to the d_2 state, let us assume that an electron from lead 1 tunnels onto the island such that it is in the virtual $|11; N_C\rangle$ state. As lead 4 couple to the d_2 state, the electron can now simply tunnel into it, and hence an electron has been transferred from lead 1 to lead

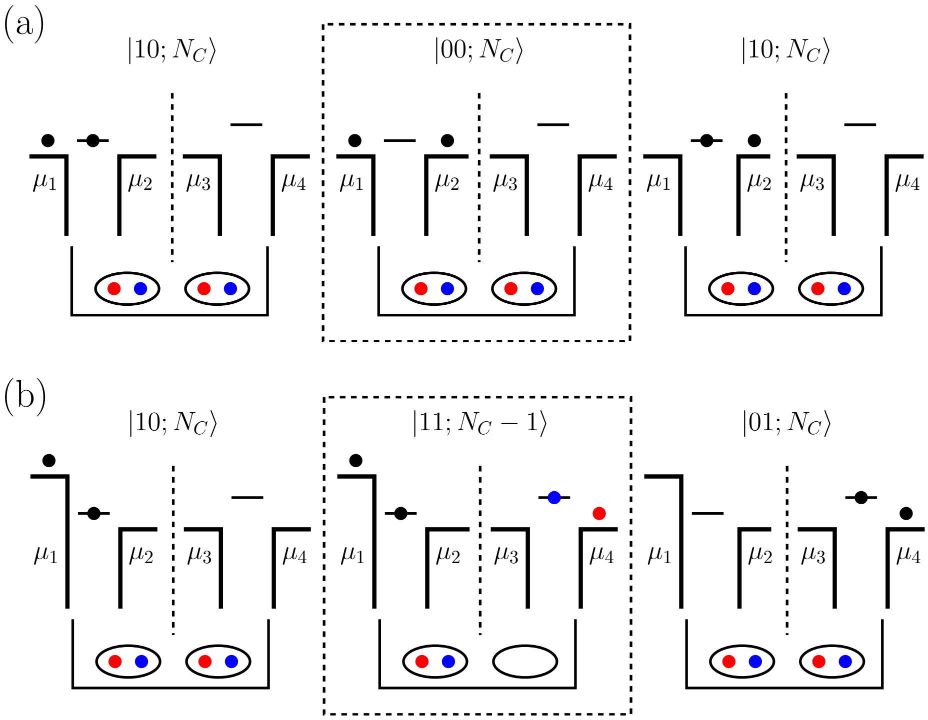

FIGURE 3.16: Examples of (a) elastic and (b) inelastic cotunneling in the Majorana box. The dashed boxes indicate virtual states. (a) An electron occupying the MBSs of the first wire is transferred to the second lead. After that an electron from the first lead is transferred into the MBSs. The MBSs goes from being occupied to empty to once again occupied and an electron has been transferred from the first to the second lead. The process of the island is $|10; N_C\rangle \rightarrow |00; N_C\rangle \rightarrow |10; N_C\rangle$. (b) Inelastic cotunneling: initially an electron occupies the MBSs on the first wire. A Cooper pair is broken and one of the electrons goes to lead 4 and the other to occupy the MBSs of the second wire. The electron in the MBSs on the first wire then forms a Cooper pair with an electron from the first lead. In total an electron has been transferred from lead 1 to lead 3 or 4. The island has changed between the following states: $|10; N_C\rangle \rightarrow |11; N_C - 1\rangle \rightarrow |01; N_C\rangle$.

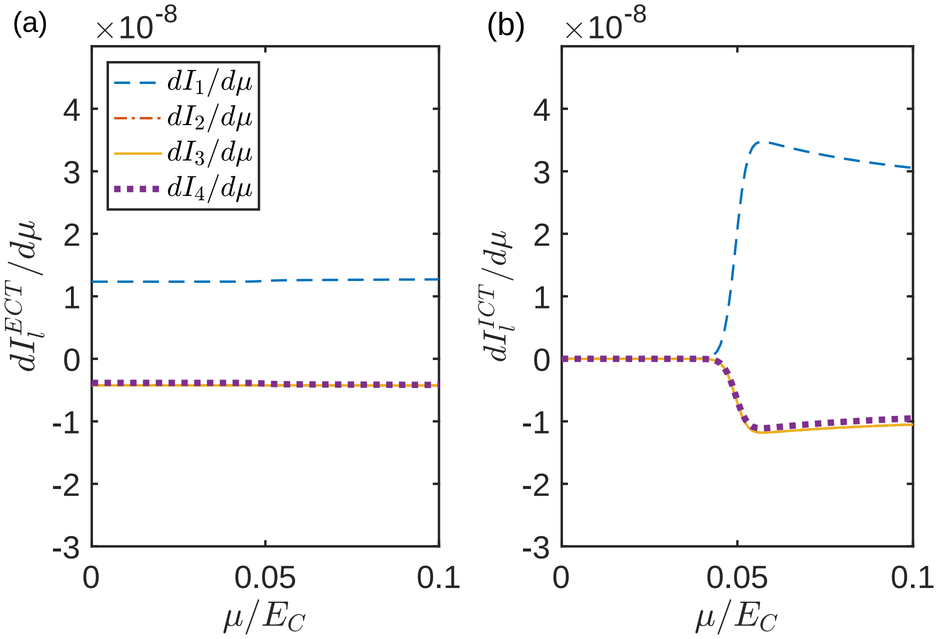

FIGURE 3.17: Differential conductance in the Coulomb blockade for the T-junction. The bias on lead 1 is $\mu_1 = \mu$. The biases applied to leads $2-4$ are $\mu_2 = \mu_3 = \mu_4 = -\mu$. The differential conductance is due to (a) elastic cotunneling and (b) inelastic cotunneling. Note that in both plots In both plots $dI_2/d\mu = dI_3/d\mu$. The parameters are $E_C = 1$, $W_i = 1 \cdot 10^{-4}$, $\xi_T = 0.05$, $\beta = 900$ and $n_g = -1$.

4, and energy has throughout the process been conserved.

As a concluding remark, we note that due to that the d_2 state couples to all leads, ECT can drive a current between all leads. This is the reason why no current is observed due to ECT between lead 1 and leads 3 and 4 in the Majorana box.

Chapter 4

Light-matter interaction in nodal loop semimetals

This chapter is devoted to the interaction between light and matter. More specifically, we will discuss the optical activity in a nodal loop semimetal, introduced in Section 2.4.2. The interplay between light and matter has for long been, among others, an important tool for the understanding of materials. Different optical techniques allow us to obtain information about different properties of the material. In the same way, knowing how a material reacts under the influence of light can lead to the creation of new technologies.

With the discovery of topological materials, understanding how light interacts with these has become a growing topic [145, 11, 74, 127, 75, 155, 67, 66]. Many interesting effects have been discovered. Among these are axion electrodynamics [145], quantized photocurrents [75], photogalvanic effects [66], and large second harmonic generation [127, 155].

Two optical techniques that have been around for a long time are the Kerr and Faraday effects. The Kerr and Faraday angles measure, respectively, the rotation of polarization angles from reflected and transmitted waves with respect to incident light, due to the interaction between the light and the material. Historically these techniques required an external magnetic field. However, many topological materials have an intrinsic Hall conductivity, even without the application of external magnetic fields. Hence, the Kerr and Faraday effect are promising techniques for obtaining some of the properties of topological materials.

The Kerr and Faraday effects of topological materials have mainly been under theoretical investigations. An early study shows that topological insulators should indeed give rise to large Kerr and Faraday angles [164]. Furthermore, it is shown that the Faraday rotation takes a universal value at low frequencies proportional to the fine structure constant, α. The effects have as well been investigated in other topological phases that are based on the Haldane model [131].

In Weyl semimetals, especially the Kerr effect has been under investigation [78, 151]. Similar to topological insulators, one should be able to observe Kerr angles in thin-film Weyl semimetals that are of the same order of magnitude as those observed in topological insulators, indicating a strong optical activity in these materials. A model taking into account four Weyl nodes in a magnetic field is studied in [126]. This study further shows how the Kerr effect is modified by magnetic fields and furthermore shows how features of the chiral anomaly and valley polarization can be observed in the spectrum of the Kerr angle.

As discussed in the introductory chapter, topological materials exist beyond topological insulators and Weyl semimetals. In this chapter, we discuss the Kerr effect of one of those materials, the nodal loop semimetals. The results discussed here are based on those we obtained in the paper titled *Kerr effect in tilted nodal loop semimetals* [49]. Similar to other topological materials, we find that the nodal loop as well features large Kerr rotations. On the contrary, the Kerr rotations strongly depend on the tilt of the nodal loop. We further elucidate on how properties of the nodal loop can be observed in the Kerr rotation spectrum.

We begin the following sections by discussing Maxwell's equations and introducing the Kerr and Faraday effects. After that, we present the model of the tilted nodal loop semimetal. Maxwells's equations tell us that to describe the reflected light due to an incident beam, we must know the conductivity tensor of the material. We thus introduce the Kubo formula and calculate the full conductivity tensor of the tilted nodal loop Hamiltonian. With this information and applying Maxwell's equations, we obtain the Kerr rotations for a thin film and bulk nodal loop semimetal[1].

4.1 Light-matter interaction

The interaction between light and matter has been a long-studied topic. The first breakthrough came when Maxwell formulated a set of equations, that successfully describes the interaction between light and matter. The equations have ever since been the foundation of classical electromagnetism and are, on differential form written as

$$\nabla \cdot \mathbf{D} = 4\pi\rho \tag{4.1}$$

$$\nabla \times \mathbf{H} - \frac{1}{c}\frac{\partial}{\partial t}\mathbf{D} = \frac{4\pi}{c}\mathbf{J} \tag{4.2}$$

$$\nabla \times \mathbf{E} + \frac{1}{c}\frac{\partial}{\partial t}\mathbf{B} = 0 \tag{4.3}$$

$$\nabla \cdot \mathbf{B} = 0. \tag{4.4}$$

where **D** is the displacement field, **H** is the magnetic field, **E** is the electric field and **B** is the magnetic flux. The quantities on the right-hand side of the equations are the charge density, ρ and the current, **J**. The first equation is Gauss' law for electricity. It gives a relationship between the charge density and the displacement field. Integrating over the whole system, one has a relationship between the total charge and the displacement field. The second equation is Ampère's circuit law. It gives a

---

[1] In this chapter we set $e = \hbar = 1$.

relationship between the current and the magnetic field it creates around itself. The third equation is Faraday's law of inductions. This equation states that a change in the magnetic field will create a potential difference, which will mean a possibility for the creation of a current flow. The last equation is Gauss' law of magnetism. It states that the divergence of the magnetic flux equals zero. An implication of this is that there cannot exist any magnetic monopoles. By integrating the equation (over some region in space), the equation then states that the field lines penetrating the surface must sum to zero, i.e., the number of field lines going into the encapsulated region must be the same as the number going out. Hence, no magnetic charge can build up in space.

The electric field can be related to the current by Ohm's law,

$$\mathbf{J} = \sigma \mathbf{E}, \tag{4.5}$$

where σ is the conductivity tensor which depends on the macroscopic properties of the material. The constitutive relations give the relations between the electric and displacement fields and between the magnetic flux and the magnetic field. These are of importance when considering the propagation of electromagnetic waves in dispersive media. The displacement field is related to the electric field by

$$\mathbf{D} = \epsilon_b \mathbf{E} + \mathbf{P}, \tag{4.6}$$

where ϵ_b is the static permittivity and $\mathbf{P}$ is the polarization. The relation between the magnetic flux and the magnetic field is given by

$$\mathbf{H} = \frac{1}{\mu}\mathbf{B} - \mathbf{M}, \tag{4.7}$$

where μ is the magnetization of the material, not to be confused with the chemical potential, and $\mathbf{M}$ is the magnetization field. For the ensuing discussion we will consider materials that are neither magnetized nor polarized and hence, $\mathbf{D} = \epsilon_b \mathbf{E}$ and $\mathbf{H} = \frac{1}{\mu}\mathbf{B}$.

Many physical quantities can be obtained from the knowledge of the electromagnetic field. However, with the above equations it is not always straight forward to obtain it. Hence we seek another equation which only describes the time evolution of the electric field. We obtain this equation by combining Maxwell's equations. First we take the curl of the third equation, Eq. (4.3) and use the identity for double curls, $\nabla \times (\nabla \times \mathbf{E}) = \nabla(\nabla \cdot \mathbf{E}) - \nabla^2 \mathbf{E}$. We then obtain

$$\nabla(\nabla \cdot \mathbf{E}) - \nabla^2 \mathbf{E} + \frac{1}{c}\frac{\partial}{\partial t}(\nabla \times \mathbf{B}) = 0. \tag{4.8}$$

Next we take the derivative of Eq. (4.2) with respect to time and insert it in the above equation. Furthermore, Ohm's law is applied to right hand side such that

$$\nabla(\nabla \cdot \mathbf{E}) - \nabla^2 \mathbf{E} = \frac{\mu}{c^2}\left[\epsilon_b \frac{\partial^2}{\partial t^2}\mathbf{E} + 4\pi\sigma\frac{\partial}{\partial t}\mathbf{E}\right] \tag{4.9}$$

This is the *electromagnetic wave equation* and describes the time evolution of the electromagnetic field in time and space. The equation is in Fourier space written as

$$(\mathbf{k}\cdot\mathbf{k})\,\mathbf{E}(\mathbf{k},\omega) - \mathbf{k}\,(\mathbf{k}\cdot\mathbf{E}(\mathbf{k},\omega)) = \frac{\mu\omega^2}{c^2}\left[\epsilon_b + \frac{4\pi i}{\omega}\sigma\right]\mathbf{E}(\mathbf{k},\omega). \tag{4.10}$$

The term inside the bracket on the right hand side correspond to the permittivity, $\epsilon = \epsilon_b \mathbf{I} + \frac{4\pi i}{\omega}\sigma$, where here $\mathbf{I}$ represents the 3 by 3 identity matrix. Once we have the knowledge of the electric field, the other fields follow by solving Maxwell's equations. By Fourier transforming Eq. (4.3) we have a simple relation between the electric field and the magnetic flux,

$$\mathbf{B} = \frac{c}{\omega}\mathbf{k}\times\mathbf{E}. \tag{4.11}$$

As with so many other physical phenomena, these equations have to be accompanied by boundary conditions. The details of these are given in Appendix D. There are in total four conditions. For the following discussion only two of them matters. Consider the interface between two materials. The first boundary condition tells us that the electric field parallel to the surface must be equal on both sides, or more precise it has to be continuous across the interface, hence

$$\mathbf{E}_1^{\parallel} = \mathbf{E}_2^{\parallel}. \tag{4.12}$$

The second boundary condition relates the magnetic flux on the two sides of the surface to each other. Contrary to the electric field, the second boundary condition states that the magnetic flux parallel to the surface is discontinuous. The discontinuity is equal to any induced currents. The boundary condition is written as

$$\hat{\mathbf{n}}_{12} \times \left(\frac{\mathbf{B}_1^{\parallel}}{\mu_1} - \frac{\mathbf{B}_2^{\parallel}}{\mu_2}\right) = \frac{4\pi}{c}\mathbf{J}, \tag{4.13}$$

where $\hat{\mathbf{n}}_{12}$ is the unit vector pointing from material 1 to 2.

4.2 Kerr and Faraday effects

The Kerr and Faraday effects are optical effects that describe the polarization of a reflected and a transmitted beam on a material surface, respectively. The Faraday effect was first discovered by Michael Faraday already in 1846 [52]. During his experiment, he observed that the polarization plane of a linearly polarized light beam was rotated upon transmission through a material, in this case, borosilicate (mixture of silica and boron trioxide) glass, upon the application of a magnetic field. The effect was quickly confirmed and is nowadays a common tool in the field of magneto-optics, the field where optical tools are combined with magnetism.

Three decades later, in 1876, it was discovered by John Kerr that, similarly to the observation of Faraday, the polarization plane of linearly polarized light was rotated upon the reflection on a material surface [72]. In this experiment, the pole of a magnet was used to reflect the incident light. This gave rise to the polar magneto-optical Kerr effect. Two years later, the effect was observed for an in-plane magnetized piece of iron, giving rise to the longitudinal magneto-optical Kerr effect.

Note that during the discovery of the Kerr and Faraday effects, the development of quantum mechanics had yet to begin. Because of this, there did not exist a theoretical description of the observed phenomena. One of the early, suggested theories, was based on the idea that the left- and right-circularly polarized light coupled differently to classical electron oscillators in solids.

Once quantum mechanics took a leap, the basic understanding of the Faraday and Kerr effects was developed. The first proposed model was developed by Hulme, [69], where he proposed that the Faraday effect arises from the spin-polarized electron motion due to spin-orbit coupling. He considered how the refractive index depends on the left and right-handed polarized beams by considering the spin-orbit induced splitting of the energy eigenvalues. On the other hand, the effect on the wave functions was neglected.

Later on, it was argued by Kittel [83] that the contribution from the wave functions could be of the same order of magnitude. A few years later, Argyres, [7], developed a complete formulation of the model. In this case, both the spin-orbit coupling and the spin-polarization were accounted for. Hence the Kerr and Faraday effects were in the 1950s understood as being caused by the spin-orbit coupling and the exchange splitting.

The 50s also saw an improvement in the experimental techniques, and two discoveries created a spark for experimental research in the field. The first one was the discovery that the magnetic domains could be observed using the Kerr effect [171]. The second was the discovery that the Kerr effect could be used for reading out suitably stored magnetic information [172, 39].

The field has since then developed both on the experimental side, with more powerful equipment, as well as on the theoretical side with the development of linear response and density functional theory. The Kerr and Faraday effects have now become a powerful tool for studying materials. They can be used, for example, to acquire information about the band structure of materials as well as giving information about their optical conductivity.

A property of many topological materials is their intrinsic Hall conductivity. As the Faraday and Kerr effects are directly dependent on the dynamical Hall conductivity, they should serve as excellent tools for understanding certain aspects of these materials. Many theoretical works has indeed shown that we can learn a great deal about topological materials from Kerr and Faraday measurements [164, 78, 151, 131, 126].

We will in the next section describe the theoretical model used to calculate the Kerr and Faraday effects. After that, we apply it to the nodal loop semimetal and describe the behavior of the Kerr effect in this class of materials.

4.2.1 Theoretical model

To describe the Kerr effect, theoretically, we consider the setup depicted in Fig. 4.1. A linearly polarized incident beam is reflected (transmitted) upon the surface of the material. Upon reflection (transmission) the reflected (transmitted) beam may acquire a change of phase such that in general the reflected (transmitted) light is no more linearly polarized but rather elliptically polarized. The reflected light can be represented by two circularly polarized light beams

$$\mathbf{E}_r = \left(E_r^R \hat{e}'_R + E_r^L \hat{e}'_L \right) e^{-i(\mathbf{k}\cdot\mathbf{r}+\omega t)}, \tag{4.14}$$

where $\hat{e}'_{R/L} = \hat{\mathbf{i}} \pm i\hat{\mathbf{j}}$, for some arbitrary directions $\hat{\mathbf{i}}$ and $\hat{\mathbf{j}}$, obeying the direction of the reflected light. E_r^R and E_r^L are the amplitudes of the right and left-handed reflected light, respectively. The Kerr angles are now obtained by considering the quotient of the right and left handed circularly polarized light. Writing the quotient on polar form amounts to $E_r^R / E_r^L = \frac{|E_r^R|}{|E_r^L|} e^{i(\alpha_R - \alpha_L)}$. The change in polarization angle, the Kerr angle is from this defined as

$$\theta_K = \frac{1}{2}(\alpha_R - \alpha_L), \tag{4.15}$$

and the ellipticity, a measure of how circular[2] the reflected light is, is defined as

$$\epsilon_K = \frac{|E_r^R|}{|E_r^L|}. \tag{4.16}$$

From the ellipticity one can conclude that: if ϵ_K becomes zero or infinite, this means that the reflected light is either entirely right or left-handed, circularly polarized. If it is close to one, we need the information of the Kerr angle to fully determine the polarization of the reflected light.

To obtain the Kerr angle and the ellipticity, we thus have to find the reflected fields given an incident beam on a material surface. This amounts to solving Maxwell's equations in the different materials and match the different fields by using the boundary conditions given by Eqs. (4.12) and (4.13). Before defining a specific system, let us consider a general setup for the Kerr rotations of a thin film and for a bulk material.

---

[2] The polarization of the reflected light can vary between linear, elliptical and circular.

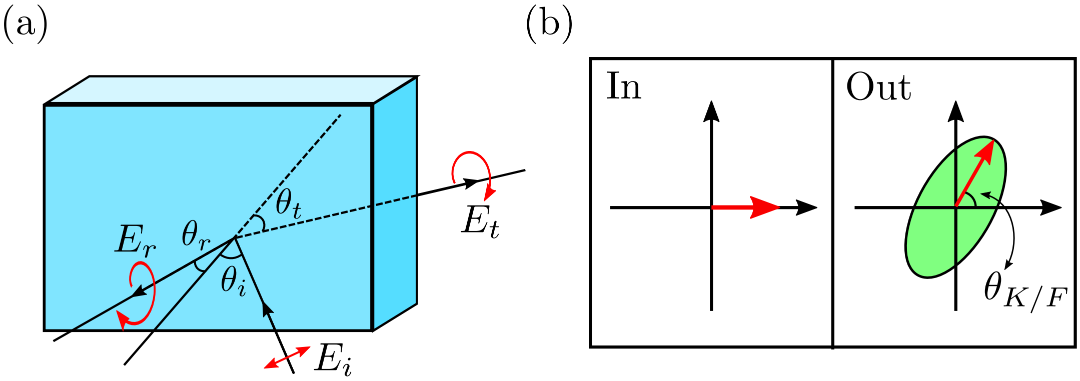

FIGURE 4.1: Schematic figure of the Kerr and Faraday effects. (a) An incoming linearly polarized light beam, E_i, is reflected (E_r) and transmitted (E_t) upon the the material surface. The outgoing light may have a polarization that is distinct from the incoming one. The polarization rotation of the reflected is denoted the Kerr rotation, whereas the rotation of the transmitted is denoted the Faraday rotation. (b) The left part represents the polarization of the incoming light, which is of linear polarization. The right represents the outgoing light which might have obtained a polarization rotation depicted by the ellipse.

Thin film

A thin film is characterized by that its thickness is much smaller than the wavelength of incident light. Because of this, the inside of the material has no influence on the light propagation, and only the surfaces matter. Let us first consider a normal incident, linearly polarized beam, on the $x - y$ surface of the thin film. The light beam thus propagates in the k_z direction. The incoming wave is written

$$\mathbf{E_0} = \frac{E_0}{2} \left(\hat{e}_R + \hat{e}_L\right) e^{ik_z z - i\omega t}, \tag{4.17}$$

where $e_{R/L} = \hat{\mathbf{x}} \mp \hat{\mathbf{y}}$. In this notation, the linearly polarized beam has been decomposed into a left and right-handed polarized beam, but by summing them correspond to a beam linearly polarized along the x-axis. The reflected beam is given by Eq. (4.14). As we consider an incident beam traversing in the k_z direction, the reflected beam must be reflected back in the $-k_z$ direction. Furthermore, this implies that the electric field can only have components in the $\hat{\mathbf{x}}$ and $\hat{\mathbf{y}}$ directions. The reflected field is hence written as

$$\mathbf{E}_r = \left(E_r^R \hat{e}'_R + E_r^L \hat{e}'_L\right) e^{-i(k_z z + \omega t)}, \tag{4.18}$$

with $\hat{e}'_{R/L} = \hat{\mathbf{x}} \pm i\hat{\mathbf{y}}$. The transmitted field must, according to Snell's law take the following form

$$\mathbf{E}_t = \left(E_t^R \hat{e}_R + E_t^L \hat{e}_L\right) e^{ik_z z - i\omega t}. \tag{4.19}$$

The magnetic field corresponding to the incident, reflected and transmitted fields are calculated using Eq. (4.11). We then set $\mathbf{E}_1 = \mathbf{E}_r + \mathbf{E}_0$ and $\mathbf{E}_2 = \mathbf{E}_t$; the incident and reflected beams are present on one side of the film, whereas, the transmitted field are present on the other. For the same reasons we set $\mathbf{B}_1 = \mathbf{B}_r + \mathbf{B}_0$. As stated above, only the material surface matters for the influence the material has on the incident beam. Thus, we have to consider the boundary conditions of the material. The surface conductivity, σ^S, is approximated by the bulk conductivity tensor and the width, d, of the thin film as $\sigma^S_{ij} = d\sigma_{ij}$ [78]. The boundary conditions, Eqs. (4.12) and (4.13), now give us four equations. These are

$$\begin{aligned} \left[E_r^R + E_r^L\right] + 2E_0 &= \left[E_t^R + E_t^L\right] && (4.20)\\ i\left[E_r^L - E_r^R\right] &= i\left[E_t^R - E_t^L\right] && (4.21)\\ \lambda_2\left[E_t^R - E_t^L\right] - \lambda_1\left[E_r^R - E_t^L\right] &= J_y, && (4.22)\\ \lambda_2\left[E_t^R + E_t^L\right] + \lambda_1\left[E_r^R + E_r^L\right] - 2\lambda_1 E_0 &= J_x, && (4.23) \end{aligned}$$

where

$$\begin{aligned} J_y &= \sigma^S_{yy}\left[E_t^R - E_t^L\right] - i\sigma^S_{yx}\left[E_t^R + E_t^L\right], && (4.24)\\ J_x &= \sigma^S_{xx}\left[E_t^R + E_t^L\right] + i\sigma^S_{xy}\left[E_t^R - E_t^L\right], && (4.25) \end{aligned}$$

and $\lambda_1 = n_1/\mu_1 c$ and $\lambda_2 = n_2/\mu_1 c$. Solving these equations we obtain the amplitudes of the right respectively left-handed reflected circularly polarized light beams,

$$\begin{aligned} E_r^{R,L} &= 2E_0\left[\kappa_2 + \sigma^S_{xx} \mp i\frac{\kappa_1 - \sigma_1^{\pm}}{\kappa_1 - \sigma_2^{\pm}}\sigma^S_{xy}\right]\frac{\kappa_1 - \sigma_2^{\pm}}{C} && (4.26)\\ & && (4.27) \end{aligned}$$

where

$$\begin{aligned} C &= \left(2\kappa_1 - \sigma_1^-\right)\left(2\kappa_1 - \sigma_2^+\right) + \left(2\kappa_1 - \sigma_1^+\right)\left(2\kappa_1 - \sigma_2^-\right),\\ \sigma_1^{\pm} &= \sigma^S_{xx} \pm i\sigma^S_{xy},\\ \sigma_2^{\pm} &= \sigma^S_{yy} \pm i\sigma^S_{xy}, && (4.28) \end{aligned}$$

$\kappa_1 = \lambda_1 + \lambda_2$ and $\kappa_2 = \lambda_1 - \lambda_2$. It is now rather clear that the optical conductivity has a strong influence on the behavior of the reflected light. And so, it also becomes clear that the Kerr rotation depends on the conductivity of the material. We furthermore note that if $\sigma_{xy} = 0$, no Kerr rotation should be observed as this implies that $E_r^R = E_r^L$.

Here we considered incidence on the $x - y$ surface. If one wants to consider incidence on another surface, a rotation of the coordinate system is sufficient. This is equivalent to rotating the conductivity tensor or by permuting the indices. Next we consider the bulk material.

Bulk material

We will now consider a semi-infinite bulk material. What sets this apart from the thin film is that the material now influences the beam as it propagates inside the material. This is because, opposite to the thin film, the bulk thickness is at least comparable to the wavelength of the incident light. Compared to a finite but thick slab, no transmitted field is considered in the semi-infinite slab.

Because the wavelength of the incident light is smaller than the bulk thickness, one has to determine the allowed field inside the material. Hence, one has to solve the electromagnetic wave equation, Eq. (4.10). Because of the conductivity being a 3×3 matrix, that in general, can have non-zero components, this is analytically impossible. However, for many materials the conductivity tensor has at least some components that are zero and it is possible to find solutions analytically.

We will consider a system for which $\sigma_{xz} = \sigma_{zx} = \sigma_{yz} = \sigma_{zy} = 0$. This is for example the case for the polar geometry, in which the magnetization is parallel to the z axis [121]. Similarly it is the case for Weyl semimetals [151], and as will be shown below, the case for nodal loop semimetals. Thus, the conductivity tensor that we have in mind has the following structure

$$\sigma = \begin{pmatrix} \sigma_{xx} & \sigma_{xy} & 0 \\ \sigma_{yx} & \sigma_{yy} & 0 \\ 0 & 0 & \sigma_{zz} \end{pmatrix}. \tag{4.29}$$

We consider incidence on the $x - y$ surface and the $y - z$ surface. Light incident on the $x - z$ surface is equivalent to a rotation and hence is obtained by $x \leftrightarrow y$. For normal incident light on the $x - y$ surface, the light propagates in the k_z direction. Hence the incident and reflected light can be written as

$$\mathbf{E}_0 = \left(E_0^R \hat{e}_R + E_0^L \hat{e}_L\right) e^{i(k_z z - \omega t)} \tag{4.30}$$

$$\mathbf{E}_r = \left(E_r^R \hat{e}'_R + E_r^L \hat{e}'_L\right) e^{-i(k_z z + \omega t)}. \tag{4.31}$$

The transmitted light is written as

$$\mathbf{E}_t(z,t) = \mathbf{E}_t(k'_z, \omega) e^{ik'_z z - i\omega t}, \tag{4.32}$$

where $\omega > 0$. The electromagnetic wave equation, Eq. (4.10), for the transmitted field now reads

$$\begin{pmatrix} -(k'_z)^2 + \frac{\omega^2}{c^2}\epsilon_{xx} & \frac{\omega^2}{c^2}\epsilon_{xy} & 0 \\ -\frac{\omega^2}{c^2}\epsilon_{xy} & -(k'_z)^2 + \frac{\omega^2}{c^2}\epsilon_{xx} & 0 \\ 0 & 0 & \frac{\omega^2}{c^2}\epsilon_{zz} \end{pmatrix} \begin{pmatrix} E_x \\ E_y \\ E_z \end{pmatrix} = \mathbf{0} \tag{4.33}$$

The first solution to this system of equations is $E_z = 0$. The other solutions are found by first solving the following determinant

$$\begin{vmatrix} (k_z')^2 + \frac{\omega^2}{c^2}\epsilon_{xx} & \frac{\omega^2}{c^2}\epsilon_{xy} \\ -\frac{\omega^2}{c^2}\epsilon_{xy} & (k_z')^2 + \frac{\omega^2}{c^2}\epsilon_{yy} \end{vmatrix} = 0. \tag{4.34}$$

This has the following solutions

$$(k_z')^2 = \frac{\omega^2}{2c^2}(\epsilon_{xx} + \epsilon_{yy}) \pm \frac{\omega^2}{c^2}\sqrt{\frac{1}{4}\left(\epsilon_{xx} + \epsilon_{yy}\right)^2 - \epsilon_{xx}\epsilon_{yy} - \epsilon_{xy}^2} \equiv k_\pm^2. \tag{4.35}$$

As we see we obtain in total four solutions for k_z'. However, two of these are unphysical since they correspond to a wave traveling out of the material.

The basis for the electric field inside the material is found by going back to the electromagnetic wave equation and inserting the allowed wave vectors. The basis for the electric field inside the material is

$$\mathbf{e}_\pm = c_1^\pm \hat{\mathbf{x}} + c_2^\pm \hat{\mathbf{y}}, \tag{4.36}$$

where

$$c_1^\pm = \frac{\epsilon_{xy}}{\sqrt{\epsilon_\pm + \epsilon_{xy} - \epsilon_{xx}}}, \tag{4.37}$$

$$c_2^\pm = \frac{\epsilon_\pm - \epsilon_{xx}}{\sqrt{\epsilon_\pm + \epsilon_{xy} - \epsilon_{xx}}}, \tag{4.38}$$

and $\epsilon_\pm = \frac{c^2}{\omega^2}k_\pm^2$. The transmitted field is then written

$$\mathbf{E}_t = E_+\mathbf{e}_t^+ + E_-\mathbf{e}_t^- . \tag{4.39}$$

The reflected field is now found by proceeding in the same manner as for the thin film, we apply the boundary conditions, given by Eqs. (4.12) and (4.13). We now assume that the light penetrate deep into the bulk such that any presence of surface states can be neglected, and hence no currents are generated at the interface[3]. The reflected light is in this case given by

$$E_{r,z}^{R,L} = \frac{1}{4}\left(1 - \frac{k_+}{\omega}\right)\left(c_1^+ \pm ic_2^+\right)E_+ + \frac{1}{4}\left(1 - \frac{k_-}{\omega}\right)\left(c_1^- \pm ic_2^-\right)E_-, \tag{4.40}$$

where subscript z denotes reflection of incident light propagating along the k_z axis and

$$E_+ = \frac{4E_0}{\left(1 + \frac{k_+}{\omega}\right)\left(c_1^+ - \frac{c_2^+}{c_2^-}c_1^-\right)}, \tag{4.41}$$

---

[3] For a nodal loop semimetal this is reasonable because the spatial depth of the surface states is typically a few nanometers whereas the penetration depth of the incident light is usually on the order of hundred nanometers.

$$E_- = \frac{4E_0}{\left(1+\frac{k_-}{\omega}\right)\left(c_1^- - \frac{c_2^-}{c_2^+}c_1^+\right)}. \tag{4.42}$$

In the case of light incident on the $y-z$ surface, the incident light propagates along the k_x axis. The transmitted light is now written as

$$\mathbf{E}_t(x,t) = \mathbf{E}_t(k_x', \omega)e^{ik_x' x - i\omega t}. \tag{4.43}$$

Inserting this into the electromagnetic wave equation, Eq. (4.10), we are bound to solve the following determinant

$$\begin{vmatrix} \frac{\omega^2}{c^2}\epsilon_{xx} & \frac{\omega^2}{c^2}\epsilon_{xy} & 0 \\ -\frac{\omega^2}{c^2}\epsilon_{xy} & -\left(k_x'\right)^2 + \frac{\omega^2}{c^2}\epsilon_{yy} & 0 \\ 0 & 0 & -\left(k_x'\right)^2 + \frac{\omega^2}{c^2}\epsilon_{zz} \end{vmatrix} = 0. \tag{4.44}$$

The solutions to this equation are of two types,

$$\left(k_x'\right)^2 = \frac{\omega^2}{c^2}\epsilon_{zz} \equiv k_1^2, \tag{4.45}$$

$$\left(k_x'\right)^2 = \frac{\omega^2}{c^2}\left(\epsilon_{yy} - \frac{\epsilon_{xy}^2}{\epsilon_{xx}}\right) \equiv k_2^2. \tag{4.46}$$

Each solution further has two solutions due to the square. We again select the positive solutions since the wave has to propagate into the material. The basis for the transmitted field is now given by

$$\mathbf{e}_t^1 = \hat{\mathbf{z}}, \tag{4.47}$$

$$\mathbf{e}_t^2 = a\frac{\epsilon_{xy}}{\epsilon_{xx}}\hat{\mathbf{x}} - a\hat{\mathbf{y}}, \tag{4.48}$$

where $a = (1 + |\epsilon_{xy}/\epsilon_{xx}|^2)^{-1/2}$. The transmitted field is then given by

$$\mathbf{E}_t' = E^2\mathbf{e}_t^2 + E^1\mathbf{e}_t^1. \tag{4.49}$$

Proceeding in the same manner as for light incident on the $x-y$ surface, we obtain

$$E_{r,x}^{R,L} = \frac{1}{2}\left[\frac{1-\frac{c}{\omega}k_2}{1+\frac{c}{\omega}k_2}aE_0^y \mp i\frac{1-\frac{c}{\omega}k_1}{1+\frac{c}{\omega}k_1}E_0^z\right], \tag{4.50}$$

where E_0^y and E_0^z are the components in the y and z directions respectively of the incident field. It is then clear from the equation that if either E_0^y or E_0^z equals 0, then $E_r^R = E_r^L$ and neither a Kerr angle nor an ellipticity should be observed. The above equations are general up to the point that they describe the reflected light of a material that can be characterized by a conductivity tensor that has the form given in Eq. (4.29). We will now introduce the tilted nodal loop semimetal. As the reflected fields depend on the conductivity, we thereafter present the Kubo formula for calculating the conductivity tensor and obtaining it for the nodal loop semimetal.

4.3 Titled nodal loop semimetal

In this section, we introduce the tilted nodal loop semimetal that has been studied in [106, 49]. We then calculate the optical conductivity in the bulk of this material using the Kubo formula.

The low energy Hamiltonian that describes the nodal loop that was presented in Section 2.4.2 is described by

$$H_0(\mathbf{k}) = \frac{1}{\Lambda}\left(k_0^2 - k_\rho^2\right)\tau_x + v_z k_z \tau_z, \tag{4.51}$$

where $k_\rho^2 = k_x^2 + k_y^2$, $\tau_{x,y,z}$ are the Pauli matrices, here representing an effective orbital degree of freedom, v_z is the Fermi velocity in the k_z direction and Λ represent the effective electron mass. This Hamiltonian represents a band structure with a nodal loop in the $k_x - k_y$ plane whose radius is given by k_0 (see Fig. 2.4(b)). The tilt is added by introducing the following term

$$\hat{H}_{\text{tilt}}(\mathbf{k}) = \mathbf{u}\cdot\mathbf{k}\tau_0, \tag{4.52}$$

where $\mathbf{u} = \left(u_x, u_y, u_z\right)$ defines the tilt in k space and τ_0 is the 2×2 identity matrix. We will here restrict the tilt to the $k_x - k_y$ plane. The tilt can then be written as $\mathbf{u} = u\left(\cos\theta, \sin\theta, 0\right)$, where u defines the tilt velocity and θ the tilt direction. This term makes the Hamiltonian break time-reversal symmetry, which is otherwise preserved. The geometry of the tilt velocity is demonstrated in Fig. 4.2.

The total Hamiltonian for the tilted nodal loop semimetal is given by

$$H_{tot} = H_0 + H_{\text{tilt}}. \tag{4.53}$$

The spectrum is given by

$$\varepsilon_\pm = \mathbf{u}\cdot\mathbf{k} \pm \sqrt{v_z^2 k_z^2 + \frac{1}{4m^2}\left(k_0^2 - k_\rho^2\right)}. \tag{4.54}$$

A expected the tilt is seen in the spectrum. It has been plotted in Fig. 4.2 (a). The eigenfunctions are given by

$$\Psi_\pm = \frac{1}{\sqrt{|B|^2 + \left(v_z k_z \mp A\right)^2}}\begin{pmatrix} -B \\ v_z k_z \mp A, \end{pmatrix} \tag{4.55}$$

where $A = \sqrt{v_z^2 k_z^2 + B^2}$ and $B = \frac{1}{\Lambda}\left(k_0^2 - k_\rho^2\right)$. As seen the eigenfunctions are not affected by the tilt. This will be seen later on to have an important consequence.

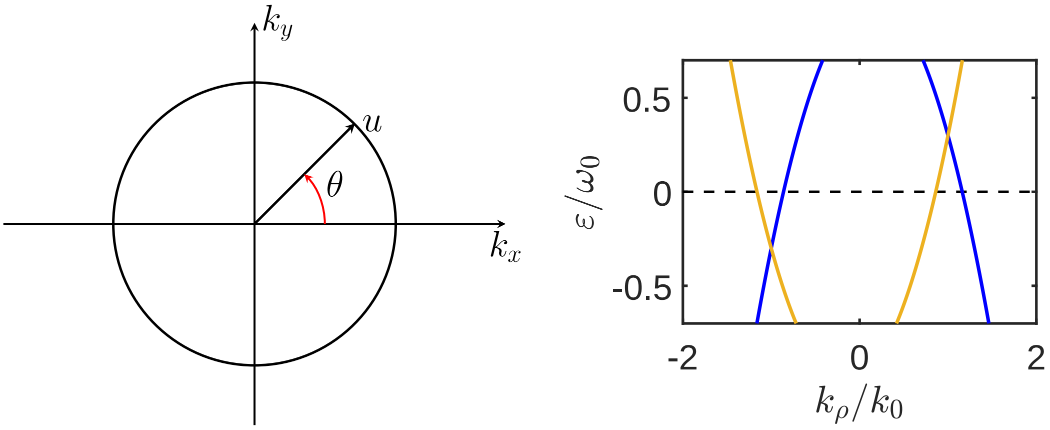

FIGURE 4.2: (a) Description of the tilt velocity vector and (b) the effect of tilting the nodal loop, where $\omega_0 = k_0^2/\Lambda$.

Before we are able to calculate the Kerr rotations we now have to calculate the conductivity tensor. The conductivity tensor can be obtained in linear response by using the Kubo formula. We derive it in the next section.

4.4 Kubo formula

The Kubo formula relates the expectation value of an observable given an external perturbation in the linear response regime, i.e., when the external perturbation is weak[4]. Consider a system governed by the Hamiltonian H_0. We assume that the eigenenergies and eigenfunctions of it are known. We denote them respectively with ε_n and $|\psi_n\rangle$. The expectation value of any observable, A, can now be evaluated according to

$$\langle A\rangle = \frac{1}{Z_0}\mathrm{tr}\left[\rho_0 A\right] = \frac{1}{Z_0}\sum_n \langle\psi_n|A|\psi_n\rangle e^{-\beta\varepsilon_n}, \tag{4.56}$$

$$\rho_0 = e^{-\beta H_0} = \sum_n |\psi_n\rangle\langle\psi_n| e^{-\beta\varepsilon_n}, \tag{4.57}$$

where ρ_0 is the equilibrium density operator and $Z_0 = \mathrm{tr}\left[\rho_0\right]$ is the partition function. Let us now apply an external perturbation to the system at a time $t = t_0$. The total Hamiltonian is given by

$$H = H_0 + H_I(t)\Theta(t - t_0). \tag{4.58}$$

---

[4] In this section we have re-introduced e and $\hbar$.

The question we ask now is: what is the expectation value of an observable A for $t > t_0$? To be able to calculate $\langle A(t)\rangle$ we need to know the time evolution of the density operator or equivalently the time evolution of the eigenstates of the Hamiltonian, Eq. (4.58). Once any of these two are know the expectation values are obtained as follows

$$\begin{aligned}\langle A(t)\rangle =& \frac{1}{Z_0}\mathrm{tr}\left[\rho(t)A\right] = \frac{1}{Z_0}\sum_n \langle\psi_n(t)|A|\psi_n(t)\rangle e^{-\beta\varepsilon_n}, && (4.59)\\ \rho =& \sum_n |\psi_n(t)\rangle\langle\psi_n(t)|e^{-\beta\varepsilon_n}. && (4.60)\end{aligned}$$

It will here be convenient to use the interaction picture, where

$$|\psi_n(t)\rangle = e^{-iH_0t/\hbar}|\psi_n(t)\rangle = e^{-iH_0t/\hbar}U(t,t_0)|\psi_n(t_0)\rangle, \tag{4.61}$$

where $|\hat{\psi}_n(t)\rangle$ are the eigenstates given in the interaction picture and $U(t,t_0)$ is the time evolution operator. We now expand the time evolution operator to linear order in $H_I(t)$ and insert it into Eq. (4.59). The first order expansion is written as

$$U(t,t_0) \approx 1 - \frac{i}{\hbar}\int_{t_0}^{t} dt'\, H_I(t'). \tag{4.62}$$

We then obtain

$$\begin{aligned}\langle A(t)\rangle =& \frac{1}{Z_0}\left[\sum_n \langle\psi_n|e^{-iH_0t_0}U^\dagger(t,t_0)e^{iH_0t}Ae^{-iH_0t}U(t,t_0)e^{iH_0t}|\psi_n\rangle\right] && (4.63)\\ =& \frac{1}{Z_0}\left[\langle\psi_n(t_0)|\, U^\dagger(t,t_0)A(t)U(t,t_0)\, |\psi_n(t_0)\rangle\right] && (4.64)\\ =& \langle A(t)\rangle_0 - \frac{i}{\hbar}\int_{t_0}^{t} dt'\, \left\langle\left[A(t)H_I(t') - H_I(t')A(t)\right]\right\rangle_0 && (4.65)\\ =& \langle A(t)\rangle_0 - \frac{i}{\hbar}\int_{t_0}^{t} dt'\, \left\langle\left[A(t), H_I(t')\right]\right\rangle_0, && (4.66)\end{aligned}$$

where $\langle\rangle_0$ denotes the expectation value with respect to the unperturbed ground state. The linear response is then written as

$$\delta\langle A(t)\rangle \equiv \langle A(t)\rangle_{-}\langle A(t)\rangle_0 = \int_{t_0}^{\infty} dt'\, C^R_{AH_I}(t,t')e^{-\eta(t-t')}, \tag{4.67}$$

with

$$C^R_{AH_I}(t,t') = -\frac{i}{\hbar}\Theta(t-t')\left\langle\left[A(t), H_I(t')\right]\right\rangle_0. \tag{4.68}$$

This is the Kubo formula. We have to Eq. (4.67) added the factor $e^{-\eta(t-t')}$, where η is an infinitesimal positive parameter. It is included to make the response at time t due to the perturbation at time t' to decay for $t \gg t'$. In the end of the calculation one hence have to let $\eta \to 0^+$.

4.4.1 Conductivity tensor

In this section, we derive the conductivity tensor using the Kubo formula introduced in the previous section[5]. This will be the important formula for obtaining the optical conductivity of the system. We derive the conductivity tensor by considering the response of the system due to a uniform applied electric field. This we write $\mathbf{E}(t) = \mathbf{E}e^{-i\omega t}$. According to Ohm's law, the i:th component of the current can be written

$$\delta J_i(t) = \int_{-\infty}^{t} dt' \sigma_{ij}(t-t')E_j(t'). \tag{4.69}$$

By Fourier transforming it, we obtain

$$\begin{aligned}\delta J_i(\omega) &= \int_{-\infty}^{\infty} dt \int_{-\infty}^{t} dt' \sigma_{ij}(t-t')E_j(t') \\ &= \int_{0}^{\infty} d\tau \sigma_{ij}(\tau) e^{i\omega\tau} \int_{-\infty}^{\infty} dt'' e^{i\omega t''} E_j(t'') \\ &= \sigma_{ij}(\omega)E_j(\omega).\end{aligned} \tag{4.70}$$

This defines the Fourier transform of the conductivity. The interaction between the electrons and the electric field is, in the length gauge (see Appendix E), given by

$$H_I = e\sum_l \mathbf{r}_l \cdot \mathbf{E}(t) \equiv B e^{-i\omega t}, \tag{4.71}$$

where $\mathbf{r}_l$ are the positions of the electrons and $B = e\sum_l \mathbf{r}_l \cdot \mathbf{E}$ is a time-independent operator. We furthermore assume that the field vanishes at $t = -\infty$, i.e., the perturbations is turned off. We can now apply the Kubo formula, Eq. (4.67) to Eq. (4.69) and obtain

$$\delta J_i(t) = \frac{1}{i\hbar}\int_{-\infty}^{t} dt' \left\langle [J_i(t), B(t')] \right\rangle_0 e^{-i\omega t'}, \tag{4.72}$$

We now perform an integration by parts. This leads to

$$\begin{aligned}\delta J_i(t) &= \frac{1}{i\hbar}\left[\left\langle [J_i(t), B(t')] \right\rangle_0 \frac{e^{-i\omega t'}}{-i\omega}\right]_{-\infty}^{t} - \frac{1}{i\hbar}\int_{-\infty}^{t} dt' \frac{e^{-i\omega t'}}{-i\omega}\left\langle \left[J_i(t), \frac{d}{dt'}B(t')\right]\right\rangle_0 \\ &= \frac{1}{i\hbar}\langle [J_i(t), B(t)]\rangle_0 \frac{e^{-i\omega t}}{-i\omega} - \frac{1}{i\hbar}\int_{-\infty}^{t} dt' \frac{e^{-i\omega t'}}{-i\omega}\left\langle \left[J_i(t), \frac{d}{dt'}B(t')\right]\right\rangle_0 .\end{aligned} \tag{4.73}$$

Next we treat the time derivative of B, that appears inside the integral. For this we can use the interaction Hamiltonian, Eq. (4.71). We have that

$$\frac{d}{dt}B = e\frac{d}{dt}\sum_l \mathbf{r}_l \cdot \mathbf{E}. \tag{4.74}$$

Note that $\mathbf{E}$ is independent of time and position. The time derivative of the position operator multiplied by the electric charge is related to the current operator, in the

---

[5] In this section we have re-introduced e and $\hbar$ for pedagogical purposes.

basis defined in Appendix E, such that

$$\frac{d}{dt}B = e\sum_{l}\frac{d\mathbf{r}_l}{dt}\cdot\mathbf{E} = -\mathbf{J}\cdot\mathbf{E}. \tag{4.75}$$

where $\mathbf{J} = -e\sum_l \mathbf{v}_l = -e\sum_l \frac{d\mathbf{r}}{dt}$, valid for a uniform response. We do not, at this point, evaluate the first term, but note that, for a Hamiltonian quadratic in $\mathbf{p}$, the first term becomes $\frac{ie^2\hbar}{m}N\delta_{ij}E_j$. We now have that

$$\delta J_i(t) = \frac{e}{i\hbar}\left\langle\left[J_i(t),\sum_l r_{l,j}(t)\right]\right\rangle_0 \frac{e^{-i\omega t}}{-i\omega}E_j + \frac{1}{i\hbar}\int_{-\infty}^{t}dt'\,\left\langle\left[J_i(t),J_j(t')\right]\right\rangle_0 \frac{E_j e^{-i\omega t'}}{-i\omega}, \tag{4.76}$$

By direct comparison with Eq. (4.69) we obtain that

$$\sigma_{ij}(t-t') = \frac{e}{i\hbar}\left\langle\left[J_i(t),\sum_l r_{l,j}(t)\right]\right\rangle_0 \frac{1}{-i\omega}\delta(t-t') + \frac{1}{\hbar\omega}\left\langle\left[J_i(t-t'),J_j(0)\right]\right\rangle_0. \tag{4.77}$$

We now insert this into the definition for $\sigma_{ij}(\omega)$ and obtain

$$\sigma_{ij}(\omega) = \frac{e}{\hbar\omega}\left\langle\left[J_i(0),\sum_l r_{l,j}(0)\right]\right\rangle_0 + \frac{1}{\hbar\omega}\int_0^{\infty}d\tau\,\left\langle\left[J_i(\tau),J_j(0)\right]\right\rangle_0 e^{i\omega\tau}. \tag{4.78}$$

This is the Kubo formula for the conductivity tensor. This expression is written in a many-body representation and apart from the linear response we have only assumed a uniform response. We now want to write this expression in the single particle representation. First we write the operators in second quantization. In general an observable can be written

$$O = \sum_{\kappa\kappa'}\langle\kappa|\,o\,|\kappa'\rangle\, a_\kappa^\dagger a_\kappa, \tag{4.79}$$

where $a_\kappa^{(\dagger)}$ is the annihilation (creation) operator. We will take $|\kappa\rangle$ to represent the single particle states. In second quantization we then have that

$$J_i(t) = -e\sum_{\kappa\kappa'}\langle\kappa|\,v_i\,|\kappa'\rangle\, a_\kappa^\dagger(t)a_{\kappa'}(t). \tag{4.80}$$

The time evolution of the operators are evaluated using the Heisenberg equation of motion with $H_0 = \sum_{l,ij}\alpha_{ij}p_{l,i}p_{l,j} + \sum_{l,i}\beta_i p_{l,i} + N\gamma$, where $i \in x,y,z$ and $\alpha_{ij} = \alpha_{ji}$, β_i and γ are matrix coefficients. This Hamiltonian represents a general Hamiltonian up to second order in momentum. We thus have that $a_\kappa(t) = a_\kappa(0)e^{-i\varepsilon_\kappa t/\hbar}$. Let us now return to Eq. (4.78). Inserting the expression for the current operator written in second quantization we have that

$$\sigma_{ij}^{(2)}(\omega) = \frac{1}{\hbar\omega}\int_0^{\infty}d\tau\,\left\langle\left[J_i(\tau),J_j(0)\right]\right\rangle_0 e^{i(\omega+i\eta)\tau}$$

$$= \frac{ie^2}{\omega}\sum_{mm'}\sum_{nn'}\frac{\left\langle \left[a_m^\dagger a_{m'}, a_n^\dagger a_{n'}\right]\right\rangle_0}{\hbar\omega + i\eta + \varepsilon_m - \varepsilon_{m'}} \langle m| v_i |m'\rangle \langle n| v_j |n'\rangle \tag{4.81}$$

where we have introduced a small η to take care of the convergence of the integral. In the end of calculations $\eta \to 0^+$. The expectation value is now evaluated using Wick theorem and that $\langle a_n^\dagger a_n\rangle_0 = f(\varepsilon_n)$. Hence

$$\left\langle \left[a_m^\dagger a_{m'}, a_n^\dagger a_{n'}\right]\right\rangle_0 = \delta_{mn'}\delta_{m'n}\left(f(\varepsilon_m) - f(\varepsilon_{m'})\right). \tag{4.82}$$

This then results in

$$\sigma_{ij}^{(2)}(\omega) = \frac{ie^2}{\omega}\sum_{nn'}\frac{f(\varepsilon_n) - f(\varepsilon_{n'})}{\hbar\omega + \varepsilon_n - \varepsilon'_n} \langle n| v_i |n'\rangle \langle n'| v_j |n\rangle \tag{4.83}$$

Let us now turn to the first term,

$$\begin{aligned}\sigma_{ij}^{(1)}(\omega) &= \frac{e}{\hbar\omega}\left\langle \left[J_i(0), \sum_l r_{l,j}(0)\right]\right\rangle_0 \\ &= -\frac{e^2}{\hbar\omega}\sum_{nn'}\left[f(\varepsilon_n) - f(\varepsilon_{n'})\right]\langle n| v_i |n'\rangle \langle n'| r_j |n\rangle .\end{aligned} \tag{4.84}$$

The second term is treated by considering $\langle n'| v_j |n\rangle = \frac{i}{\hbar}\langle n'| \left[H_0, r_j\right] |n\rangle$. We have that

$$\begin{aligned}\frac{i}{\hbar}\langle n'| \left[H_0, r_j\right] |n\rangle &= \frac{i}{\hbar}\left[\varepsilon_{n'}\langle n'| r_j |n\rangle - \varepsilon_n \langle n'| r_j |n\rangle\right] \\ &= \frac{i}{\hbar}\left(\varepsilon_{n'} - \varepsilon_n\right)\langle n'| r_j |n\rangle .\end{aligned} \tag{4.85}$$

This gives us

$$\sigma_{ij}^{(1)}(\omega) = -\frac{ie^2}{\omega}\sum_{nn'}\frac{f(\varepsilon_n) - f(\varepsilon_{n'})}{\varepsilon_n - \varepsilon'_n}\langle n| v_i |n'\rangle \langle n'| v_j |n\rangle \tag{4.86}$$

By combining the two components and putting them on common denominators we obtain

$$\sigma_{ij}(\omega) = -ie^2\sum_{nn'}\frac{f(\varepsilon_n) - f(\varepsilon_{n'})}{\varepsilon_n - \varepsilon_{n'}}\frac{\langle n| v_i |n'\rangle \langle n'| v_j |n\rangle}{\hbar\omega + i\eta + \varepsilon_n - \varepsilon_{n'}}. \tag{4.87}$$

This is the Kubo formula for the conductivity tensor in the single particle formulation. We note that for the following derivation we have only assumed that the current operator is given by $\mathbf{J} = -e\sum_l \mathbf{v}_l = -e\sum_l \frac{d\mathbf{r}_l}{dt} = -\frac{ie}{\hbar}\left[H_0, \sum_l \mathbf{r}_l\right]$. Considering a system where the states are given in a momentum basis. The conductivity tensor can then be written, in cylindrical coordinates[6], as

$$\sigma_{ij}(\omega) = \frac{1}{(2\pi)^3}\int_0^\infty dk_\rho k_\rho \int_0^{2\pi} d\phi \int dk_z \sigma_{\mathbf{k}}^{ij}(\omega). \tag{4.88}$$

---

[6] This proves to be handy for calculating the conductivity for the nodal loop semimetal.

where $i, j \in \{x, y, z\}$ and the integral is over all momenta $\mathbf{k}$, written in cylindrical coordinates. The conductivity kernel is defined as

$$\sigma^{ij}_{\mathbf{k}}(\omega) = -i\sum_{s,s'} \frac{f(\varepsilon_{\mathbf{k},s}) - f(\varepsilon_{\mathbf{k},s'})}{\varepsilon_{\mathbf{k},s} - \varepsilon_{\mathbf{k},s'}} \frac{j^{ss'}_{\mathbf{k}i}\, j^{s's}_{\mathbf{k}j}}{\hbar\omega + \varepsilon_{\mathbf{k},s} - \varepsilon_{\mathbf{k},s'} + i0^+}, \tag{4.89}$$

where $j^{ss'}_{\mathbf{k}i} = -\frac{e}{\hbar} \langle \mathbf{k}s| \nabla_{\mathbf{k}} H_0 |\mathbf{k}s'\rangle$ [165].

4.5 Optical conductivity of nodal loop

To calculate the optical conductivity of the nodal loop semimetal we apply the Kubo formula as outlined in the previous section. We first calculate the current operators, $j^{s,s'}_{\mathbf{k},i}$. We find for $s = s'$ that

$$j^{s}_{\mathbf{k}x} = u_x + \frac{2k_x B}{\Lambda A}, \quad j^{s}_{\mathbf{k}y} = u_y + \frac{2k_y B}{\Lambda A}, \quad j^{s}_{\mathbf{k}z} = \frac{v_z^2 k_z}{A}, \tag{4.90}$$

and for $s \neq s'$

$$j^{ss'}_{\mathbf{k}x} = \frac{2k_x v_z k_z}{\Lambda A}, \quad j^{ss'}_{\mathbf{k}y} = \frac{2k_y v_z k_z}{\Lambda A}, \quad j^{ss'}_{\mathbf{k}z} = -\frac{v_z |B|}{A},. \tag{4.91}$$

With these we are set up to calculate the optical conductivity due to both inter and intraband transitions. We first note that there is a symmetry between $j^{ss'}_{\mathbf{k}x}$ and $j^{ss'}_{\mathbf{k}y}$, $\forall s, s'$. By letting $x \to y$ in $j^{ss'}_{\mathbf{k}x}$, we obtain $j^{ss'}_{\mathbf{k}y}$.

Before we calculate the exact conductivity tensor, we first interpret the current operators and what we can expect of this in relations with the Kubo formula, Eq. (4.88). Based on symmetry arguments and the shape of $j_{\mathbf{k}i}$ we can already state some general observations about the conductivity tensor. The transverse conductivities, σ_{xz} and σ_{yz} are zero. This follows from that $\varepsilon_{\pm}$ is symmetric in k_z whereas the products, $j^{ss'}_{\mathbf{k}z} j^{ss'}_{\mathbf{k}x}$ and $j^{ss'}_{\mathbf{k}z} j^{ss'}_{\mathbf{k}y}$ are odd in k_z. By such Eq. (4.88) implies that $\sigma_{xz} = \sigma_{yz} = 0$. The physical interpretation of this is as follows: An electric field with say polarization along the y axis excites electrons that carry currents in the $+z$ and $-z$ directions with equal probability. Hence, the total current is zero. Due to symmetry the same arguments leads to $\sigma_{zx} = \sigma_{zy} = 0$.

The same cannot be applied to σ_{xy} which will depend on the tilt. In case of no tilt ($\mathbf{u} = 0$), the Hall conductivity vanishes due to that the integrand, Eq. (4.89) is asymmetric under the change, $\phi \to \phi + \pi/2$. The asymmetry can be seen in Fig. 4.3. Here we have plotted the product of $j^{+-}_{\mathbf{k}x} j^{-+}_{\mathbf{k}y}$ with an overlay corresponding to $f(\varepsilon_+) - f(\varepsilon_-)$, for a fixed k_z. Because of the system is gapped at $k_z \neq 0$ the overlay has a finite thickness even for $\tilde{\mu} = 0$. In contrast, when the tilt is introduced the Fermi distributions in Eq. (4.89) breaks the polar symmetry. Hence, a non-vanishing Hall conductivity, σ_{xy}, may exist. This means that the existence of a finite σ_{xy} is due to the difference in occupation of electronic states with different momenta $(k_\rho \cos\phi, k_\rho \sin\phi, k_z)$ and $(-k_\rho \cos\phi, -k_\rho \sin\phi, k_z)$.

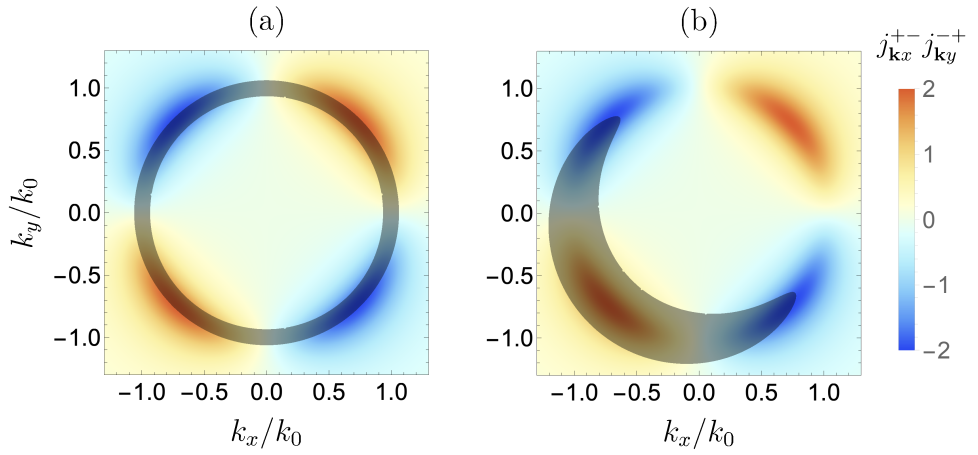

FIGURE 4.3: The figure depicts the product of $j^{+-}_{\mathbf{k}x} j^{-+}_{\mathbf{k}y}$, in units of k_0^2/Λ^2. We have fixed $v_z k_z/\omega_0 = 0.4$. The shaded overlay depicts $f(\varepsilon_+) - f(\varepsilon_-) = 0$ for (a) $\tilde{u} = 0$ and for (b) $\tilde{u} = 0$ and $\theta = \pi/4$, for a fixed chemical potential $\tilde{\mu} = 0.42$.

As have been shown in Section. 4.2.1 the Kerr angle is highly dependent on the existence of the Hall conductivity. Consider first a beam incident on the $y - z$ surface, hence the beam is propagating along the k_x axis. As $\sigma_{yz} = 0$ it is directly clear that there can be no Kerr rotation observed on a thin film since the quotient $E_r^R/E_r^L = 1$. If the light is incident on a bulk material, it is more complicated to state whether a Kerr rotation will be observed or not. In the same manner, we expect the same result for light incident on the $x - z$ surface.

On the other hand, the situation is different when light propagates along the k_z direction. We assume that the light is polarized along the y direction. If the tilt is such that $\sigma_{xy} \neq 0$ the induced current due to the incident light will produce a current that has components in both the x and y directions. Hence a Kerr signal may be expected in this case.

Let us now quantify these arguments. We will first calculate the full conductivity tensor. After that, we calculate the Kerr angle and ellipticity for a thin film and a bulk material. To obtain the explicit expressions for the optical conductivity we calculate the real and imaginary parts separately. We can separate the real and imaginary parts of Eq. (4.88) by applying the following identity

$$\lim_{\gamma \to 0^+} \frac{1}{x + i\gamma} = \mathcal{P}\frac{1}{x} - i\pi\delta(x), \tag{4.92}$$

where $\mathcal{P}$ denotes the Cauchy principal value and $\delta(x)$ is the Dirac delta function. From the delta function we obtain the real part of the optical conductivity. The imaginary part can then be obtained from the Kramers-Kronig relation

$$\text{Im}\,\sigma_{ij}(\omega) = -\frac{1}{\pi}\mathcal{P}\int_{-\infty}^{\infty} d\omega' \frac{\text{Re}\,\sigma_{ij}(\omega')}{\omega' - \omega}. \tag{4.93}$$

We are now ready to obtain the optical conductivity. As a first step we make a change of variables to obtain dimensionless expressions. By letting $k_\rho \to k_0\xi$ we write the following,

$$\tilde{\omega} = \frac{\omega}{\omega_0}, \quad \tilde{\mu} = \frac{\mu}{\omega_0} \quad \tilde{u} = \frac{\Lambda u}{k_0}, \quad \Gamma = \frac{k_0}{v_z \Lambda}, \tag{4.94}$$

where μ is the chemical potential and $\omega_0 = k_0^2/\Lambda$. We next separate the calculation into two parts. First, we calculate the contribution to the optical conductivity from the interband transitions followed by the calculation of the contribution from the intraband transitions. Interband transitions are a consequence of photons driving transitions between different bands, whereas intraband transitions are those that occur within the same band. Normally the intraband transitions can be understood in simplest terms within the Drude theory. Here we will treat them on the same basis as the interband transitions and calculate them using the Kubo formula. We begin by calculating the interband transitions.

4.5.1 Interband transtions

We obtain the interband transitions by letting $s \neq s'$ in Eq. (4.88). First we consider the real part from the interband contributions. By applying Eq. (4.92) and then evaluating the k_z and ϕ integrals we are left with

$$\begin{aligned} \text{Re}\, \sigma_{ij}^{\text{inter}}(\omega) = & \int_{k_1}^{k_2} d\xi \Theta(1 - \tilde{\omega}/2) G_{ij}(\xi) \\ & + \int_{0}^{k_2} d\xi \Theta(\tilde{\omega}/2 - 1) G_{ij}(\xi), \end{aligned} \tag{4.95}$$

where $k_1 = \sqrt{1 - \tilde{\omega}/2}$ and $k_2 = \sqrt{1 + \tilde{\omega}/2}$ results from the Dirac delta function in the integration and which furthermore represents the conservation of energy. The functions $G_{ij} = g_{ij}^{+}(\xi) - g_{ij}^{-}(\xi)$ are given by

$$\begin{aligned} g_{xx}^{\pm} = & \frac{\Gamma}{2\pi^2 \tilde{u}\tilde{\omega}^2} \Bigg\{ \pi - \left[2 \arccos\left(\frac{2\tilde{\mu} \pm \tilde{\omega}}{2\tilde{u}\xi} \right) - 2\cos 2\theta \left(\frac{2\tilde{\mu} \pm \tilde{\omega}}{2\tilde{u}\xi} \right) \sqrt{1 - \left(\frac{2\tilde{\mu} \pm \tilde{\omega}}{2\tilde{u}\xi} \right)^2} \right] \\ & \times \Theta\left[1 - \frac{2\tilde{\mu} \pm \tilde{\omega}}{2\tilde{u}\xi} \right] \Bigg\} \times \xi^3 \sqrt{\left(\frac{\tilde{\omega}}{2} \right)^2 - (1 - \xi^2)^2}, \end{aligned} \tag{4.96}$$

$$\begin{aligned} g_{yy}^{\pm} = & \frac{\Gamma}{2\pi^2 \tilde{u}\tilde{\omega}^2} \Bigg\{ \pi - \left[2 \arccos\left(\frac{2\tilde{\mu} \pm \tilde{\omega}}{2\tilde{u}\xi} \right) + 2\cos 2\theta \left(\frac{2\tilde{\mu} \pm \tilde{\omega}}{2\tilde{u}\xi} \right) \sqrt{1 - \left(\frac{2\tilde{\mu} \pm \tilde{\omega}}{2\tilde{u}\xi} \right)^2} \right] \\ & \times \Theta\left[1 - \frac{2\tilde{\mu} \pm \tilde{\omega}}{2\tilde{u}\xi} \right] \Bigg\} \times \xi^3 \sqrt{\left(\frac{\tilde{\omega}}{2} \right)^2 - (1 - \xi^2)^2}, \end{aligned} \tag{4.97}$$

$$g_{xy}^{\pm} = \Gamma \frac{2\tilde{\mu} \pm \tilde{\omega}}{\pi^2 \tilde{u}\tilde{\omega}^2} \sin 2\theta \xi \sqrt{\left(\frac{\tilde{\omega}}{2} \right)^2 - (1 - \xi^2)^2} \sqrt{\xi - \left(\frac{2\tilde{\mu} \pm \tilde{\omega}}{2\tilde{u}} \right)^2} \Theta\left[1 - \frac{2\tilde{\mu} \pm \tilde{\omega}}{2\tilde{u}\xi} \right] \tag{4.98}$$

$$g_{zz}^{\pm} = \frac{1}{\Gamma}\frac{1}{2\pi^2\tilde{\omega}^2}\left\{2\pi - 4\arccos\left(\frac{2\tilde{\mu}\pm\tilde{\omega}}{2\tilde{u}\xi}\right)\Theta\left[1-\frac{2\tilde{\mu}\pm\tilde{\omega}}{2\tilde{u}\xi}\right]\frac{\xi\left(1-\xi^2\right)^2}{\sqrt{\left(\frac{\tilde{\omega}}{2}\right)^2-\left(1-\xi^2\right)^2}}\right\}. \tag{4.99}$$

In the limit of no tilt, analytical results can be obtained. As mentioned previously in the case of no tilt $\sigma_{xy} = 0$ due to symmetries of the current operators. Furthermore in case of no tilt it follows that $\sigma_{xx} = \sigma_{yy}$ due to the rotational symmetry of the Hamiltonian. We then obtain that

$$\begin{aligned}\mathrm{Re}\{\sigma_{xx}(\omega)\} = -\sigma_0\left[f(\omega/2)-f(-\omega/2)\right]\Bigg[1-\frac{\theta(\tilde{\omega}-1)}{\pi}\Big(&\arctan(\sqrt{\tilde{\omega}^2-1})\\ &-\frac{2\tilde{\omega}^2+1}{3\tilde{\omega}^2}\sqrt{\tilde{\omega}^2-1})\Big)\Bigg]\end{aligned} \tag{4.100}$$

and

$$\begin{aligned}\mathrm{Re}\{\sigma_{zz}(\omega)\} = -\frac{v_z\Lambda}{32}\left[f(\omega/2)-f(-\omega/2)\right]\Bigg[1-\frac{\Theta(\tilde{\omega}-1)}{\pi}\Big(&\arctan\left(\sqrt{\tilde{\omega}^2-1}\right)\\ &-\frac{1}{\pi}\frac{\sqrt{\tilde{\omega}^2-1}}{\tilde{\omega}^2}\Big)\Bigg].\end{aligned} \tag{4.101}$$

Both of these results can be compared to and be seen to be identical with what is obtained in [15]. To obtain the conductivity for a tilted nodal loop one has to turn to numerical methods. However in the regime of small frequencies, $\tilde{\omega} \ll 1$, $\tilde{\omega} < \tilde{u}$ and $\tilde{\mu} = 0$, approximate results can be found. First we note that in these limits the second integral of Eq. (4.95) vanishes due to the Heaviside function being zero. Next we expand the functions in Eqs. (4.96), (4.97), (4.98) and (4.99) around $\tilde{\omega} = 0$. We then apply the mean value theorem

$$\int_a^b dx\, f(x) = f(c)(b-a). \tag{4.102}$$

As the integral boundaries of the integral in Eq. (4.95) are symmetric around 1 we pick $c = 1$. By such we find that

$$\mathrm{Re}\ \sigma_{xx}^{\mathrm{inter}}(\omega) \approx \frac{5\Gamma}{24\pi^2\tilde{u}}\left(1-\cos 2\theta\right)\tilde{\omega}, \tag{4.103}$$

$$\mathrm{Re}\ \sigma_{yy}^{\mathrm{inter}}(\omega) \approx \frac{5\Gamma}{24\pi^2\tilde{u}}\left(1+\cos 2\theta\right)\tilde{\omega}, \tag{4.104}$$

$$\mathrm{Re}\ \sigma_{zz}^{\mathrm{inter}}(\omega) \approx \frac{5}{12\pi^2\tilde{u}\Gamma}\tilde{\omega}, \tag{4.105}$$

$$\mathrm{Re}\ \sigma_{xy}^{\mathrm{inter}}(\omega) \approx \frac{5\Gamma\sin 2\theta}{12\pi^2\tilde{u}}\tilde{\omega}. \tag{4.106}$$

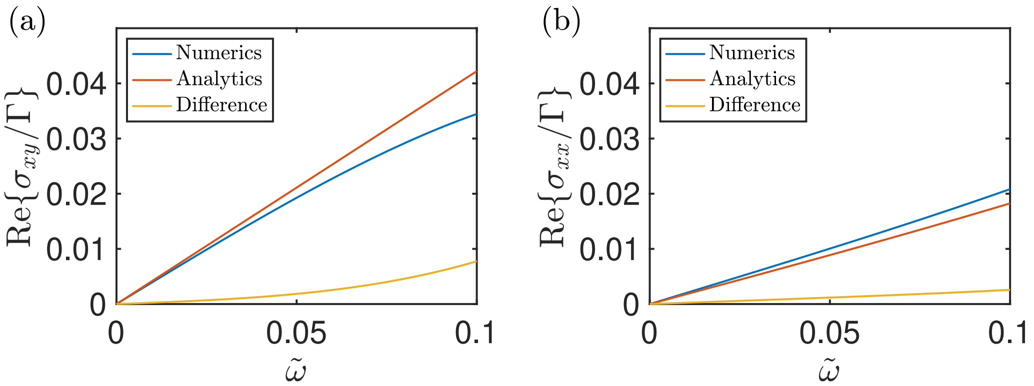

FIGURE 4.4: Comparison between the analytical and numerical evaluation of Eq. (4.95), for (a) σ_{xy} and (b) σ_{xx}, for $\theta = \pi/2$ and $\tilde{u} = 0.2$.

The transverse Hall conductivities, in the other directions, σ_{xz} and σ_{yz} vanish because of that we assume no tilt in the k_z direction ($u_z = 0$). The next-to-leading order term is to third order in frequency. This term becomes significant when the tilt direction $\theta \approx n\pi/2$ ($n \in \mathbb{Z}$). For tilt in the x direction, i.e., $\theta = 0$, the results reproduce the well known scaling of the longitudinal conductivities with frequency, $\sigma_{xx}^{\text{inter}} \propto \tilde{\omega}^3$ and $\sigma_{yy}^{\text{inter}} \propto \tilde{\omega}$. By plotting the approximate expressions and the numerical evaluation, see Fig. 4.4, we observe a good agreement between the analytical and numerical results for small $\tilde{\omega}$ and $\theta = \pi/4$.

The analytical results furthermore reveal the strong dependence of the tilt direction, θ. This especially applies to $\sigma_{xy}^{\text{inter}}$, which we notice vanishes for $\theta = n\pi/2$ ($n \in \mathbb{Z}$). For these tilt angles, the applied electric field excites an equal amount of electrons on the opposite sides of the nodal loop, leading to an equal but opposite flow of electrons. Hence $\sigma_{xy} = 0$. This has furthermore already been observed for the dc hall conductivity, which shows the same behavior [106]. The mathematical argument for the vanishing Hall conductivity follows from the fact that the angular integral in Eq. (4.88) separates from the rest and the whole integral vanishes as $\int_0^{2\pi} d\phi = 0$.

Secondly we observe that the maximum of σ_{xy} is obtained for $\theta = n\pi/4$ with odd n, for which we also obtain that $\sigma_{xx} = \sigma_{yy}$. We will now discuss this case in more detail. The full result of the numerical integration is seen in Fig. 4.5. Note that, without loss of generality, we consider in all cases $0 < \tilde{u}, \tilde{\mu} < 1$. First we look at $\tilde{\mu} < \tilde{u}$. In this case the following energy thresholds can be defined

$$\begin{aligned}
\tilde{\omega}_{\mathrm{I}} &= -2\tilde{\mu} - \tilde{u}^2 + \tilde{u}\sqrt{\tilde{u}^2 + 4(1+\tilde{\mu})}, \\
\tilde{\omega}_{\mathrm{II}} &= 2\tilde{\mu} - \tilde{u}^2 + \tilde{u}\sqrt{\tilde{u}^2 + 4(1-\tilde{\mu})}, \\
\tilde{\omega}_{\mathrm{III}} &= -2\tilde{\mu} + \tilde{u}^2 + \tilde{u}\sqrt{\tilde{u}^2 + 4(1-\tilde{\mu})}, \\
\tilde{\omega}_{\mathrm{IV}} &= 2\tilde{\mu} + \tilde{u}^2 + \tilde{u}\sqrt{\tilde{u}^2 + 4(1+\tilde{\mu})}.
\end{aligned} \tag{4.107}$$

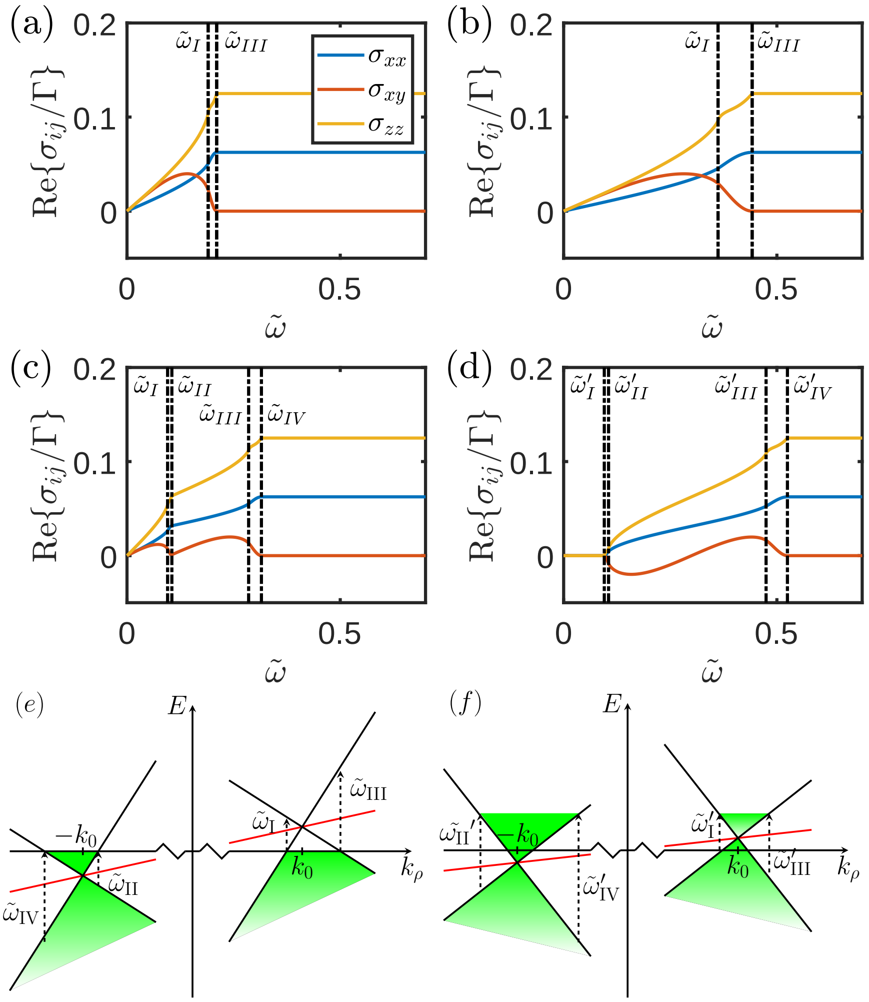

FIGURE 4.5: Real part of the optical conductivity for different values of the chemical potential, $\tilde{mu}$ and tilt velocities, $\tilde{u}$ and fixed tilt angle, $\theta = \pi/4$. (a) $\tilde{u} = 0.1$ and $\tilde{\mu} = 0$, (b) $\tilde{u} = 0.2$ and $\tilde{\mu} = 0$, (c) $\tilde{u} = 0.1$ and $\tilde{\mu} = 0.05$, (d) $\tilde{u} = 0.1$ and $\tilde{\mu} = 0.15$. The dashed lines correspond to the onset of allowed transitions that are depicted in (e) and (f). (e,f) Possible transitions for (e) $\tilde{\mu} < \tilde{u}$ and (f) $\tilde{\mu} > \tilde{u}$.

First we note that, for $\tilde{\mu} = 0$ we have $\tilde{\omega}_{\mathrm{I}} = \tilde{\omega}_{\mathrm{II}}$ and $\tilde{\omega}_{\mathrm{III}} = \tilde{\omega}_{\mathrm{IV}}$. Secondly, these thresholds defines the onset of vertical transitions, allowed on the nodal loop. The system is partially Pauli blocked as long as $\tilde{\omega} < \tilde{\omega}_{\mathrm{IV}}$. As we increase the energy of the incoming photons, transitions along the nodal loop goes from being forbidden to allowed and as the energy exceeds $\tilde{\omega}_{\mathrm{IV}}$, excitations along the whole nodal loop are possible. Hence the Pauli blockade is lifted. We display the absorption processes that give rise to the thresholds in Fig. 4.5 (e) and are furthermore indicated in the plots of the conductivity spectrum, Figs. 4.5 (a-d) and 4.6 (a-d). We furthermore note, as has previously been explained, when excitations become available along the whole nodal loop, the transverse conductivity vanishes. This is directly seen in the conductivity spectrum as $\mathrm{Re}\{\sigma_{xy}\}$ becomes zero for $\tilde{\omega} > \tilde{\omega}_{\mathrm{IV}}$.

In the case $\tilde{u} < \tilde{\mu}$ we instead define the following energy thresholds,

$$
\begin{aligned}
\tilde{\omega}'_{\mathrm{I}} &= 2\tilde{\mu} + \tilde{u}^2 - \tilde{u}\sqrt{\tilde{u}^2 + 4(1+\tilde{\mu})},\\
\tilde{\omega}'_{\mathrm{II}} &= 2\tilde{\mu} - \tilde{u}^2 - \tilde{u}\sqrt{\tilde{u}^2 + 4(1-\tilde{\mu})},\\
\tilde{\omega}'_{\mathrm{III}} &= 2\tilde{\mu} - \tilde{u}^2 + \tilde{u}\sqrt{\tilde{u}^2 + 4(1-\tilde{\mu})},\\
\tilde{\omega}'_{\mathrm{IV}} &= 2\tilde{\mu} + \tilde{u}^2 + \tilde{u}\sqrt{\tilde{u}^2 + 4(1+\tilde{\mu})}.
\end{aligned}
\tag{4.108}
$$

The interpretation of these is the same as before. The absorption processes are depicted in Fig. 4.5(f). As we go from $\tilde{u} > \tilde{\mu}$ to $\tilde{u} < \tilde{\mu}$ the allowed transitions around the nodal loop change. This is directly observed from Fig. 4.5 (d) where we now see that as long as $\tilde{\omega} < \tilde{\omega}'_{\mathrm{I}}$ the system is fully Pauli blocked, i.e., no vertical transitions are allowed along the nodal loop. As the energy of the incoming photons is increased and becomes larger than $\tilde{\omega}'_{\mathrm{I}}$ the Pauli blockade is overcome and vertical transitions becomes partially possible. Another consequence of $\tilde{u} < \tilde{\mu}$ is the fact that $\sigma^{\mathrm{inter}}_{xy}$ now takes both positive and negative values in contrast to only positive values for $\tilde{u} > \tilde{\mu}$.

As a final remark on the real part of the interband conductivity we note that for $\tilde{\omega} > \tilde{\omega}_{\mathrm{IV}}, \tilde{\omega}'_{\mathrm{IV}}$, transitions are available along the full nodal loop and the response of the system resembles that of an untitled nodal loop. In these regions, as has previously been observed, the longitudinal conductivity is constant [15, 1].

We have calculated the real part of the optical conductivity due to interband transitions. To obtain the full information of the conductivity, we are required to obtain the imaginary part as well. Due to the complicated integrals of Eq. (4.95), which we can only be evaluated numerically, the only possibility for calculating the imaginary part is by applying the Kramers-Kronig relation, Eq.(4.93). This integration as well has to be done numerically. The integral shows an unbounded logarithmic divergence, and hence we regularize it by introducing a cutoff, $\tilde{\omega}_c$. The necessity of the cutoff should not comes as a surprise. The integral that has to be calculated in the Kramers-Kronig relation has an infinite integration range. On the other hand, the effective model is only valid for small energies, and hence the integration from $-\infty$ to ∞ is unphysical. The cutoff is selected is $\tilde{\omega}_c = 2\tilde{\omega}_0$. A larger cutoff energy shows no pronounced effects on the low-energy features of the conductivity.

The imaginary part of the optical conductivity, due to interband transitions, is shown as the solid lines in Fig. 4.6. For $\tilde{\mu} = 0$, the imaginary parts take negative values and $\sigma_{xx,yy}$ remains negative as the frequency is increased. On the other hand, the transverse conductivity increases and for larger frequencies becomes positive and then decreases towards zero.

Next, we calculate the intraband transitions.

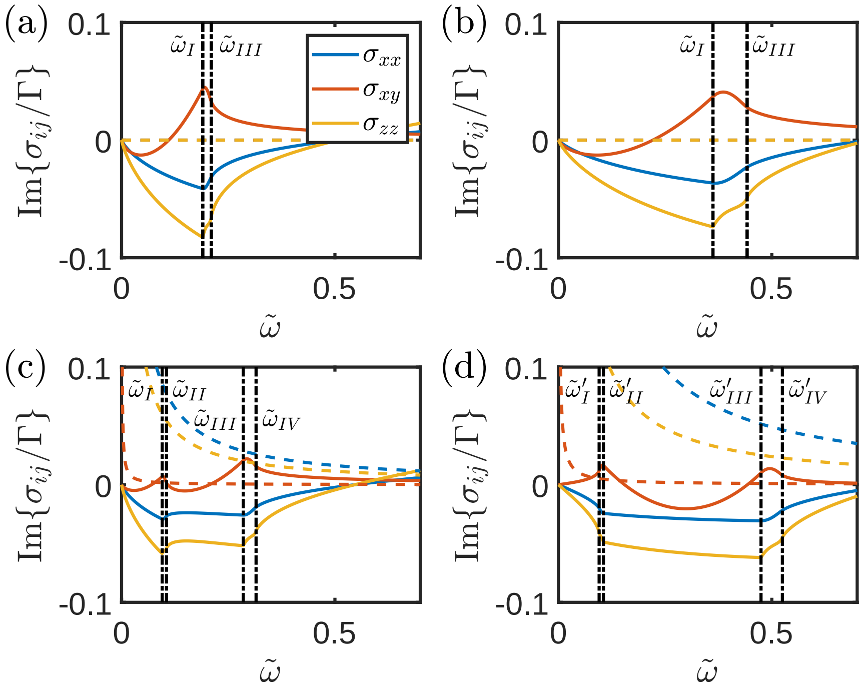

FIGURE 4.6: Imaginary part of the optical conductivity for different values of chemical potential, $\tilde{\mu}$, tilt velocity, $\tilde{u}$ and fixed tilt angle, $\theta = \pi/4$. (a) $\tilde{u} = 0.1$ and $\tilde{\mu} = 0$, (b) $\tilde{u} = 0.2$ and $\tilde{\mu} = 0$, (c) $\tilde{u} = 0.1$ and $\tilde{\mu} = 0.05$, (d) $\tilde{u} = 0.1$ and $\tilde{\mu} = 0.15$. Solid and dashed lines correspond to the contributions from interband and intraband transitions respectively. The vertical dashed lines correspond to the onset of allowed vertical transitions depicted in Fig. 4.5(e) and (f).

4.5.2 Intraband transtions

To obtain the intraband transitions we let $s = s'$ in Eq. (4.88). The conductivity kernel now reads

$$\sigma_{\mathbf{k}}^{ij,\text{intra}}(\omega) = -i \sum_s \frac{\partial f(E)}{\partial E}\bigg|_{E=\varepsilon_s} \frac{j^s_{\mathbf{k}i} j^s_{\mathbf{k}j}}{\omega + i0^+}. \tag{4.109}$$

By setting $T = 0$ the derivative of the Fermi distribution becomes a negative delta function, $\lim_{T\to 0} \frac{\partial f(E)}{\partial E}\big|_{E=\varepsilon_s} = -\delta(\varepsilon_s)$. By applying the identity, Eq. (4.92), the intraband contribution to the optical conductivity can be written

$$\sigma_{ij}^{\text{intra}}(\omega) = D_{ij}\left(\frac{i}{\omega} + \pi\delta(\omega)\right), \tag{4.110}$$

where D_{ij} is the Drude weight. By evaluating the k_z integral, the Drude weight is written as

$$D_{ij} = \frac{4}{(2\pi)^3}\int_0^\infty d\xi \int_0^{2\pi} d\phi\, \tilde{G}_{ij}(\xi,\phi), \tag{4.111}$$

where

$$\tilde{G}_{xx} = \omega_0\Gamma\xi \frac{\tilde{\mu} - \tilde{u}\xi\cos(\phi-\theta)}{\sqrt{(\tilde{\mu} - \tilde{u}\xi\cos(\phi-\theta))^2 - (1-\xi^2)^2}} \left[\tilde{u}\cos\theta + \frac{2\xi\cos\phi(1-\xi^2)}{\tilde{\mu} - \tilde{u}\xi\cos(\phi-\theta)}\right]^2$$
$$\Theta\left[(\tilde{\mu} - \tilde{u}\xi\cos(\phi-\theta))^2 - (1-\xi^2)^2\right], \tag{4.112}$$

$$\tilde{G}_{yy} = \omega_0\Gamma\xi \frac{\tilde{\mu} - \tilde{u}\xi\cos(\phi-\theta)}{\sqrt{(\tilde{\mu} - \tilde{u}\xi\cos(\phi-\theta))^2 - (1-\xi^2)^2}} \left[\tilde{u}\sin\theta + \frac{2\xi\sin\phi(1-\xi^2)}{\tilde{\mu} - \tilde{u}\xi\cos(\phi-\theta)}\right]^2$$
$$\times\,\Theta\left[(\tilde{\mu} - \tilde{u}\xi\cos(\phi-\theta))^2 - (1-\xi^2)^2\right], \tag{4.113}$$

$$\tilde{G}_{xy} = \omega_0\Gamma\xi \frac{\tilde{\mu} - \tilde{u}\xi\cos(\phi-\theta)}{\sqrt{(\tilde{\mu} - \tilde{u}\xi\cos(\phi-\theta))^2 - (1-\xi^2)^2}}$$
$$\times \left[\tilde{u}\sin\theta + \frac{2\xi\sin\phi(1-\xi^2)}{\tilde{\mu} - \tilde{u}\xi\cos(\phi-\theta)}\right]\left[\tilde{u}\cos\theta + \frac{2\xi\cos\phi(1-\xi^2)}{\tilde{\mu} - \tilde{u}\xi\cos(\phi-\theta)}\right] \tag{4.114}$$
$$\times\,\Theta\left[(\tilde{\mu} - \tilde{u}\xi\cos(\phi-\theta))^2 - (1-\xi^2)^2\right],$$

$$\tilde{G}_{zz} = \frac{\omega_0}{\Gamma}\xi \frac{\sqrt{(\tilde{\mu} - \tilde{u}\xi\cos(\phi-\theta))^2 - (1-\xi^2)^2}}{\sqrt{(\tilde{\mu} - \tilde{u}\xi\cos(\phi-\theta))^2}}\Theta\left[(\tilde{\mu} - \tilde{u}\xi\cos(\phi-\theta))^2 - (1-\xi^2)^2\right] \tag{4.115}$$

In the case of no tilt, $\tilde{u} = 0$ these integral can be calculated analytically. We obtain

$$D_{xx} = \frac{1}{4\pi^2}\omega_0\tilde{\mu}\Gamma\left[1 - \frac{\Theta[\tilde{\mu}-1]}{\pi}\left(\frac{4\tilde{\mu}^2-1}{3\tilde{\mu}^2}\sqrt{\tilde{\mu}^2-1} - \arctan\left(\sqrt{\tilde{\mu}^2-1}\right)\right)\right], \tag{4.116}$$

$$D_{zz} = \frac{1}{8\pi^2}\frac{\tilde{\omega}_0\tilde{\mu}}{\Gamma}\left[1 + \frac{\Theta[\tilde{\mu}-1]}{\pi}\left(\frac{\sqrt{\tilde{\mu}^2-1}}{\tilde{\mu}^2} - \arctan\left(\sqrt{\tilde{\mu}^2-1}\right)\right)\right], \tag{4.117}$$

and $D_{yy} = D_{xx}$. We note that these results ($\tilde{u} = 0$) directly match the ones found in [15]. To obtain the contribution from the intraband transitions, in the case of a finite tilt, the integrals have to be performed numerically. We note that the real part of the intraband contribution is a delta function, and hence we will neglect this part since we will mainly be interested in finite frequencies. The imaginary part, on the other hand, has a frequency dependence and has to be included. The results from the integrations are displayed as the dashed lines in Fig. 4.6. From Fig. 4.6 (a) and (b) we note that $D_{ij}(\tilde{\mu} = 0) = 0$. This connects with the analytical results obtained for the untilted nodal loop which also become zero for $\tilde{\mu} = 0$. We note that D_{xy} has a minor impact on $\mathrm{Im}\sigma_{xy}$ as seen from the dashed red curves and the main effect is seen for very small $\tilde{\omega}$. On the other hand, the intraband contribution to $\sigma_{xx,yy,zz}$ is larger as they do not go to zero as fast.

The full conductivity tensor is now known for the nodal loop with tilt in the $k_x - k_y$ plane. With this information, we can now calculate the Kerr response of materials with a band structure displaying a titled nodal loop.

4.6 Kerr effect in nodal loop semimetals

In the following section, we calculate the Kerr rotation for a thin film and a semi-infinite bulk material, hosting a nodal loop. We only consider light incident on the $x - y$ surface for the thin film as this is the only surface that may show a Kerr rotation. On the other hand, we consider light incident on both the $x - y$ and $y - z$ surface for the bulk. For both the thin film and the bulk, we consider three different settings where we, in general, keep all parameters fixed but vary one of them. In the first case, we vary the tilt velocity. This is followed by varying the chemical potential and the tilt direction.

4.6.1 Thin film

We first consider a nodal loop with a tilt angle of $\theta = \pi/4$. The Kerr angle for varying tilt velocity and varying chemical potential are plotted in Fig. 4.7. Let us first analyze the case when $\mu = 0$ (Figs. 4.7(a) and (c)). The Kerr angle (Fig.4.7(a)) and ellipticity (Fig.4.7(c)) shows a pronounced dip around $\tilde{\omega} \approx 2\tilde{u}$. For small tilt velocities this is also approximately equals to $\tilde{\omega}_{IV}$, for which $\mathrm{Re}\sigma_{xy} = 0$ and $\mathrm{Im}\sigma_{xy}$ reaches its maximum. From this we conclude that a finite tilt has a strong impact on the Kerr signal.

By increasing the chemical potential (Figs. 4.7(b) and (d)), the Kerr angle and ellipticity shows a signal that is in stark contrast to the case when $\tilde{\mu} = 0$. Furthermore, the amplitude of the Kerr angle is reduced but still remains what is to be considered large. The Kerr angle now reaches its maximum between $\tilde{\omega} \approx 2\tilde{\mu} + \tilde{u}/2$ and $\tilde{\omega} \approx 2\tilde{\mu} + 2\tilde{u}$. In the case of $\tilde{\mu} > \tilde{u}$, the region of positive Kerr angles is preceded by a region, defined by $2\tilde{\mu} - 3\tilde{u}/2 \lessapprox \tilde{\omega} \lessapprox 2\tilde{\mu} + \tilde{u}/2$, where it takes negative values, on the same order as the positive ones.

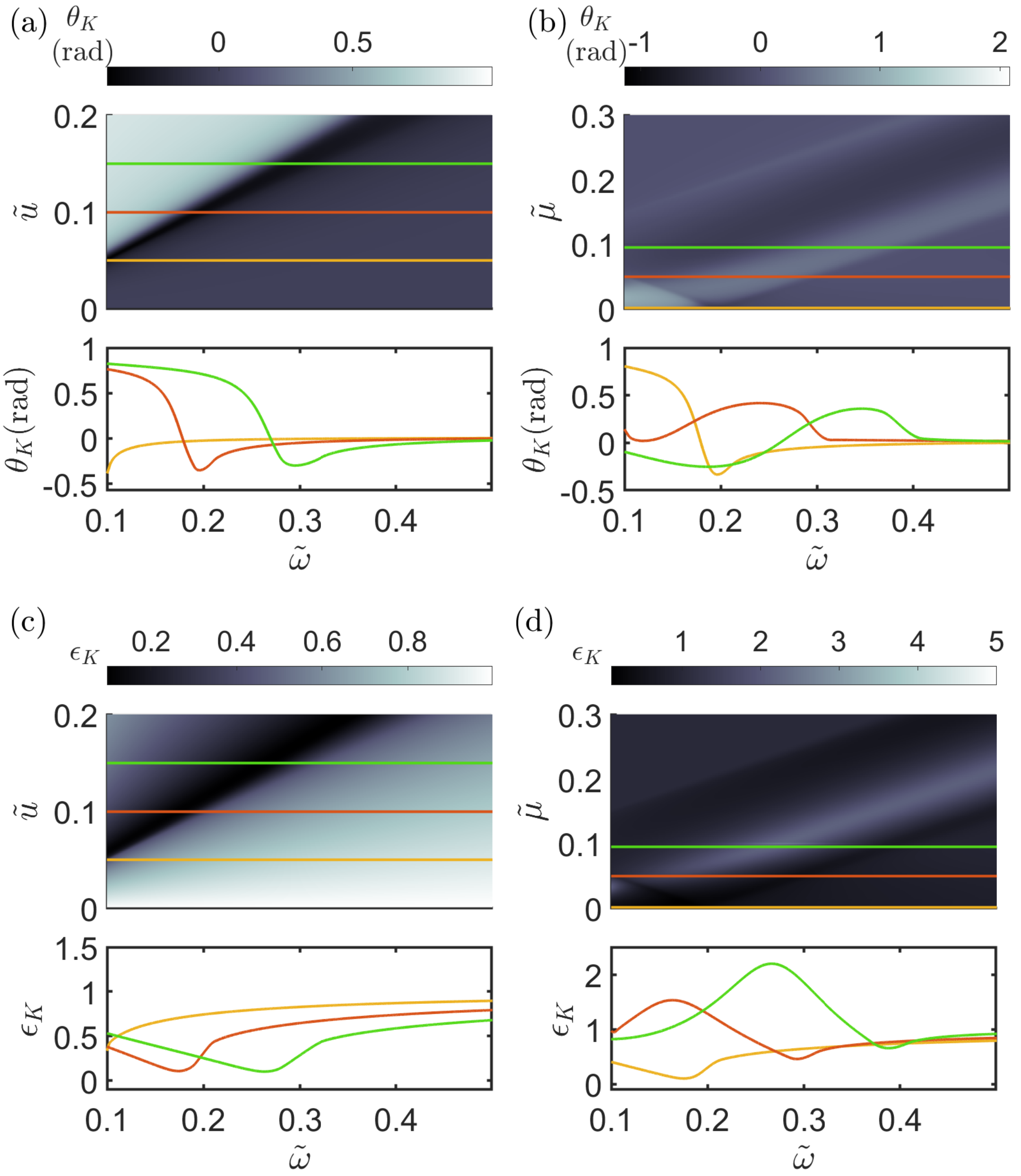

FIGURE 4.7: *(a,b):* Kerr angle θ_K for a thin film. *(c,d):* Kerr ellipticity ϵ_K for a thin film. For (a) and (c) we fix the chemical potential at $\tilde{\mu} = 0$ and vary the tilt velocity. The sharp peak dip corresponds to $\tilde{\omega} = 2\tilde{u}$. For (b) and (d) we fix the tilt velocity at $\tilde{u} = 0.1$ and vary the chemical potential.

The results from varying the tilt angle are displayed in Fig. 4.8. We observe that both the Kerr angle and the ellipticity highly depend on the tilt direction. When the tilt direction takes any value equal to $n\pi/2$ ($n \in \mathbb{Z}$), we note that the Kerr angle equals zero, and the ellipticity equals one. This is due to that σ_{xy} vanishes for these tilt directions. Hence, the polarization of the reflected light is the same as for the incident. The variation of the tilt angle is especially observed in the ellipticity. Here we observe that it takes very large values in the second and fourth quadrants, whereas it almost disappears in the first and third. This is due to $E_r^R(\theta) = E_r^L(\theta + \pi/2)$. Again, this is a consequence of the Hall conductivity, now because $\sigma_{xy}(\theta) = -\sigma_{xy}(\theta + \pi/2)$.

4.6.2 Bulk material

Light reflected on a bulk material is described by Eqs. (4.40) and (4.50) for light incident on the $x - y$ and $y - z$ surfaces, respectively. We consider a nodal loop that has a static permittivity of $\varepsilon_b = 10$. We first look at light incident on the $x - y$ surface. The results for varying tilt velocity and chemical potential are plotted in Fig. 4.9.

For $\tilde{\mu} = 0$, the results show similar patterns to those of the thin film. The main difference is seen in the amplitude of the Kerr angle, which is reduced for the bulk material. It is furthermore decreased as the static permittivity increases. Experimentally it should still be detectable as Kerr angles on the order of 10^{-9} radians have been detected [176]. We note that for larger frequencies, the ellipticity equals one. This is anchored in that excitations become possible along the whole nodal loop and the real part of the Hall conductivity, $\mathrm{Re}\{\sigma_{xy}\} = 0$.

As we increase the chemical potential (Fig. 4.9 (b)), the dip that is observed around $\tilde{\omega} = 2\tilde{u}$ (see Fig. 4.9 (a)) splits into two dips that are centered around $\tilde{\omega} = 2\tilde{u} \pm 2\tilde{\mu}$. As we increase the chemical potential such that $\tilde{\mu} > \tilde{u}$ the dips center around $\tilde{\omega} = 2\tilde{u}$ and $\tilde{\omega} = 2\tilde{u} + 2\tilde{\mu}$. For large chemical potentials the system furthermore becomes Pauli blocked. This is especially observed in the ellipticity, Fig. 4.9(d), which equals 1 in this case (see the upper left part of the colormap).

Let us now look at the results from the Kerr angle and ellipticity as we vary the tilt angle. These are plotted in Figs. 4.8 (c) and (d). The results are similar to those of the thin film, as one might expect. Mainly one observed a decrease in the amplitude.

Next we look at the Kerr rotations on the $y - z$ surface. We let the incident beam be such that $E_0^y = E_z^0 = 1/\sqrt{2}$, such that potential Kerr rotations can be observed. The Kerr and ellipticity for a varying tilt velocity and chemical potential are shown in Fig. 4.10. Compared to light incident on the $x - y$ surface, the Kerr angle is of an order of magnitude smaller. The ellipticity, furthermore, remains close to 1 over the whole spectrum. This is due to that $\varepsilon_{yz} = 0$, which would otherwise strongly contribute to the behavior of the Kerr rotations, and furthermore, that ε_{xy} is strongly suppressed by ε_{xx}.

By increasing the chemical potential (Fig. 4.10 (b) and (d)) the features of the Kerr rotation does not change much; the Kerr angle increases slightly in amplitude for smaller $\tilde{\omega}$ and the ellipticity shifts towards $\varepsilon_K = 1$. The reason for the shift of

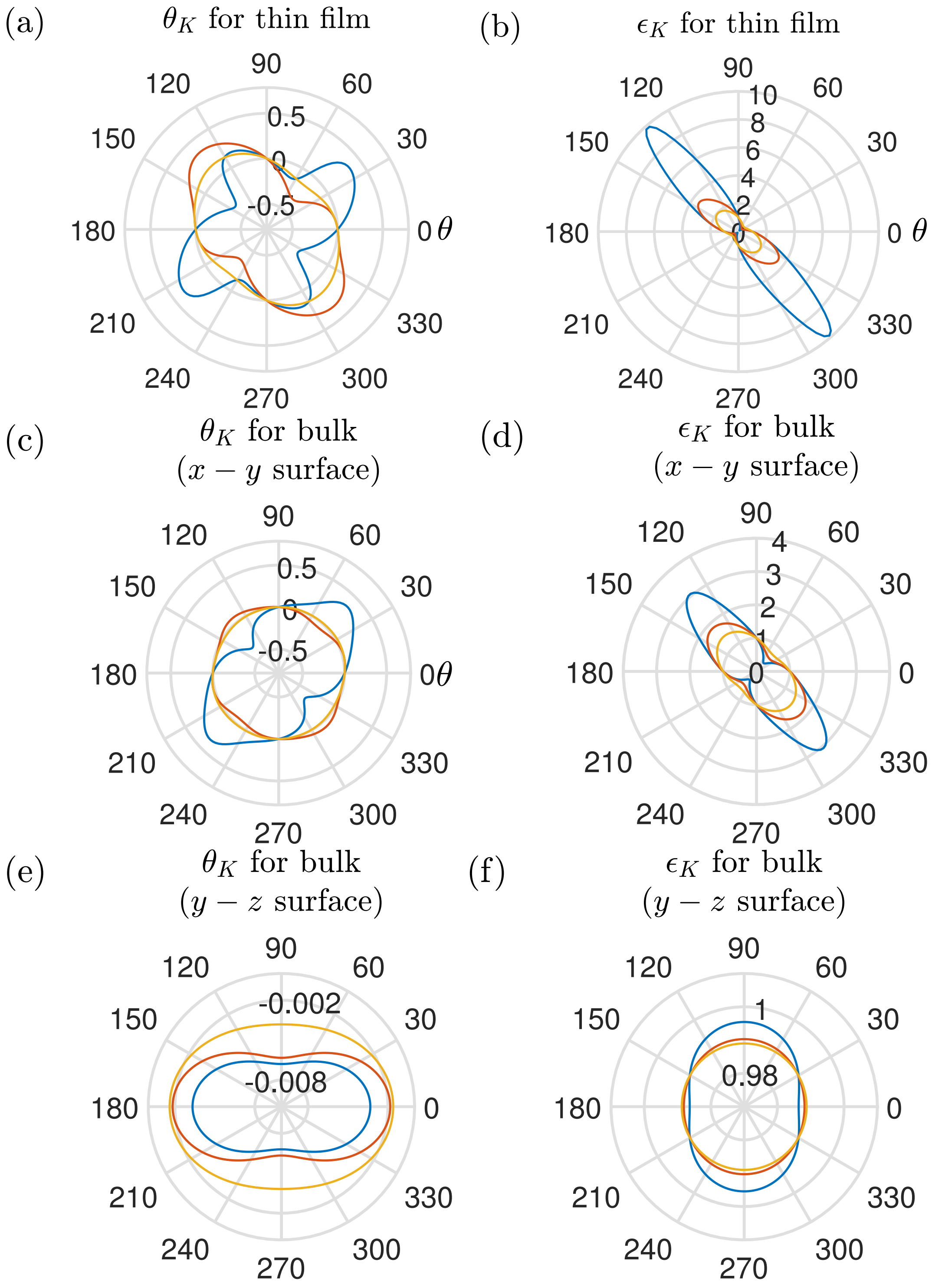

FIGURE 4.8: Kerr angle for (a) a thin film with light incident on the $x - y$ surface, (c) bulk material with light incident on the $x - y$ surface and (e) bulk material with light incident on the $y - z$ surface and ellipticity for (b) the thin film, (d) the bulk material with light incident on the $x - y$ surface and (e) the bulk material with light incident on the $y - z$ surface. In all plots we are varying the tilt direction, θ. The chemical potential $\tilde{\mu} = 0$ and the tilt velocity $\tilde{u} = 0.1$. For all plots $\tilde{\omega}$ is set to the fixed values $\tilde{\omega} = 0.17$ (blue), $\tilde{\omega} = 0.2$ (red) and $\tilde{\omega} = 0.23$ (yellow).

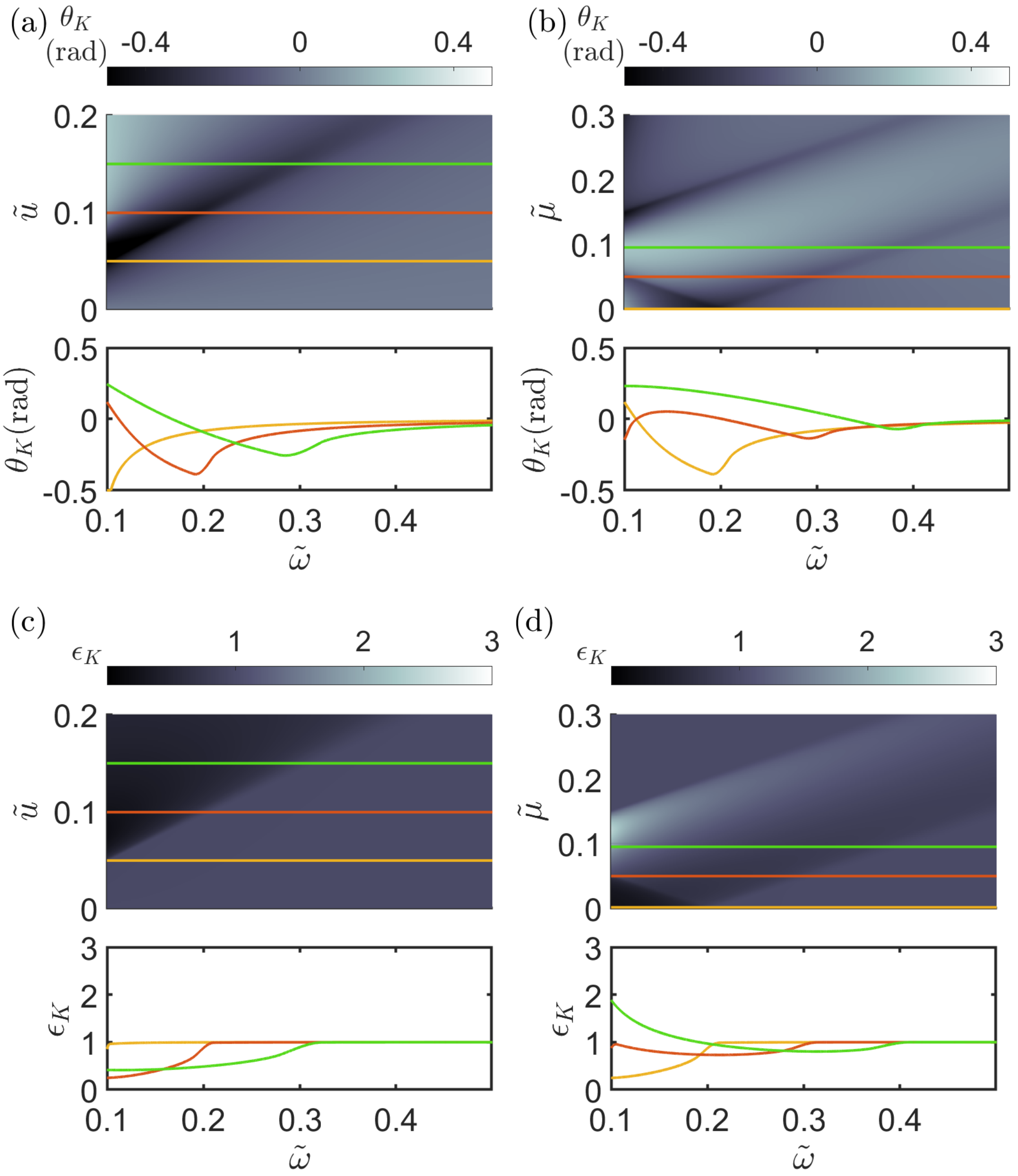

FIGURE 4.9: *(a,b):* Kerr angle θ_K and *(c,d):* Kerr ellipticity ϵ_K for a bulk material and light incident on the $x - y$ surface. For (a) and (c) we fix the chemical potential at $\tilde{\mu} = 0$ and vary the tilt velocity. The sharp peak dip corresponds to $\tilde{\omega} = 2\tilde{u}$. For (b) and (d) we fix the tilt velocity at $\tilde{u} = 0.1$ and vary the chemical potential.

the ellipticity is, as for incidence on the $x-y$ surface, that the system becomes Pauli blocked.

We finally discuss the Kerr angle and ellipticity as we vary the tilt angle. The results are seen in Fig. 4.8 (e) and (f). The features observed here are distinct from those when light is incident on the $x-y$ surface. The Kerr rotation remains small as the tilt angle is varied. However, compared to what is observed on the $x-y$ surface, there are no strong variations as we vary the tilt angle. The reason for this is that the tilt angle does not affect $\varepsilon_{xx,yy,zz}$ as much as it does ε_{xy}.

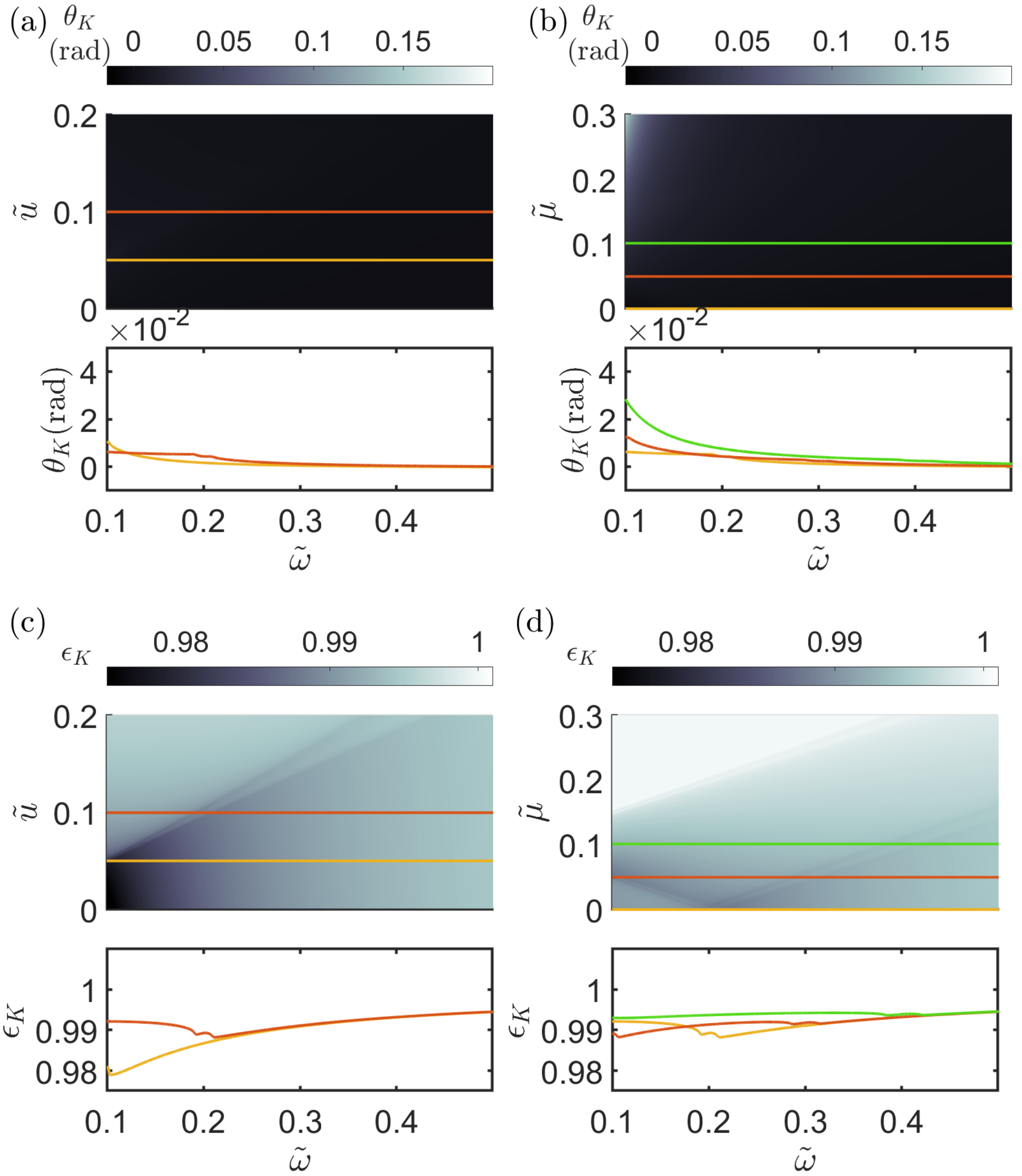

FIGURE 4.10: *(a,b):* Kerr angle θ_K and *(c,d):* Kerr ellipticity ϵ_K for a bulk material and light incident on the $y-z$ surface. For (a) and (c) we fix the chemical potential at $\tilde{\mu} = 0$ and vary the tilt velocity. For (b) and (d) we fix the tilt velocity at $\tilde{u} = 0.1$ and vary the chemical potential.

Chapter 5

Hydrodynamic equations for two dimensional topological materials

This chapter revolves around electronic hydrodynamics, and the results presented are based on the results we reported on in *Electron hydrodynamics of two-dimensional anomalous Hall materials* [62]. Here the effects of topology on hydrodynamic transport in electronic systems are investigated. The Berry curvature, which defines the topological properties of the material, will show to affect hydrodynamic transport.

Electronic hydrodynamics is a relatively new branch of condensed matter physics. It had its beginning in the second half of the nineteen hundreds with the first ideas proposed by Gurzhi [58, 57]. The field, however, did not take hold until recently with the discovery of graphene. Ever since, the field has been flourishing, both theoretically and experimentally. On the theoretical side, much work has been poured into establishing a formalism and finding signatures that are related to electron hydrodynamics [116, 115, 96, 51, 128, 28, 101, 162]. Many experiments reporting a hydrodynamic electron flow have as well been conducted [13, 14, 109, 40, 90, 19]. Furthermore, topological effects on hydrodynamic transport have already entered the discussion as well [163, 157]. Theoretically, systems with time-reversal symmetry and a non-vanishing Berry curvature have been investigated.

This chapter begins with an introduction to electronic hydrodynamics in two-dimensional (2D) materials. First, we describe the early theoretical predictions that should serve as indicators for hydrodynamic flow. After that, we briefly discuss some experiments where hydrodynamic electron flow has been observed. We follow this with a detailed description of the theory of hydrodynamics for 2D electronic systems. This demands us to introduce the Boltzmann equation, which is the main tool for deriving the equations that govern hydrodynamics in electronic systems [116]. The complete derivation of the equations requires one to specify the band structure of the system. Throughout this chapter, we will consider an anomalous Hall insulator (AHI), which can be modeled by a gapped 2D Dirac Hamiltonian. This Hamiltonian breaks TR symmetry and has a non-vanishing Berry curvature. As a consequence of that the Hamiltonian breaks TR symmetry, the Berry curvature is odd in momentum, contrary to materials that break inversion symmetry, which has a Berry curvature that is even in momentum [163, 157].

We obtain the hydrodynamic equations for the specified Hamiltonian and specifically investigate the effects of the non-vanishing Berry curvature and how it modifies different types of hydrodynamic flow. First, we consider the effect it has on a flow thorough a long but narrow channel. This normally leads to what is known as Poiseuille flow. Here we observe deviations from the standard flow profile that are directly set by the Berry curvature. Next, we study the hydrodynamic equations for two different geometries, a semi-infinite half-plane, and a finite geometry. For the semi-infinite half-plane, we use analytical techniques and show that the Berry curvature induces vortices in the flow. We show that these can be observed by measuring the non-local resistance.

For the finite geometry, we use a numerical method, the finite element method. Here we first observe the effects the Berry curvature has on vortices induced by the finite geometry. We find a shift of the positions of these, which furthermore can be compared with a system without Berry curvature, for which analytical results have been obtained [96]. Secondly, we find that a modification in the electrical potential, which will be seen, serves as a more robust indicator of the presence of the Berry curvature. We furthermore find that the numerical results are qualitatively in line with the analytical results.

5.1 Hydrodynamics for electronic systems in 2D

Hydrodynamics, or more precisely, fluid mechanics, is a theory that has been around since the formulation of the Navier-Stokes equations during the 19th century. The equations describe the dynamics of a Newtonian fluid and can be applied to most gases and liquids. This is the case even though, for example, a macroscopic body of water contains about $\sim 10^{23}$ molecules. The reason why it works so well is that we only consider the water dynamics on long length scales. Hence, the only degrees of freedom which can be reasonably measured are conserved quantities. These are the number of water molecules and the energy and momentum of those. In the case of a Newtonian, incompressible fluid and for constant viscosity the classical Navier-Stokes equations yields

$$\rho\left(\frac{\partial \mathbf{u}}{\partial t}+\mathbf{u}\cdot\nabla\mathbf{u}\right)=-\nabla P+\eta\nabla^2\mathbf{u}+\mathbf{F}, \tag{5.1}$$

where $\mathbf{u}$ is the velocity of the fluid, P is the pressure, ρ is the fluid density and, η is the viscosity of the fluid. The term on the left-hand side describes the inertial forces. The terms on the right-hand side, from left to right, describe the pressure forces, viscous forces and external forces, that are applied to the fluid. This equation is always solved together with the continuity equation, which for an incompressible fluid is[1],

$$\nabla\cdot\mathbf{u}=0. \tag{5.2}$$

---

[1] For an incompressible fluid the density remains constant in time and hence, $\partial_t\rho = 0$

With the success of this theory, one might then wonder whether this could also be applied to electronic systems considered in condensed matter physics.

In 1963 it was for the first time that hydrodynamics was suggested as a possible theory for not only describing liquid or gas flows but as well electronic flows [58]. The ideas were improved on a few years later [57]. The motivation of applying hydrodynamics to electronic flow relies on length scales of different scattering mechanisms.

The most common scattering mechanisms in solids are impurity-electron scattering, electron-phonon-scattering, and electron-electron scattering. The mean free path, that is, the distance traveled of the electron between different collisions, depends highly on temperature. At small temperatures, the dominant mechanism is impurity-electron scattering. This leads to, e.g., the residual resistance in metals at low temperatures. On the other hand, at high temperatures, the dominating scattering mechanism is between electrons and phonons.

In most cases, it is commonly known that either electron-impurity scattering or electron-phonon scattering dominates over the scattering between electrons themselves. Formulated in terms of the mean free path of the different scattering mechanisms this means that $l_{e-e} \gg l_{e-imp}, l_{e-ph}$, where l_{e-e}, l_{e-imp} and l_{e-ph} are the length scales associated with the electron-electron, electron-impurity and the electron-phonon scattering respectively. A consequence of this is that hydrodynamic flow would be rare.

Let us now, following Gurzhi [58], consider electron flow through a narrow channel with a width equal to d, as depicted in Fig. 5.1. Gurzhi predicted that if hydrodynamic transport was going to be observed, this would be seen in the resistance of the material as the temperature is increased. Let us first explain this phenomenon in terms of the mean free path of the different scattering mechanisms.

We denote by l_V the mean free path that accounts for any scattering against inhomogeneities (impurities, phonons, etc.). If $l_V \gg d$, then the resistance should be determined by collisions between the electrons and the boundaries of the channel. From this, it appears that the effective mean free path is then determined by d. However, electron-electron scattering can substantially affect the process of momentum transfer to the channel boundaries. This can be understood by considering Navier-Stokes equations for the average velocity of the electrons under the application of an electric field [58]. This should furthermore have an impact on the resistance of the channel. Hence, there are two regimes to consider, $l_{e-e} \ll d$ and $l_{e-e} \gg d$.

If $l_{e-e} \gg d$, then the electrons mainly scatter against the boundaries of the sample. The resistance is mainly determined by the inverse of the mean free path, and hence it is expected to be proportional to d^{-1}, as depicted in Fig. 5.2. If all other scattering mechanisms are smaller than the length of the channel, L, such that the next smallest mean free path is set by L, then the system is in the ballistic regime. If L does not define the next smallest mean free path, then the system is in the so-called Knudsen regime [80]. These are both depicted in Fig. 5.1(a). If the mean free path

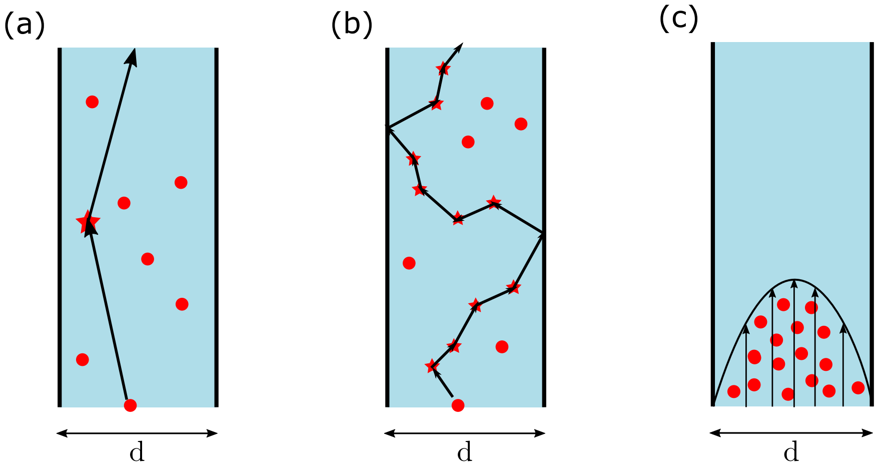

FIGURE 5.1: The different transport regimes describing the Gurzhi argument. (a) Ballistic transport regime. (b) Diffusive transport and (c) Hydrodynamic transport regime – Gurzhi effect.

of the impurities becomes smaller than the width of the channel then the main scattering is between electrons and impurities and the system is in the diffusive regime, depicted in Fig. 5.1(b).

At some temperature T_1 for which $l_{e-e} \sim d$, a cross-over may occur from the ballistic/Knudsen/diffusive regime, and the resistance, as argued by Gurzhi, is proportional to T^{-2}. Hence if the system is in the hydrodynamic regime, a drop in the resistance should be observed. Physically, in this regime, the fluid becomes pinned to the boundary at the edges. This results in a stationary flow at the edges that will pull back at the fluid in the middle of the channel. Because of this, the resistance should furthermore increase if the channel is made smaller. The described effect is what is known as the Gurzhi effect. The type of flow that this leads to is commonly known as Poiseuille flow. This is depicted in Fig. 5.1(c). The flow profile is parabolic such that the maximum flow velocity is reached in the middle of the sample, and it is decreasing towards the boundaries. If at some temperature T_2 scattering between electrons and impurities dominate over scattering between electron and phonons, then the resistance should remain constant.

At some point, as temperature is increased, scattering against phonons will dominate, and the resistance should obtain the normal growth with $R \propto T^5$. Concluding, if the hydrodynamic regime is present, one would possibly observe something similar to the prediction by Gurzhi, Fig. 5.2.

The Gurzhi effect was the first proposal for the observation of hydrodynamic flow. However, the hydrodynamic theory was long neglected and was only until recently given little attention. The reason for this is clear: electrons in solids, unlike water molecules, for example, are confined to the crystal lattice, which means that their momentum is not conserved. Consequently, the motions of electrons are typically either diffusive or, if the sample size is much smaller than the mean free path of the electrons, ballistic.

Now let us imagine a material for which the opposite is true and the dominant

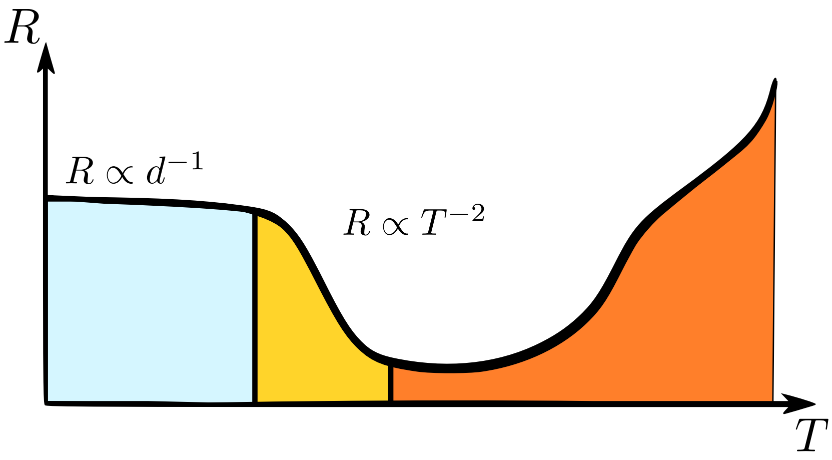

FIGURE 5.2: Resistance of a sample as a function of temperature. The graph is separated into three regions. In the left-most region (light blue), the main scattering mechanism is between the electrons and the boundaries. In this regime, the resistance remains constant, determined by the inverse of the channel width. In the midsection (yellow), the resistance decrease due to hydrodynamic flow. As the temperature is increased, the system enters the third part (orange). The resistance is increasing, mainly due to scattering between electrons and phonons. The image adapted from [58].

scattering mechanisms are electron-electron interactions. If there exists such a material, there would be a good incentive to study hydrodynamic models. Apart from one experiment done by de Jong and Molenkamp, [108], where they investigated electron flow in two-dimensional wires made from $(\mathrm{Al}, \mathrm{Ga})\mathrm{As}$, and a theoretical work by the same authors [73], not much effort was put into the search for such materials.

However, with the experimental discovery of graphene [120], in which the regime where electron-electron scattering is dominating is large [65], the field of electronic hydrodynamics had an upswing. An increasing effort has been put into theoretical studies of electronic hydrodynamics [111, 96, 128, 116, 115]. Furthermore, there have also been experiments performed that elucidate on hydrodynamic flow in graphene. The first experiment came from the group of Geim [13]. In contrast to the suggestion by Gurzhi, another hallmark of hydrodynamic flow was measured. This is a non-local resistance that arises due to whirlpools causing a backflow towards the inlet. The non-local resistance on the inlet is defined as [96]

$$R_{nl}(x) = \frac{V_{nl}(x)}{I}, \tag{5.3}$$

where $V_{nl}(x) = V(x) - V(0)$ for which $x = 0$ defines the inlet position, and I is the current (independent of position). For viscous flow, for which whirlpools appear (see Fig. 5.3(b)), a sign change in V_{nl} will be observed, contrary to a conventional current for which it remains positive (see Fig. 5.3(a)). The experiments performed by [13] clearly exhibit this feature (see Fig. 5.3(c)).

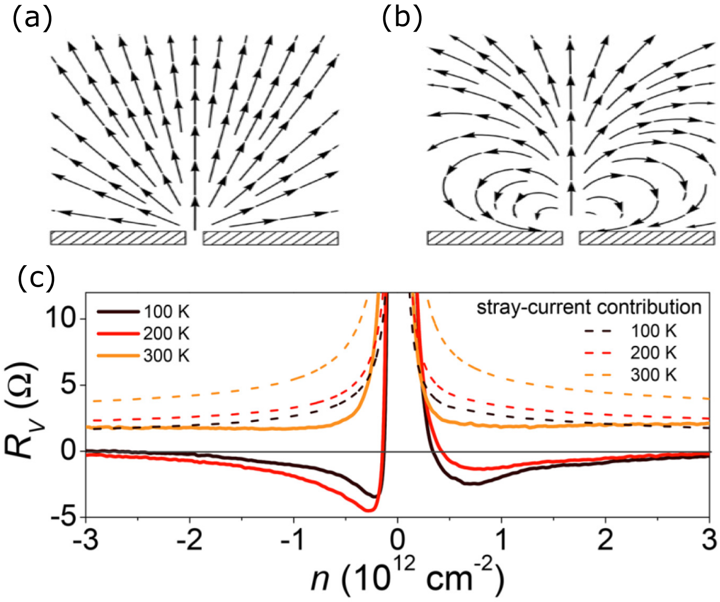

FIGURE 5.3: (a) Conventional flow as a current is flowing through a small constriction. (b) Hydrodynamic flow with whirlpools due to backflow. (c) Non-local resistance due to hydrodynamic flow for different temperatures. Figure is adapted from [13]

Within the last years, further experiments have been done, confirming the hydrodynamic flow in graphene [40, 90, 14]. Hydrodynamic flow has further been investigated in $PdCoO_2$ and is claimed to be observed [109].

This summarizes the state of hydrodynamics for electronic systems and some of the effects caused by hydrodynamic flow. Now one might ask why a hydrodynamic description is useful? In general, since the number of particles in condensed matter physics is so large, solving a Schrödinger equation for the considered systems is often impossible. Hence, like many other theories, the hydrodynamic description is an effective theory. The idea of the hydrodynamic theory is to reduce the degrees of freedom from many to very few ones and then impose conservation laws. By applying thermodynamic relations, we then obtain a theory for quantifying macroscopic variables that can be measured in experiments.

There are different ways of deriving the hydrodynamic equations. Two of these are phenomenological in nature. The first approach is treated on the level of classical mechanics where the equations are derived from a perspective of an element of the fluid [93]. The other is more general and relies on thermodynamics rather than classical mechanics [31]. The third method relies on the semi-classical Boltzmann theory. Like the other methods, this also comes with its drawbacks. The Boltzmann equation suffers from the assumption that the constituent particles are free between successive collisions. This results in the applicability of the Boltzmann theory being very narrow and will carry over to the hydrodynamic theory, based on the Boltzmann equation, as well. The validity of the hydrodynamic theory is commonly extended to a larger region based on the assumption of universality. The assumption of universality states that all fluids with the same symmetry properties must obey the same hydrodynamics equations whether the interactions between the particles are weak or strong [116].

We will next derive the hydrodynamic equations. The general steps are the following

- Write down the Boltzmann equation. The Boltzmann equation tells us how the local distribution function evolves in time as electric and magnetic fields are applied. The local distribution function is defined through the H-theorem, derived in Appendix. F.
- Next, a set of continuity equations are derived. This is done by defining the particle number, energy density, and momentum density. The derivation follows by considering how the defined quantities evolve in time and applying the Boltzmann equation.
- The particle number, energy density, and momentum density are now related to macroscopic quantities. The macroscopic quantities are defined by the local distribution function, given by the Boltzmann H-theorem. As the macroscopic details are specific for each material, one here has to define the Hamiltonian for the material of interest.
- Finally, the continuity equations, written in terms of macroscopic quantities, can be combined to form the Euler equation, and the Navier-Stokes equation if the viscosity is taken into account.

Following this outline, we will next derive the semi-classical Boltzmann equation.

5.2 Boltzmann equation

Historically, the Boltzmann equation was derived using classical arguments and was applied to classical particles, described by the Maxwell-Boltzmann distribution. The Boltzmann equation generally describes the dynamics of a distribution function

$$f_\lambda(\mathbf{r}(t), \mathbf{k}(t), t) \tag{5.4}$$

which gives the probability density, $f_\lambda(\mathbf{r}(t), \mathbf{k}(t), t) d\mathbf{r} d\mathbf{k}$, to find a particle in a region $d\mathbf{r} d\mathbf{k}$ in phase space, centered around $(\mathbf{r}, \mathbf{k})$ at time t. As we are here considering electrons, $f_\lambda(\mathbf{r}(t), \mathbf{k}(t), t)$ in equilibrium takes the form of a Fermi distribution and λ denotes any quantum number such as band index or spin.

To understand how the distribution function changes in time we know from Liouville's theorem that any distribution function stays constant along any trajectory in phase space. Now, on a second thought, in many cases this seems rather unphysical. Indeed, moving particles will normally encounter either each other or other obstacles that directly impact the trajectory of the distribution function. The statement is then formally expressed as

$$f_\lambda(\mathbf{r},\mathbf{k},t) = f_\lambda(\mathbf{r}+d\mathbf{r},\mathbf{k}+d\mathbf{k},t+dt) - \mathcal{I}\left[f\right]_{coll} dt, \tag{5.5}$$

where $\mathcal{I}\left[f_\lambda\right]_{coll}$ is the collision integral, which describes the rate of change of the distribution function due to interactions of the specific system. One now proceed with expanding the right hand side to first order in $\frac{d}{dt}$. In doing so we obtain

$$f_\lambda(\mathbf{r},\mathbf{k},t) = f_\lambda(\mathbf{r},\mathbf{k},t) + \frac{\partial f_\lambda}{\partial t}dt + \frac{\partial f_\lambda}{\partial \mathbf{r}}\frac{d\mathbf{r}}{dt}dt + \frac{\partial f_\lambda}{\partial \mathbf{k}}\frac{d\mathbf{k}}{dt}dt - \mathcal{I}\left[f\right]_{coll} dt. \tag{5.6}$$

Reordering the equation and dividing through by dt we obtain

$$\frac{\partial f_\lambda}{\partial t} + \dot{\mathbf{r}}\frac{\partial f_\lambda}{\partial \mathbf{r}} + \dot{\mathbf{k}}\frac{\partial f_\lambda}{\partial \mathbf{k}} = \mathcal{I}\left[f_\lambda\right]_{coll}. \tag{5.7}$$

This is the Boltzmann equation. The time derivative of the position and wave vector are given by the semi-classical equations of motions as presented in Section 2.2.4. Let us for convenience present them here again. The semi classical equation of motions are given by

$$\dot{\mathbf{r}} = \frac{1}{\hbar}\frac{\partial \epsilon_{\lambda\mathbf{k}}}{\partial \mathbf{k}} - \dot{\mathbf{k}} \times \mathbf{\Omega}_\lambda, \tag{5.8}$$

$$\dot{\mathbf{k}} = -\frac{e}{\hbar}\left(\mathbf{E} + \dot{\mathbf{r}} \times \mathbf{B}\right), \tag{5.9}$$

where $\epsilon_{\lambda\mathbf{k}}$ is the energy, given by the dispersion relation, $\mathbf{\Omega}_\lambda$ is the Berry curvature, $\mathbf{E}$ is the applied electrical field and $\mathbf{B}$ the applied magnetic field. The presence of magnetic fields will however not be considered here, hence we set $\mathbf{B} = 0$ throughout the rest of this chapter.

The collision integral describes, as stated above, different collisions between electrons and impurities, phonons, or other electrons. In the hydrodynamic description, the electron-electron interactions are dominating. The collision integral for such two-body interactions is given by

$$\begin{aligned}\mathcal{I}\left[f_1\right]_{coll} = \frac{1}{\hbar}\sum_{n_2,n_3,n_4}\int\frac{d^2\mathbf{k}_2}{(2\pi)^2}\int\frac{d^2\mathbf{k}_3}{(2\pi)^2}\int\frac{d^2\mathbf{k}_4}{(2\pi)^2}\left|M_{12}^{34}\right|^2\delta(\mathbf{k}_1+\mathbf{k}_2-\mathbf{k}_3-\mathbf{k}_4)\\ \times\,\delta(\epsilon_1+\varepsilon_2-\varepsilon_3-\varepsilon_4)\left[f_1f_2(1-f_3)(1-f_4)-f_3f_4(1-f_1)(1-f_2)\right],\end{aligned} \tag{5.10}$$

where we have used a suppressed notation such that $f_i = f_{n_i\mathbf{k}_i}$. This describes the process of an electron of species n_1 and momentum $\mathbf{k}_1$ that interacts with an electron of species n_2 and momenta $\mathbf{k}_2$ and scatters into electrons of species n_3 and n_4 with momenta $\mathbf{k}_3$ and $\mathbf{k}_4$, respectively, and as well the reversed process. The probability for this process is given by the scattering amplitude M_{12}^{34}, which is determined by Fermi's golden rule [101].

5.3 Hydrodynamic equations

To obtain the hydrodynamic equations, one has to perform two steps. First, a set of continuity equations have to be obtained. After that, the quantities given by the continuity equations have to be related to measurable quantities, such as the current and temperature.

5.3.1 Particle number conservation

The first conserved quantity that we consider is the number of particles. The number of particles in a system is defined as the integral over the distribution function. Hence

$$N = \sum_{\lambda} \int \frac{d\mathbf{k}}{(2\pi)^2} f_{\lambda}(\mathbf{r}, \mathbf{k}, t). \tag{5.11}$$

To understand how the number of particles change over time, we differentiate with respect to it. Taking the time derivative of this equation and moving the derivative on the right hand side inside the integral sign we obtain the following

$$\frac{\partial N}{\partial t} = \sum_{\lambda} \int \frac{d\mathbf{k}}{(2\pi)^2} \frac{\partial f_{\lambda}}{\partial t} \tag{5.12}$$

Now one observes that the time derivative of the distribution function appears in the Boltzmann equation, Eq. (5.7). Hence, we re-write the time-derivative in terms of Eq. (5.7). This gives us

$$\frac{\partial N}{\partial t} = -\int \frac{d\mathbf{k}}{(2\pi)^2} \left[\dot{\mathbf{r}} \frac{\partial f_{\lambda}}{\partial \mathbf{r}} + \dot{\mathbf{k}} \frac{\partial f_{\lambda}}{\partial \mathbf{k}} - \mathcal{I}\left[f_{\lambda}\right]_{coll} \right] \tag{5.13}$$

Next, we perform the integration on the right-hand side. We consider each term separately. First, we note that the integration of the collision integral equals zero. This is a consequence of the fact that charge has to be conserved. The middle term inside the integral is

$$\sum_{\lambda} \int \frac{d\mathbf{k}}{(2\pi)^2} \dot{\mathbf{k}} \frac{\partial f_{\lambda}}{\partial \mathbf{k}} = 0. \tag{5.14}$$

This follows from the fact that the distribution function must go to zero as $|\mathbf{k}| \to \infty$, or in other words, there cannot exist any particles with an infinite momentum. The final integral defines the particle number current, i.e.,

$$\sum_{\lambda} \int \frac{d\mathbf{k}}{(2\pi)^2} \dot{\mathbf{r}} \frac{\partial f_{\lambda}}{\partial \mathbf{r}} = \frac{\partial}{\partial \mathbf{r}} \cdot \mathbf{J}_N, \tag{5.15}$$

where $\mathbf{J}_N = \sum_{\lambda} \int \frac{d\mathbf{k}}{(2\pi)^2} \dot{\mathbf{r}} f_{\lambda}(\mathbf{r}, \mathbf{k}, t)$. This gives us the first (normal) continuity equation

$$\frac{\partial N}{\partial t} + \frac{\partial}{\partial \mathbf{r}} \cdot \mathbf{J}_N = 0, \tag{5.16}$$

where $\mathbf{J}_N = \mathbf{J}_N^{(0)} + \mathbf{J}_N^{(a)}$ and

$$\mathbf{J}_N^{(0)} = \frac{1}{\hbar}\sum_\lambda \int \frac{d\mathbf{k}}{(2\pi)^2} \frac{\partial \epsilon_{\lambda\mathbf{k}}}{\partial \mathbf{k}} f_\lambda(\mathbf{r},\mathbf{k},t), \tag{5.17}$$

$$\tag{5.18}$$

$$\mathbf{J}_N^{(a)} = \frac{e}{\hbar}\sum_\lambda \int \frac{d\mathbf{k}}{(2\pi)^2} \left[\mathbf{E}\times\mathbf{\Omega}_\lambda\right] f_\lambda(\mathbf{r},\mathbf{k},t), \tag{5.19}$$

are the normal and anomalous currents respectively, defined through the semi-classical equations of motion. Note that the anomalous part of the current depends on the Berry curvature and hence can only be determined once the Hamiltonian has been defined. The electrical current is given by

$$\mathbf{J} = e\mathbf{J}_N. \tag{5.20}$$

Next we consider the conservation of energy.

5.3.2 Energy conservation

Like particle number, energy is a conserved quantity. As a next step, one looks for an equation for the energy density, N_ε. We define the energy density as

$$N_\varepsilon(\mathbf{r},t) = \sum_\lambda \int \frac{d\mathbf{k}}{(2\pi)^2} \epsilon_{\lambda\mathbf{k}} f(\mathbf{r},\mathbf{k},t). \tag{5.21}$$

Proceeding in the same manner as for the particle density, we take the time derivative of the energy density, move it inside the integral, and re-write the expression for the time derivative of the distribution function using Eq. (5.7). Noting that the energy does not depend on time we write

$$\frac{\partial}{\partial t}N_\epsilon(\mathbf{r},t) = -\sum_\lambda \int \frac{d\mathbf{k}}{(2\pi)^2} \epsilon_{\lambda\mathbf{k}} \left[\dot{\mathbf{r}}\frac{\partial f_\lambda}{\partial \mathbf{r}} + \dot{\mathbf{k}}\frac{\partial f_\lambda}{\partial \mathbf{k}} - \mathcal{I}\left[f_\lambda\right]_{coll}\right] \tag{5.22}$$

Similarly to the particle number the integral over the collision integral vanishes. Assuming that $\dot{\mathbf{r}}$ does not depend on $\mathbf{r}$, the integral over the first term on the right hand side results in

$$\sum_\lambda \int \frac{d\mathbf{k}}{(2\pi)^2} \epsilon_{\lambda\mathbf{k}} \dot{\mathbf{r}} \frac{\partial f_\lambda}{\partial \mathbf{r}} = \frac{\partial}{\partial \mathbf{r}} \sum_\lambda \int \frac{d\mathbf{k}}{(2\pi)^2} \epsilon_{\lambda\mathbf{k}} \dot{\mathbf{r}} f_\lambda(\mathbf{r},\mathbf{k},t) = \frac{\partial}{\partial \mathbf{r}} \cdot \mathbf{J}_\varepsilon, \tag{5.23}$$

where after the last equality we defined the energy current, $\mathbf{J}_\varepsilon = \sum_\lambda \int \frac{d\mathbf{k}}{(2\pi)^2} \epsilon_{\lambda\mathbf{k}} \dot{\mathbf{r}} f_\lambda(\mathbf{r},\mathbf{k},t)$. Just like the particle current the energy current has two contributions due to Eq. (5.8). Thus

$$\mathbf{J}_\varepsilon^{(0)} = \frac{1}{\hbar}\sum_\lambda \int \frac{d\mathbf{k}}{(2\pi)^2} \epsilon_{\lambda\mathbf{k}} \frac{\partial \epsilon_{\lambda\mathbf{k}}}{\partial \mathbf{k}} f_\lambda(\mathbf{r},\mathbf{k},t), \tag{5.24}$$

$$\mathbf{J}_{\varepsilon}^{(a)} = -\frac{e}{\hbar}\sum_{\lambda}\int \frac{d\mathbf{k}}{(2\pi)^2}\epsilon_{\lambda\mathbf{k}}\left[\mathbf{E}\times\mathbf{\Omega}_{\lambda}\right] f_{\lambda}(\mathbf{r},\mathbf{k},t). \tag{5.25}$$

For the second term of the right-hand side of Eq. (5.22) it is useful to directly apply Eq. (5.9). In absence of magnetic fields we then have that

$$\begin{aligned}\sum_{\lambda}\int \frac{d\mathbf{k}}{(2\pi)^2}\epsilon_{\lambda\mathbf{k}}\dot{\mathbf{k}}\frac{\partial f_{\lambda\mathbf{k}}}{\partial\mathbf{k}} &= \frac{e}{\hbar}\mathbf{E}\sum_{\lambda}\int \frac{d\mathbf{k}}{(2\pi)^2}\epsilon_{\lambda\mathbf{k}}\frac{\partial f_{\lambda\mathbf{k}}}{\partial\mathbf{k}} \\ &= -\frac{e}{\hbar}\mathbf{E}\sum_{\lambda}\int \frac{d\mathbf{k}}{(2\pi)^2}\frac{\partial\varepsilon_{\lambda\mathbf{k}}}{\partial\mathbf{k}} f_{\lambda\mathbf{k}} = -e\mathbf{E}\cdot\mathbf{J}_N^0. \end{aligned}\tag{5.26}$$

To obtain the second line we have performed an integration by parts. As before we have used that $f_{\lambda\mathbf{k}} \to 0$ as $|\mathbf{k}| \to \infty$. The normal current $\mathbf{J}_N^{(0)}$ is defined in Eq. (5.18). The above equations can now be collected to form the energy continuity equation

$$\frac{\partial}{\partial t}N_{\varepsilon} + \frac{\partial}{\partial\mathbf{r}}\cdot\mathbf{J}_{\varepsilon} = e\mathbf{E}\cdot\mathbf{J}_N^0 \tag{5.27}$$

5.3.3 Momentum conservation

We will finally consider the conservation of momentum. Proceeding in the same manner as for particle and energy conservation, we integrate the distribution function weighted by the momentum $\hbar\mathbf{k}$ and then apply the Boltzmann equation. Hence

$$\sum_{\lambda}\int \frac{d\mathbf{k}}{(2\pi)^2}\hbar\mathbf{k}\frac{\partial f_{\lambda\mathbf{k}}}{\partial t} = -\sum_{\lambda}\int \frac{d\mathbf{k}}{(2\pi)^2}\hbar\mathbf{k}\left[\dot{\mathbf{r}}\frac{\partial f_{\lambda}}{\partial\mathbf{r}} + \dot{\mathbf{k}}\frac{\partial f_{\lambda}}{\partial\mathbf{k}} - \mathcal{I}\left[f_{\lambda}\right]_{coll}\right] \tag{5.28}$$

First, we define the left-hand side as the momentum density

$$\sum_{\lambda}\int \frac{d\mathbf{k}}{(2\pi)^2}\hbar\mathbf{k}\frac{\partial f_{\lambda\mathbf{k}}}{\partial t} = \frac{\partial}{\partial t}\mathbf{n}_{\mathbf{k}}. \tag{5.29}$$

The integral over the collision integral is again zero. For the velocity component of Eq. (5.7) we consider each component on its own. We then have that

$$\hbar\sum_{\lambda}\int \frac{d\mathbf{k}}{(2\pi)^2}k_{\alpha}\dot{r}_{\beta}\frac{\partial f_{\lambda\mathbf{k}}}{\partial r_{\beta}} = \hbar\frac{\partial}{\partial r_{\beta}}\sum_{\lambda}\int \frac{d\mathbf{k}}{(2\pi)^2}k_{\alpha}\dot{r}_{\beta}f_{\lambda\mathbf{k}} = \frac{\partial}{\partial r_{\beta}}\Pi_{\alpha\beta}, \tag{5.30}$$

where $\Pi_{\alpha\beta} = \hbar\sum_{\lambda}\int\frac{d\mathbf{k}}{(2\pi)^2}k_{\alpha}\dot{r}_{\beta}f_{\lambda\mathbf{k}}$ is the momentum flux tensor. As seen before, the Berry curvature contributes an anomalous part. Hence, we have the normal and anomalous flux tensors that are respectively given by

$$\Pi_{\alpha\beta}^{(0)} = \sum_{\lambda}\int \frac{d\mathbf{k}}{(2\pi)^2}k_{\alpha}\left(\frac{\partial\varepsilon_{\lambda\mathbf{k}}}{\partial\mathbf{k}}\right)_{\beta} f_{\lambda}(\mathbf{r},\mathbf{k},t), \tag{5.31}$$

$$\Pi_{\alpha\beta}^{(a)} = \hbar\sum_{\lambda}\int \frac{d\mathbf{k}}{(2\pi)^2}k_{\alpha}\left[\mathbf{E}\times\mathbf{\Omega}_{\lambda}\right]_{\beta} f_{\lambda}(\mathbf{r},\mathbf{k},t), \tag{5.32}$$

Finally we consider the force term. As we are considering a system in absence of magnetic fields we have that

$$eE_\beta \sum_\lambda \int \frac{d\mathbf{k}}{(2\pi)^2} k^\alpha \frac{\partial f_{\lambda\mathbf{k}}}{\partial k_\beta} = -eE_\beta \sum_\lambda \int \frac{d\mathbf{k}}{(2\pi)^2} \frac{\partial k_\alpha}{\partial k_\beta} f_{\lambda\mathbf{k}} = -eE_\alpha N \tag{5.33}$$

where we in the first equality integrated by parts, and in the second have used that $\frac{\partial k_\alpha}{\partial k_\beta} = \delta_{\alpha\beta}$. Collecting the different terms we obtain the continuity equation for the momentum density:

$$\frac{\partial}{\partial t} n_{\mathbf{k},\alpha} + \frac{\partial}{\partial r_\beta} \Pi_{\alpha\beta} = eE_\alpha N \tag{5.34}$$

5.3.4 Continuity equations

To this end we have obtained a set of continuity equations, in the absence of magnetic fields. These three are:

$$\frac{\partial N}{\partial t} - \nabla_\mathbf{r} \cdot \mathbf{J}_N = 0 \tag{5.35}$$

$$\frac{\partial}{\partial t} N_\varepsilon + \nabla_\mathbf{r} \mathbf{J}_\varepsilon = e\mathbf{E} \cdot \mathbf{J}_N^0 \tag{5.36}$$

$$\frac{\partial}{\partial t} n_{\mathbf{k},\alpha} + \frac{\partial}{\partial r_\beta} \Pi_{\alpha\beta} = eE_\alpha N \tag{5.37}$$

Note that all quantities related to some flux have both a "normal" contribution and an anomalous contribution arising from the Berry curvature. These are defined in Eqs. (5.18) and (5.19) for the particle current, in Eqs. (5.24) and (5.25) for the energy current, and in Eqs. (5.31) and (5.32) for the momentum flux. To make use of these equations, we will write them in terms of macroscopic quantities of the system. We next define these.

Macroscopic quantities

To make any use of the derived equations, Eqs. (5.35) - (5.37), we have to relate them to the macroscopic quantities of our system. To advance on this we need to state the main assumption of hydrodynamic theory. This underlying assumption is that a local equilibrium is established by electron-electron collisions on length scales much smaller than the electron-electron mean free path, l_{ee}. Because of this one can define a local equilibrium function,

$$f^0_{\lambda\mathbf{k}}(\mathbf{r}) = \frac{1}{1 + e^{\beta[\epsilon_{\lambda\mathbf{k}} - \hbar\mathbf{u}(\mathbf{r})\cdot\mathbf{k} - \mu_\lambda(\mathbf{r})]}}. \tag{5.38}$$

Here $\mu_\lambda(\mathbf{r})$ is the local chemical potential and $\mathbf{u}(\mathbf{r})$ is the hydrodynamic velocity, more commonly known as the drift velocity, $\beta = 1/k_B T$ and λ denotes any quantum numbers such as band index, spin etc. The chemical potential will from here on be taken to be independent of position, i.e., $\mu_\lambda(\mathbf{r}) \equiv \mu$. The shape and dependence of the specific quantities is again a consequence of the H-theorem and the details are found in Appendix F. To relate the macroscopic quantities to the specific system, we must define the system we are interested in. Next, we define the Hamiltonian for an anomalous Hall insulator which has a non-vanishing Berry curvature. After that, we derive the Navier-Stokes equation for this type of material.

5.3.5 Navier-Stokes equitation for two dimensional anomalous Hall insulators

We will in this section derive the Navier-Stokes equations for an anomalous Hall insulator, using the previously derived continuity equations and the local distribution function. We first define the Hamiltonian and its properties. The Hamiltonian is described by a gapped 2D Dirac Hamiltonian [62],

$$H_{2D} = \hbar v_F \left(k_x\sigma_x + k_y\sigma_y\right) + \Delta\sigma_z, \tag{5.39}$$

where v_F is the Fermi velocity and 2Δ is the bandgap. The dispersion relation is given by

$$\varepsilon_{\mathbf{k},\pm} = \pm\sqrt{\hbar^2 v_F^2 \mathbf{k}^2 + \Delta^2}, \tag{5.40}$$

where $\mathbf{k} = (k_x, k_y)$. The Berry curvature is given by

$$\mathbf{\Omega}^{\pm} = \frac{v_F^2\hbar^2\Delta}{2(\varepsilon_{\mathbf{k},\pm})^3}. \tag{5.41}$$

Now, for this problem, we will assume that the Fermi level is placed inside the conduction band, and hence this is the only band we will take into account.

Continuity equations revisited

Let us now write the continuity equations in terms of the conserved quantities $\varepsilon_{\mathbf{k}}$, $\mathbf{u}$ and μ, given that the Fermi level is placed within the conduction band. For this the following relation will be important

$$\frac{\partial}{\partial\mathbf{k}}\ln\left[1+e^{-\beta(\varepsilon_{\mathbf{k}}-\hbar\mathbf{u}\cdot\mathbf{k}-\mu)}\right] = -\beta f_{\mathbf{k}}\frac{\partial}{\partial\mathbf{k}}\left(\varepsilon_{\mathbf{k}}-\hbar\mathbf{u}\cdot\mathbf{k}-\mu\right). \tag{5.42}$$

We now turn to the normal part of Eq. (5.35) and consider $\mathbf{J}^{(0)} - N\mathbf{u}$,

$$\begin{aligned}\mathbf{J}_N^{(0)} - N\mathbf{u} &= \int\frac{d\mathbf{k}}{(2\pi)^2}\left[\frac{1}{\hbar}\frac{\partial\epsilon_{\mathbf{k}}}{\partial\mathbf{k}} - \mathbf{u}\right]f_{\mathbf{k}} \\ &= \int\frac{d\mathbf{k}}{(2\pi)^2}\frac{1}{\hbar}\frac{\partial}{\partial\mathbf{k}}\left[\epsilon_{\mathbf{k}}-\hbar\mathbf{u}\cdot\mathbf{k}-\mu\right]f_{\mathbf{k}}\end{aligned} \tag{5.43}$$

Now we apply Eq. (5.42) and obtain

$$\frac{1}{\hbar}\int\frac{d\mathbf{k}}{(2\pi)^2}\frac{\partial}{\partial\mathbf{k}}\left[\epsilon_{\mathbf{k}}-\hbar\mathbf{u}\cdot\mathbf{k}-\mu_l\right]f_{\mathbf{k}} = -\frac{1}{\hbar\beta}\int\frac{d\mathbf{k}}{(2\pi)^2}\frac{\partial}{\partial\mathbf{k}}\ln\left[1+e^{-\beta(\varepsilon_{\mathbf{k}}-\mathbf{u}\cdot\mathbf{k}-\mu)}\right]$$

$$= 0. \tag{5.44}$$

Hence we have shown that $\mathbf{J}^{(0)} = N\mathbf{u}$, as one might have guessed. Next we look at the energy current. Just like for the particle current we similarly consider $\mathbf{J}_E^{(0)} - N_E\mathbf{u}$. We then have that

$$\begin{aligned}
\mathbf{J}_\varepsilon^{(0)} - N_\varepsilon \mathbf{u} &= \int \frac{d\mathbf{k}}{(2\pi)^2} \left[\frac{1}{\hbar} \varepsilon_{\mathbf{k}} \frac{\partial \varepsilon_{\mathbf{k}}}{\partial \mathbf{k}} - \varepsilon_{\mathbf{k}} \mathbf{u} \right] f_{\mathbf{k}} \\
&= \frac{1}{\hbar} \int \frac{d\mathbf{k}}{(2\pi)^2} \varepsilon_{\mathbf{k}} \frac{\partial}{\partial \mathbf{k}} \left[\epsilon_{\mathbf{k}} - \hbar \mathbf{u} \cdot \mathbf{k} - \mu_l \right] f_{\mathbf{k}} \\
&= \frac{1}{\hbar\beta} \int \frac{d\mathbf{k}}{(2\pi)^2} \frac{\partial \varepsilon_{\mathbf{k}}}{\partial \mathbf{k}} \ln \left[1 + e^{-\beta(\varepsilon_{\mathbf{k}} - \hbar \mathbf{u} \cdot \mathbf{k} - \mu)} \right] f_{\mathbf{k}} \\
&\quad - \frac{1}{\hbar\beta} \underbrace{\varepsilon_{\mathbf{k}} \ln \left[1 + e^{-\beta(\varepsilon_{\mathbf{k}} - \hbar \mathbf{u} \cdot \mathbf{k} - \mu)} \right] \Big|_{-\infty}^{\infty}}_{=0}
\end{aligned} \tag{5.45}$$

We extend the derivative of the energy like in the calculation of the normal current such that $\frac{\partial \varepsilon_{\mathbf{k}}}{\partial \mathbf{k}} = \frac{\partial}{\partial \mathbf{k}} \left(\varepsilon_{\mathbf{k}} + \hbar \mathbf{u} \cdot \mathbf{k} - \hbar \mathbf{u} \cdot \mathbf{k} - \mu \right)$. We then find that

$$\frac{1}{\hbar\beta} \int \frac{d\mathbf{k}}{(2\pi)^2} \frac{\partial \varepsilon_{\mathbf{k}}}{\partial \mathbf{k}} \ln \left[1 + e^{-\beta(\varepsilon_{\mathbf{k}} - \hbar \mathbf{u} \cdot \mathbf{k} - \mu)} \right] f_{\mathbf{k}} = \frac{\mathbf{u}}{\beta} \int \frac{d\mathbf{k}}{(2\pi)^2} \ln \left[1 + e^{-\beta(\varepsilon_{\mathbf{k}} - \hbar \mathbf{u} \cdot \mathbf{k} - \mu)} \right]. \tag{5.46}$$

This is the the pressure multiplied by the drift velocity [101]! Hence we have found that $\mathbf{J}_\varepsilon^{(0)} = (N_\varepsilon + P)\, \mathbf{u}$, where $P = \frac{1}{\beta} \int \frac{d\mathbf{k}}{(2\pi)^2} \ln \left[1 + e^{-\beta(\varepsilon_{\mathbf{k}} - \hbar \mathbf{u} \cdot \mathbf{k} - \mu)} \right]$. Furthermore, the enthalpy density is defined as $W = N_\varepsilon + P$. Thus $\mathbf{J}_\varepsilon^{(0)} = W\mathbf{u}$. Let us now investigate the momentum flux tensor. The velocity is given by $\frac{\partial \varepsilon_{\mathbf{k}}}{\partial \mathbf{k}} = \frac{\hbar^2 v_F^2 \mathbf{k}}{\sqrt{\hbar^2 v_F^2 \mathbf{k}^2 + \Delta^2}}$. Consider the energy current,

$$\mathbf{J}_\varepsilon^{(0)} = \frac{1}{\hbar} \int \frac{d\mathbf{k}}{(2\pi)^2} \varepsilon_{\mathbf{k}} \frac{\partial \varepsilon_{\mathbf{k}}}{\partial \mathbf{k}} f_{\mathbf{k}} = \frac{1}{\hbar} \int \frac{d\mathbf{k}}{(2\pi)^2} \frac{\hbar^2 v_F^2 \mathbf{k}}{\sqrt{\hbar^2 v_F^2 \mathbf{k}^2 + \Delta^2}} \sqrt{\hbar^2 v_F^2 \mathbf{k}^2 + \Delta^2} f_{\mathbf{k}} \tag{5.47}$$

$$= \hbar v_F^2 \int \frac{d\mathbf{k}}{(2\pi)^2} \mathbf{k} f_{\mathbf{k}} = v_F^2 n_{\mathbf{k}} \tag{5.48}$$

We can then write

$$n_{\mathbf{k}} = \frac{\mathbf{J}_\varepsilon^{(0)}}{v_F^2} = \frac{W}{v_F^2} \mathbf{u}. \tag{5.49}$$

We are now left with considering the normal part of the momentum flux tensor. Taking each component separately we have that

$$\begin{aligned}
\Pi_{xx}^{(0)} &= \int \frac{d\mathbf{k}}{(2\pi)^2} k_x \left(\frac{\partial \varepsilon_{\mathbf{k}}}{\partial \mathbf{k}} f_{\mathbf{k}} \right)_x \\
&= \int \frac{d\mathbf{k}}{(2\pi)^2} k_x \left(\frac{\partial}{\partial \mathbf{k}} \left[\varepsilon_{\mathbf{k}} - \hbar u_x k_x - \hbar u_y k_y - \mu + \hbar u_x k_x \right] \right)_x
\end{aligned}$$

$$
\begin{aligned}
&= \hbar u_x \int \frac{d\mathbf{k}}{(2\pi)^2} k_x f_{\mathbf{k}} - \frac{1}{\beta} \int \frac{d\mathbf{k}}{(2\pi)^2} k_x \left(\frac{\partial}{\partial \mathbf{k}} \ln \left[1 + e^{-\beta(\varepsilon_{\mathbf{k}} - \hbar \mathbf{u}\cdot\mathbf{k} - \mu)} \right] \right)_x \\
&= u_x n_{k_x} + \frac{1}{\beta} \int \frac{d\mathbf{k}}{(2\pi)^2} \ln \left[1 + e^{-\beta(\dots)} \right] - \frac{1}{\beta} \ln \left[1 + e^{-\beta(\dots)} \right] \\
&= P + \frac{W}{v_F^2} u_x u_x, \qquad (5.50)
\end{aligned}
$$

and

$$
\begin{aligned}
\Pi^{(0)}_{xy} &= \int \frac{d\mathbf{k}}{(2\pi)^2} k_x \left(\frac{\partial \varepsilon_{\mathbf{k}}}{\partial \mathbf{k}} f_{\mathbf{k}} \right)_y \\
&= \int \frac{d\mathbf{k}}{(2\pi)^2} k_x \left(\frac{\partial}{\partial \mathbf{k}} \left[\varepsilon_{\mathbf{k}} - \hbar u_x k_x - \hbar u_y k_y - \mu + \hbar u_y k_y \right] \right)_y \\
&= \hbar u_y \int \frac{d\mathbf{k}}{(2\pi)^2} k_x f_{\mathbf{k}} - \frac{1}{\beta} \int \frac{d\mathbf{k}}{(2\pi)^2} k_x \left(\frac{\partial}{\partial \mathbf{k}} \ln \left[1 + e^{-\beta(\varepsilon_{\mathbf{k}} - \hbar \mathbf{u}\cdot\mathbf{k} - \mu)} \right] \right)_y \\
&= u_y n_{k_x} \\
&= \frac{W}{v_F^2} u_x u_y \qquad (5.51)
\end{aligned}
$$

By symmetry, the other two components are given by

$$
\Pi^{(0)}_{yy} = \frac{W}{v_F^2} u_y u_y + P, \quad \Pi^{(0)}_{yx} = \frac{W}{v_F^2} u_y u_x. \qquad (5.52)
$$

Collecting the components we can write

$$
\Pi^{(0)}_{\alpha\beta} = P\delta_{\alpha\beta} + \frac{W}{v_F^2} u_\alpha u_\beta. \qquad (5.53)
$$

We now, following the terms of the equation for the momentum density, have to consider two terms. The first one is the time derivative of the momentum density $\frac{\partial}{\partial t} n_{\mathbf{k}}$. We have that

$$
\frac{\partial}{\partial t} n_{\mathbf{k}} = \frac{\partial}{\partial t} \left(\frac{W}{v_F^2} \mathbf{u} \right) = \frac{W}{v_F^2} \frac{\partial \mathbf{u}}{\partial t} + \frac{\mathbf{u}}{v_F^2} \frac{\partial W}{\partial t}. \qquad (5.54)
$$

Next we consider the gradient, with respect to position, of the normal momentum flux. This results in

$$
\nabla^{\beta}_{\mathbf{r}} \Pi^{(0)}_{\alpha\beta} = \nabla^{\beta}_{\mathbf{r}} \left(P\delta_{\alpha\beta} + \frac{W}{v_F^2} u_\alpha u_\beta \right) \quad = \nabla^{\alpha}_{\mathbf{r}} P + \frac{1}{v_F^2} \left[W \left(\mathbf{u} \cdot \nabla \right) u_\alpha + u_\alpha \nabla \left(W\mathbf{u} \right) \right] \qquad (5.55)
$$

With the above calculations, let us now restate the continuity equations. In terms of macroscopic quantities they are given by

$$
\frac{\partial}{\partial t} N = \nabla_{\mathbf{r}} \cdot \left(N\mathbf{u} + \mathbf{J}^{(a)}_N \right) \qquad (5.56)
$$

$$\frac{\partial}{\partial t}(W-P)+\nabla_{\mathbf{r}}\cdot\left(W\mathbf{u}+\mathbf{J}_{\varepsilon}^{(a)}\right)=e\mathbf{E}\cdot(N\mathbf{u}) \quad (5.57)$$

$$\frac{1}{v_F^2}\frac{\partial}{\partial t}(Wu_\alpha)+\nabla_{\mathbf{r}}^{\alpha}P+\frac{1}{v_F^2}\left[W(\mathbf{u}\cdot\nabla)u_\alpha+u_\alpha\nabla(W\mathbf{u})\right]+\nabla_{\mathbf{r}}^{\beta}\Pi_{\alpha\beta}^{(a)}=eNE_\alpha \quad (5.58)$$

Apart from the anomalous contributions due to the Berry curvature these equations can be seen to coincide with the ones for the dispersion in gapless graphene [115].

To make progress with the anomalous quantities we first linearize the distribution function such that [9]

$$f=f^0+\delta f, \quad (5.59)$$

where f^0 is the equilibrium distribution function for constant temperature and chemical potential and for $\mathbf{u}=0$, and

$$\delta f=\frac{\partial f^0}{\partial\epsilon}\left(\frac{\epsilon-\mu}{\beta}\delta\beta-\delta\mu-\hbar\mathbf{u}\cdot\mathbf{k}\right) \quad (5.60)$$

is a small perturbation that accounts for the system being out of equilibrium. Limiting the study to dynamics that are of linear order in $\mathbf{u}$, $\delta\beta$ and $\delta\mu$ can be assumed to be small and absorbed by the external electric field. It should furthermore be noted that $\delta\beta$ and $\delta\mu$ are even in $\mathbf{k}$ while the term $\mathbf{k}\cdot\mathbf{u}$ is odd in $\mathbf{k}$.

We will further make progress by considering linear response. To this end we note that the contribution from the anomalous velocity in the linear response regime to the continuity equations for the particle and energy current is zero. This is seen by defining the electric potential ϕ, through $-\nabla\phi=\mathbf{E}$. It then follows that $\nabla\cdot\mathbf{J}^a=0$ and $\nabla\cdot\mathbf{J}_\epsilon^a=0$ from that $\partial_x\partial_y\phi=\partial_y\partial_x\phi$ [150]. Because $\nabla\cdot\mathbf{J}^a$ and $\nabla\cdot\mathbf{J}_\epsilon^a$ are to leading order proportional to either $\phi\delta\beta$ or $\phi\delta\mu$, these are neglected since they are not captured well within the linear response treatment. The contribution from the Berry curvature will however show up in the anomalous part of the momentum flux tensor.

The drift velocity, $\mathbf{u}$ is proportional to $\mathbf{E}$ for small fields. For systems with broken time reversal symmetry, $\Pi_{\alpha\beta}^{(a)}=0$ to first order in $\mathbf{E}$. This is because $\mathbf{\Omega}$ is even in $\mathbf{k}$. Instead the anomalous part of the momentum flux tensor is of first order in $\mathbf{E}$ and $\mathbf{u}$. It can be written

$$\begin{aligned}\Pi_{\alpha\beta}^{(a)}&=e\hbar\int\frac{d\mathbf{k}}{(2\pi)^2}k_\alpha\varepsilon_{\beta\delta\gamma}E_\delta\Omega_\gamma\left(-\frac{\partial f^0}{\partial\epsilon}\right)\mathbf{k}\cdot\mathbf{u}\\&=-e\hbar u_\alpha\varepsilon_{\beta\delta\gamma}E_\alpha\int\frac{d\mathbf{k}}{(2\pi)^2}k_\alpha^2\Omega_\gamma\frac{\partial f^{(0)}}{\partial\epsilon}\\&=u_\alpha\varepsilon_{\beta\delta\gamma}E_\delta\mathcal{B}_\gamma,\end{aligned} \quad (5.61)$$

where

$$\mathcal{B}_\gamma=\mathcal{B}_{\alpha,\gamma}=-e\hbar\int\frac{d\mathbf{k}}{(2\pi)^2}k_\alpha^2\Omega_\gamma\left(-\frac{\partial f^0}{\partial\epsilon}\right) \quad (5.62)$$

From this we observe that $\mathcal{B}_\gamma$ depends on the Berry curvature around the Fermi surface. For the rotational symmetric, 2D system that is considered here, it is independent of the index α such that $\mathcal{B}_{x,\gamma} = \mathcal{B}_{y,\gamma}$. We now take the derivative of Eq. (5.61) with respect to $\mathbf{r}$ and obtain

$$\partial_\beta \Pi^{(a)}_{\alpha\beta} = \mathcal{B}_\gamma \varepsilon_{\beta\delta\gamma} \partial_\beta \left(u_\alpha E_\delta\right) = u_\alpha \left(\nabla \times \mathbf{E} \cdot \mathcal{B}\right) + \left(\mathbf{E} \times \cdot \nabla\right) u_\alpha. \tag{5.63}$$

We can now obtain the Euler equation for anomalous Hall materials by combining Eqs. (5.56), (5.57), (5.58) and Eq. (5.63). Assuming that the pressure gradient, ∇P, acts in the same way as the electric field [101] and hence absorbing it in the electric field, the Euler equation is written as

$$\partial_t \left(\rho \mathbf{u}\right) + \left[\rho \left(\mathbf{u} \cdot \nabla\right) \mathbf{u} + \mathbf{u} \nabla \left(\rho \mathbf{u}\right)\right] + \mathbf{u} \left(\nabla \times \mathbf{E} \cdot \mathcal{B}\right) + \left(\mathbf{E} \times \mathcal{B} \cdot \nabla\right) \mathbf{u} = eN\mathbf{E}, \tag{5.64}$$

where $\rho = W/v_F^2$ is the mass density, determined from Eq. (5.49), which we assume to be constant. We will now focus on the steady state, $\partial_t \mathbf{u} = 0$. Furthermore, for small drift velocities a good approximation is to consider that the fluid is incompressible, which is equivalent to $\nabla \cdot \mathbf{u} = 0$. We will furthermore add a phenomenological viscous term, η which accounts for the dissipative electron-electron interactions, [28, 132]. By such we obtain the Navier-Stokes equation (compare to Eq. (5.1)) for the electronic fluid including the contribution from the Berry curvature,

$$\rho \left(\mathbf{u} \cdot \nabla\right) \mathbf{u} + \left(\mathbf{E} \times \mathcal{B} \cdot \nabla\right) \mathbf{u} = eN\mathbf{E} + \eta \nabla^2 \mathbf{u} \tag{5.65}$$

We now continue studying different types of flow by studying how the derived Navier-Stokes equation behaves in different geometries.

5.4 Poiseuille flow

Let us now consider the simplest possible flow, Poiseuille flow. In this case we assume that the electrons can only move in one direction, specifically the x-direction, such that $u_y = 0$ and $u_x \equiv u_x(y)$, resulting from an applied electric field in the x -direction, $\mathbf{E} = E\hat{\mathbf{x}}$. Furthermore, for the 2D anomalous Hall material we have that $\mathcal{B} = \mathcal{B}\hat{\mathbf{z}}$. The Navier-Stokes equation, Eq. (5.65) can then be written as

$$-E_x \mathcal{B} \partial_y u_x = eNE_x + \eta \partial_y^2 u_x. \tag{5.66}$$

In this case the convective term equals zero because $\partial_x u_x = 0$, since u_x is only a function of y. By defining $\tilde{y} = y/w$, where w is the sample width, the equation is made dimensionless,

$$-b \partial_{\tilde{y}} \tilde{u}_x = 1 + \partial_{\tilde{y}}^2 \tilde{u}_x. \tag{5.67}$$

Here we have introduced

$$b = \frac{w \mathcal{B} E_x}{\eta}, \quad \frac{\tilde{u}_x}{u_0}, \quad u_0 = \frac{w^2 eNE_x}{\eta}. \tag{5.68}$$

No-slip boundary conditions are applied, i.e., $\tilde{u}_x(0) = \tilde{u}_x(1) = 0$. The differential equation then has the following solution

$$\tilde{u}_x(\tilde{y}) = \frac{e^{b(1-\tilde{y})} - e^b(1-\tilde{y}) - \tilde{y}}{b(1-e^b)}. \tag{5.69}$$

We confirm the result by taking $b \to 0$, implying that the Berry curvature becomes zero. In this case we obtain

$$\tilde{u} = \frac{\tilde{y}(1-\tilde{y})}{2}. \tag{5.70}$$

This describes the standard Poiseuille flow profile, i.e., a parabolic profile centered around the middle of the sample, $y = w/2$. However, the flow profile will deviate from the normal Poiseuille flow as the Berry curvature is increased. In this case, the Berry curvature will set how much the maximum of the flow profile deviates from the unperturbed profile.

Poiseuille flow can be observed in anomalous Hall materials if the magnitude of the viscous longitudinal current, $J_x = eNu_x$ (corresponding to the normal current $\mathbf{J}^{(0)}$) exceeds the Hall current, $J_y = \frac{e^2}{\hbar}\mathcal{C}E_x$ (corresponding to the anomalous current, $\mathbf{J}^{(a)}$), where $\mathcal{C} = \frac{1}{2\pi}\sum_{\pm}\int d^2\mathbf{k}\Omega^{\pm}f^0$ is the Berry flux. For the gapped Dirac system under consideration we set $\Delta = 100\,\mathrm{meV}$. The Fermi energy is placed at the bottom of the conduction band, i.e., $\mu = \Delta$. This ensures that any contributions from the chiral edge states in the gap is suppressed. The temperature is set to $T = 100\,\mathrm{K}$ which should put us in a regime where the electron-electron interactions are dominating. These parameters results in $N = 2\times 10^{10}\,\mathrm{cm}^{-2}$, $\frac{\mathcal{B}}{e} = 0.005\,\mathrm{fs/nm}^2$ and $\mathcal{C} = 0.47$. Note that the Chern numbers of a gapped Dirac system are $\pm 1/2$.

We plot the currents, J_x and J_y, the current profile and the maximum current position in Figs. 5.4 (a), (b) and (c) respectively. We first observe that the Hall current (blue curve of Fig. 5.4 (a)) shows a linear behavior proportional to the applied electric field. The longitudinal current shows a similar behavior but saturates for large E_x. It is important to note that the longitudinal current is larger than the Hall current for a small electric field, which is the condition for observing Poiseuille flow. The saturation of J_x can be understood by considering Eq. (5.66). If E_x becomes much larger than the viscosity, η, then u_x is essentially independent of E_x.

From Fig. 5.4 (b), it can be seen that there exists a window, which is proportional to the applied electric field, where the Berry curvature drastically modifies the profile of the Poiseuille flow. By varying E_x, we observe in Fig. 5.4 (c) that the maximum velocity does no longer occur at the middle of the sample. This asymmetric flow should be possible to be measured by, for example, scanning-probe microscopy [91].

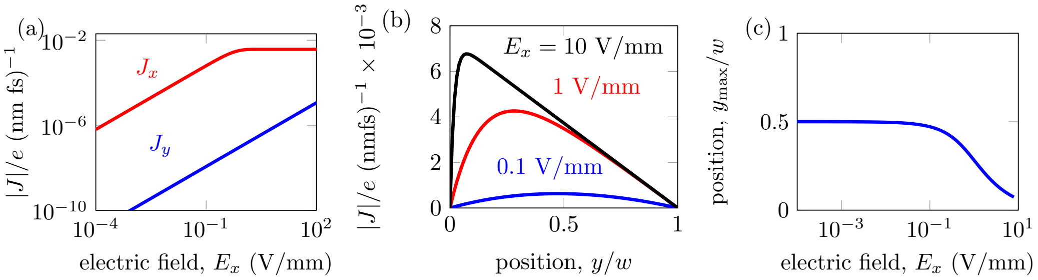

FIGURE 5.4: Poiseuille flow of a viscous anomalous Hall material. (a) The longitudinal current J_x (red) and the Hall current, J_y (blue) in the middle of the sample, $y = w/2$ and as function of the applied electric field, E_x. (b) Profile of the longitudinal current for different values of the applied electric field, E_x, indicated in the figure. (c) Position of the maximum of J_x as a function of E_x. For all figures we have used the Dirac model presented in Eq. (5.39) and the following parameters: $\Delta = 100\,\text{meV}$, $T = 100\,\text{K}$, $w = 1$¯m and $\eta = 6 \times 10^{-3}\hbar\text{N}$. The Fermi energy is fixed at the bottom of the conduction band, $\mu = \Delta$.

5.5 Berry curvature and vorticity

We now consider the vorticity that is induced by the Berry curvature. The vorticity is defined as

$$\boldsymbol{\omega} = \nabla \times \mathbf{u}. \tag{5.71}$$

For a 2D system confined in the $x - y$ plane the vorticity is naturally written $\boldsymbol{\omega} = \omega\hat{\mathbf{z}}$. We take the curl of the Navier-Stokes equation, Eq. (5.65). We then obtain that

$$\left(\mathbf{E} \times \mathcal{B} \cdot \nabla\right) \omega = \eta \nabla^2 \omega. \tag{5.72}$$

From the equation, it is seen that the Berry curvature has a direct impact on the vorticity. However, non-zero vorticity does not imply that there exist whirlpools. An example of this is laminar flow in a pipe. The particles travel along the axis of the pipe, with a flow that is largest in the middle of the pipe and almost stationary at the walls. This creates a vorticity that is zero in the middle of the pipe and reaches its maximum at the walls. Furthermore, previous work has directly proved that the viscous electron fluids in a semi-infinite 2D system have non-zero vorticity, but still, whirlpools are absent [128, 51]. On the other hand, when whirlpools are present, these arise due to the backflow create by the boundaries of a finite geometry. Next, we will show that this is not the case in the presence of Berry curvature, which induces whirlpools even for the semi-infinite geometry.

5.6 Electron hydrodynamics in semi-infinite half plane

We now consider the Navier-Stokes equation on a 2D semi-infinite half plane. The geometry is depicted in Fig. 5.5 (a). A current is is injected at the origin. Assuming

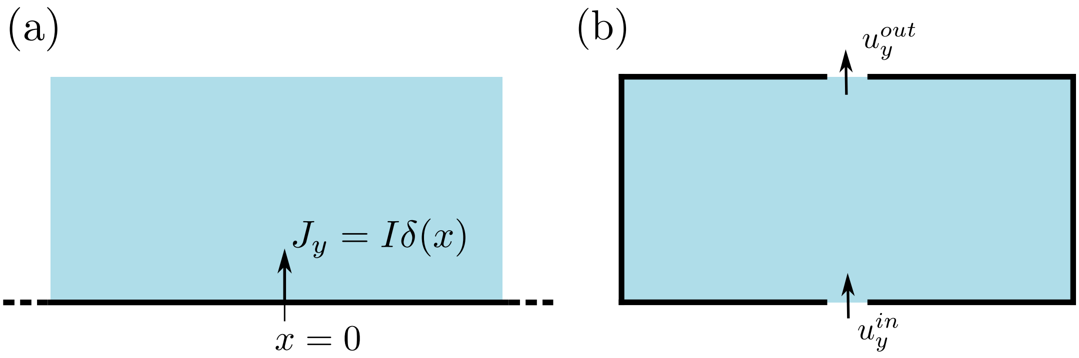

FIGURE 5.5: Set-ups in which the hydrodynamic equations are considered. (a) Semi-infinite half plane. A current density $J_y = I\delta(x)$ is applied at $x = y = 0$ which serves as the inlet point. The inlet point is considered infinitesimal. (b) Finite sample with a width of 2D and height of 1D, where $D = \sqrt{\nu\tau}$ is defined in Eq. (5.74). The sample has a finite inlet and outlet width.

small Reynolds numbers[2] or equivalently small flow velocities the convective term, $(\mathbf{u} \cdot \nabla)\,\mathbf{u}$ as well as the Hall current can be neglected. We now divide both sides of the equation by the mass density, mN, and introduce a term, $\mathbf{u}/\tau$, that accounts for electron-phonon or electron-impurity scattering, where τ is the relaxation time of these processes. The Navier-Stokes equation, Eq. (5.65) is then written as

$$\frac{1}{mN}\left(-\nabla\phi \times \mathcal{B} \cdot \nabla\right)\mathbf{u} = -\frac{e}{m}\nabla\phi + \nu\nabla^2\mathbf{u} - \frac{1}{\tau}\mathbf{u}, \tag{5.73}$$

where $\nu = \eta/\rho = \eta/(mN)$ is the kinematic viscosity. By introducing the term $\mathbf{u}/\tau$, the diffusion length,

$$D = \sqrt{\nu\tau}, \tag{5.74}$$

is defined. We now consider an applied current at the origin such that $J_y = I\delta(\mathbf{r})$. We define the following, dimensionless, quantities

$$\tilde{\phi} = \frac{\phi}{\phi_0}, \tag{5.75}$$

$$\phi_0 = \frac{Im}{e^2 N\tau}, \tag{5.76}$$

$$\tilde{u} = \frac{u}{u_0}, \tag{5.77}$$

$$u_0 = \frac{I}{eDN}, \tag{5.78}$$

$$(\tilde{x}, \tilde{y}) = \left(\frac{x}{D}, \frac{y}{D}\right), \tag{5.79}$$

$$\mathcal{K} = \frac{I\Delta^2 b(\mu, T)}{eD^2N^2hv^2k_BT} \tag{5.80}$$

---

[2] The Reynolds number is defined as $\mathrm{Re} = \frac{uL}{\nu}$, where u is the flow velocity, L is a characteristic linear dimension and $\nu = \eta/(mN)$ is the kinematic viscosity.

where we have used that $\mathcal{B} = \mathcal{B}\hat{\mathbf{z}}$, $\mathcal{B}_z = e\Delta^2 b(\mu, T)/hv^2 k_B T$ and

$$b(\tilde{\mu}, \tilde{T}) = \frac{1}{4}\int_1^\infty dx \left(1 - \frac{1}{x}\right) \frac{e^{(x-\tilde{\mu})/\tilde{T}}}{\left(1 + e^{(x-\tilde{\mu})/\tilde{T}}\right)^2}, \tag{5.81}$$

where $\tilde{\mu} = \mu/\Delta$ and $\tilde{T} = k_B T/\Delta$. Equation (5.73) can now be written as

$$-\mathcal{K}\left(\tilde{\nabla}\tilde{\phi} \times \hat{\mathbf{z}} \cdot \tilde{\nabla}\right)\tilde{\mathbf{u}} = -\tilde{\nabla}\tilde{\phi} + \tilde{\nabla}^2\tilde{\mathbf{u}} - \tilde{\mathbf{u}}. \tag{5.82}$$

This Navier-Stokes equation is a non-linear equation due to the coupling between the potential and flow velocity (terms on the left hand side of the equation). We will first treat this equation perturbatively in the coupling constant $\mathcal{K}$. To this end we linearize the equation by introducing

$$\tilde{\mathbf{u}} = \tilde{\mathbf{u}}^0 + \mathcal{K}\delta\tilde{\mathbf{u}}, \quad \tilde{\phi} = \tilde{\phi}^0 + \mathcal{K}\delta\tilde{\phi}. \tag{5.83}$$

Inserting this into Eq. (5.82) and comparing terms we obtain that

$$-\tilde{\nabla}\tilde{\phi}^{(0)} + \tilde{\nabla}^2\tilde{\mathbf{u}}^{(0)} - \tilde{\mathbf{u}}^{(0)} = 0, \tag{5.84}$$

$$-\tilde{\nabla}\delta\tilde{\phi} + \tilde{\nabla}^2\delta\tilde{\mathbf{u}} - \delta\tilde{\mathbf{u}} = -\left(\tilde{\nabla}\tilde{\phi}^{(0)} \times \hat{\mathbf{z}} \cdot \tilde{\nabla}\right)\tilde{\mathbf{u}}^{(0)}. \tag{5.85}$$

The Laplace equation for the unperturbed solution is given by

$$\tilde{\nabla}^2\tilde{\phi}^{(0)} = 0, \tag{5.86}$$

which follows from the incompressibility condition $\tilde{\nabla} \cdot \tilde{\mathbf{u}} = 0$. The perturbation on the other hand satisfies

$$\tilde{\nabla}^2\delta\tilde{\phi} \neq 0, \tag{5.87}$$

due to the right hand side of Eq. (5.85). This implies that the Berry curvature induces a charge in the system. As we come to the solution of the equations we will see that, as a consequence of Eq. (5.85), $\delta\tilde{\nabla}\tilde{\phi}$ displays an electric dipole. This is due to the coupling between the electric field and the flow velocity created by the Berry curvature (see inset of Fig. 5.8 (b)).

To find the solutions of Eqs. (5.84) and (5.85) we make use of the fact that the system is translational invariant along the x-direction. Hence we can perform a Fourier transform. This gives us that

$$\tilde{\mathbf{u}} = \int dk\, \tilde{\mathbf{u}}_k(y)e^{ikx}, \quad \tilde{\phi} = \int dk\, \tilde{\phi}_k(y)e^{ikx}. \tag{5.88}$$

The general boundary conditions, along the edge $\tilde{y} = 0$ are given by

$$\left(\partial_{\tilde{y}}\tilde{u}_{\tilde{x}}^{(0)} + \partial_{\tilde{x}}\tilde{u}_{\tilde{y}}^{(0)}\right)\Big|_{\tilde{y}=0} = \frac{1}{l_b}\tilde{u}_{\tilde{x}}^0(\tilde{y} = 0), \tag{5.89}$$

$$\delta\tilde{\mathbf{u}} = 0, \tag{5.90}$$

where no slip boundary conditions correspond to $l_b = 0$ and $l_b \to \infty$ results in no-stress boundary conditions. Using that the derivative under a Fourier transform transforms as $\partial_{\tilde{x}} \to ik$, the first boundary condition is in Fourier space written as

$$\left(\partial_{\tilde{y}}\tilde{u}_{\tilde{x}}^{(0)} + ik\tilde{u}_{\tilde{y}}^{(0)}\right)\Big|_{\tilde{y}} = \frac{1}{l_b}\tilde{u}_x^0(\tilde{y}=0), \tag{5.91}$$

while the second condition remains zero. The flow at the inlet, due to the injected current is given by the following boundary conditions:

$$\tilde{u}_{\tilde{x}}^{(0)}(\tilde{y}=0) = 0, \quad \tilde{u}_{\tilde{y}}^{(0)}(\tilde{y}=0) = \delta(x). \tag{5.92}$$

Hence the injected current is directed along the y axis. In Fourier space this simply becomes

$$\tilde{u}_{\tilde{x}}^{(0)}(\tilde{y}=0) = 0, \quad \tilde{u}_{k,\tilde{y}}^{(0)}(\tilde{y}=0) = 1, \tag{5.93}$$

Naturally the solution must furthermore vanish as $\tilde{y} \to \infty$. This is inscribed in the following boundary conditions:

$$\tilde{u}_{\tilde{x}}^{(0)}(\tilde{y}=\infty) = 0, \quad \tilde{u}_{\tilde{y}}^{(0)}(\tilde{y}=\infty) = 0, \tag{5.94}$$

We now first solve Eq. (5.84). Writing in on component form we have that

$$\begin{pmatrix} ik\tilde{\phi}_k^{(0)} \\ \partial_{\tilde{y}}\tilde{\phi}_k^0 \end{pmatrix} = (k^2 - \partial_{\tilde{y}}^2 + 1)\begin{pmatrix} \tilde{u}_{k,\tilde{x}}^{(0)} \\ \tilde{u}_{k,\tilde{y}}^{(0)} \end{pmatrix} \tag{5.95}$$

Using the incompressibility condition, $\tilde{\nabla} \cdot \tilde{\mathbf{u}} = 0$ we can now write

$$\partial_{\tilde{y}}\begin{pmatrix} k\tilde{u}_{k,\tilde{x}} \\ k\tilde{u}_{k,\tilde{y}} \\ \partial_{\tilde{y}}\tilde{u}_{k,\tilde{x}} \\ k^2\tilde{\phi}^{(0)} \end{pmatrix} = k\underbrace{\begin{pmatrix} 0 & 0 & 1 & 0 \\ -i & 0 & 0 & 0 \\ \frac{q^2}{k^2} & 0 & 0 & \frac{i}{k^2} \\ 0 & -q^2 & -ik^2 & 0 \end{pmatrix}}_{M}\begin{pmatrix} k\tilde{u}_{k,\tilde{x}} \\ k\tilde{u}_{k,\tilde{y}} \\ \partial_{\tilde{y}}\tilde{u}_{k,\tilde{x}} \\ k^2\tilde{\phi}^{(0)}, \end{pmatrix} \tag{5.96}$$

where $q = \sqrt{1+k^2}$. To solve this system of equations we first find the eigenvalues of M. These are given by

$$\lambda_{1,2} = \mp 1, \quad \lambda_{3,4} = \frac{\mp q}{|k|}. \tag{5.97}$$

The corresponding eigenvectors are given by

$$v_1 = \begin{pmatrix} -i \\ 1 \\ i \\ 1 \end{pmatrix}, \quad v_2 = \begin{pmatrix} -i \\ -1 \\ -i \\ 1 \end{pmatrix}, \quad v_3 = \begin{pmatrix} -\frac{|k|}{q} \\ -i\frac{k^2}{q^2} \\ 1 \\ 0 \end{pmatrix}, \quad v_4 = \begin{pmatrix} \frac{|k|}{q} \\ -i\frac{k^2}{q^2} \\ 1 \\ 0 \end{pmatrix} \tag{5.98}$$

The solution to the system of equations, Eq. (5.96) is given by linear combinations on the form

$$\begin{pmatrix} k\tilde{u}_{k,\tilde{x}} \\ k\tilde{u}_{k,\tilde{y}} \\ \partial_{\tilde{y}}\tilde{u}_{k,\tilde{x}} \\ k^2\tilde{\phi}^{(0)} \end{pmatrix} = \sum_{i=1}^{4} a_i v_i e^{\lambda_i k \tilde{y}}, \tag{5.99}$$

where a_i are coefficients to be determined by the boundary conditions. As the solution has to decay as $\tilde{y} \to \infty$, according to Eq. (5.94), we have to select different signs for k such that this is satisfied by the solutions to the equation system. For $\lambda_{1,3}$ we then select $k \geq 0$ and $k < 0$ for $\lambda_{2,4}$. The solution is now reduced to

$$\begin{pmatrix} k\tilde{u}_{k,\tilde{x}} \\ k\tilde{u}_{k,\tilde{y}} \\ \partial_{\tilde{y}}\tilde{u}_{k,\tilde{x}} \\ k^2\tilde{\phi}^{(0)} \end{pmatrix} = \begin{cases} a_1 v_1 e^{-k\tilde{y}} + a_3 v_3 e^{-q\tilde{y}}, & k \geq 0, \\ a_2 v_2 e^{k\tilde{y}} + a_4 v_4 e^{-q\tilde{y}}, & k < 0. \end{cases} \tag{5.100}$$

Using the boundary conditions we then obtain, for $k \geq 0$,

$$a_1 = -k\frac{kl_b(k^2+q^2)+q|k|}{k(k+k^2l_b-q^2l_b)-q|k|}, \quad a_3 = ikq^2\frac{(1+2kl_b)}{k(k+k^2l_b-q^2l_b)-q|k|}. \tag{5.101}$$

In the same way we obtain, for $k < 0$,

$$a_2 = k\frac{kl_b(k^2+q^2)-q|k|}{k(-k+k^2l_b-q^2l_b)+q|k|} \quad a_4 = ikq^2\frac{(2kl_b-1)}{k(-k+k^2l_b-q^2l_b)+q|k|}. \tag{5.102}$$

The solutions to the unperturbed system is then given by

$$\tilde{u}^{(0)}_{k,x} = \frac{ik}{|k|}\left[\frac{l_b(k^2+q^2)+q|k|}{|k|-q+(k^2-q^2)l_b}e^{-|k|\tilde{y}} - \frac{q(1+2|k|l_b)}{|k|-q+(k^2-q^2)l_b}e^{q\tilde{y}}\right], \tag{5.103}$$

$$\tilde{u}^{(0)}_{k,x} = -\left[\frac{l_b(k^2+q^2)+q|k|}{|k|-q+(k^2-q^2)l_b}e^{-|k|\tilde{y}} - \frac{|k|(1+2|k|l_b)}{|k|-q+(k^2-q^2)l_b}e^{q\tilde{y}}\right], \tag{5.104}$$

$$\tilde{\phi}^{(0)} = -\frac{1}{|k|}\left[\frac{(k^2+q^2)l_b+q}{|k|-q(k^2-q^2)l_b}e^{-|k|\tilde{y}}\right]. \tag{5.105}$$

As we are mainly interested in no-slip boundary conditions we let $l_b \to 0$. The solutions are then reduced to

$$\tilde{u}^{(0)}_{k,x} = \frac{ikq}{|k|(|k|-q)}\left[e^{-|k|\tilde{y}} - e^{-q\tilde{y}}\right], \tag{5.106}$$

$$\tilde{u}^{(0)}_{k,x} = -\frac{1}{|k|-q}\left[qe^{-|k|\tilde{y}} - |k|e^{q\tilde{y}}\right], \tag{5.107}$$

$$\tilde{\phi}^{(0)} = -\frac{1}{|k|}\frac{q}{|k|-q}e^{-|k|\tilde{y}}. \tag{5.108}$$

These solutions have previously been calculated in [128]. We now turn to the perturbation, Eq. (5.85). The homogeneous part of the equation looks the same as the unperturbed one, Eq. (5.84), except from that it satisfies slightly different boundary conditions, Eq. (5.90). The full solution is that of the homogeneous solution plus the particular solution, $\delta\tilde{u}_{k,\tilde{x}} = \delta\tilde{u}^h_{k,\tilde{x}} + \delta\tilde{u}^p_{k,\tilde{x}}$ and $\delta\tilde{\phi}_k = \delta\tilde{\phi}^h_k + \delta\tilde{\phi}^p_k$. The general solution is given by

$$\delta\tilde{u}_{k,\tilde{x}}(\tilde{y}) = -\frac{ia_1}{k}e^{-|k|\tilde{y}} - \frac{a_3}{q}e^{-q\tilde{y}} + \delta\tilde{u}^p_{k,\tilde{x}}e^{-(q+|k|)\tilde{y}} \tag{5.109}$$

$$\delta\tilde{u}_{k,\tilde{y}}(\tilde{y}) = \frac{a_1}{|k|}e^{-|k|\tilde{y}} - \frac{ia_3k}{q^2}e^{-q\tilde{y}} + \delta\tilde{u}^p_{k,\tilde{y}}e^{-(q+|k|)\tilde{y}} \tag{5.110}$$

$$\delta\tilde{\phi}_k(\tilde{y}) = \frac{a_1}{k^2}e^{-|k|\tilde{y}} + \delta\tilde{\phi}^p_k e^{-(q+|k|)\tilde{y}}, \tag{5.111}$$

where

$$\delta\tilde{u}^p_{k,\tilde{x}} = \frac{q^3 + 2q^2|k| - |k|^3}{(q-|k|)\left[5k^2q + +2|k|(k^2+q^2)\right]} \tag{5.112}$$

$$\delta\tilde{u}^p_{k,\tilde{y}} = \frac{ik}{|k|+q}\frac{q^3 + 2q^2|k| - |k|^3}{(q-|k|)\left[5k^2q + +2|k|(k^2+q^2)\right]} \tag{5.113}$$

$$\delta\tilde{\phi}^p_k = \frac{ik|k|}{q^2 + q|k| - 2k^2}, \tag{5.114}$$

where $\delta\tilde{u}^p_{k,\tilde{y}}$ was obtained by using $\tilde{\nabla}\cdot\tilde{\mathbf{u}} = 0$. The boundary conditions, Eq. (5.90) gives the coefficients a_1 and a_3,

$$a_1 = -\frac{ik^3(k^2 - q^2 - q|k|)}{(q-|k|)^2\left[5k^2q + 2|k|(k^2+q^2)\right]} \tag{5.115}$$

$$a_3 = -\frac{q^3(k^2 - q^2 - q|k|)}{(q-|k|)^2\left[5k^2q + 2|k|(k^2+q^2)\right]}. \tag{5.116}$$

The fact that a_1 and a_3 are antisymmetric and symmetric in $\mathbf{k}$ respectively, implies that $\delta\tilde{\mathbf{u}}_{k,\tilde{x}}$ is symmetric in $\mathbf{k}$ and that $\delta\tilde{\mathbf{u}}_{k,\tilde{y}}$ and $\delta\tilde{\phi}_k$ are antisymmetric in $\mathbf{k}$. The unperturbed functions on the other hand have the opposite symmetry. A consequence of the symmetries will become clear in the next passage.

The solutions due to the perturbation are now combined with the unperturbed ones. By performing an inverse Fourier transform numerically, we obtain the solutions in real space. The solutions, for $\mathcal{K} = 1$, are depicted in Figs. 5.6 and 5.7. We first note that the solutions inherit the symmetry from the Fourier components. Hence as observed $\tilde{u}^{(0)}_{\tilde{x}}$ and $\tilde{u}^{(0)}_{\tilde{y}}$ are asymmetric and symmetric in $\tilde{x}$ respectively. In the same way are $\delta\tilde{u}_{\tilde{x}}$ symmetric and $\delta\tilde{u}_{\tilde{y}}$ asymmetric in $\tilde{x}$. A consequence of this is a constructive and destructive interference causing an asymmetric flow structure in the full solution, $\tilde{\mathbf{u}}$. The perturbation, $\delta\tilde{\mathbf{u}}$, strongly modifies the flow at the inlet whereas far from the inlet the unperturbed solution is dominating. An important feature to note is the negative flow velocities in the y direction, occurring near the inlet. This is due to the vorticity created by the Berry curvature, causing a non-trivial backflow.

We investigate the flow profile further by looking at the streamlines of $\tilde{\mathbf{u}}$. These

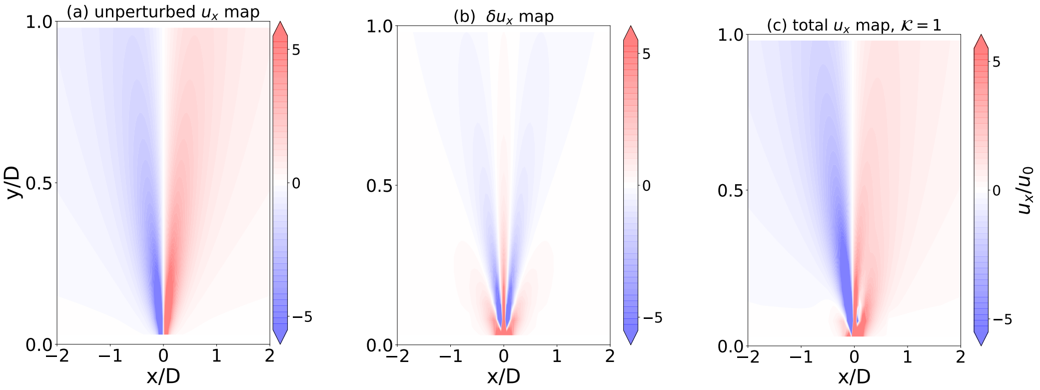

FIGURE 5.6: Colormap of the $\tilde{x}$ component of $\tilde{\mathbf{u}}$. (a) The unperturbed solution, $\tilde{u}_{\tilde{x}}^{(0)}$, (b) the $\tilde{x}$ component correction due to the perturbation, $\delta\tilde{u}_{\tilde{x}}$ and (c) the $\tilde{x}$ component of the total solution $\tilde{u}_{\tilde{x}}$. The perturbation strength $\mathcal{K} = 1$.

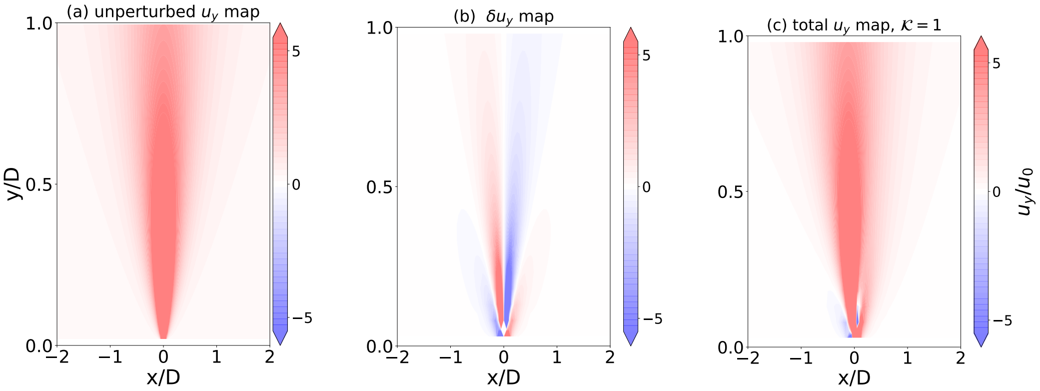

FIGURE 5.7: Colormap of the $\tilde{y}$ component of $\tilde{\mathbf{u}}$. (a) The unperturbed solution, $\tilde{u}_{\tilde{y}}^{(0)}$, (b) the $\tilde{y}$ component correction due to the perturbation, $\delta\tilde{u}_{\tilde{y}}$ and (c) the $\tilde{y}$ component of the total solution $\tilde{u}_{\tilde{y}}$. The perturbation strength $\mathcal{K} = 1$.

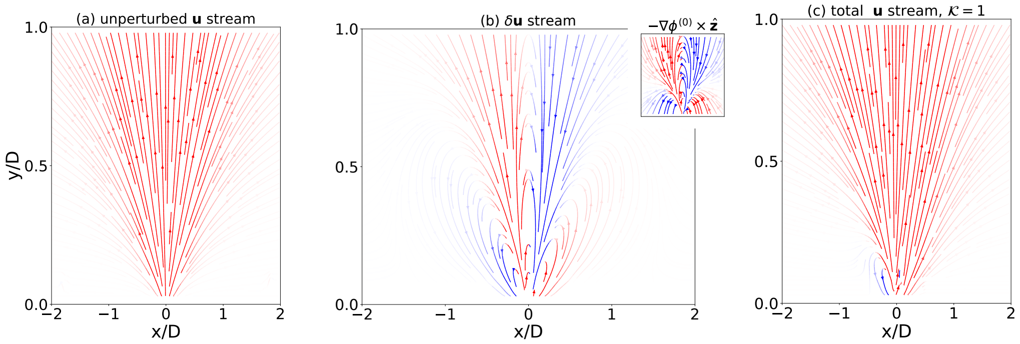

FIGURE 5.8: Stream lines for the hydrodynamic flow for (a) the unperturbed solution, $\tilde{\mathbf{u}}^{(0)}$, for (b) the correction, $\delta\tilde{\mathbf{u}}$ and for (c) the total solution $\tilde{\mathbf{u}}$. The perturbation strength $\mathcal{K} = 1$. The inset of inset of (b) shows the stream lines of $-\tilde{\nabla}\tilde{\phi}^{(0)} \times \hat{\mathbf{z}}$. The scale of the axes are the same as figures.

are plotted in Fig. 5.8. The color-coding follows the amplitude of $\tilde{u}_{\tilde{y}}$ such that red and blur color denote a positive and negative flow in the y direction, respectively. The unperturbed solution shows a positive flow away from the inlet throughout the sample, as expected [51]. As we move away from $\tilde{x} = 0$, the amplitude drops and becomes a tenth of the streamlines in the middle of the sample. We observe no whirlpools, however the vorticity, $\omega = \tilde{\nabla} \times \tilde{\mathbf{u}}^{(0)}$ is non-zero as can be understood from the curving streamlines, and furthermore changes sign around $\tilde{x} = 0$. The flow pattern of $\delta\tilde{\mathbf{u}}$ is much more complicated compared to the unperturbed flow. Going from the right to the left, we note from Fig. 5.8 (b) that the vorticity changes sign from positive to negative then back to positive. This flow pattern is related to the coupling between the Berry curvature and the electric field, as is depicted in the inset. It should be noted that the profile of $-\tilde{\nabla}\tilde{\phi} \times \hat{\mathbf{z}}$ does not strongly depend on the boundary conditions and will persist even for no-stress boundary conditions. The stream plot of the full solution is shown in Fig. 5.8 (c).

Similar to the previous analysis, we note that the streamlines are close to those of the unperturbed solutions far from the inlet. On the other hand, the flow is asymmetric close to the inlet. As seen, a whirlpool is created due to the perturbation. Compared to whirlpools created by boundaries, the size of the whirlpool due to the Berry curvature, which is governed by the diffusion length, will differ from the whirlpools due to the sample boundaries.

In an experimental set-up, the Berry curvature and the applied current might be small. This results in small $\mathcal{K}$'s, which in turn will lead to small whirlpools and might be challenging to measure in an experimental set-up. However, to observe the effects of the Berry curvature in electron hydrodynamics, utilizing the potential profile might result in higher success since it is more sensitive to the Berry curvature, as will be seen below.

We first focus on the potential profile of the unperturbed system. It is depicted in Fig. 5.9 (a). The result reproduces the results obtained in [128, 51]. The potential

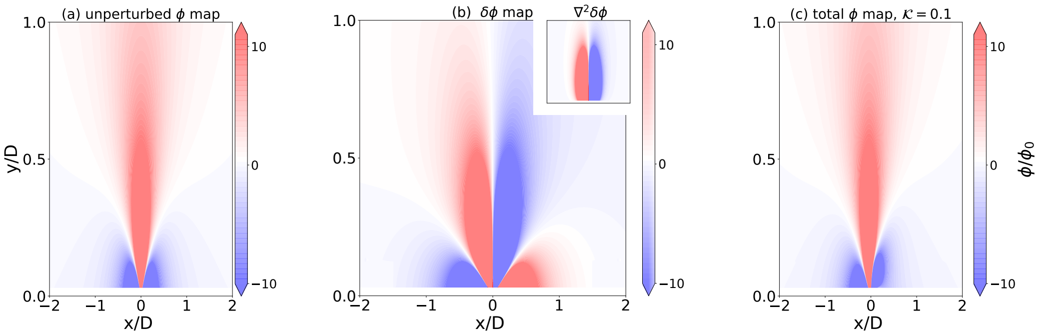

FIGURE 5.9: Colormap of the potential profile for (a) the unperturbed solution, $\tilde{\phi}^{(0)}$, (b) the correction, $\delta\tilde{\phi}$, due to the perturbation and (c) the full solution $\tilde{\phi}$ for $\mathcal{K} = 0.1$. The inset shows the Laplacian of the correction, $\tilde{\nabla}^2\tilde{\phi}$ with the axes the same as the main figure.

show a change of sign along the x-axis. As explained in the introduction, this is the hallmark of viscous flow that leads to a negative non-local resistance even without a backflow. Compared to the unperturbed solution, the perturbed one, depicted in Fig. 5.9 (b) changes sign multiple times. The asymmetry that is observed here is due to the dipole moment that the Berry curvature creates. This is readily shown in the plot of $\nabla^2\phi$ which is depicted in the inset of Fig. 5.9 (b).

Due to the imposed current profile, $\tilde{u}_{\tilde{y}}(0,0) = \delta(\tilde{x})$, both the unperturbed and perturbed potential profile diverge at the origin. Both the singularity and asymmetry of $\delta\tilde{\phi}$ can be seen to have a strong impact on the total potential close to the origin, and similarly, as for the velocity flow, the perturbation has only a minimal impact far away it, and the potential profile here resembles that of the unperturbed one. To observe the differences between the unperturbed and perturbed system more clearly, we scan the potential profile along the $\tilde{x}$-axis and fix $\tilde{y} = 0.03D$. The results are shown in Fig. 5.10 (a). The blue and red curves show the unperturbed and the perturbed potential profile, respectively. The maximum value of the perturbed potential profile is significantly larger than the unperturbed one. Furthermore, in contrast to the unperturbed potential profile, the perturbed one changes sign at $\tilde{x} = 0$. From the definition of the non-local resistance, Eq. (5.3), we write

$$R_{nl}(\tilde{x}) = \frac{\tilde{\phi}(\tilde{x}) - \tilde{\phi}(0)}{I}. \tag{5.117}$$

This is plotted in Fig. 5.10 (b). The non-local resistance of the unperturbed system (blue curve) remains negative as we sweep along the $\tilde{x}$ axis. The perturbed system, on the other hand, takes on both positive and negative values. The results from the perturbative analysis only hold in the case when the inlet current takes the shape of a delta function. However, the features of ϕ and R_{nl} are qualitatively not expected to change when a finite inlet width is considered.

To validate the analytical results, we also study the equations numerically. We apply the finite element method. This method is introduced in the next section,

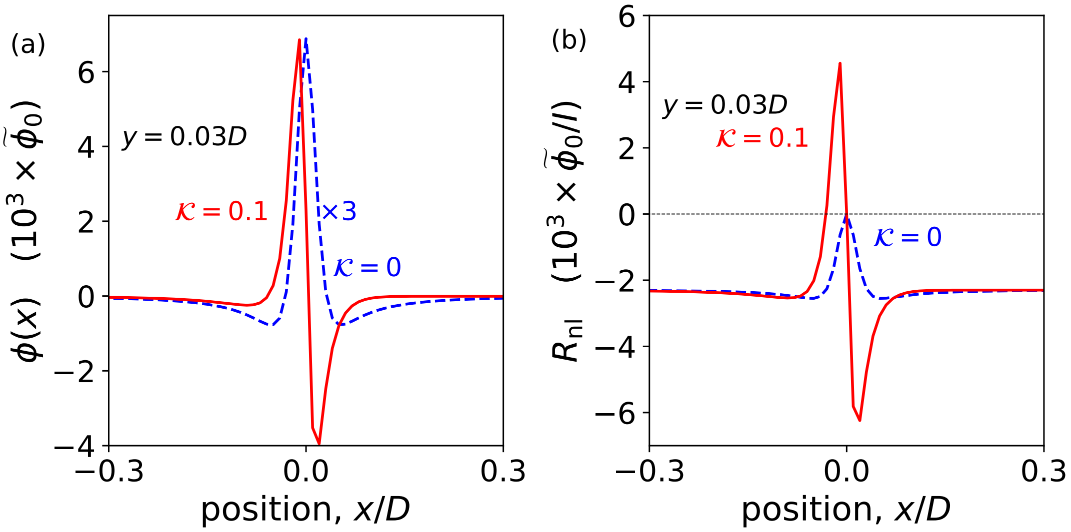

FIGURE 5.10: (a) The potential profile, ϕ and (b) the non-local resistance R_{nl} defined in Eq. (5.117) for a system with Berry curvature (blue) and a system without Berry curvature (red).

followed by the results obtained from the numerical implementations.

5.7 Finite element method and finite geometry

The finite element method (FEM) is a numerical method for solving partial differential equations (PDE). It has since long been established as a powerful method for solving PDEs and is being applied in many different situations, especially in the field of continuum mechanics. That being said we will here utilize it to solve the electronic Navier-Stokes equations that includes the Berry curvature. Before the method is applied to our problem we will give a short introduction to how the method works.

5.7.1 Receipt FEM

The finite element method follows six essential steps for a numerical implementation of the solution of the given partial differential equation. These are as follows,

1. The first step is to discretize the continuous model; the region over which we want to solve the given PDE is divided into *finite elements*. The mesh is usually generated by a "preprocessor" which assigns the nodes on the grid and their connectivity.

2. As the finite elements have been created, the next step is to select the *trial functions* which are used to interpolate the field variables for the elements. There are many options for picking the interpolation functions. For many problems, polynomials are chosen.

3. Next one has to establish a matrix equation of the finite element that relates the values at the nodes of the unknown function to other parameters. Here

one has different methods at hand. The two most common are the *Galerkin* method and the variational approach. We will here use the Galerkin method where one write the PDE on the weak form. The outline of this follows below.

4. As the equations for a specific element has been established the full matrix for the total system has to be constructed, using the information about the nodal point and their connectivity. In this step one also imposes particular boundary conditions.
5. Finally, as the whole system has been assembled one is ready to obtain the solution for the given problem. The result is given by the values of the nodal points in combination with the interpolation functions.
6. For many problems one further require another step for calculating specific properties, which can be obtained from the result produced using the FEM.

To demonstrate how the FEM work we apply it to a simple problem for which we also introduce the Galerkin method.

5.7.2 Galerkin method

We here introduce the Galerkin method as part of the finite element method and show how the FEM can be implemented by considering a simple differential equation such that we can solve it by hand. Let us consider the following differential equation,

$$a\frac{d^2v}{dx^2} + b = 0, \quad 0 \le x \le 2L, \tag{5.118}$$

where v is the function we are seeking. We take the following boundary conditions

$$v|_{x=0} = 0 \tag{5.119}$$

$$a\frac{dv}{dx}|_{x=2L} = R \tag{5.120}$$

As we are considering a one dimensional problem our finite elements are one dimensional. The line is divided into two parts resulting in 3 nodes. Let us first consider the system only between the two first nodes. On this interval we approximate the solution by

$$v = N_1v_1 + N_2v_2 = N_{12}v_{12}, \tag{5.121}$$

where $N_{12} = [N_1\, N_2]$ and $v_{12} = [v_1\, v_2]^T$. The N_is are the trial functions. For the given problem we pick them as follows

$$N_1 = 1 - \frac{x - x_1}{x_2 - x_1}, \tag{5.122}$$

$$N_2 = \frac{x - x_1}{x_2 - x_1}, \tag{5.123}$$

where x_1 and x_2 marks the position of the first and second node respectively. These functions are used to interpolate the functions $v(x)$ for its nodal values. The nodal values are given by v_1 and v_2, and are obtained by setting up a system of equations describing the total system.

Substituting the above approximate solution into the differential equation, Eq. (5.118) we have the following equation

$$a\frac{d^2}{dx^2}N_{12}v_{12} + b = r, \tag{5.124}$$

where r is the residual due to the that we are inserting an approximate solution into the differential equation. Next, we use the Galerkin method, which means that we minimize the residual by multiplying Eq. (5.124) by a *test function*, taken to be the same as the trial function, integrate over the element, and set the equation equal to zero. This results in

$$a\int_{x_1}^{x_2} dx\, N_{12}^T \frac{d^2}{dx^2}N_{12}v_{12} + b\int_{x_1}^{x_2} dx\, N_{12}^T = 0. \tag{5.125}$$

The next step is to perform an integration by parts. By doing so we obtain

$$a\int_{x_1}^{x_2} dx \left[\frac{dN_{12}}{dx}\right]^T \frac{dN_{12}}{dx}v_{12} - b\int_{x_1}^{x_2} dx\, N_{12}^T - a\begin{bmatrix}0\\1\end{bmatrix}\frac{dv}{dx}\Big|_{x=x_2} + a\begin{bmatrix}1\\0\end{bmatrix}\frac{dv}{dx}\Big|_{x=x_1} = 0. \tag{5.126}$$

In the literature this equation is normally presented as

$$\mathbf{k}v_{12} = \mathbf{f}, \tag{5.127}$$

where

$$\mathbf{k} = a\int_{x_1}^{x_2} dx \left[\frac{dN_{12}}{dx}\right]^T \frac{dN_{12}}{dx}v_{12} \tag{5.128}$$

is the stiffness matrix and

$$f = b\int_{x_1}^{x_2} dx\, N_{12}^T + a\begin{bmatrix}0\\1\end{bmatrix}\frac{dv}{dx}\Big|_{x=x_2} - a\begin{bmatrix}1\\0\end{bmatrix}\frac{dv}{dx}\Big|_{x=x_1} \tag{5.129}$$

is the load vector. The names for these two are justified by that they stem from solid mechanics. By the same principles, we obtain for the second element the following stiffness and load matrices

$$\mathbf{k}_1 = \mathbf{k}_2 = \frac{a}{L}\begin{bmatrix}1 & -1\\-1 & 1\end{bmatrix}, \tag{5.130}$$

$$\mathbf{f}_1 = \frac{bL}{2}\begin{bmatrix}1\\1\end{bmatrix}, \tag{5.131}$$

$$\mathbf{f}_2 = \frac{bL}{2}\begin{bmatrix}1\\1\end{bmatrix} + \begin{bmatrix}0\\R\end{bmatrix} \tag{5.132}$$

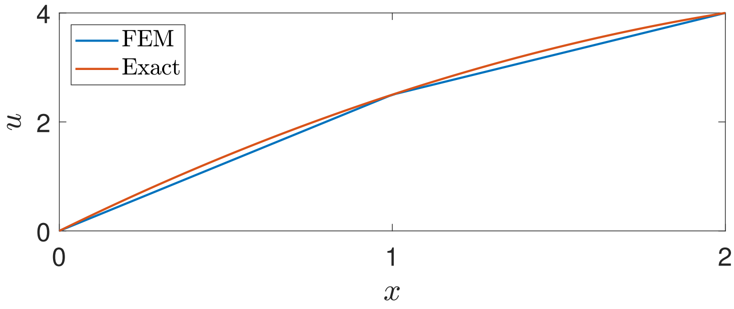

FIGURE 5.11: The solution to Eq. (5.118) using the finite element method along with the exact solution.

Assembling the stiffness and load matrices for the global system and applying the boundary condition at $v(x=0)$ results in the following system of equations

$$\frac{a}{L}\begin{bmatrix} 1 & 0 & 0 \\ 0 & 2 & -1 \\ 0 & -1 & 1 \end{bmatrix}\begin{bmatrix} v_1 \\ v_2 \\ v_3 \end{bmatrix} = \frac{bL}{2}\begin{bmatrix} 0 \\ 2 \\ 1 \end{bmatrix} + \begin{bmatrix} 0 \\ 0 \\ R \end{bmatrix} \tag{5.133}$$

Solving the system we obtain the approximate solution to the differential equation. The solution is plotted in Fig. 5.11 along with the exact result.

Let us furthermore make some clarifications regarding the above example and the Galerkin method. The Galerkin method is an example of a so-called residual method. We consider again the steps from Eq. (5.124) to (5.126). In the first step we require that after multiplying by the shape function and integrating over the element the result is zero. This means that we require that the integral over the residual, r weighted by the shape functions is zero,

$$\int_{x_1}^{x_2} dx\, N_{12} r = 0. \tag{5.134}$$

In fact one does not have to chose to multiply Eq. (5.124) by the shape function but in general one can chose any function v, commonly known as *test function*. The Galerkin method essentially boils down to picking the test functions equal to the trail functions.

Eq. (5.126) is the so-called weak form of Eq. (5.118) on the interval $0 \leq x \leq x_1$. Eq. (5.118) is the strong form of the PDE. Writing the weak form of the PDE is a general step for the FEM. Hence a common procedure is to start with writing the PDE on its weak form. This can then be easily treated by a finite element solver, such as the *FEniCS project*. Thus to obtain the weak form of Eq. (5.118) we multiply it by a test function and integrate over the domain for which we are interested in finding the solution. An integration by parts is then performed such that all functions have a derivative of as small order as possible. In most cases, this means that we have derivatives of no higher order than one. One can now ask the question of what is the advantage of the weak form compared to the strong form since they can be shown to be equivalent. To understand this, we consider the strong form. It is clear that the unknown function is differentiated twice. Since the FEM is an approximate method, we will have to replace the function appearing in the strong form with the approximation. When this is done for the strong form, it means that we have to consider an approximation that is twice differentiable. On the contrary, in the weak form, the sought function must be a function that is only one time differentiable. Hence, in this case, we only have to deal with approximations that are one time differentiable. Hence, from this aspect, the weak form is strongly favorable.

Another advantage of the weak form is that it provides a more general formulation of the differential equation. This might sound contradictory because we previously stated that the weak form is equivalent to the strong form. The proof of the equivalence of the two requires that the unknown function can be differentiated as many times as necessary, i.e., in most cases, two. However, what is important to notice is that the weak form holds even in the presence of discontinuities. On the contrary, if there are discontinuities present, the strong form has to be modified.

We have in the section presented the framework of the FEM. Many of the steps are implemented in finite element solvers. For the following study, we have utilized the finite element solver that is implemented under the *FEniCS project*. In the next section, we derive the weak form of the electronic Navier-Stokes equations including the Berry curvature, studied in the previous section, and then solve it using the FEM.

5.7.3 Finite elements for electronic Navier-Stokes equations in a finite geometry

With the finite element method being introduced, we can now apply it to the electronic Navier-Stokes equation, Eq. (5.82). For the approach taken to solve the equation analytically, we considered a half-plane geometry. This is not feasible when working with numerics. We will hence consider a finite geometry that is similar to a geometry that has been studied analytically [96]. The geometry is a rectangle of width $W = 2D$ and height $H = D$. We denote the system volume by Ω. The inlet and outlet are positioned in the center of the longest sides and are taken to be small compared to D. The geometry is depicted in Fig. 5.5 (b).

As a next step, we want to write the equations on the weak form. Since the equation is vector-valued, we have to multiply it by a test function that is also vector-valued. Hence we multiply the equation by $\mathbf{v} \in V$, where V denotes the space of all vector valued test functions (specified below). By further integrating over the entire system, Ω we have that

$$-\mathcal{K} \int_{\Omega} d\mathbf{r}\mathbf{v} \cdot \left(\tilde{\nabla}\tilde{\phi} \times \boldsymbol{\mathcal{B}} \cdot \tilde{\nabla}\right) \tilde{\mathbf{u}} + \int_{\Omega} d\mathbf{r}\mathbf{v} \cdot \left(\tilde{\nabla}\tilde{\phi} - \tilde{\mathbf{u}}\right) + \int_{\Omega} d\mathbf{r}\mathbf{v}\tilde{\nabla}^2\tilde{\mathbf{u}} = 0, \tag{5.135}$$

where $\mathcal{K} = \frac{\tilde{u}_0 \tilde{\mathcal{B}}_0}{ND}$. The incomperssibility condition, $\tilde{\nabla} \cdot \tilde{\mathbf{u}} = 0$, is multiplied by another test function, $q \in Q$, where Q denotes the space of test functions for the single valued functions (specified below), q, such that

$$\int_\Omega d\mathbf{r}\,(\nabla\cdot\tilde{\mathbf{u}})\,q = 0 \tag{5.136}$$

To obtain the weak form, we perform the integration by parts. We only have to perform the integration by parts on the last term of Eq. (5.135) since we only apply first-order derivatives to the other terms. Using Green's theorem, we obtain

$$\begin{aligned}-\mathcal{K}\int_\Omega d\mathbf{r}\,\mathbf{v}\cdot\left(\tilde\nabla\tilde\phi\times\boldsymbol{\mathcal{B}}\cdot\tilde\nabla\right)\tilde{\mathbf{u}}+\int_\Omega d\mathbf{r}\,\mathbf{v}\cdot\left(\tilde\nabla\tilde\phi-\tilde{\mathbf{u}}\right)&\\ +\int_\Omega d\mathbf{r}\,\tilde\nabla\tilde{\mathbf{u}}\cdot\tilde\nabla\mathbf{v}-\int_{\partial\Omega}ds\,\mathbf{v}\frac{\partial\tilde{\mathbf{u}}}{\partial\hat{\mathbf{n}}}&=0,\end{aligned} \tag{5.137}$$

where $\hat{\mathbf{n}}$ is the unit normal pointing out from the surface. The problem is completed by specifying the boundary conditions. We let the in- and outlet velocity in the y direction be equal, $\tilde{u}_y^{in} = \tilde{u}_y^{out} = 1$ and the potential on the in- and outlet are of equal amplitude but opposite sign, $\tilde\phi_{in} = 1$ and $\tilde\phi_{out} = -1$. Finally we have to specify the test-function spaces. A common practice for Navier-Stokes equations is to pick for the velocity the space of Lagrange polynomials of second order and for the potential the space of Lagrange polynomials of first order. These two then form the well known Taylor-Hood element which implies that the approximations are optimal [18].

We are now in position to state the full variational problem: find $\tilde{\mathbf{u}} \in V$ and $\tilde\nabla\tilde\phi \in Q$ such that

$$\begin{aligned}-\mathcal{K}\int_\Omega d\mathbf{r}\,\mathbf{v}\cdot\left(\tilde\nabla\tilde\phi\times\boldsymbol{\mathcal{B}}\cdot\tilde\nabla\right)\tilde{\mathbf{u}}+\int_\Omega d\mathbf{r}\,\mathbf{v}\cdot\left(\tilde\nabla\tilde\phi-\tilde{\mathbf{u}}\right)&\\ +\int_\Omega d\mathbf{r}\,\tilde\nabla\tilde{\mathbf{u}}\cdot\tilde\nabla\mathbf{v}-\int_{\partial\Omega}ds\,\mathbf{v}\frac{\partial\tilde{\mathbf{u}}}{\partial\hat{\mathbf{n}}}&=0, \qquad (5.138)\\ \int_\Omega d\mathbf{r}\,\left(\tilde\nabla\cdot\tilde{\mathbf{u}}\right)q&=0,\end{aligned} \tag{5.139}$$

given that

$$\tilde{u}_{\tilde{y}}^{in} = \tilde{u}_{\tilde{y}}^{out} = 1 \text{ on } \partial\Omega_{in}, \partial\Omega_{out}, \tag{5.140}$$

$$\tilde{\mathbf{u}} = 0 \text{ on } \partial\Omega \setminus \{\partial\Omega_{in}, \partial\Omega_{out}\} \tag{5.141}$$

$$\tilde\phi_{in} = 1 \text{ on } \partial\Omega_{in}, \tag{5.142}$$

$$\tilde\phi_{out} = -1 \text{ on } \partial\Omega_{out}, \tag{5.143}$$

where $\partial\Omega_{in}$ and $\partial\Omega_{out}$ denote the inlet and outlet respectively. The problem is now implemented using the *FEniCS* package. We plot the stream plots of the unperturbed velocity $\tilde{\mathbf{u}}^0$ and the difference between the perturbed and the unperturbed $\delta\tilde{\mathbf{u}}$ in Figs. 5.12 (a) and (b) respectively. The respective plots of the potential and potential

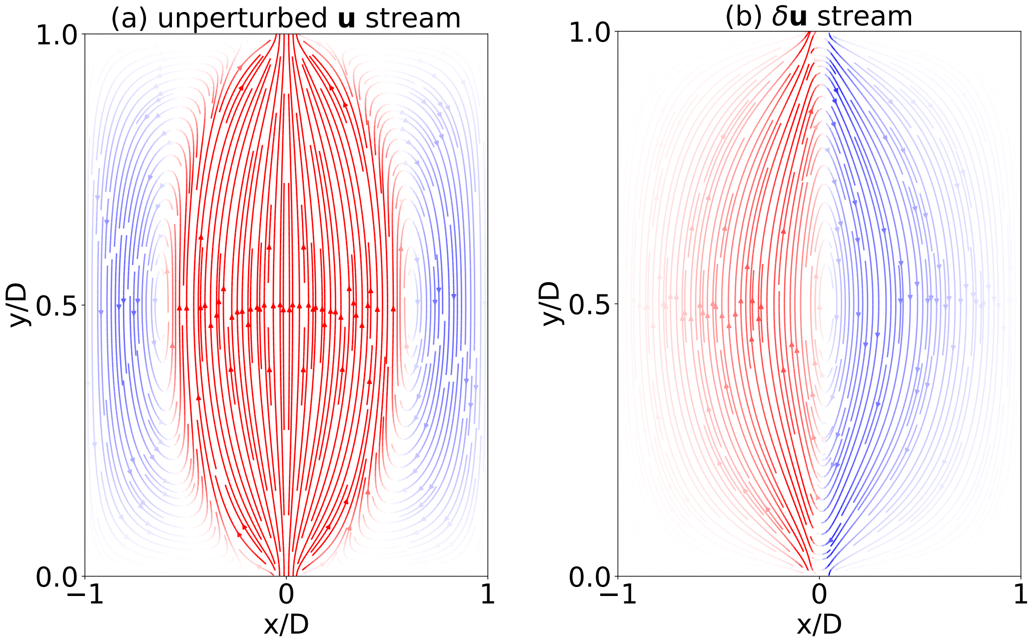

FIGURE 5.12: Stream plots of (a) $\tilde{\mathbf{u}}^0$ and (b) $\delta\tilde{\mathbf{u}}$, for $\mathcal{K} = 0.01$.

difference are plotted in 5.13 (a) and (b).

We first discuss the stream plots. In Fig. 5.12 (a) we observe the velocity profile of $\mathbf{u}^{(0)}$. We see that a couple of whirlpools form, one on each side of the line $\tilde{x} = 0$, due to the backflow created by the geometry boundaries. This can be directly compared to what has been obtained in [96, 128]. The positions of the whirlpools are in good agreement with what is obtained in [96].

Let us now discuss the effect of the Berry curvature. One best observes the effects in the difference between the unperturbed and the perturbed velocity profile, $\delta\tilde{\mathbf{u}}$. This is plotted in Fig. 5.12 (b). A small Berry curvature has been introduced such that $\mathcal{K} = 0.01$. The most notable effect of the Berry curvature is that a whirlpool is created in the center of the geometry for $\delta\tilde{\mathbf{u}}$, rotating in the anti-clockwise direction. This results in a reduced velocity on the right-hand side of the sample whereas, the velocity is increased on the left-hand side. A consequence of this is that the whirlpools shift towards the left of the sample.

Compared to the perturbative solution, we do not observe any whirlpools at the inlet. However, finding quantitative agreements between the analytical and numerical results should not be expected since we use an infinite geometry and a finite geometry for the perturbative solution and the numerical solution, respectively. Furthermore, the in- and outlet widths are infinitesimal and finite for the two different approaches. The two approaches however shows very good agreement for the different symmetries observed in $\tilde{\mathbf{u}}$ and $\delta\tilde{\mathbf{u}}$ and the asymmetric flow is observed in both approaches.

We now turn to the results of the potential. The unperturbed results (see Fig. 5.13 (a)) are in qualitative agreement with the results obtained in [96, 128]. Compared to the

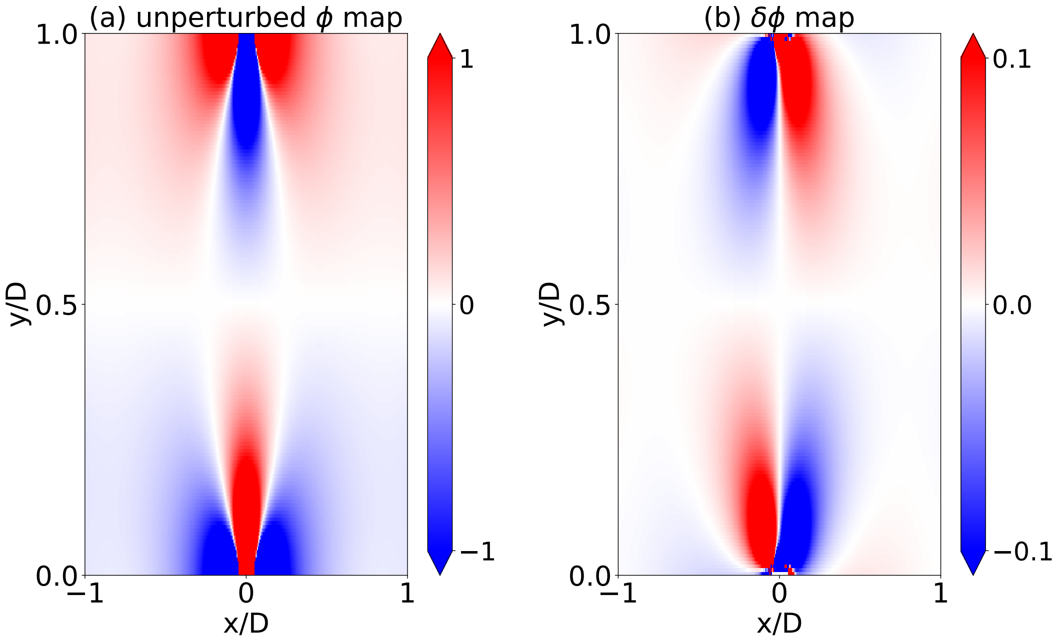

FIGURE 5.13: Potential maps of (a) $\tilde{\phi}^{(0)}$ and (b) $\delta\tilde{\phi}$, for $\mathcal{K} = 0.01$.

analytical solution, there is no singularity for the potential at the in- and outlet. This is due to the finite width of the in- and outlets in the finite geometry. On the other hand, the sign change observed in the potential is in close agreement between the analytical and numerical solutions. The changes in signs of the potential can again be seen as a signature of viscous flow.

The effect of the Berry curvature is depicted in Fig. 5.13 (b). We consider the lower half-plane. The difference, $\delta\phi$, shows an asymmetric profile that will expand the positive and negative regions of $\phi^{(0)}$ on the left, respectively, the right-hand side of the inlet. The results obtained here are consistent with the results for the half-plane geometry used for the analytical calculations.

Chapter 6

Summary and outlook

Summary

In this thesis, we have explored a few different directions of how topological materials react to external applied fields. In Chapter 3, we investigated the transport properties of systems hosting Majorana bound states. The set-ups that were studied were the minimal ones for constructing a qubit using Majorana bound states. These are the Majorana box and the T-junction. Importantly, we looked closer at the implications of the combination of overlap between the Majorana bound states, charging effects, and several terminals connected to the systems. We investigated the transport in both the sequential tunneling regime and the cotunneling regime.

We applied a master equation to elucidate on the transport in the sequential tunneling regime. Here the transport processes are due to single electrons tunneling on and off the Majorana box/T-junction. Furthermore, transport involving the creation and annihilation of Cooper pairs is as well present. Single electrons facilitate transport between the different leads coupled to the same wires, whereas in the T-junction, the transport occurs between the outer leads for small biases. Furthermore, depending on the overlap, the Cooper pairs facilitate non-local transport between the different wires in the Majorana box. Furthermore, a non-local Coulomb blockade can be observed depending on the overlap between the Majoranas.

Next, we investigated the cotunneling regime. Transport is due to transitions via virtual states and leads to elastic and inelastic cotunneling. The transport signatures in the Majorana box behave similarly to the sequential transport. On the other hand, in the T-junction, transport is now allowed between all leads, even for small biases, contrary to the sequential tunneling. Moreover elucidating on the effects and the transport signatures, the results furthermore show the importance of the overlap and how it makes the different structures distinct.

In Chapter 4 we investigated the optical activity of nodal loop semimetals, specifically in terms of the Kerr effect. The Kerr effect describes the polarization properties of the reflection of a linearly polarized incident beam on a material. The polarization of the reflected light is related to the conductivity of the material, which depends on the properties of the material. Hence, measuring the Kerr effect, properties of materials can be obtained.

Here we applied it both to a thin film and a semi-infinite bulk material hosting a nodal loop in the $x-y$ plane with a possible tilting of the nodal loop. The tilting is shown to be of uttermost importance for observing a polarization shift of the reflected light. The properties of the reflected light are directly affected by the Hall conductivity, and in its absence, the polarization of the reflected light is the same as for the incident. In the absence of tilt the Hall conductivity $\sigma_{xy}(\omega) = 0$ for a nodal loop. Hence, as we show, the Kerr effect is absent in un-tilted nodal loop semimetals.

When the nodal loop is tilted we find, both for the thin film and the bulk material, that the Kerr angle and ellipticity are large when the light is incident on the $x-y$ surface. This is in agreement with what is observed for other topological materials. When light is incident on the $x-z$ and $y-z$ surfaces the Kerr effect is absent due to that $\sigma_{xz} = \sigma_{yz} = 0$. For the bulk material, the effect is present but very small. We furthermore vary the chemical potential and the tilt direction. By increasing the chemical potential, the features of the Kerr rotation change. The amplitude is decreased but remains large. For the thin film, we furthermore see an increase in the amplitude of the ellipticity. By varying the tilt direction, we show that the Kerr effect is very sensitive to the tilt direction when light is incident on the $x-y$ surface. On the contrary, the Kerr angle is almost insensitive to light incident on the $x-z$ and $y-z$ surfaces.

Finally, in Chapter 5, we discuss the theory of electronic hydrodynamics. We extended the already well-known theory to account for anomalous Hall insulators as well. The anomalous Hall insulator was modeled by using a gapped Dirac Hamiltonian which display a non-vanishing Berry curvature. We find that the Berry curvature modifies the electronic Navier-Stokes equation and play an important role for describing hydrodynamic flow in topological materials.

As the Navier-Stokes equation had been formulated, we calculated different types of flow. First, we considered Poiseuille flow, laminar flow in a narrow channel. Usually, this leads to a parabolic flow profile with the maximum velocity in the middle of the channel. Because of the effects of the Berry curvature, the flow profile is changed. A shift of maximum flow is directly attributed to the Berry curvature.

We next studied the flow in two other geometries, an infinite half-plane, and a finite geometry. For the semi-infinite half-plane, we were able to apply analytical methods by using perturbation theory. However, for the finite geometry, we were bound to use numerical methods. In this case, we applied the finite element method. For both geometries, we investigated the electrical potential and the flow profile. Even though there is a difference between the two geometries, we found qualitative agreement between the results. We have further shown that the results should be experimentally accessible by measuring the non-local resistance

Outlook

The field of Majorana physics has evolved a lot in the last years. It would be interesting to device experiments where the devices that has been studied in this thesis are investigated. However, first the existence of Majoranas has to be settled. The work considered here could theoretically be extended to consider more complex structures while accounting for charging effects and overlap between the Majoranas.

Regarding the investigation on Kerr effect in nodal loop semimetals one could further consider tilt in the k_z plane. As some of these materials exhibit spin-orbit coupling, it could also be interesting to investigate the effect of this and the effects it has on Kerr measurements. The theory of the Kerr effect can as well be applied to other materials. This we already initiated in [59].

Our investigation of hydrodynamics in anomalous Hall materials clearly shows that the Berry curvature impacts the hydrodynamic flow. A further important question to answer is whether or not these materials support a hydrodynamic regime. This would mean that one has to investigate the different scattering mechanisms and find whether or not there is a regime where electron-electron scattering dominates over electron-impurity and electron-phonon scattering. Another direction would be to further study the possibility of hydrodynamic flow in other topological materials and the existence of a hydrodynamic regime in these materials.

Appendix A

Semi classical equations of motion

We will, in this appendix, derive the semiclassical equation of motion and show that the well-known equations are modified due to the Berry curvature. We follow [33]. The idea is to construct a wave packet $|W\rangle$ and study its motion. The system is under the influence of a (strong) homogeneous magnetic field that is described by the vector potential $\mathbf{A}_0$. When the magnetic field can no longer be treated in perturbation theory, one has to solve the Schrödinger equation for the following Hamiltonian

$$H = \frac{1}{2m}\left[-i\hbar\frac{\partial}{\partial \mathbf{r}} + e\mathbf{A}_0(\mathbf{r})\right]^2 + V(\mathbf{r}), \tag{A.1}$$

where $V(\mathbf{r})$ is a periodic potential.

To take into account for external fields, the dynamics of the wave packet will be governed by the following Hamiltonian

$$H = \frac{1}{2m}\left[-i\hbar\frac{\partial}{\partial \mathbf{r}} + e\mathbf{A}_0(\mathbf{r}) + e\delta\mathbf{A}(\mathbf{r},t)\right]^2 + V(\mathbf{r}), \tag{A.2}$$

where $\delta\mathbf{A}$ describe the external fields, and $-\partial\delta A/\partial t = \mathbf{E}$, and $\nabla \times \delta\mathbf{A} = \delta\mathbf{B}$. We will assume that both $\mathbf{E}$ and $\mathbf{B}$ are uniform and small, such that $\delta\mathbf{A}$ can be treated as an perturbation.

The wave packets that we will construct are based on Bloch functions. As we are considering magnetic fields, we have to consider the more general magnetic Bloch functions. For simplicity, we consider electrons confined to a two-dimensional plane. A magnetic Bloch state is then defined such that it satisfies

$$H_0\Psi_{n\mathbf{k}} = \mathcal{E}_n\Psi_{n\mathbf{k}}(\mathbf{r}). \tag{A.3}$$

The Hamiltonian is, in general, not translational invariant unless the mean value of $\mathbf{B}$ is zero. It can, on the other hand, be made invariant under magnetic translation operators. These operators are similar to the normal translation operators multiplied by a phase factor that depends on the position. The magnetic Bloch states then furthermore have to satisfy

$$T_1(R_1)\Psi_{n\mathbf{k}}(\mathbf{r}) = e^{ik_1R_1}\Psi_{n\mathbf{k}}(\mathbf{r}), \tag{A.4}$$

$$T_2(R_2)\Psi_{n\mathbf{k}}(\mathbf{r}) = e^{ik_2R_2}\Psi_{n\mathbf{k}}(\mathbf{r}). \tag{A.5}$$

These operators commute with the Hamiltonian by construction. They, however, only commute with each other if there is an integer number of flux quantum ϕ_0 contained in $\mathbf{R}_1 \times \mathbf{R}_2$. Because of this, when the magnetic flux is a rational multiple of p/q of the flux quantum ϕ_0 per unit cell of the lattice, a magnetic unit cell must be chosen which contains q plaquettes. If not, then k_1 and k_2 are not good quantum numbers. On the other hand, if this is satisfied the wave functions $\Psi_{n\mathbf{k}}$ furthermore forms a complete set such that

$$\langle \Psi_{n\mathbf{k}} | \Psi_{n'\mathbf{k}'} \rangle = \delta_{nn'} \delta_{\mathbf{k}\mathbf{k}'}, \tag{A.6}$$

and the domain of $\mathbf{k}$ is the magnetic Brillouin zone (MBZ). Compared to the normal Brillouin zone this is q times smaller.

We are now set to construct the wave packet $|W_0\rangle$. For simplicity we consider only a single band. The wave packet is centered around $\mathbf{r}_c$ in $\mathbf{r}$ space and is formed by a superposition of Bloch states

$$|W_0\rangle = \int_{MBZ} d\mathbf{k}\, w(\mathbf{k}) \, |\Psi(\mathbf{k})\rangle \, , \tag{A.7}$$

where $|\Psi(\mathbf{k})\rangle$ are Bloch wave functions, $w(\mathbf{k})$ is a function that is localized around $\mathbf{k}_c$ in $\mathbf{k}$ space and MBZ denotes the magnetic Brillouin zone (in case of no magnetic fields this boils down to the normal Brillouin zone). The function $w(\mathbf{k})$ has to be chosen such that is fulfills

$$\int d\mathbf{k}\, \mathbf{k} |w(\mathbf{k})|^2 = \mathbf{k}_c, \tag{A.8}$$

such that it makes sense to speak of the wave vector $\mathbf{k}_c$, and

$$\langle W_0 | \, \mathbf{r} \, | W_0 \rangle = \mathbf{r}_c. \tag{A.9}$$

The second condition tells us that the wave packet has to be narrowly localized around its center of mass, $\mathbf{r}_c$, in real space. An illustration of the wave packet can be seen in Fig. 2.3.

Let us define $u_{\mathbf{k}}(\mathbf{r}) = e^{-i\mathbf{k}\cdot\mathbf{r}} \Psi_{\mathbf{k}}(\mathbf{r})$. The mean position of the wave packet can be written as

$$\begin{aligned} \langle W_0 | \, \mathbf{r} \, | W_0 \rangle &= \int d\mathbf{k}' \int d\mathbf{k}\, w^*(\mathbf{k})' w(\mathbf{k}) \, \langle \Psi(\mathbf{k}') | \left(-i \frac{\partial}{\partial \mathbf{k}} e^{i\mathbf{k}\cdot\mathbf{r}} \right) |u(\mathbf{k})\rangle \\ &= \int d\mathbf{k}' \int d\mathbf{k}\, w^*(\mathbf{k}') w(\mathbf{k}) \left[\left(-i \frac{\partial}{\partial \mathbf{k}} \right) \delta(\mathbf{k}-\mathbf{k}') + \delta(\mathbf{k}-\mathbf{k}') \, \langle u(\mathbf{k}) | \, i \frac{\partial}{\partial \mathbf{k}} \, |u(\mathbf{k})\rangle_{cell} \right] \\ &= \int d\mathbf{k} \left[w^*(\mathbf{k}) i \frac{\partial}{\partial \mathbf{k}} w(\mathbf{k}) + |w(\mathbf{k})|^2 \, \langle (\mathbf{k}) | \, i \frac{\partial}{\partial \mathbf{k}} \, |u(\mathbf{k})\rangle_{cell} \right], \end{aligned} \tag{A.10}$$

where we have use that $\langle (\mathbf{k}') | \, e^{i(\mathbf{k}-\mathbf{k}')\cdot\mathbf{r}} i \frac{\partial}{\partial \mathbf{k}} \, |u(\mathbf{k})\rangle = \delta(\mathbf{k}-\mathbf{k}') \, \langle (\mathbf{k}) | \, i \frac{\partial}{\partial \mathbf{k}} \, |u(\mathbf{k})\rangle_{cell}$. The subscript means that the integration is taken over a unit cell. We define

$$\boldsymbol{\mathcal{A}}(\mathbf{k}) = i \, \langle (\mathbf{k}) | \, \frac{\partial}{\partial \mathbf{k}} \, |u(\mathbf{k})\rangle_{cell} \, , \tag{A.11}$$

which we know as the Berry connection. We can then write Eq. (A.9) as

$$\mathbf{r}_c = \int d\mathbf{k}\left[w^*(\mathbf{k})i\frac{\partial}{\partial\mathbf{k}}w(\mathbf{k}) + |w(\mathbf{k})|^2\boldsymbol{\mathcal{A}}(\mathbf{k})\right]. \tag{A.12}$$

Next, we will construct the Lagrangian. By using a time-dependent variational principle, the Lagrangian governing the dynamics of the wave packet is given by [89]

$$L(\mathbf{r}_c, \mathbf{k}_c, \dot{\mathbf{r}}_c, \dot{\mathbf{k}}_c) = \langle W| i\hbar\frac{\partial}{\partial t}|W\rangle - \langle W| H |W\rangle, \tag{A.13}$$

where $|W\rangle$ is a wave packet centered at $\mathbf{r}_c$ and $\mathbf{k}_c$. The Lagrangian is minimized by the wave function satisfying the wave time-dependent Schrödinger equation. A gauge can always be chosen for which the vector potential $\delta\mathbf{A}$ is locally gauged away at a specific point, in this case $\mathbf{r} = \mathbf{r}_c$. Thus, at this point W and W_0 coincides. Near $\mathbf{r}_c$ the value of W can be approximated by

$$W(\mathbf{r}) = e^{-ie\hbar\delta\mathbf{A}(\mathbf{r}_c,t)\cdot\mathbf{r}}W_0(\mathbf{r}). \tag{A.14}$$

By using Eq. (A.14), the energy of the wave packet can be evaluated, and is given by $\langle W| H |W\rangle = \langle W_0| H' |W_0\rangle$, where

$$\begin{aligned} H' &= \frac{1}{2m}\left\{-i\hbar\frac{\partial}{\partial\mathbf{r}} + \mathbf{A}_0(\mathbf{r}) + e\left[\delta\mathbf{A}(\mathbf{r},t) - \delta\mathbf{A}(\mathbf{r}_c,t)\right]\right\}^2 + V(\mathbf{r}) \\ &\simeq H_0 + \frac{e}{2m}\left\{\left[\delta\mathbf{A}(\mathbf{r},t) - \delta\mathbf{A}(\mathbf{r}_c,t)\right]\cdot\mathbf{P} + \text{h.c.}\right\}. \end{aligned} \tag{A.15}$$

Here $\mathbf{P}$ is the mechanical momentum operator corresponding to H_0. By choosing a circular gauge for δB, resulting in $\delta\mathbf{A}(\mathbf{r},t) = -\mathbf{E}t + \frac{1}{2}\delta\mathbf{B}\times\mathbf{r}$, the Hamiltonian can be written as

$$H' \simeq H_0 + \frac{e}{2m}\delta\mathbf{B}\cdot\mathbf{L}, \tag{A.16}$$

with $\mathbf{L} = (\mathbf{r} - \mathbf{r}_c)\times\mathbf{P}$ being the mechanical angular momentum operator of the wave packet, around the center of mass. Thus, for the second term of Eq. (A.13) we obtain

$$\langle W| H |W\rangle \simeq \mathcal{E}(\mathbf{k}_c) + \frac{e}{2m}\delta\mathbf{B}\cdot\langle W_0| \mathbf{L} |W_0\rangle. \tag{A.17}$$

The second term here represents the correction of the energy due to the magnetic moment of the wave packet. This arises because, contrary to a wave packet in a normal Bloch band, a wave packet in a magnetic Bloch band rotates.

The first term of Eq. (A.13) can be evaluated to give

$$\begin{aligned} \langle W_0| i\hbar\frac{\partial}{\partial t}|W_0\rangle &= \langle W_0| e\delta\dot{\mathbf{A}}(\mathbf{r}_c,t)\cdot\mathbf{r}|W_0\rangle + \int d\mathbf{k}\, w^*(\mathbf{k})i\hbar\frac{\partial}{\partial t}w(\mathbf{k}) \\ &= e\delta\dot{\mathbf{A}}(\mathbf{r}_c,t)\cdot\mathbf{r}_c + \int d\mathbf{k}\,|w(\mathbf{k})|^2\hbar\frac{\partial}{\partial t}\gamma(\mathbf{k},t) \\ &\simeq e\delta\dot{\mathbf{A}}(\mathbf{r}_c,t)\cdot\mathbf{r}_c + \hbar\frac{\partial}{\partial t}\gamma(\mathbf{k}_c,t), \end{aligned} \tag{A.18}$$

where we have used that we can write $w(\mathbf{k}) = |w(\mathbf{k})|e^{-i\gamma(\mathbf{k},t)}$ and that $|w(\mathbf{k})|^2$ can be approximated by $\delta(\mathbf{k}-\mathbf{k}_c)$. A total time derivative have no effects on the dynamics, hence, the last line can also be written as

$$\langle W_0|\, i\hbar\frac{\partial}{\partial t}\,|W_0\rangle \simeq -e\delta\mathbf{A}\cdot\dot{\mathbf{r}}_c - \hbar\dot{\mathbf{k}}_c\frac{\partial}{\partial\mathbf{k}_c}\gamma(\mathbf{k}_c,t). \tag{A.19}$$

We now use Eq. (A.12) and neglecting a total time derivative, as again, it will have no effects on the dynamics, we obtain

$$\langle W_0|\, i\hbar\frac{\partial}{\partial t}\,|W_0\rangle \simeq= -e\delta\mathbf{A}\cdot\mathbf{r}_c + \hbar\mathbf{k}_c\cdot\dot{\mathbf{r}}_c + \hbar\dot{\mathbf{k}}_c\cdot\boldsymbol{\mathcal{A}}(\mathbf{k}_c). \tag{A.20}$$

The Lagrangian describing the wave packet dynamics, Eq. A.13, can then be written

$$L(\mathbf{r}_c,\mathbf{k}_c,\dot{\mathbf{r}}_c,\dot{\mathbf{k}}_c) = -e\delta\mathbf{A}(\mathbf{r},t)\cdot\dot{\mathbf{r}}_c + \hbar\mathbf{k}_c\cdot\dot{\mathbf{r}}_c + \hbar\dot{\mathbf{k}}_c\cdot\boldsymbol{\mathcal{A}}(\mathbf{k}_c) - \mathcal{E}(\mathbf{k}_c) + \frac{e}{2m}\delta\mathbf{B}\cdot\mathbf{L}(\mathbf{k}), \tag{A.21}$$

where $\mathbf{L}(\mathbf{k}) = \langle W_0|\,\mathbf{L}\,|W_0\rangle$. This equation can be shown to be gauge invariant because under a gauge transformation for $\mathbf{A}_0(\mathbf{r})$, the Lagrangian will only change by a total time derivative. This also holds when specifying a different gauge for $\delta\mathbf{B}$. This implies that the dynamics are invariant under a gauge transformation. The dynamics are now found by applying the Euler-Lagrange equation, $\frac{d}{dt}\left(\frac{\partial L}{\partial\dot{x}}\right) - \frac{\partial L}{\partial x} = 0$. Consider first the r variable. Then

$$\frac{\partial L}{\partial r_i} = -e\sum_j\frac{\partial\delta A_j}{\partial r_i}\dot{r}_j \tag{A.22}$$

$$\frac{d}{dt}\left(\frac{\partial L}{\partial\dot{r}_i}\right) = \frac{d}{dt}\left(-e\delta A_i + \hbar k_i\right) = \hbar\dot{k}_i - e\frac{\partial\delta A_i}{\partial t} - e\sum_j\frac{\partial\delta A_i}{\partial r_j}\dot{r}_j \tag{A.23}$$

From this we obtain that

$$\hbar\dot{k}_i = e\frac{\partial\delta A_i}{\partial t} - e\sum_j\left[\frac{\partial\delta A_j}{\partial r_i} - \frac{\partial\delta A_i}{\partial r_j}\right]\dot{r}_j. \tag{A.24}$$

The first term here is just the negative of the ith component of the electric field, whereas the second component is $(\dot{\mathbf{r}}\times\delta\mathbf{B})_i$. We now continue with the $\mathbf{k}$ variable. We have that

$$\frac{\partial L}{\partial k_i} = \dot{r}_i + \sum_j\dot{k}_j\frac{\partial\mathcal{A}_j}{\partial k_i} - \frac{\partial\mathcal{E}}{\partial k_i} + \frac{e}{2m}\sum_j\delta B_j\frac{\partial L_j}{\partial k_i}, \tag{A.25}$$

$$\frac{d}{dt}\left(\frac{\partial L}{\partial\dot{k}_i}\right) = \frac{d}{dt}\left(\hbar\mathcal{A}_i\right) = \sum_j\frac{\partial\mathcal{A}_i}{\partial k_j}\dot{k}_j \tag{A.26}$$

Again, combining these equations we obtain

$$\dot{r}_i = \frac{\mathcal{E}}{\partial k_i} - \frac{e}{2m}\sum_j\delta B_j\frac{\partial L_j}{\partial k_i} + \sum_j\left[\frac{\partial\mathcal{A}_i}{\partial k_j} - \frac{\partial\mathcal{A}_j}{\partial k_i}\right]\dot{k}_j \tag{A.27}$$

The third term can now be shown to become $\left[\dot{\mathbf{k}} \times (\nabla \times \boldsymbol{\mathcal{A}})\right]_i$. Summing everything up, we have obtained the semicalssical equations of motion

$$\dot{\mathbf{r}} = \frac{1}{\hbar}\frac{\partial}{\partial \mathbf{k}}\left(\mathcal{E}_n(\mathbf{k}) + \frac{e}{2m}\delta\mathbf{B}\cdot\mathbf{L}(\mathbf{k})\right) - \dot{\mathbf{k}} \times \boldsymbol{\Omega}_n(\mathbf{k}) \tag{A.28}$$

$$\dot{\mathbf{k}} = -e\mathbf{E} - e\dot{\mathbf{r}} \times \delta\mathbf{B}, \tag{A.29}$$

where $\boldsymbol{\Omega}_n(\mathbf{k}) = \nabla \times \boldsymbol{\mathcal{A}}(\mathbf{k})$ is the Berry curvature. We have furthermore introduced the band indices, n. As seen there is a modification of the equation of the velocity due to the Berry curvature.

Appendix B

Cooper pair creation and annihilation operators

In this appendix we show that the operator $e^{-i\hat{\phi}}$ annihilates a Cooper pair in the Cooper pair condensate. The number of Cooper pairs in the condensate are given by N_C and the Cooper pair number operator tells us that $\hat{N}_C \left|N_C\right\rangle = N_C \left|N_C\right\rangle$. As the number of Cooper pairs and the superconducting phase ϕ are conjugate variables, we have that $\left[\hat{N}_C, \hat{\phi}\right] = i$ [54]. We now want to prove that

$$e^{-i\hat{\phi}} \left|N_C\right\rangle = \left|N_C - 1\right\rangle . \tag{B.1}$$

To do this we first study $\left[\hat{N}_C, e^{-i\hat{\phi}}\right]$. We apply the commutator to some wave function ψ and Taylor expand the exponential. This gives us

$$\begin{aligned}\left[\hat{N}_C, e^{-i\hat{\phi}}\right] \psi &= \left[\hat{N}_C \left(1 + i\hat{\phi} + \frac{\left(i\hat{\phi}\right)^2}{2!} + \dots\right) - \left(1 + i\hat{\phi} + \frac{\left(i\hat{\phi}\right)^2}{2!} + \dots\right) \hat{N}_C\right] \psi \\ &= \left[i\left[\hat{N}_C, \hat{\phi}\right] + \frac{i^2}{2!}\left[\hat{N}_C, \hat{\phi}^2\right] + \frac{i^3}{3!}\left[\hat{N}_C, \hat{\phi}^3\right] + \dots\right] \psi.\end{aligned} \tag{B.2}$$

Next we use the following commutator relation: $\left[\hat{A}, \hat{B}^n\right] = n\left[\hat{A}, \hat{B}\right]\hat{B}^{n-1}$. We then obtain

$$\left[\hat{N}_C, e^{-i\hat{\phi}}\right] \psi = -e^{-i\hat{\phi}}\psi. \tag{B.3}$$

This implies that

$$\left[\hat{N}_C, e^{-i\hat{\phi}}\right] = -e^{-i\hat{\phi}}. \tag{B.4}$$

We can now use this when considering $e^{-i\hat{\phi}} \left|N_C\right\rangle$. By direct calculation we obtain

$$\begin{aligned}e^{-i\hat{\phi}} \left|N_C\right\rangle &= -\left[\hat{N}_C, e^{-i\hat{\phi}}\right] \left|N_C\right\rangle \\ &= \left[e^{-i\hat{\phi}}\hat{N}_C - \hat{N}_C e^{-i\hat{\phi}}\right] \left|N_C\right\rangle \\ &= N_C e^{-i\hat{\phi}} \left|N_C\right\rangle - \hat{N}_C \left|N_C\right\rangle .\end{aligned} \tag{B.5}$$

This is equivalent to that

$$\left(N_C - 1\right) e^{-i\hat{\phi}} \left|N_C\right\rangle = \hat{N}_C e^{-i\hat{\phi}} \left|N_C\right\rangle . \tag{B.6}$$

This implies that

$$e^{-i\hat{\phi}} \left| N_C \right\rangle = \left| N_C - 1 \right\rangle . \tag{B.7}$$

Hence $e^{-i\hat{\phi}}$ destroys a Cooper pair. We can similarly show that $e^{i\hat{\phi}}$ creates a Cooper pair, i.e, $e^{i\hat{\phi}} \left| N_C \right\rangle = \left| N_C + 1 \right\rangle$.

Appendix C

Bogoliubov transform

This appendix outlines a general method to obtain the Bogoliubov transform for an arbitrary quadratic Hamiltonian. The Bogoliubov transform, also known as the Bogoliubov-Valentin transform, is applied to diagonalize a quadratic Hamiltonian. It can be applied to both bosonic as well as fermionic Hamiltonians. Below we will outline the method for finding the Bogoliubov transform for a fermionic system. The very same approach can be taken for bosonic Hamiltonians. However, certain care has to be taken. For extensive work on this, see [178].

Consider the Hamiltonian

$$H = \sum_{i,j=1}^{n} \left[\alpha_{ij} c_i^\dagger c_j + \frac{1}{2}\gamma_{ij} c_i^\dagger c_j^\dagger + \frac{1}{2}\gamma_{ij}^* c_j c_i \right], \tag{C.1}$$

where $n \geq 1$ and $\alpha_{ij}, \gamma_{ij} \in \mathbb{C}$. It is clear that this Hamiltonian in general is not diagonal. The creation and annihilation operators $c_i^\dagger$ and c_i obey the standard anti-commutation relations. The coefficients α_{ij}, γ_{ij}, furthermore have the following symmetries,

$$\alpha_{ij} = \alpha_{ij}^*, \quad \gamma_{ij} = -\gamma_{ji}. \tag{C.2}$$

By introducing

$$\Psi = \begin{bmatrix} c \\ \left(c^\dagger\right)^{\mathrm{T}} \end{bmatrix}, \quad \Psi^\dagger = \left[c^\dagger, \, c^{\mathrm{T}} \right], \tag{C.3}$$

where T denotes the transpose and

$$c = \begin{bmatrix} c_1 \\ c_2 \\ \vdots \\ c_n \end{bmatrix}, \quad c^\dagger = \left[c_1^\dagger, \, c_2^\dagger, \ldots, c_n^\dagger \right]. \tag{C.4}$$

The Hamiltonian, Eq. (C.1), can now be recast in the following form

$$H = \frac{1}{2}\Psi^\dagger M \Psi + \mathrm{tr}\left[\alpha\right], \tag{C.5}$$

where

$$M = \begin{bmatrix} \alpha & \gamma \\ \gamma^{\dagger} & -\alpha^{\mathrm{T}} \end{bmatrix}. \tag{C.6}$$

This is the first step towards obtaining the Bogoliubov transform. We are now looking for a transformation that diagonalizes the Hamiltonian given by Eq. (C.5). Finding a matrix that diagonalizes Eq. (C.5) is not necessarily hard. However the transformation must furthermore make sure that the anti-commutation relations are satisfied. To this end Bogoliubov and Valantin introduced the following linear transformation

$$c = Ad + B\left(d^{\dagger}\right)^{\mathrm{T}}, \tag{C.7}$$

where d and $d^{\dagger}$ are defined in the same fashion as the c's (see Eq. (C.4)) and they as well satisfy the fermionic anti commutation relations. A and B are square matrices of size n. Defining

$$\varphi = \begin{bmatrix} d \\ \left(d^{\dagger}\right)^{\mathrm{T}} \end{bmatrix}, \quad \varphi^{\dagger} = \left[d^{\dagger}, d^{\mathrm{T}}\right], \tag{C.8}$$

one obtains that

$$\Psi = T\varphi, \tag{C.9}$$

with

$$T = \begin{bmatrix} A & B \\ B^{*} & A^{*}. \end{bmatrix} \tag{C.10}$$

The Hamiltonian, Eq. (C.5) can now be written

$$H = \frac{1}{2}\varphi^{\dagger}T^{\dagger}MT\varphi + \mathrm{tr}\left[\alpha\right]. \tag{C.11}$$

For the Hamiltonian to be diagonal after the transformation it is obvious that $T^{\dagger}MT$ must be a diagonal matrix. The anti-commutation relations can be expressed through the following

$$\Psi \cdot \Psi^{\dagger} = \varphi \cdot \varphi^{\dagger} = I, \tag{C.12}$$

where I is the identity matrix. This implies that

$$TT^{\dagger} = I. \tag{C.13}$$

In conclusion, for a transformation to be a Bogoliubov transformation it must then satisfy that $T^{\dagger}MT$ and $TT^{\dagger} = I$. What remains is to find T. Before we outline how to find T, let us note the following: The matrix M is Hermitian and can always be diagonalized by a unitary transformation. This does not, however, mean that the same unitary transformation will necessarily diagonalize the Hamiltonian. In general, the unitary transformation will not satisfy Eq. (C.10). This is because the fields Ψ and φ are vectors of operators and not just complex numbers.

The matrix T is found by considering the eigenvalues and eigenvectors of M. We denote by ω_n the n:th eigenvalue and the corresponding eigenvector by $v(\omega_n)$. The transformation matrix is then given by [178]

$$T = [v(\omega_1),\, v(\omega_2), \ldots, v(\omega_n),\, v(-\omega_1),\, v(-\omega_2), \ldots, v(-\omega_n)]] \,. \tag{C.14}$$

Here $\omega_i \geq 0$, $i = 1, 2, \ldots, n$. This means the left half of T has eigenvectors corresponding to the positive eigenvalues and the right half contains the eigenvectors corresponding to the negative eigenvalues. Thus, we have here presented how to obtain a correct Bogoliubov transformation which will in every case diagonalize the Hamiltonian, Eq. C.1.

Appendix D

Boundary conditions for Maxwell's equations

In this appendix we give a derivation of the boundary conditions for Maxwell's equations. We follow [71]. Maxwell's equations can be cast on integral form by means of the divergence theorem and Stokes's theorem. Let $\mathcal{V}$ be a finite volume in space and $\mathcal{S}$ the closed surface bounding it. We let da denote an area element on the surface, and $\hat{\mathbf{n}}$ the unit normal pointing outward from the closed volume (see Fig. D.1 (a)). By applying the divergence and Stokes's theorems, the first and last of Maxwell's equations (Eqs. (4.1) and (4.4)) are written

$$\oint_{\mathcal{S}} da\, \mathbf{D} \cdot \hat{\mathbf{n}} = 4\pi \int_{\mathcal{V}} d\mathbf{r} \rho, \tag{D.1}$$

$$\oint_{\mathcal{S}} da\, \mathbf{B} \cdot \hat{\mathbf{n}} = 0. \tag{D.2}$$

$$\tag{D.3}$$

Similarly we let $\mathcal{C}$ be a closed contour in space and $\mathcal{S}'$ an open surface spanning the contour. We let $d\mathbf{l}$ denote a line element on the contour, da an element of the area $\mathcal{S}'$ and $\hat{\mathbf{t}}$ the unit normal at da pointing in the direction given by the right hand rule in the sense of the direction of the integration along the contour $\mathcal{C}$ (see Fig. D.1 (b)). Applying Stokes theorem to the two middle equations (Eqs. (4.2) and (4.3)) we obtain

$$\oint_{\mathcal{C}} \mathbf{H} \cdot d\mathbf{l} = \int_{\mathcal{S}'} da \left[\frac{4\pi}{c} \mathbf{J} + \frac{1}{c} \frac{\partial \mathbf{D}}{\partial t} \right] \cdot \hat{\mathbf{t}}, \tag{D.4}$$

$$\oint_{\mathcal{C}} \mathbf{E} \cdot d\mathbf{l} = -\frac{1}{c} \int_{\mathcal{S}'} da \frac{\partial \mathbf{B}}{\partial t} \cdot \hat{\mathbf{t}}. \tag{D.5}$$

We will now use these equations to deduce the normal and tangential components of the fields at the surface of two different media. The geometrical arrangements are displayed in Fig. D.1. In Fig. D.1 (a), an infinitesimal pillbox encapsulates part of the boundary between two media of different electromagnetic properties. Now we apply Eqs. (D.1) and (D.2) to the pillbox. As the sides of the pillbox are shrunk to zero, $\delta \to 0$, only the top and bottom contribute to the integral. If the top

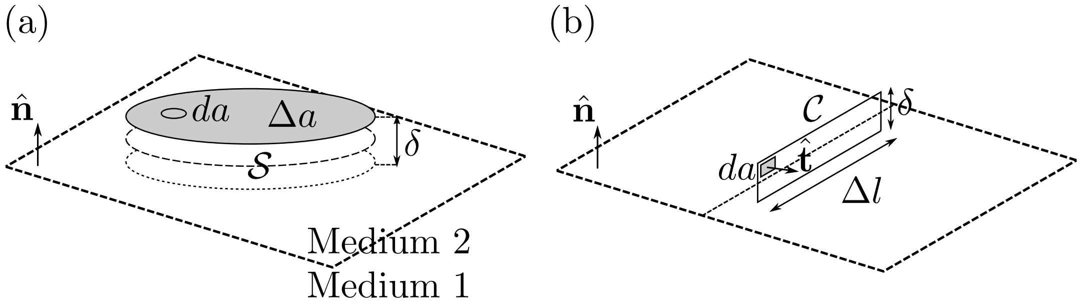

FIGURE D.1: Geometries for determining the boundary conditions of Maxwell's equations at the interface of two media, medium 1 and medium 2. The surface normal is given by $\hat{n}$. (a) A pillbox is constructed through the boundary between the two media. The surface bounding the pillbox is $\mathcal{S}$, the thickness is δ and the top and bottom surface areas are given by Δa. The area element of the surface area is denoted by da. (b) A sheet is inserted through the boundary between the media. The contour spanning the sheet is denoted by $\mathcal{C}$. The unit normal of the sheet is $\hat{\mathbf{t}}$ and the area element is denoted by da. The short side of the sheet which is perpendicular to the surface is δ and the long side, parallel to the surface is Δl.

and bottom are parallel and with the area Δa, the left-hand side of the integrals read

$$\oint_{\mathcal{S}} da\, \mathbf{D} \cdot \hat{\mathbf{n}} = (\mathbf{D}_2 - \mathbf{D}_1) \cdot \hat{\mathbf{n}} \Delta a, \tag{D.6}$$

$$\oint_{\mathcal{S}} da\, \mathbf{B} \cdot \hat{\mathbf{n}} = (\mathbf{B}_2 - \mathbf{B}_1) \cdot \hat{\mathbf{n}} \Delta a \tag{D.7}$$

$$\tag{D.8}$$

Assuming that the charge density ρ is singular on the interface, producing an ideal surface charge density σ, the the right-hand side of Eq. D.1 becomes

$$4\pi \int_{\mathcal{V}} d\mathbf{x} \rho = 4\pi\sigma\Delta a. \tag{D.9}$$

The first boundary conditions are hence given by

$$(\mathbf{D}_2 - \mathbf{D}_1) \cdot \hat{\mathbf{n}} = 4\pi\sigma \tag{D.10}$$

$$(\mathbf{B}_2 - \mathbf{B}_1) \cdot \hat{\mathbf{n}} = 0. \tag{D.11}$$

These equations tells us that the normal component of **B** is continuous over the interface whereas the normal component of **D** has a discontinuity equal to 4π times the surface charge density at a given point. We can now consider the same setting for Eqs. D.4 and D.5 by appllying them to the countour $\mathcal{C}$, see Fig. D.1 (b). If the short sides of the contour are negligible, $\delta \to 0$, and the long sides are parallel to the surface, then the left-hand side of Eqs. D.4 and D.5 become

$$\oint_{\mathcal{C}} \mathbf{H} \cdot d\mathbf{l} = (\hat{\mathbf{t}} \times \hat{\mathbf{n}}) \cdot (\mathbf{E}_2 - \mathbf{E}_1) \Delta l, \tag{D.12}$$

$$\oint_C \mathbf{E}\cdot d\mathbf{l} = \left(\hat{\mathbf{t}}\times\hat{\mathbf{n}}\right)\cdot\left(\mathbf{H}_2 - \mathbf{H}_1\right)\Delta l. \tag{D.13}$$

The right hand side of Eq. D.5 vanishes because the area of the loop goes to zero as the sides of the contour are shrunk to zero. If an ideal surface current density **J** flows along the interface, the left-hand side of Eq. D.4 does not vanish. In this case the left-hand side can be written as

$$\int_{S'} da \left[\frac{4\pi}{c}\mathbf{J} + \frac{1}{c}\frac{\partial \mathbf{D}}{\partial t}\right]\cdot\mathbf{t} = \frac{4\pi}{c}\mathbf{J}\cdot\mathbf{t}\Delta l, \tag{D.14}$$

where the second term under the integral sign vanishes for the same reason as the derivative of **B** with respect to time vanishes. The third and fourth boundary conditions can then be written as

$$\hat{\mathbf{n}}\times\left(\mathbf{E}_2 - \mathbf{E}_1\right) = 0, \tag{D.15}$$

$$\hat{\mathbf{n}}\times\left(\mathbf{H}_2 - \mathbf{H}_1\right) = \frac{4\pi}{c}\mathbf{J}. \tag{D.16}$$

Appendix E

Length gauge

We will here derive the Hamiltonian for system interacting with external electric field in the length gauge. The assumption for the length gauge is such that the wavelength of the external field is large compared to the Fermi wavelength. In this case, we can neglect any position dependence of the vector potential or equivalently we are considering a uniform external field.

A general Hamiltonian can, up to second order in momentum, be written as

$$H_2 = \sum_{l,ij} \alpha_{ij} p_{l,i} p_{l,j} + \sum_{l,i} \beta_i p_{l,i} + N\gamma + \sum_{l<l'} V_{ll'} \tag{E.1}$$

where $i \in x, y, z$, $\alpha_{ij} = \alpha_{ji}$, β_i and γ are matrix coefficients and $V_{ll'}$ is a two-body interaction potential. The index l runs from 1 to N. The wave function is a many-body wave function written as $\phi(\mathbf{r}_1, \ldots, \mathbf{r}_N, t)$, for N particles. Making the minimal coupling substitution, $\mathbf{p} \to \mathbf{p} + \frac{e}{c}\mathbf{A}(t)$, we can write the time-dependent Schrödinger equation as

$$\begin{aligned} i\hbar \frac{\partial \phi(\mathbf{r}_1, \ldots, \mathbf{r}_N, t)}{\partial t} = &\left\{ \sum_{l,ij} \alpha_{ij} \left(p_{l,i} + \frac{e}{c} A_i(t) \right) \left(p_{l,j} + \frac{e}{c} A_j(t) \right) \right. \\ &\left. + \sum_{l,i} \beta_i \left(p_{l,i} + \frac{e}{c} A_i(t) \right) + N\gamma + \sum_{l<l'} V_{ll'} \right\} \phi(\mathbf{r}_1, \ldots, \mathbf{r}_N, t), \end{aligned} \tag{E.2}$$

This form is also known as the velocity gauge. The vector potential is restricted to $\mathbf{E}(t) = -(1/c)\,\partial_t \mathbf{A}(t)$. We now make the following gauge transformation [137]

$$\phi(\mathbf{r}_1, \ldots, \mathbf{r}_N, t) = \Pi_l e^{-i\frac{e}{\hbar c}\mathbf{A}(t)\cdot\mathbf{r}_l} \Psi(\mathbf{r}_1, \ldots, \mathbf{r}_N, t). \tag{E.3}$$

We now calculate

$$p_{l,i} e^{-i\frac{e}{\hbar c} A_j(t) r_{l,j}} \Psi = -\frac{e}{c} A_i(t) e^{-i\frac{e}{\hbar c} A_i(t) r_{l,i}} \Psi + e^{-i\frac{e}{\hbar c} A_j(t) r_{l,j}} p_{l,i} \Psi \tag{E.4}$$

where we have used that $p_{l,i} = -i\hbar \frac{\partial}{\partial r_{l,i}}$. For the right-hand side of Eq. (E.2) we obtain

$$i\hbar \frac{\partial \phi(\mathbf{r}_1, \ldots, \mathbf{r}_N, t)}{\partial t} = i\hbar \frac{\partial}{\partial t} \Pi_l e^{-i\frac{e}{\hbar c}\mathbf{A}(t)\cdot\mathbf{r}_l} \Psi(\mathbf{r}_1, \ldots, \mathbf{r}_N, t)$$

$$= -e\sum_l \mathbf{E}\cdot\mathbf{r}_l\Psi + i\hbar\Pi_l e^{-i\frac{e}{\hbar c}\mathbf{A}(t)\cdot\mathbf{r}_l}\frac{\partial}{\partial t}\Psi. \tag{E.5}$$

This then implies that Eq. (E.2) can be written as

$$\begin{aligned} i\hbar\frac{\partial\psi(\mathbf{r}_1,\ldots,\mathbf{r}_N,t)}{\partial t} = &\Bigg\{\sum_{l,ij}\alpha_{ij}p_{l,i}p_{l,j} + \sum_{l,i}\beta_i p_{l,i} \\ &+ N\gamma + \sum_{l<l'}V_{ll'} + e\sum_l \mathbf{E}\cdot\mathbf{r}_l\Bigg\}\psi(\mathbf{r}_1,\ldots,\mathbf{r}_N,t). \end{aligned} \tag{E.6}$$

We have by the gauge transformation re-written the Schrödinger equation in terms of the electric field rather than the vector potential. The external field (often due to perturbations) is given by the new term

$$H_{ext} = e\sum_l \mathbf{E}\cdot\mathbf{r}_l. \tag{E.7}$$

We use this to derive the conductivity tensor in the main text. As a further remark, note that this can by generalized to Hamiltonians of any order in p.

Appendix F

H-Theorem

In this appendix we justify why the local distribution function in Section 5 takes the form of a modified Fermi-Dirac distribution. This is explained by the H-theorem which was developed by Boltzmann using the second law of thermodynamic. Boltzmann defined a function

$$H = \int d\mathbf{k}\, f \log f. \tag{F.1}$$

By taking the derivative of this function with respect to time and using the kinetic equations under the integral sign one can conclude that

$$\frac{dH}{dt} \leq 0. \tag{F.2}$$

This quantity was later to be defined as the negative of the entropy and furthermore proved that the entropy can never decrease with time. Equation F.2 furthermore tells us that if the rate of change of the netropy is zero then the term inside the collision integral necessarily has to be zero. This implies that the system is in a steady state with a distribution function f^0 [134].

In the case of strong interactions, which is the regime where electronic hydrodynamics is observed, there is another way of obtaining the distribution function. If the interactions are very strong the system will relax to its equilibrium very fast. Because of this, the relaxation time approximation is a good approximation [9]. Hence,

$$\frac{df}{dt} \simeq -\frac{f - f^0}{\tau}, \tag{F.3}$$

where τ is the relaxation time. Now we use the Boltzmann equation, as defined in Eq. 5.7 and write

$$\dot{\mathbf{r}}\frac{\partial f}{\partial \mathbf{r}} + \dot{\mathbf{k}}\frac{\partial f}{\partial \mathbf{k}} \simeq -\frac{f - f^0}{\tau}. \tag{F.4}$$

Re-arranging the equation we have that

$$f \simeq f^0 - \tau\left(\dot{\mathbf{r}}\frac{\partial f}{\partial \mathbf{r}} + \dot{\mathbf{k}}\frac{\partial f}{\partial \mathbf{k}}\right). \tag{F.5}$$

By expanding the distribution function on the right hand side we obtain

$$f \simeq f^0 - \tau \left[\dot{\mathbf{r}} \frac{\partial f^0}{\partial \mathbf{r}} + \dot{\mathbf{k}} \frac{\partial f^0}{\partial \mathbf{k}} + \mathcal{O}(\tau^2) \right] \tag{F.6}$$

In the case of strong interactions one take $\tau \to 0$ which results in

$$f \to f^0. \tag{F.7}$$

Now we have shown that the distribution function relaxes to an equilibrium distribution function. We furthermore want to find an expression for the equilibrium distribution function. The equilibrium distribution function is found by considering the collision integral for electron-electron interactions. The collision integral for electron-electron interactions is one for two-particle problems and can be written

$$\begin{aligned} \mathcal{I}[f] = \int\int \frac{d^3\mathbf{k}'}{(2\pi)^3} \frac{d^3\mathbf{k}}{(2\pi)^3} W^{\mathbf{k}\mathbf{k}'}_{\mathbf{k}+\mathbf{q},\mathbf{k}'+\mathbf{q}} \big[& f_{\mathbf{k}+\mathbf{q}} f_{\mathbf{k}'-\mathbf{q}} (1 - f_{\mathbf{k}})(1 - f_{\mathbf{k}'}) \\ & - f_{\mathbf{k}} f_{\mathbf{k}'} (1 - f_{\mathbf{k}+\mathbf{q}})(1 - f_{\mathbf{k}'-\mathbf{q}}) \big]. \end{aligned} \tag{F.8}$$

The above equation tells us how two electrons with momentum $\mathbf{k} + \mathbf{q}$ and $\mathbf{k}' - \mathbf{q}$ scatter into states with momentum $\mathbf{k}$ and $\mathbf{k}'$ and as well the reversed process. $W^{\mathbf{k}\mathbf{k}'}_{\mathbf{k}+\mathbf{q},\mathbf{k}'+\mathbf{q}}$ is the scattering amplitude and for example be obtained by Fermi's golden rule and the T-matrix expansion as described in Eq. 3.78. According to Eq. (F.7) $f \to f^0$ as $\tau \to 0$. From this it also follows that $\mathcal{I}[f^0]$ also tends to zero . Using that $\mathcal{I}[f^0] = 0$ implies that

$$f_{\mathbf{k}+\mathbf{q}} f_{\mathbf{k}'-\mathbf{q}} (1 - f_{\mathbf{k}})(1 - f_{\mathbf{k}'}) - f_{\mathbf{k}} f_{\mathbf{k}'} (1 - f_{\mathbf{k}+\mathbf{q}})(1 - f_{\mathbf{k}'-\mathbf{q}}) = 0. \tag{F.9}$$

Let us introduce the following function

$$g_{\mathbf{k}} = \log \left(\frac{1 - f_{\mathbf{k}}}{f_{\mathbf{k}}} \right) \tag{F.10}$$

We can now reorganize Eq. (F.9) and take the logarithm of it. Using the above equation we can then write

$$g_{\mathbf{k}} + g_{\mathbf{k}'} = g_{\mathbf{k}+\mathbf{q}} + g_{\mathbf{k}'-\mathbf{q}}. \tag{F.11}$$

Now momentum and energy conservation implies that

$$\mathbf{k} + \mathbf{k}' = (\mathbf{k} + \mathbf{q})(\mathbf{k}' - \mathbf{q}) \tag{F.12}$$

$$E(\mathbf{k}) + E(\mathbf{k}') = E(\mathbf{k} + \mathbf{q}) + E(\mathbf{k}' - \mathbf{q}). \tag{F.13}$$

We can now make an anzats for $g_{\mathbf{k}}$ in terms of conserved quantities. Hence we write

$$g_{\mathbf{k}} = \alpha_0 + \hbar \boldsymbol{\alpha}_1 \cdot \mathbf{k} + \beta E(\mathbf{k}), \tag{F.14}$$

where $\beta = 1/k_BT$. The conserved quantities are particle number (μ), momentum ($\hbar\boldsymbol{\alpha}_1 \cdot \mathbf{k}$) and energy, $\beta E(\mathbf{k})$. The quantities μ, $\boldsymbol{\alpha_1}$ and β can be treated as Lagrange multipliers for N (number of particles), $\mathbf{k}$ and E. Thus

$$\alpha_0 = -\beta\mu, \quad \boldsymbol{\alpha}_1 = \beta\boldsymbol{\alpha}. \tag{F.15}$$

This results in

$$\log\left(\frac{1-f_{\mathbf{k}}}{f_{\mathbf{k}}}\right) = \beta E(\mathbf{k}) + \beta\hbar\boldsymbol{\alpha}\cdot\mathbf{k} - \beta\mu. \tag{F.16}$$

This is equivalent to that

$$f^0_{\mathbf{k}} = \left(1 + e^{\beta(E(\mathbf{k})+\hbar\boldsymbol{\alpha}\cdot\mathbf{k}-\mu)}\right)^{-1}. \tag{F.17}$$

We have hereby finished the proof and conclude that the equilibrium distribution function is a Fermi-Dirac distribution that is modified by the addition of a drift velocity.

Bibliography

[1] Seongjin Ahn, E. J. Mele, and Hongki Min. "Electrodynamics on Fermi Cyclides in Nodal Line Semimetals". In: *Phys. Rev. Lett.* 119 (14 2017), p. 147402. DOI: `10.1103/PhysRevLett.119.147402`.

[2] S. M. Albrecht et al. "Exponential protection of zero modes in Majorana islands". In: *Nature* 531.7593 (2016), pp. 206–209. ISSN: 1476-4687. DOI: `10.1038/nature17162`.

[3] Jason Alicea. "New directions in the pursuit of Majorana fermions in solid state systems". In: *Reports on Progress in Physics* 75.7 (2012), p. 076501. DOI: `10.1088/0034-4885/75/7/076501`.

[4] A Altland et al. "Bethe ansatz solution of the topological Kondo model". In: *Journal of Physics A: Mathematical and Theoretical* 47.26 (2014), p. 265001. DOI: `10.1088/1751-8113/47/26/265001`.

[5] A. Altland et al. "Multichannel Kondo Impurity Dynamics in a Majorana Device". In: *Phys. Rev. Lett.* 113.7 (2014), p. 076401. DOI: `10.1103/PhysRevLett.113.076401`.

[6] Alexander Altland and Reinhold Egger. "Multiterminal Coulomb-Majorana Junction". In: *Phys. Rev. Lett.* 110.19 (2013), p. 196401. DOI: `10.1103/PhysRevLett.110.196401`.

[7] Petros N. Argyres. "Theory of the Faraday and Kerr Effects in Ferromagnetics". In: *Phys. Rev.* 97 (2 1955), pp. 334–345. DOI: `10.1103/PhysRev.97.334`.

[8] N. P. Armitage, E. J. Mele, and Ashvin Vishwanath. "Weyl and Dirac semimetals in three-dimensional solids". In: *Rev. Mod. Phys.* 90 (1 2018), p. 015001. DOI: `10.1103/RevModPhys.90.015001`.

[9] N.W. Ashcroft et al. *Solid State Physics*. HRW international editions. Holt, Rinehart and Winston, 1976. ISBN: 9780030839931.

[10] R. C. Ashoori. "Electrons in artificial atoms". In: *Nature* 379.6564 (1996), pp. 413–419. ISSN: 1476-4687. DOI: `10.1038/379413a0`.

[11] Alexander Avdoshkin, Vladyslav Kozii, and Joel E. Moore. "Interactions Remove the Quantization of the Chiral Photocurrent at Weyl Points". In: *Phys. Rev. Lett.* 124 (19 2020), p. 196603. DOI: `10.1103/PhysRevLett.124.196603`.

[12] Frank T. Avignone, Steven R. Elliott, and Jonathan Engel. "Double beta decay, Majorana neutrinos, and neutrino mass". In: *Rev. Mod. Phys.* 80 (2 2008), pp. 481–516. DOI: `10.1103/RevModPhys.80.481`.

[13] D. A. Bandurin et al. “Negative local resistance caused by viscous electron backflow in graphene”. In: *Science* 351.6277 (2016), pp. 1055–1058. ISSN: 0036-8075. DOI: `10.1126/science.aad0201`.

[14] Denis A. Bandurin et al. “Fluidity onset in graphene”. In: *Nature Communications* 9.1 (2018), p. 4533. ISSN: 2041-1723. DOI: `10.1038/s41467-018-07004-4`.

[15] Shahin Barati and Saeed H. Abedinpour. “Optical conductivity of three and two dimensional topological nodal-line semimetals”. In: *Phys. Rev. B* 96 (15 2017), p. 155150. DOI: `10.1103/PhysRevB.96.155150`.

[16] J. Bardeen, L. N. Cooper, and J. R. Schrieffer. “Microscopic Theory of Superconductivity”. In: *Phys. Rev.* 106 (1 1957), pp. 162–164. DOI: `10.1103/PhysRev.106.162`.

[17] C.W.J. Beenakker. “Search for Majorana Fermions in Superconductors”. In: *Annu. Rev. Con. Mat. Phys.* 4.1 (2013), pp. 113–136. DOI: `10.1146/annurev-conmatphys-030212-184337`.

[18] M. Bercovier and O. Pironneau. “Error estimates for finite element method solution of the Stokes problem in the primitive variables”. In: *Numerische Mathematik* 33.2 (1979), pp. 211–224. ISSN: 0945-3245. DOI: `10.1007/BF01399555`.

[19] A. I. Berdyugin et al. “Measuring Hall viscosity of graphene’s electron fluid”. In: *Science* 364.6436 (2019), pp. 162–165. ISSN: 0036-8075. DOI: `10.1126/science.aau0685`.

[20] B. Béri. “Exact Nonequilibrium Transport in the Topological Kondo Effect”. In: *Phys. Rev. Lett.* 119 (2 2017), p. 027701. DOI: `10.1103/PhysRevLett.119.027701`.

[21] B. Béri. “Majorana-Klein Hybridization in Topological Superconductor Junctions”. In: *Phys. Rev. Lett.* 110.21 (2013), p. 216803. DOI: `10.1103/PhysRevLett.110.216803`.

[22] B. Béri and N. R. Cooper. “Topological Kondo Effect with Majorana Fermions”. In: *Phys. Rev. Lett.* 109.15 (2012), p. 156803. DOI: `10.1103/PhysRevLett.109.156803`.

[23] B. Andrei Bernevig and Shou-Cheng Zhang. “Quantum Spin Hall Effect”. In: *Phys. Rev. Lett.* 96 (10 2006), p. 106802. DOI: `10.1103/PhysRevLett.96.106802`.

[24] B.A. Bernevig and T.L. Hughes. *Topological Insulators and Topological Superconductors*. Princeton University Press, 2013. ISBN: 9780691151755.

[25] Michael Victor Berry. “Quantal phase factors accompanying adiabatic changes”. In: *Proc. R. Soc. Lond. A* 392 (1802 1984), 45—57. DOI: `10.1098/rspa.1984.0023`.

[26] Guang Bian et al. “Topological nodal-line fermions in spin-orbit metal $PbTaSe_2$”. In: *Nat. Comm.* 7.1 (2016), p. 10556. DOI: `10.1038/ncomms10556`.

[27] C. J. Bolech and Eugene Demler. "Observing Majorana bound States in *p*-Wave Superconductors Using Noise Measurements in Tunneling Experiments". In: *Phys. Rev. Lett.* 98 (23 2007), p. 237002. DOI: `10.1103/PhysRevLett.98.237002`.

[28] U. Briskot et al. "Collision-dominated nonlinear hydrodynamics in graphene". In: *Phys. Rev. B* 92 (11 2015), p. 115426. DOI: `10.1103/PhysRevB.92.115426`.

[29] Henrik Bruus and Karsten Flensberg. *Many-body quantum theory in condensed matter physics - an introduction*. English. United States: Oxford University Press, 2004.

[30] A.A. Burkov. "Weyl Metals". In: *Annual Review of Condensed Matter Physics* 9.1 (2018), pp. 359–378. DOI: `10.1146/annurev-conmatphys-033117-054129`.

[31] Lubensky T.C. Chaikin P.M. *Principles of Condensed Matter Physics*. Cambridge University Press, 2000.

[32] Y.-H. Chan et al. "Ca_3P_2 and other topological semimetals with line nodes and drumhead surface states". In: *Phys. Rev. B* 93 (20 2016), p. 205132. DOI: `10.1103/PhysRevB.93.205132`.

[33] Ming-Che Chang and Qian Niu. "Berry phase, hyperorbits, and the Hofstadter spectrum: Semiclassical dynamics in magnetic Bloch bands". In: *Phys. Rev. B* 53 (11 1996), pp. 7010–7023. DOI: `10.1103/PhysRevB.53.7010`.

[34] C. Chen et al. "Dirac line nodes and effect of spin-orbit coupling in the nonsymmorphic critical semimetals M SiS ($M = Hf$, Zr)". In: *Phys. Rev. B* 95 (12 2017), p. 125126. DOI: `10.1103/PhysRevB.95.125126`.

[35] Ching-Kai Chiu, Jay D. Sau, and S. Das Sarma. "Conductance of a superconducting Coulomb-blockaded Majorana nanowire". In: *Phys. Rev. B* 96 (5 2017), p. 054504. DOI: `10.1103/PhysRevB.96.054504`.

[36] Ching-Kai Chiu et al. "Classification of topological quantum matter with symmetries". In: *Rev. Mod. Phys.* 88 (3 2016), p. 035005. DOI: `10.1103/RevModPhys.88.035005`.

[37] H. O. H. Churchill et al. "Superconductor-nanowire devices from tunneling to the multichannel regime: Zero-bias oscillations and magnetoconductance crossover". In: *Phys. Rev. B* 87 (24 2013), p. 241401. DOI: `10.1103/PhysRevB.87.241401`.

[38] A. A. Clerk and S. M. Girvin. "Shot noise of a tunnel junction displacement detector". In: *Phys. Rev. B* 70 (12 2004), 121303(R). DOI: `10.1103/PhysRevB.70.121303`.

[39] R. L. Conger and J. L. Tomlinson. "Magneto-Optic Readout for Computer Memories". In: *Journal of Applied Physics* 33.3 (1962), pp. 1059–1060. DOI: `10.1063/1.1728598`.

[40] Jesse Crossno et al. “Observation of the Dirac fluid and the breakdown of the Wiedemann-Franz law in graphene”. In: *Science* 351.6277 (2016), pp. 1058–1061. ISSN: 0036-8075. DOI: `10.1126/science.aad0343`.

[41] Anindya Das et al. “Zero-bias peaks and splitting in an Al–InAs nanowire topological superconductor as a signature of Majorana fermions”. In: *Nature Physics* 8.12 (2012), pp. 887–895. ISSN: 1745-2481. DOI: `10.1038/nphys2479`.

[42] S. Das Sarma, Jay D. Sau, and Tudor D. Stanescu. “Splitting of the zero-bias conductance peak as smoking gun evidence for the existence of the Majorana mode in a superconductor-semiconductor nanowire”. In: *Phys. Rev. B* 86 (22 2012), p. 220506. DOI: `10.1103/PhysRevB.86.220506`.

[43] Sankar Das Sarma and Haining Pan. “Disorder-induced zero-bias peaks in Majorana nanowires”. In: *Phys. Rev. B* 103 (19 2021), p. 195158. DOI: `10.1103/PhysRevB.103.195158`.

[44] J.H. Davies. *The Physics of Low-dimensional Semiconductors: An Introduction*. ISBN: 9780521484916.

[45] Dirk van Delft and Peter Kes. “The discovery of superconductivity”. In: *Physics Today* 63.9 (2010), pp. 38–43. DOI: `10.1063/1.3490499`.

[46] M. T. Deng et al. “Anomalous Zero-Bias Conductance Peak in a Nb–InSb Nanowire–Nb Hybrid Device”. In: *Nano Letters* 12.12 (2012), pp. 6414–6419. ISSN: 1530-6984. DOI: `10.1021/nl303758w`.

[47] M. T. Deng et al. “Majorana bound state in a coupled quantum-dot hybrid-nanowire system”. In: *Science* 354.6319 (2016), pp. 1557–1562. ISSN: 0036-8075. DOI: `10.1126/science.aaf3961`.

[48] M. T. Deng et al. “Parity independence of the zero-bias conductance peak in a nanowire based topological superconductor-quantum dot hybrid device”. In: *Scientific Reports* 4.1 (2014), p. 7261. ISSN: 2045-2322. DOI: `10.1038/srep07261`.

[49] Johan Ekström et al. *Kerr effect in tilted nodal loop semimetals*. 2021. arXiv: `2102.03231 [cond-mat.mes-hall]`.

[50] Johan Ekström, Patrik Recher, and Thomas L. Schmidt. “Transport properties of coupled Majorana bound states in the Coulomb blockade regime”. In: *Phys. Rev. B* 101 (19 2020), p. 195420. DOI: `10.1103/PhysRevB.101.195420`.

[51] Gregory Falkovich and Leonid Levitov. “Linking Spatial Distributions of Potential and Current in Viscous Electronics”. In: *Phys. Rev. Lett.* 119 (6 2017), p. 066601. DOI: `10.1103/PhysRevLett.119.066601`.

[52] Michael Faraday. “Experimental researches in electricity. —Nineteenth series”. In: *Phil. Trans. R. Soc.* 136 (1846), pp. 1–20. DOI: `doi.org/10.1098/rstl.1846.0001`.

[53] Marcel Franz and Laurens Molenkamp (Eds.) *Topological Insulators*. 1st ed. Contemporary Concepts of Condensed Matter Science 6. Elsevier, 2013. ISBN: 978-0-444-63314-9.

[54] Liang Fu. "Electron Teleportation via Majorana Bound States in a Mesoscopic Superconductor". In: *Phys. Rev. Lett.* 104.5 (2010), p. 056402. DOI: `10.1103/PhysRevLett.104.056402`.

[55] Liang Fu and C. L. Kane. "Superconducting Proximity Effect and Majorana Fermions at the Surface of a Topological Insulator". In: *Phys. Rev. Lett.* 100 (9 2008), p. 096407. DOI: `10.1103/PhysRevLett.100.096407`.

[56] Matthias Gau, Stephan Plugge, and Reinhold Egger. "Quantum transport in coupled Majorana box systems". In: *Phys. Rev. B* 97.18 (2018), p. 184506. DOI: `10.1103/PhysRevB.97.184506`.

[57] R N Gurzhi. "Hydrodynamic effects in solids at low temperature". In: *Soviet Physics Uspekhi* 11.2 (1968), pp. 255–270. DOI: `10.1070/pu1968v011n02abeh003815`.

[58] R.N. Gurzhi. "Minimum of Resistance in Impurity-free Conductors". In: *Sov. Phys. JETP* 17 (1963).

[59] Alireza Habibi et al. *Optical properties of topological flat and dispersive bands*. 2021. arXiv: `2103.15085 [cond-mat.mes-hall]`.

[60] F. D. M. Haldane. "Model for a Quantum Hall Effect without Landau Levels: Condensed-Matter Realization of the "Parity Anomaly"". In: *Phys. Rev. Lett.* 61 (18 1988), pp. 2015–2018. DOI: `10.1103/PhysRevLett.61.2015`.

[61] E. H. Hall. "On a New Action of the Magnet on Electric Currents". In: *American Journal of Mathematics* 2.3 (1879), pp. 287–292. ISSN: 00029327, 10806377.

[62] Eddwi H. Hasdeo et al. "Electron hydrodynamics of two-dimensional anomalous Hall materials". In: *Phys. Rev. B* 103 (12 2021), p. 125106. DOI: `10.1103/PhysRevB.103.125106`.

[63] E. Hassinger et al. "Vertical Line Nodes in the Superconducting Gap Structure of Sr_2RuO_4". In: *Phys. Rev. X* 7 (1 2017), p. 011032. DOI: `10.1103/PhysRevX.7.011032`.

[64] B. van Heck, R. M. Lutchyn, and L. I. Glazman. "Conductance of a proximitized nanowire in the Coulomb blockade regime". In: *Phys. Rev. B* 93.23 (2016), p. 235431. DOI: `10.1103/PhysRevB.93.235431`.

[65] Derek Y. H. Ho et al. "Theoretical determination of hydrodynamic window in monolayer and bilayer graphene from scattering rates". In: *Phys. Rev. B* 97 (12 2018), p. 121404. DOI: `10.1103/PhysRevB.97.121404`.

[66] Pavan Hosur. "Circular photogalvanic effect on topological insulator surfaces: Berry-curvature-dependent response". In: *Phys. Rev. B* 83 (3 2011), p. 035309. DOI: `10.1103/PhysRevB.83.035309`.

[67] Pavan Hosur and Xiao-Liang Qi. "Tunable circular dichroism due to the chiral anomaly in Weyl semimetals". In: *Phys. Rev. B* 91 (8 2015), p. 081106. DOI: 10.1103/PhysRevB.91.081106.

[68] S. M. Huang et al. "A Weyl Fermion semimetal with surface Fermi arcs in the transition metal monopnictide TaAs class". In: *Nat Commun* 6 (2015), p. 7373.

[69] H. R. Hulme. "The Faraday effect in ferromagnetics". In: *Proc. R. Soc. Lond.* 135 (826 1932), pp. 237–257. DOI: doi.org/10.1098/rspa.1932.0032.

[70] R. Hützen et al. "Majorana Single-Charge Transistor". In: *Phys. Rev. Lett.* 109 (2012), p. 166403. DOI: doi.org/10.1103/PhysRevLett.109.166403.

[71] J.D. Jackson. *Classical Electrodynamics*. Wiley India Pvt. Limited, 2007. ISBN: 9788126510948.

[72] Kerr John. "XLIII. On rotation of the plane of polarization by reflection from the pole of a magnet". In: *The London, Edinburgh, and Dublin Philosophical Magazine and Journal of Science* 3.19 (1877), pp. 321–343. DOI: 10.1080/14786447708639245.

[73] M. J. M. de Jong and L. W. Molenkamp. "Hydrodynamic electron flow in high-mobility wires". In: *Phys. Rev. B* 51 (19 1995), pp. 13389–13402. DOI: 10.1103/PhysRevB.51.13389.

[74] F. de Juan et al. "Difference frequency generation in topological semimetals". In: *Phys. Rev. Research* 2 (1 2020), p. 012017. DOI: 10.1103/PhysRevResearch.2.012017.

[75] Fernando de Juan et al. "Quantized circular photogalvanic effect in Weyl semimetals". In: *Nature Communications* 8.1 (2017), p. 15995. ISSN: 2041-1723. DOI: 10.1038/ncomms15995.

[76] C. L. Kane and E. J. Mele. "Quantum Spin Hall Effect in Graphene". In: *Phys. Rev. Lett.* 95 (22 2005), p. 226801. DOI: 10.1103/PhysRevLett.95.226801.

[77] C. L. Kane and E. J. Mele. "Z_2 Topological Order and the Quantum Spin Hall Effect". In: *Phys. Rev. Lett.* 95 (14 2005), p. 146802. DOI: 10.1103/PhysRevLett.95.146802.

[78] Mehdi Kargarian, Mohit Randeria, and Nandini Trivedi. "Theory of Kerr and Faraday rotations and linear dichroism in Topological Weyl Semimetals". In: *Sci. Rep.* 5.1 (2015), p. 12683. ISSN: 2045-2322. DOI: 10.1038/srep12683.

[79] Torsten Karzig et al. "Scalable designs for quasiparticle-poisoning-protected topological quantum computation with Majorana zero modes". In: *Phys. Rev. B* 95 (23 2017), p. 235305. DOI: 10.1103/PhysRevB.95.235305.

[80] Oleksiy Kashuba, Björn Trauzettel, and Laurens W. Molenkamp. "Relativistic Gurzhi effect in channels of Dirac materials". In: *Phys. Rev. B* 97 (20 2018), p. 205129. DOI: 10.1103/PhysRevB.97.205129.

[81] A. Yu Kitaev. "Unpaired Majorana fermions in quantum wires". In: *Phy.–Usp* 44 (2001), pp. 131–136. DOI: 10.1070/1063-7869/44/10S/S29.

[82] A.Yu. Kitaev. “Fault-tolerant quantum computation by anyons”. In: *Annals of Physics* 303.1 (2003), pp. 2–30. ISSN: 0003-4916. DOI: `https://doi.org/10.1016/S0003-4916(02)00018-0`.

[83] C. Kittel. “Theory of Antiferromagnetic Resonance”. In: *Phys. Rev.* 82 (4 1951), pp. 565–565. DOI: `10.1103/PhysRev.82.565`.

[84] K. v. Klitzing, G. Dorda, and M. Pepper. “New Method for High-Accuracy Determination of the Fine-Structure Constant Based on Quantized Hall Resistance”. In: *Phys. Rev. Lett.* 45 (6 1980), pp. 494–497. DOI: `10.1103/PhysRevLett.45.494`.

[85] Christina Knapp. “Topological Quantum Computing with Majorana Zero Modes and Beyond”. Doctoral Thesis. UC Santa Barbara, 2019.

[86] Jens Koch, Felix von Oppen, and A. V. Andreev. “Theory of the Franck-Condon blockade regime”. In: *Phys. Rev. B* 74 (20 2006), p. 205438. DOI: `10.1103/PhysRevB.74.205438`.

[87] Jens Koch et al. “Thermopower of single-molecule devices”. In: *Phys. Rev. B* 70 (19 2004), p. 195107. DOI: `10.1103/PhysRevB.70.195107`.

[88] Markus König et al. “Quantum Spin Hall Insulator State in HgTe Quantum Wells”. In: *Science* 318.5851 (2007), pp. 766–770. ISSN: 0036-8075. DOI: `10.1126/science.1148047`.

[89] Peter Kramer and Marcos Saraceno, eds. *Geometry of the TDVP*. Berlin, Heidelberg: Springer Berlin Heidelberg, 1981. ISBN: 978-3-540-38576-9. DOI: `10.1007/3-540-10579-4_23`.

[90] R. Krishna Kumar et al. “Superballistic flow of viscous electron fluid through graphene constrictions”. In: *Nature Physics* 13.12 (2017), pp. 1182–1185. ISSN: 1745-2481. DOI: `10.1038/nphys4240`.

[91] Mark J. H. Ku et al. “Imaging viscous flow of the Dirac fluid in graphene”. In: *Nature* 583.7817 (2020), pp. 537–541. ISSN: 1476-4687. DOI: `10.1038/s41586-020-2507-2`.

[92] L. A. Landau and E. Sela. “Two-channel Kondo physics in a Majorana island coupled to a Josephson junction”. In: *Phys. Rev. B* 95 (3 2017), p. 035135. DOI: `10.1103/PhysRevB.95.035135`.

[93] L. D. Landau and E. M. Lifshitz. *Fluid Mechanics, Second Edition: Volume 6 (Course of Theoretical Physics)*. 2nd ed. Course of theoretical physics / by L. D. Landau and E. M. Lifshitz, Vol. 6. Butterworth-Heinemann. ISBN: 0750627670.

[94] Martin Leijnse and Karsten Flensberg. “Introduction to topological superconductivity and Majorana fermions”. In: *Semicond. Sci. Technol.* 27.12 (2012), p. 124003. DOI: `10.1088/0268-1242/27/12/124003`.

[95] Martin Leijnse and Karsten Flensberg. “Introduction to topological superconductivity and Majorana fermions”. In: *Semiconductor Science and Technology* 27.12 (2012), p. 124003. DOI: `10.1088/0268-1242/27/12/124003`.

[96] Leonid Levitov and Gregory Falkovich. “Electron viscosity, current vortices and negative nonlocal resistance in graphene”. In: *Nature Physics* 12.7 (2016), pp. 672–676. ISSN: 1745-2481. DOI: `10.1038/nphys3667`.

[97] Peng Li et al. “Evidence for topological type-II Weyl semimetal WTe2”. In: *Nature Communications* 8.1 (2017), p. 2150. ISSN: 2041-1723. DOI: `10.1038/s41467-017-02237-1`.

[98] Chaoxing Liu et al. “Quantum Spin Hall Effect in Inverted Type-II Semiconductors”. In: *Phys. Rev. Lett.* 100 (23 2008), p. 236601. DOI: `10.1103/PhysRevLett.100.236601`.

[99] Dong E. Liu and Harold U. Baranger. “Detecting a Majorana-fermion zero mode using a quantum dot”. In: *Phys. Rev. B* 84 (20 2011), 201308(R). DOI: `10.1103/PhysRevB.84.201308`.

[100] Hai-Feng Lü, Hai-Zhou Lu, and Shun-Qing Shen. “Enhanced current noise correlations in a Coulomb-Majorana device”. In: *Phys. Rev. B* 93 (24 2016), p. 245418. DOI: `10.1103/PhysRevB.93.245418`.

[101] Andrew Lucas and Kin Chung Fong. “Hydrodynamics of electrons in graphene”. In: *Journal of Physics: Condensed Matter* 30.5 (2018), p. 053001. DOI: `10.1088/1361-648x/aaa274`.

[102] Rex Lundgren, Pontus Laurell, and Gregory A. Fiete. “Thermoelectric properties of Weyl and Dirac semimetals”. In: *Phys. Rev. B* 90 (16 2014), p. 165115. DOI: `10.1103/PhysRevB.90.165115`.

[103] R. M. Lutchyn et al. “Majorana zero modes in superconductor–semiconductor heterostructures”. In: *Nature Reviews Materials* 3.5 (2018), pp. 52–68. ISSN: 2058-8437. DOI: `10.1038/s41578-018-0003-1`.

[104] Roman M. Lutchyn and Leonid I. Glazman. “Transport through a Majorana Island in the Strong Tunneling Regime”. In: *Phys. Rev. Lett.* 119 (5 2017), p. 057002. DOI: `10.1103/PhysRevLett.119.057002`.

[105] Roman M. Lutchyn, Jay D. Sau, and S. Das Sarma. “Majorana Fermions and a Topological Phase Transition in Semiconductor-Superconductor Heterostructures”. In: *Phys. Rev. Lett.* 105 (7 2010), p. 077001. DOI: `10.1103/PhysRevLett.105.077001`.

[106] Alberto Martín-Ruiz and Alberto Cortijo. “Parity anomaly in the nonlinear response of nodal-line semimetals”. In: *Phys. Rev. B* 98 (15 2018), p. 155125. DOI: `10.1103/PhysRevB.98.155125`.

[107] Karen Michaeli et al. “Electron teleportation and statistical transmutation in multiterminal Majorana islands”. In: *Phys. Rev. B* 96 (20 2017), p. 205403. DOI: 10.1103/PhysRevB.96.205403.

[108] L.W. Molenkamp and M.J.M. de Jong. “Observation of Knudsen and Gurzhi transport regimes in a two-dimensional wire”. In: *Solid-State Electronics* 37.4 (1994), pp. 551–553. ISSN: 0038-1101. DOI: https://doi.org/10.1016/0038-1101(94)90244-5.

[109] Philip J. W. Moll et al. “Evidence for hydrodynamic electron flow in PdCoO2”. In: *Science* 351.6277 (2016), pp. 1061–1064. ISSN: 0036-8075. DOI: 10.1126/science.aac8385.

[110] V. Mourik et al. “Signatures of Majorana Fermions in Hybrid Superconductor-Semiconductor Nanowire Devices”. In: *Science* 336.6084 (2012), pp. 1003–1007. ISSN: 0036-8075. DOI: 10.1126/science.1222360.

[111] Markus Müller, Jörg Schmalian, and Lars Fritz. “Graphene: A Nearly Perfect Fluid”. In: *Phys. Rev. Lett.* 103 (2 2009), p. 025301. DOI: 10.1103/PhysRevLett.103.025301.

[112] S. Nadj-Perge et al. “Proposal for realizing Majorana fermions in chains of magnetic atoms on a superconductor”. In: *Phys. Rev. B* 88 (2 2013), p. 020407. DOI: 10.1103/PhysRevB.88.020407.

[113] S. Nadj-Perge et al. “Topological matter. Observation of Majorana fermions in ferromagnetic atomic chains on a superconductor”. In: *Science* 346.6209 (2014), pp. 602–607.

[114] M. Nakahara. *Geometry, Topology and Physics, Third Edition*. Taylor & Francis, 2021. ISBN: 9781439840719.

[115] Boris N. Narozhny. “Electronic hydrodynamics in graphene”. In: *Annals of Physics* 411 (2019), p. 167979. ISSN: 0003-4916. DOI: https://doi.org/10.1016/j.aop.2019.167979.

[116] Boris N. Narozhny et al. “Hydrodynamic Approach to Electronic Transport in Graphene”. In: *Annalen der Physik* 529.11 (2017), p. 1700043. DOI: https://doi.org/10.1002/andp.201700043.

[117] Chetan Nayak et al. “Non-Abelian anyons and topological quantum computation”. In: *Rev. Mod. Phys.* 80 (3 2008), pp. 1083–1159. DOI: 10.1103/RevModPhys.80.1083.

[118] Yuli V. Nazarov and Yaroslav M. Blanter. *Quantum Transport: Introduction to Nanoscience*. Cambridge University Press, 2009. DOI: 10.1017/CBO9780511626906.

[119] Fabrizio Nichele et al. “Scaling of Majorana Zero-Bias Conductance Peaks”. In: *Phys. Rev. Lett.* 119 (13 2017), p. 136803. DOI: 10.1103/PhysRevLett.119.136803.

[120] K. S. Novoselov et al. “Electric Field Effect in Atomically Thin Carbon Films”. In: *Science* 306.5696 (2004), pp. 666–669. ISSN: 0036-8075. DOI: `10.1126/science.1102896`.

[121] Peter Oppeneer. *Theory of the Magneto-Optical Kerr Effect in Ferromagnetic Compounds*. Mar. 1999. DOI: `10.13140/2.1.3171.4083`.

[122] Yuval Oreg, Gil Refael, and Felix von Oppen. “Helical Liquids and Majorana Bound States in Quantum Wires”. In: *Phys. Rev. Lett.* 105 (17 2010), p. 177002. DOI: `10.1103/PhysRevLett.105.177002`.

[123] Haining Pan and S. Das Sarma. “Physical mechanisms for zero-bias conductance peaks in Majorana nanowires”. In: *Phys. Rev. Research* 2 (1 2020), p. 013377. DOI: `10.1103/PhysRevResearch.2.013377`.

[124] Haining Pan and Sankar Das Sarma. *Crossover between trivial zero modes in Majorana nanowires*. 2021. arXiv: `2102.07296 [cond-mat.mes-hall]`.

[125] Haining Pan et al. “Quantized and unquantized zero-bias tunneling conductance peaks in Majorana nanowires: Conductance below and above $2e^2/h$”. In: *Phys. Rev. B* 103 (21 2021), p. 214502. DOI: `10.1103/PhysRevB.103.214502`.

[126] Jean-Michel Parent, René Côté, and Ion Garate. “Magneto-optical Kerr effect and signature of the chiral anomaly in a Weyl semimetal in magnetic field”. In: *Phys. Rev. B* 102 (24 2020), p. 245126. DOI: `10.1103/PhysRevB.102.245126`.

[127] Shreyas Patankar et al. “Resonance-enhanced optical nonlinearity in the Weyl semimetal TaAs”. In: *Phys. Rev. B* 98 (16 2018), p. 165113. DOI: `10.1103/PhysRevB.98.165113`.

[128] Francesco M. D. Pellegrino et al. “Electron hydrodynamics dilemma: Whirlpools or no whirlpools”. In: *Phys. Rev. B* 94 (15 2016), p. 155414. DOI: `10.1103/PhysRevB.94.155414`.

[129] Sébastien R. Plissard et al. “Formation and electronic properties of InSb nanocrosses”. In: *Nat. Nanotechnol.* 8 (Nov. 2013), pp. 859–864. ISSN: 1748-3395. DOI: `10.1038/nnano.2013.198`.

[130] S. Plugge et al. “Roadmap to Majorana surface codes”. In: *Phys. Rev. B* 94 (17 2016), p. 174514. DOI: `10.1103/PhysRevB.94.174514`.

[131] F. R. Pratama, M. Shoufie Ukhtary, and Riichiro Saito. “Circular dichroism and Faraday and Kerr rotation in two-dimensional materials with intrinsic Hall conductivities”. In: *Phys. Rev. B* 101 (4 2020), p. 045426. DOI: `10.1103/PhysRevB.101.045426`.

[132] Alessandro Principi et al. “Bulk and shear viscosities of the two-dimensional electron liquid in a doped graphene sheet”. In: *Phys. Rev. B* 93 (12 2016), p. 125410. DOI: `10.1103/PhysRevB.93.125410`.

[133] Xiaofeng Qian et al. “Quantum spin Hall effect in two-dimensional transition metal dichalcogenides”. In: *Science* 346.6215 (2014), pp. 1344–1347. ISSN: 0036-8075. DOI: `10.1126/science.1256815`.

[134] L. Rezzolla and O. Zanotti. *Relativistic Hydrodynamics*. Oxford University Press, 2018. ISBN: 9780198807599.

[135] Michael Ruby et al. “End States and Subgap Structure in Proximity-Coupled Chains of Magnetic Adatoms”. In: *Phys. Rev. Lett.* 115 (19 2015), p. 197204. DOI: `10.1103/PhysRevLett.115.197204`.

[136] W. B. Rui, Y. X. Zhao, and Andreas P. Schnyder. “Topological transport in Dirac nodal-line semimetals”. In: *Phys. Rev. B* 97 (16 2018), p. 161113. DOI: `10.1103/PhysRevB.97.161113`.

[137] K. Rzążewski and R. W. Boyd. “Equivalence of interaction hamiltonians in the electric dipole approximation”. In: *Journal of Modern Optics* 51.8 (2004), pp. 1137–1147. DOI: `10.1080/09500340408230412`.

[138] J.J. Sakurai and J. Napolitano. *Modern Quantum Mechanics*. ISBN: 9781108422413.

[139] Sankar Das Sarma, Michael Freedman, and Chetan Nayak. “Majorana zero modes and topological quantum computation”. In: *npj Quantum Information* 1.1 (2015), p. 15001. ISSN: 2056-6387. DOI: `10.1038/npjqi.2015.1`.

[140] Sankar Das Sarma, Michael Freedman, and Chetan Nayak. “Majorana zero modes and topological quantum computation”. In: *npj Quantum Information* 1.1 (2015), p. 15001. ISSN: 2056-6387. DOI: `10.1038/npjqi.2015.1`.

[141] M. B. Schilling et al. “Flat Optical Conductivity in ZrSiS due to Two-Dimensional Dirac Bands”. In: *Phys. Rev. Lett.* 119 (18 2017), p. 187401. DOI: `10.1103/PhysRevLett.119.187401`.

[142] Kai Phillip Schmidt, Sébastien Dusuel, and Julien Vidal. “Emergent Fermions and Anyons in the Kitaev Model”. In: *Phys. Rev. Lett.* 100 (5 2008), p. 057208. DOI: `10.1103/PhysRevLett.100.057208`.

[143] Thomas L. Schmidt et al. “Detection of Qubit-Oscillator Entanglement in Nanoelectromechanical Systems”. In: *Phys. Rev. Lett.* 104 (17 2010), p. 177205. DOI: `10.1103/PhysRevLett.104.177205`.

[144] Andreas P. Schnyder et al. “Classification of topological insulators and superconductors in three spatial dimensions”. In: *Phys. Rev. B* 78 (19 2008), p. 195125. DOI: `10.1103/PhysRevB.78.195125`.

[145] Akihiko Sekine and Kentaro Nomura. “Axion electrodynamics in topological materials”. In: *Journal of Applied Physics* 129.14 (2021), p. 141101. DOI: `10.1063/5.0038804`.

[146] Yinming Shao et al. “Optical signatures of Dirac nodal lines in $NbAs_2$”. In: *PNAS* 116.4 (2019), pp. 1168–1173. ISSN: 0027-8424. DOI: `10.1073/pnas.1809631115`.

[147] S.Q. Shen. *Topological Insulators: Dirac Equation in Condensed Matter*. Springer Series in Solid-State Sciences. Springer Singapore, 2017. ISBN: 9789811046063.

[148] Rob Shields. “Cultural Topology: The Seven Bridges of Königsburg, 1736”. In: *Theory, Culture & Society* 29.4-5 (2012), pp. 43–57. DOI: `10.1177/0263276412451161`.

[149] Alexey A. Soluyanov et al. “Type-II Weyl semimetals”. In: *Nature* 527.7579 (2015), pp. 495–498. ISSN: 1476-4687. DOI: `10.1038/nature15768`.

[150] Justin C. W. Song and Mark S. Rudner. “Chiral plasmons without magnetic field”. In: *Proceedings of the National Academy of Sciences* 113.17 (2016), pp. 4658–4663. ISSN: 0027-8424. DOI: `10.1073/pnas.1519086113`.

[151] Kabyashree Sonowal, Ashutosh Singh, and Amit Agarwal. “Giant optical activity and Kerr effect in type-I and type-II Weyl semimetals”. In: *Phys. Rev. B* 100 (8 2019), p. 085436. DOI: `10.1103/PhysRevB.100.085436`.

[152] T D Stanescu and S Tewari. “Majorana fermions in semiconductor nanowires: fundamentals, modeling, and experiment”. In: *Journal of Physics: Condensed Matter* 25.23 (2013), p. 233201. DOI: `10.1088/0953-8984/25/23/233201`.

[153] Ady Stern. “Non-Abelian states of matter”. In: *Nature* 464.7286 (2010), pp. 187–193. ISSN: 1476-4687. DOI: `10.1038/nature08915`.

[154] Yan Sun et al. “Prediction of Weyl semimetal in orthorhombic MoTe_2”. In: *Phys. Rev. B* 92 (16 2015), p. 161107. DOI: `10.1103/PhysRevB.92.161107`.

[155] Kazuaki Takasan et al. *Current-induced second harmonic generation in inversion-symmetric Dirac and Weyl semimetals*. 2020. arXiv: `2007.08887 [cond-mat.mes-hall]`.

[156] E. F. Talantsev et al. “p-wave superconductivity in iron-based superconductors”. In: *Scientific Reports* 9.1 (2019), p. 14245. ISSN: 2045-2322. DOI: `10.1038/s41598-019-50687-y`.

[157] Omid Tavakol and Yong Baek Kim. “Artificial electric field and electron hydrodynamics”. In: *Phys. Rev. Research* 3 (1 2021), p. 013290. DOI: `10.1103/PhysRevResearch.3.013290`.

[158] Barbara M. Terhal, Fabian Hassler, and David P. DiVincenzo. “From Majorana fermions to topological order”. In: *Phys. Rev. Lett.* 108 (26 2012), p. 260504. DOI: `10.1103/PhysRevLett.108.260504`.

[159] D. J. Thouless et al. “Quantized Hall Conductance in a Two-Dimensional Periodic Potential”. In: *Phys. Rev. Lett.* 49 (6 1982), pp. 405–408. DOI: `10.1103/PhysRevLett.49.405`.

[160] David Tong. *Lectures on the Quantum Hall Effect*. 2016. arXiv: `1606.06687 [hep-th]`.

[161] Andreas Topp et al. “Surface Floating 2D Bands in Layered Nonsymmorphic Semimetals: ZrSiS and Related Compounds”. In: *Phys. Rev. X* 7 (4 2017), p. 041073. DOI: `10.1103/PhysRevX.7.041073`.

[162] Iacopo Torre et al. “Nonlocal transport and the hydrodynamic shear viscosity in graphene”. In: *Phys. Rev. B* 92 (16 2015), p. 165433. DOI: `10.1103/PhysRevB.92.165433`.

[163] Riki Toshio, Kazuaki Takasan, and Norio Kawakami. “Anomalous hydrodynamic transport in interacting noncentrosymmetric metals”. In: *Phys. Rev. Research* 2 (3 2020), p. 032021. DOI: `10.1103/PhysRevResearch.2.032021`.

[164] Wang-Kong Tse and A. H. MacDonald. “Giant Magneto-Optical Kerr Effect and Universal Faraday Effect in Thin-Film Topological Insulators”. In: *Phys. Rev. Lett.* 105 (5 2010), p. 057401. DOI: `10.1103/PhysRevLett.105.057401`.

[165] G. B. Ventura et al. “Gauge covariances and nonlinear optical responses”. In: *Phys. Rev. B* 96 (3 2017), p. 035431. DOI: `10.1103/PhysRevB.96.035431`.

[166] Xiangang Wan et al. “Topological semimetal and Fermi-arc surface states in the electronic structure of pyrochlore iridates”. In: *Phys. Rev. B* 83 (20 2011), p. 205101. DOI: `10.1103/PhysRevB.83.205101`.

[167] Xiao-Bo Wang et al. “Topological surface electronic states in candidate nodal-line semimetal CaAgAs”. In: *Phys. Rev. B* 96 (16 2017), 161112(R). DOI: `10.1103/PhysRevB.96.161112`.

[168] Luzie Weithofer, Patrik Recher, and Thomas L. Schmidt. “Electron transport in multiterminal networks of Majorana bound states”. In: *Phys. Rev. B* 90.20 (2014), p. 205416. DOI: `10.1103/PhysRevB.90.205416`.

[169] Hongming Weng et al. “Weyl Semimetal Phase in Noncentrosymmetric Transition-Metal Monophosphides”. In: *Phys. Rev. X* 5 (1 2015), p. 011029. DOI: `10.1103/PhysRevX.5.011029`.

[170] Frank Wilczek. “Majorana returns”. In: *Nature Physics* 5.9 (2009), pp. 614–618. ISSN: 1745-2481. DOI: `10.1038/nphys1380`.

[171] H. J. Williams, F. G. Foster, and E. A. Wood. “Observation of Magnetic Domains by the Kerr Effect”. In: *Phys. Rev.* 82 (1 1951), pp. 119–120. DOI: `10.1103/PhysRev.82.119`.

[172] H. J. Williams et al. “Magnetic Writing on Thin Films of MnBi”. In: *Journal of Applied Physics* 28.10 (1957), pp. 1181–1184. DOI: `10.1063/1.1722603`.

[173] Benjamin D. Woods, Sankar Das Sarma, and Tudor D. Stanescu. *Charge impurity effects in hybrid Majorana nanowires*. 2021. arXiv: `2103.06880 [cond-mat.mes-hall]`.

[174] B. H. Wu and J. C. Cao. “Tunneling transport through superconducting wires with Majorana bound states”. In: *Phys. Rev. B* 85 (8 2012), p. 085415. DOI: `10.1103/PhysRevB.85.085415`.

[175] Sanfeng Wu et al. “Observation of the quantum spin Hall effect up to 100 kelvin in a monolayer crystal”. In: *Science* 359.6371 (2018), pp. 76–79. ISSN: 0036-8075. DOI: `10.1126/science.aan6003`.

[176] Jing Xia et al. “High Resolution Polar Kerr Effect Measurements of Sr_2RuO_4: Evidence for Broken Time-Reversal Symmetry in the Superconducting State”. In: *Phys. Rev. Lett.* 97 (16 2006), p. 167002. DOI: `10.1103/PhysRevLett.97.167002`.

[177] Di Xiao, Ming-Che Chang, and Qian Niu. “Berry phase effects on electronic properties”. In: *Rev. Mod. Phys.* 82 (3 2010), pp. 1959–2007. DOI: `10.1103/RevModPhys.82.1959`.

[178] Ming-Wen Xiao. “Theory of transformation for the diagonalization of quadratic Hamiltonians”. In: *arXiv e-prints*, arXiv:0908.0787 (2009), arXiv:0908.0787. arXiv: `0908.0787 [math-ph]`.

[179] N. Xu et al. “Trivial topological phase of CaAgP and the topological nodal-line transition in $\mathrm{CaAg}(\mathrm{P}_{1-x}\mathrm{As}_x)$”. In: *Phys. Rev. B* 97 (16 2018), 161111(R). DOI: `10.1103/PhysRevB.97.161111`.

[180] S. Y. Xu et al. “TOPOLOGICAL MATTER. Discovery of a Weyl fermion semimetal and topological Fermi arcs”. In: *Science* 349.6248 (2015), pp. 613–617.

[181] L. X. Yang et al. “Weyl semimetal phase in the non-centrosymmetric compound TaAs”. In: *Nature Physics* 11.9 (2015), pp. 728–732. ISSN: 1745-2481. DOI: `10.1038/nphys3425`.

[182] A. Zazunov, A. Levy Yeyati, and R. Egger. “Coulomb blockade of Majorana-fermion-induced transport”. In: *Phys. Rev. B* 84.16 (2011), p. 165440. DOI: `10.1103/PhysRevB.84.165440`.

[183] Hao Zhang et al. “RETRACTED ARTICLE: Quantized Majorana conductance”. In: *Nature* 556.7699 (2018), pp. 74–79. ISSN: 1476-4687. DOI: `10.1038/nature26142`.

[184] Björn Zocher and Bernd Rosenow. “Modulation of Majorana-Induced Current Cross-Correlations by Quantum Dots”. In: *Phys. Rev. Lett.* 111 (3 2013), p. 036802. DOI: `10.1103/PhysRevLett.111.036802`.

List of Publications

Published papers

- Ref. [50]: J. Ekström, P. Recher and T. L. Schmidt
  "*Transport properties of coupled Majorana bound states in the Coulomb blockade regime*" Phys. Rev. B **101**, 195420
- Ref. [62]: E. H. Hasdeo, J. Ekström, E. G. Idrisov, and T. L. Schmidt
  "*Electron hydrodynamics of two-dimensional anomalous Hall materials*"
  Phys. Rev. B **103**, 125106
- Ref. [49]: J. Ekström, E. H. Hasdeo, M. B. Farias, and T. L. Schmidt
  "*Kerr effect in tilted nodal loop semimetals*"
  Phys. Rev. B **104**, 125411

Papers submitted for publication

- Ref. [59]: A. Habibi, A. Z. Musthofa, E. Adibi, J. Ekström, T. L. Schmidt, E. H. Hasdeo
  "*Optical properties of topological flat and dispersive bands*" arXiv:2103.15085